# Solid-State NMR on
# Columnar Supramolecular Structures

Benzene-1,3,5-Tricarboxamides
Oligo-(*p*-Phenylenevinylene)s
Metal-Free Phthalocyanine $H_2$Pc-*op*-S-C12

## Dissertation zur Erlangung des Grades
## „Doktor der Naturwissenschaften“

im Promotionsfach Chemie am Fachbereich Chemie, Pharmazie und Geowissenschaften
der Johannes Gutenberg-Universität Mainz

vorgelegt von
Martin Wegner
geboren in Heide in Holstein

Mainz 2010

**Meinen Eltern**

# Abstract

The present work deals with the characterisation of three columnar self-assembled systems, that is, benzene-1,3,5-tricarboxamides, a peripherally thioalkyl-substituted phthalocyanine, and several oligo-(*p*-phenylenevinylene)s. In order to probe the supramolecular organisation solid-state NMR has been used as the main technique, supported by X-ray measurements, theoretical methods, and thermal analysis.

Benzene-1,3,5-tricarboxamides (BTAs) turned out to be well suited model compounds to study various fundamental supramolecular interactions, such as $\pi$-$\pi$-interactions, hydrogen bonding, as well as dynamic and steric effects of attached side chains. Six BTAs have been investigated in total, five with a CO-centred amide group bearing different side chains and one with an inverted N-centred amide group. The physical properties of these BTAs have been investigated as a function of temperature. The results indicated that in case of the CO-centred BTAs the stability of the columnar mesophase depends strongly on the nature of the side chains. Further experiments revealed a coplanar orientation of adjacent BTA molecules in the columnar assembly of CO-centred BTAs, whereas the N-centred BTA, showed a deviating not fully coplanar arrangement. These differences were ascribed to distinct hydrogen bonding schemes, involving a parallel alignment of hydrogen bonds in case of CO-centred BTAs and an antiparallel alignment in case of the N-centred counterpart.

The fundamental insights of the supramolecular organisation of BTAs could be partially adapted to an octa-substituted phthalocyanine with thiododecyl moieties. Solid-state NMR in combination with chemical shift calculations determined a tilted herringbone arrangement of phthalocyanine rings in the crystalline phase as well as in the mesophase. Moreover, $^1$H NMR measurements in the mesophase of this compound suggested an axial rotation of molecules, which is inhibited in the crystalline phase.

As a third task, the supramolecular assembly of oligo-(*p*-phenylenevinylene)s of varying length and with different polar head groups have been investigated by a combined X-ray and solid-state NMR study. The results revealed a columnar structure formation of these compounds, being promoted by phase separation of alkyl side chains and aromatic rigid rods. In this system solid-state NMR yielded meaningful insight into the isotropisation process of butoxy and 2-*S*-methylbutoxy substituted oligo-(*p*-phenylenevinylene) rods.

# Zusammenfassung

Die vorliegende Arbeit befasst sich mit der Charakterisierung von verschiedenen Benzol-1,3,5-tricarboxamiden (BTAs), eines substituierten Phthalocyanins und mehreren Oligo-($p$-Phenylvinylen)en (OPVs). Die supramolekulare Organisation dieser Verbindungen wurde mittels Festkörper-NMR untersucht. Zusätzlich wurden Röntgenstreumethoden, thermische Analyse und theoretische Berechnungen angewendet.

Benzol-1,3,5-tricarboxamide erwiesen sich als nützliche Modellsubstanzen für die Untersuchung verschiedener supramolekularer Wechselwirkungen, wie z.B. $\pi$-$\pi$-Wechselwirkungen, Wasserstoffbrückenbindungen sowie dynamische und sterische Effekte der Seitenketten. Insgesamt wurden sechs BTAs untersucht. Fünf davon waren CO-zentrierte BTAs mit Amidgruppen, die über den Carbonyl-Kohlenstoff mit dem Benzolring verbunden waren, während eines eine umgekehrte, N-zentrierte Konnektivität aufwies. In Abhängigkeit von der Temperatur wurden NMR-Spektren aller BTAs gemessen. Hierbei stellte sich die Stabilität der thermotropen flüssigkristallinen Phase als abhängig von der Art der Seitenkette dar. Im Falle der CO-zentrierten BTAs wurde eine koplanare Packung innerhalb der kolumnaren Architektur gefunden, während das N-zentrierte BTA offensichtlich eine weniger symmetrische, helikale Struktur bevorzugt, die sich durch einen Symmetriebruch in den $^1$H NMR Spektren bemerkbar machte. Die unterschiedliche Anordnung der Moleküle konnte zwei verschiedenen Wasserstoffbrückenbindungsmustern zugeordnet werden. Während sich im Fall der CO-zentrierten BTAs alle Amidgruppen am Ring parallel anordnen, so weist die Organisation des N-zentrierten BTAs eine antiparallele Orientierung auf.

Die Erkenntnisse über die supramolekulare Organisation der BTAs konnten teilweise auch auf die Untersuchungen eines achtfach substituierten Phthalocyanins mit Thiododecyl-Seitenkette angewendet werden. Durch Festkörper-NMR Spektren konnte, im Vergleich mit berechneten chemischen Verschiebungen, eine gekippte Orientierung von Phthalocyaninmolekülen sowohl in der kristallinen Phase als auch in der flüssigkristallinen Phase nachgewiesen werden. Darüber hinaus deuteten $^1$H NMR Messungen auf eine axiale Rotation von Phthalocyaninmolekülen in der Mesophase.

Der letzte experimentelle Abschnitt behandelt die Organisation einer Reihe von Oligo-($p$-Phenylvinylen)en verschiedener Länge und Modifikation. Die Verbindungen, die zudem mit unterschiedlichen polaren Gruppen ausgestattet waren, wurden mittels Festkörper-NMR und Röntgenbeugung untersucht. Auch diese Verbindungen zeigten eine kolumnare Organisation, die jedoch hauptsächlich durch eine Phasenseparation der aliphatischen Seitenketten vom starren $\pi$-System verursacht wird. In diesem System konnten geringfügige Unterschiede im Isotropisierungsverhalten von Butoxy- und 2-$S$-Methylbutoxy-substituierten Oligo-($p$-Phenylvinylen)en festgestellt werden.

# Contents

# List of Abbreviations

| | |
|---|---|
| 1D | one-dimensional |
| 2D | two-dimensional |
| 2D WAXS | 2-*two-dimensional* wide angle X-ray scattering |
| *cw* | continuous wave |
| AFM | atomic force microscopy |
| AHT | average hamiltonian theory |
| BABA | back-to-back |
| BTA | benzene-1,3,5-tricarboxamides |
| CD | circular dichroism |
| CR | composite refocusing |
| CRAMPS | combined rotation and multiple pulses |
| CSA | chemical shift anisotropy |
| CTP | coherence transfer pathway |
| DQ | double quantum |
| DSC | differential scanning calorimetry |
| EFG | electric field gradient |
| ERM | evolution rotor modulation |
| EXCY | exchange spectroscopy |
| FET | field effect transistor |

| | |
|---|---|
| FID | free induction decay |
| FSLG | frequency switched LEE-GOLDBURG |
| FWHM | full width at half maximum |
| $H_2Pc$ | metal-free phthalocyanine |
| HETCOR | heteronuclear correlation |
| HOMO | highest occupied molecular orbital |
| HSQC | heteronuclear single quantum correlation |
| INADEQUATE | incredible natural abundance double quantum transfer |
| INEPT | insensitive nuclei enhancement by polarisation transfer |
| LUMO | lowest unoccupied molecular orbital |
| MAS | magic angle spinning |
| MQC | multiple quantum coherence |
| NICS map | nucleus independent chemical shift map |
| NMR | nuclear magnetic resonance |
| NOESY | nuclear OVERHAUSER enhancement spectroscopy |
| OLED | organic light-emitting diode |
| OMAS | off-magic angle spinning |
| OPV | oligo-(*p*-phenylenevinylene) |
| PA | polyacetylene |
| Pc | phthalocyanine |
| PISSARRO | phase-inverted supercycled sequence for attenuation of rotary resonance |
| PMLG | phase modulated LEE-GOLDBURG |
| POM | polarised optical microscopy |

| | |
|---|---|
| PPV | poly-(*p*-phenylenevinylene) |
| RF | radio frequency |
| RFID | radio frequency identification |
| SANS | small angle neutron scattering |
| SPE | single pulse excitation |
| SPINAL | small phase incremental alternation decoupling |
| SQ | single quantum |
| TMS | tetramethylsilane |
| TOBSY | total through-bond correlation spectroscpy |
| TPPM | two pulse phase modulation |
| TQ | triple quantum |
| TTSS | tetrakis(trimethylsilyl)silane |
| UV | ultraviolet |
| XiX | x inverse-x |

# 1. Introduction

Most electronic devices used in daily life are based on elaborate silicon technology. Common production schemes like high-vacuum photolithographic procedures fabricate electronic items, which often require clean-room facilities for further processing. This technology is challenging in itself; it is costly, heat and energy intensive, and requires robust substrates. It appears that silicon technology is the appropriate method, facilitating high standard devices as computer chips or solar cells. However, silicon based components are lacking certain desirable properties such as flexibility, transparency, and the ability to be deposited onto a soft surface.

For lower level applications and everyday use like the "electronic newspaper", wallet-ready cards and Radio Frequency Identification (RFID) tags, a cheaper method for large-volume production is desirable. Most of these requirements, in particular those improving the cost efficiency, can be met by means of *plastic electronics*[1]. Yet 30 years ago, organic chemists began to discover semiconducting properties of conjugated compounds, real polymers, and smaller oligomers[2]. Some of these materials are capable of emitting light[3] and have entered the market as so-called *organic light-emitting diodes* (OLEDs), already being used in display panels[4]. Other possible applications followed quickly and today research expands towards organic photovoltaic[5] and organic sensors[6]. Since organic electronics is intended to perform logic operations, devices like organic *field effect transistors* (FETs) are investigated[7].

In the field of organic electronics, columnar liquid-crystals have recently been attracting a lot of interest. The electric properties of these materials are based on the overlap of molecular orbitals facilitating *one-dimensional* charge carrier transport along the columnar axis. In a simple way of putting it, the disc-shaped molecule, known as the *discotic mesogen*, forms a conductive channel surrounded by an insulating periphery of alkyl chains. However, applications involving columnar liquid crystals are still scarce, since 1D electric conduction puts high demands on the internal degree of order of the columnar arrangement. The term "order" depends on the application and may reach from intermolecular order on the *nanometer* scale to defectless charge carrier transport on the *millimeter* scale. Thus, besides general requirements to the electronic structure of the molecules (*e.g.*, a small band gap, high charge carrier mobilities, high quantum yields, *etc.*), the order of the assembly is of outstanding importance for the electric performance of a material.

Another important issue relating to the applicability of a compound is the need for low processing temperatures, since the upper temperature limit for the fabrication of soft electronic devices is about 200 °C. The lowering of melting or clearing point temperatures (*i.e.*, the transition temperature between the liquid-crystalline phase and the isotropic melting) can be achieved by introducing mobile substituents, which induce disorder into the system. Thus, the processability and the high degree of order are two opposing aspects in the field of columnar liquid-crystals, which will be addressed in this work.

This doctoral thesis deals with three different types of mesogenes, which are known to form columnar assemblies. By far, the most information about the investigated supramolecular systems have been obtained from solid-state *Nuclear Magnetic Resonance* (NMR) studies. Subsequent to the introduction, **Chapter 2** will therefore provide a broad and thorough introduction to solid-state NMR, beginning with the fundamental principles of quantum mechanics and the theoretical framework of NMR. Thereafter, relevant NMR interactions in solids will be treated and basic methods necessary to perform high-resolution solid-state NMR will be presented. Finally, more advanced solid-state NMR methods, which have been applied in this work, will be described in detail.

In **Chapter 3**, the results on the self-assembling properties of benzene-1,3,5-tricarboxamides will be presented. Electric conduction based on a single benzene ring is not possible, since effective charge carrier transport requires more extended $\pi$-conjugated systems such as phthalocyanines or hexabenzocoronenes[8]. However, benzene-1,3,5-tricarboxamides may serve as model compounds for the assembling process of disc-shaped mesogens, capable of forming intermolecular hydrogen bonds. In this study a total number of six molecules have been investigated thoroughly, five of them with the carbonyl group of the amide functionality attached to the ring and one compound with an inverted amide group, that is, with the nitrogen atom linked to the benzene ring. With respect to the order requirement for electric conduction in discotic materials, it will be seen how varying aliphatic moieties change the stability of the columnar assembly and which parameters cause the molecules to assemble in a columnar mesophase, a columnar crystalline phase, or even a non-columnar phase. Due to the dependence of the $^1$H chemical shift on the strength of the hydrogen bonds, solid-state NMR is a powerful tool to identify the importance of the hydrogen bonding units for the columnar arrangement. It will be seen that the symmetry of the assembly is closely related to its supramolecular order, hence the question of whether or not the intrinsic symmetry of molecules persists in the supramolecular environment or a symmetry breaking occurs. As will be this relates to the periphery of the column as well as to the hydrogen-bonded scaffold itself. To support the results obtained from solid-state NMR experiments, elaborate molecular dynamics simulations have been conducted.

**Chapter 4** deals with a substituted phthalocyanine, that is known to be a classical discotic mesogene prone to $\pi$-mediated stacking. Phthalocyanines have been widely investigated in terms of their suitability for various applications. The sample investigated in this NMR study is equipped with eight thioalkyl side chains. The stability of the columnar assembly might therefore be influenced by both, the electronic impact of sulphur to the aromatic ring as well as the steric effect of the larger sulphur atom. The thermal behaviour of the compound was investigated by thermal analysis and variable temperature NMR. Additionally, the long-range organisation of the material was probed by wide angle X-ray scattering (WAXS). Like in the case of tricarboxamides, *density functional theory* calculations in combination with solid-state $^1$H NMR methods enabled insight into the symmetry of the molecules within the columnar arrangement.

In **Chapter 5**, the topic of discotic liquid-crystals is extended towards rod-like molecules. In this last part of the work oligo-($p$-phenylenevinylene)s are investigated, containing a large aromatic rigid rod as well as a hydrogen bonding polar head group. These compounds are known to form large helical assemblies in apolar solvents, suggesting that this class of compounds forms columnar architectures in the bulk as well. The main question here will focus on how hydrogen bonding competes with strong tendency of the aromatic backbone to form $\pi$-$\pi$-stacking. To this end, solid-state $^1$H and $^2$H NMR measurements in combination with extended X-ray analysis turned out to be particular helpful.

Finally, all experimental results are summarised in **Chapter 6**.

# 2. Theory of Basic and Advanced NMR Experiments

In this first chapter the most important aspects of *Nuclear Magnetic Resonance* (NMR) will be reviewed thoroughly to enable a decent understanding of even advanced solid-state NMR methods used in this thesis for the sake of completeness but with a reasonable brevity. This approach is addressed to someone already having a background in NMR and a basic knowledge about quantum mechanics. A general introduction can be found in the textbooks of KEELER[9] and LEVITT[10], whereas the monograph of DUER[11] offers a more detailed description of solid-state NMR in particular. It should be noted that a general introduction to NMR with regard to the experimental chapter is essential for the integrity of the current work, however, all spectra, their interpretations, and conclusions will be explicitly discussed in a rather self-contained manner. It is therefore possible to proceed to the experimental chapter without being at the risk of missing an important point of the argumentation. Moreover, the discussion refers to the corresponding section in this theoretical chapter if a more profound knowledge about a certain method might be helpful.

The following paragraph will start with the observation of split energy levels in the presence of a magnetic field due to the ZEEMAN effect. The expressions for energy levels in Magnetic Resonance will be given and the density matrix formalism as a method of characterising the time evolution of a spin system will be introduced accordingly. This leads to the *product operator* algebra which sufficiently explains most advanced NMR pulse sequences. Furthermore, the necessary mathematical framework for treating a rotating sample under so-called magic angle conditions will be presented. A theoretical description of the basic single pulse FT-NMR experiment will be given and the recording schemes for 1 and 2D data acquisition will be explained. After that, the focus changes towards the description of anisotropic internal spin interactions, present in a solid sample, whereupon certain basic techniques of solid-state NMR in particular will be examined. This section covers techniques such as magic angle spinning, cross polarisation, as well as homo- and heteronuclear decoupling techniques. The last paragraph finally will be concerned with recoupling methods in general and more specifically with Double Quantum NMR. Firstly, double quantum coherences in the solid state are commonly generated by homonuclear dipolar recoupling methods. Secondly, double quantum excitation can be based on isotropic J-couplings, which is commonly used in solution NMR experiments. In this paragraph experiments such as INADEQUATE and BABA, enabling Double Quantum NMR by means of completely different mechanisms will be compared. In a final step solid state version of the HSQC experiment will be introduced.

As mentioned above, this first chapter is not meant as an introduction to solid-state NMR; therefore equations will not be derived one by one. It is aimed to give a suitable overview about the common formalism used in modern NMR spectroscopy. Besides the cited books by KEELER and LEVITT a more precise standard work on continuous NMR is that by ABRAGAM[12], whereas a standard reference for pulsed FT-NMR experiments can be found in the work of ERNST, BODENHAUSEN and WOKAUN[13]. Among others, a few textbooks on solid-state NMR should be mentioned here. Apart from the introduction by DUER[11] there are standard works by MEHRING[14] and SCHIDT-ROHR/SPIESS[15], the latter mostly deals with amorphous materials or polymers. Due to the affinity of Magnetic Resonance and *Rotational Microwave Spectroscopy* some expressions in particular those related to Density Matrix Formalism might also be found in the textbooks of GORDY and COOK[16] or KROTO[17]. The most suitable introduction to Density Matrix Formalism as well as all fields of quantum mechanics can be found in the textbook of SAKURAI[18].

## 2.1. Introduction to NMR

The quantum state of a sample and its evolution in time are fully described by the time-dependent Schrödinger Equation. Due to its complexity, however, it is only a purely formal starting point for a first simplification known as the so-called *Spin Hamiltonian Hypothesis*[10]. Thereby factorised into a spin part and a residual wave function containing all other information about the system the Schrödinger equation can be quoted as:

$$\begin{aligned} \frac{\partial}{\partial t}|\psi_{spin}(t)\rangle &= -i\hat{\mathcal{H}}_{spin}|\psi_{spin}(t)\rangle \\ \text{with}: |\Psi_{full}(t)\rangle \quad &\rightarrow \quad |\psi'(t)\rangle\ |\psi_{spin}(t)\rangle \end{aligned} \tag{2.1}$$

where the wave function $|\psi_{spin}(t)\rangle$ describes the spin state of the system and the Hamiltonian $\hat{\mathcal{H}}_{spin}$ bears all nuclear spin interactions. Since the energy differences between spin interactions and other molecular interactions are large, the Spin Hamiltonian Hypothesis is a valid approximation at ambient temperature. At very low temperature, the thermal energy is small and comparable to energy states in NMR. Here, the assumption is not fulfilled anymore[a].

The Spin Hamiltonian $\hat{\mathcal{H}}_{spin}$ can be divided into several parts that refer to different interactions important in NMR:

$$\hat{\mathcal{H}} = \underbrace{\hat{\mathcal{H}}_Z + \hat{\mathcal{H}}_{RF}}_{external} + \underbrace{\hat{\mathcal{H}}_Q + \hat{\mathcal{H}}_{CS} + \hat{\mathcal{H}}_D + \hat{\mathcal{H}}_J}_{internal} \tag{2.2}$$

Two of these Hamiltonian are denoted *external* because they describe the interactions of the nuclear spins with the macroscopic environment. First of all, there is $\hat{\mathcal{H}}_Z$ describing the ZEEMAN *interaction* of spins and the external magnetic field. This is the most important term, since it leads to a discrimination of energy levels and therefore facilitates the observation of NMR transitions. It is the strongest interaction except for nuclei having a large quadrupole moment. The second external Hamiltonian $\hat{\mathcal{H}}_{RF}$ incorporates a specific (purposive) interference of radio frequency (RF) pulses and the spin system. All other interactions are so-called *internal* spin interactions which will be discussed one by one in section 2.1.6. Barring the Hamiltonian of the *quadrupolar interaction*, which is often quite large, all other terms are small compared to the ZEEMAN term, which leads to a major simplification in the theoretical description of NMR interactions (see section 2.1.3). The remaining internal interactions important in this work are the *chemical shift* $\hat{\mathcal{H}}_{CS}$, the *dipolar interaction* $\hat{\mathcal{H}}_D$ and the J-*coupling* $\hat{\mathcal{H}}_J$. $\hat{\mathcal{H}}_{CS}$ describes the interaction of the magnetic moment of the nuclei with the local magnetic field within the molecule. Due to the non-uniform valence electron distribution this usually differs slightly from the external magnetic field in magnitude and direction. The dipolar term $\hat{\mathcal{H}}_D$ takes the interaction between the magnetic moments of the spins into account. The J-coupling is a weak interaction and in solids is it usually superimposed by stronger interactions. Since it is mediated via bond electrons it can however be used to probe the connectivity of carbon atoms, which has been of great use for this work, hence J-coupling will also be discussed in section 2.1.6.4.

### 2.1.1. The ZEEMAN Effect

In presence of a magnetic field molecular or atomic energy levels may split into several states depending on the $z$-component of the *total angular momentum* and the quantum

---

a) Also at ordinary temperatures some interactions cannot be explained by a pure spin Hamiltonian, as for example the *spin-rotation interaction*. This shows that *Spin Hamiltonian Hypothese* is a very loose term.

number $M_J$ defining it. This effect was fist observed by the Dutch physicist *Pieter* ZEEMAN in 1896 who found spectral lines breaking up in a static magnetic field. The so-called ZEEMAN effect does not only refer to the splitting of optical lines, but generally denotes the magnetic field induced splitting of energy states that would otherwise be degenerate. In a semiclassical picture, the magnetic dipole moment $\vec{\mu}$ is proportional to the angular momentum $\vec{\mathrm{I}}$ of the nucleus with the gyromagnetic constant $\gamma$ being a nucleus dependent factor:

$$\vec{\mu}_I = \gamma \vec{\mathrm{I}} \tag{2.3}$$

According to the quantum theory of the angular momentum, the squared angular momentum operator and one of its components, by convention the $z$-component, share a common set of eigenfunctions. Thus, energy states in Magnetic Resonance are defined by two quantum numbers $I$ and $m$, which can be represented by vectors as depicted in figure 2.1. For the eigenvalues of the total angular momentum we find:

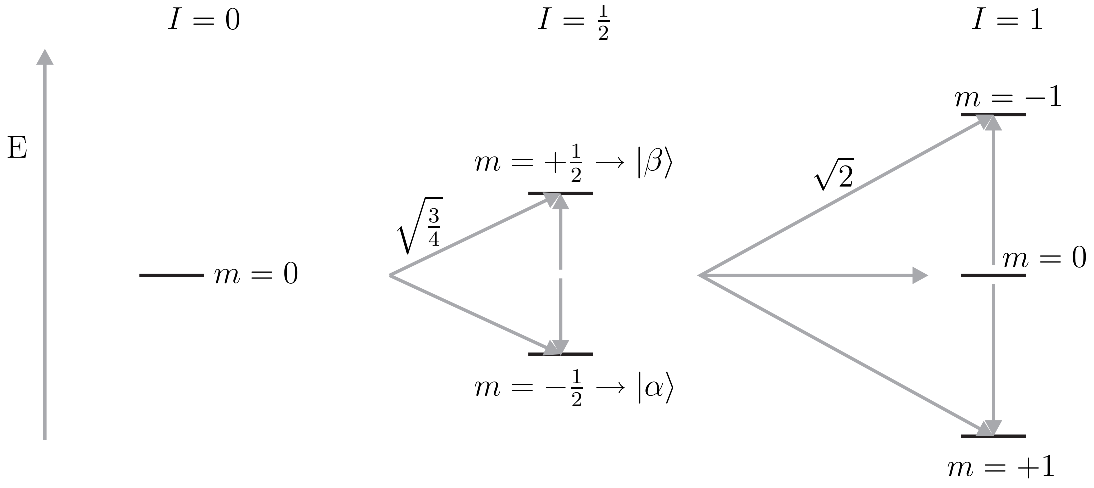

**Figure 2.1.** Illustration of the ZEEMAN-states. The length of the diagonal or horizontal vectors represents the magnitude of the total angular momentum, whereas vertical arrows represent the magnitude of the $z$-component of the total angular momentum.

$$|\vec{\mathrm{I}}| = \sqrt{I\,(I+1)}\hbar \tag{2.4}$$

In NMR a nuclear spin state with $I \geq 1/2$ splits into different states with the ZEEMAN Hamiltonian describing the interaction:

$$\hat{\mathcal{H}}_Z = -\gamma \hbar \mathrm{B}_0 \hat{\mathrm{I}}_z \tag{2.5}$$

$\hat{\mathcal{H}}_Z$ contains the angular momentum operator $\hat{\mathrm{I}}_z$ whose eigenvalues are given as:

$$|\mathrm{I}_z| = |m|\hbar \qquad \text{with } m = \{-I,\ -I+1, \ldots\ +I\} \tag{2.6}$$

Thus, the energy states given in figure 2.1 can simply be written as:

$$E_m = -m\gamma\hbar \mathrm{B}_0 \tag{2.7}$$

The number of states depends on the spin quantum number of $I$, hence on the nucleus. In case $I = 0$, there is only one state, whereas for $I = 1/2$ two states are possible. In the particular case of an $I = 1/2$, the state with $m = +1/2$ is commonly denoted $|\alpha\rangle$ and that with $m = -1/2$ is termed $|\beta\rangle$, which is higher in energy as can be seen in figure 2.1.

### 2.1.2. Density Matrix Formalism

Although quantum mechanics is already obeyed, the derived equations are still intuitive. By measuring the spin state of an $I = 1/2$ atom we find it in one of the two ZEEMAN eigenstates. As illustrated in figure 2.1 these can be represented by a vector pointing either parallel or antiparallel to the direction of the external magnetic field. In case of a single nucleus, the general ansatz for the wave function is a linear combination of the two eigenstates:

$$|\psi\rangle = c_\alpha|\alpha\rangle + c_\beta|\beta\rangle \tag{2.8}$$

The expectation value of the angular momentum, hence the magnetic moment of the nucleus is proportional to the probability it occupies one of the two states:

$$\langle\vec{\mu}_z\rangle \quad \propto \quad c_\alpha c_\alpha^* - c_\beta c_\beta^* \tag{2.9}$$

This level of theory is already sufficient to describe transition frequencies and populations in continuous wave NMR. Today's high resolution NMR, however, makes use of pulsed RF fields and techniques for fast data acquisition. In order to fully exploit this technique an efficient way to describe the time evolution of the spin system is required. In principle it can be achieved by solving the time-dependent Schrödiger equation 2.1, although that implies a very tedious procedure. It involves basically three steps, the solution itself, the calculation of components of the angular momentum, and finally the computation of the ensemble average which is another non-trivial step. The difficulties arise mainly due to the fact that in case of a standard NMR experiment a large number spins, a spin ensemble, is probed and not merely a single spin. Going back to equation 2.8 we could naively write down the magnetisation of a spin ensemble by summing up the population differences. In fact this would be possible if we were looking at a *pure ensemble*, sharing the same wave function, thus having only one set of coefficients of ZEEMAN eigenstates. A more realistic situation for a sample in a thermal equilibrium is the so-called *mixed ensemble*, considering different wave function for the nuclei. For a large number of spins, however, it is sufficient to include a statistical weighting factor that allows for the probability of finding a particular spin state and its corresponding coefficient. In case of the $z$-magnetisation we can now write:

$$\vec{\mathrm{M}}_z \quad \propto \quad \overline{c_\alpha c_\alpha^* - c_\beta c_\beta^*} \tag{2.10}$$

The contribution of the spin state can be "mapped" within the so-called *Density Matrix* being mathematically written as:

$$\hat{\rho} = \sum_{i=1}^{n} p_i |\psi\rangle\langle\psi| \tag{2.11}$$

In this expression a two-dimensional array of pure state probabilities, like $c_{\alpha i} c_{\alpha i}^*$, is generated by the outer product of the wave functions. These are averaged by means of their statistical contribution $p_i$ to the mixed state. In case of an ensemble of isolated spins the density matrix of the mixed state has the simple form:

$$\hat{\boldsymbol{\rho}}_{1\ spin} = \begin{pmatrix} \overline{c_\alpha c_\alpha^*} & \overline{c_\alpha c_\beta^*} \\ \overline{c_\beta c_\alpha^*} & \overline{c_\beta c_\beta^*} \end{pmatrix} \tag{2.12}$$

Here, the diagonal terms as $\overline{c_\alpha c_\alpha^*}$ are denoted populations which for example define the $z$-magnetisation as in equation 2.10. The mixed off-diagonal elements like $\overline{c_\alpha c_\beta^*}$ are the complex magnitudes of a superposition of the two eigenstates $|\alpha\rangle$ and $|\beta\rangle$ called *coherences*. In order to demonstrate the power of the formalism the density matrix of a coupled two-spin system is given in figure 2.2. Apparently, this density matrix is a four times four array bearing populations of and coherences between the four eigenstates $|\alpha\alpha\rangle$, $|\alpha\beta\rangle$, $|\alpha\beta\rangle$, and $|\beta\beta\rangle$. The off-diagonal elements in a density matrix of a coupled two-spin system can further be divided into coherences of different orders, that is, 0, 1, or 2, depending on how many indices in the product $c_{ij} c_{kl}^*$ do not coincide. Two elements can therefore be assigned to zero quantum (ZQ) of the order 0, eight elements to single- (SQ) having the order 1 and two elements define a double- (DQ) coherence of the order 2. The coherences can be understood as a persisting polarisation transfer between two levels as it is indicated by the arrows on the left-hand side in figure 2.2. It should be mentioned that ZQ and DQ coherences cannot be detected directly. They are collectively denoted *multiple quantum coherences* (MQ) which need to be converted into SQ coherences prior to detection.

The actual usefulness of the formalism, however, is demonstrated by calculating the expectation value of an interaction $A$ given by the trace of the density matrix times the corresponding operator $\hat{A}$:

$$\langle \hat{A} \rangle = Tr\{\hat{\boldsymbol{\rho}} \hat{A}\} \tag{2.13}$$

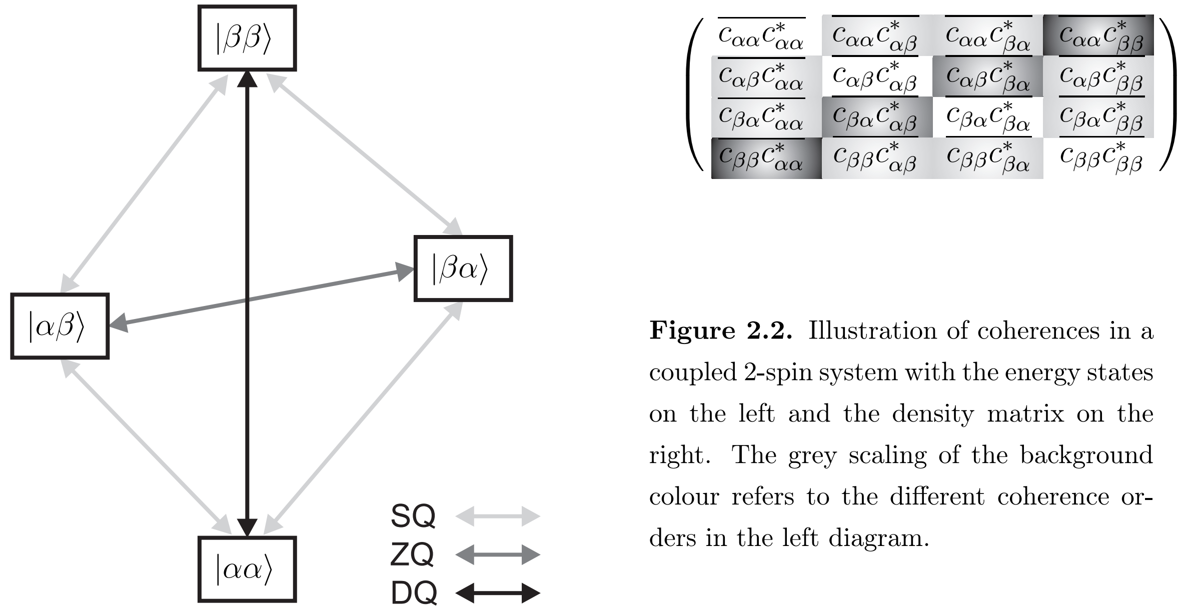

$$\begin{pmatrix} \overline{c_{\alpha\alpha}c^*_{\alpha\alpha}} & \overline{c_{\alpha\alpha}c^*_{\alpha\beta}} & \overline{c_{\alpha\alpha}c^*_{\beta\alpha}} & \overline{c_{\alpha\alpha}c^*_{\beta\beta}} \\ \overline{c_{\alpha\beta}c^*_{\alpha\alpha}} & \overline{c_{\alpha\beta}c^*_{\alpha\beta}} & \overline{c_{\alpha\beta}c^*_{\beta\alpha}} & \overline{c_{\alpha\beta}c^*_{\beta\beta}} \\ \overline{c_{\beta\alpha}c^*_{\alpha\alpha}} & \overline{c_{\beta\alpha}c^*_{\alpha\beta}} & \overline{c_{\beta\alpha}c^*_{\beta\alpha}} & \overline{c_{\beta\alpha}c^*_{\beta\beta}} \\ \overline{c_{\beta\beta}c^*_{\alpha\alpha}} & \overline{c_{\beta\beta}c^*_{\alpha\beta}} & \overline{c_{\beta\beta}c^*_{\beta\alpha}} & \overline{c_{\beta\beta}c^*_{\beta\beta}} \end{pmatrix}$$

**Figure 2.2.** Illustration of coherences in a coupled 2-spin system with the energy states on the left and the density matrix on the right. The grey scaling of the background colour refers to the different coherence orders in the left diagram.

Furthermore, the density matrix formalism enables a computation of the time evolution of a spin system provided the initial state is known. The evolution can then be calculated using the VON NEUMANN equation:

$$\frac{\partial \hat{\boldsymbol{\rho}}}{\partial t} = -i[\hat{\mathcal{H}}, \hat{\boldsymbol{\rho}}_{(t)}] \tag{2.14}$$

The general solution to this equation is given by:

$$\hat{\boldsymbol{\rho}}_{(t)} = \hat{U}_{(t)}\hat{\boldsymbol{\rho}}_0\hat{U}^{-1}_{(t)} \qquad \text{with } \hat{U}_{(t)} = e^{-i\hat{\mathcal{H}}t} \tag{2.15}$$

The initial state for all experiments is indeed known, since it is defined by the thermal equilibrium. In this state the sample is polarised having a bulk magnetisation in $z$-axis, i.e., aligned with the axis of the external magnetic field. Due to the equilibrium condition the equality $\frac{\partial \hat{\boldsymbol{\rho}}}{\partial t} = 0$ is met. All off-diagonal terms are zero and the populations are given by the BOLTZMANN distribution, leading to a general definition of the initial state of a spin system[12]:

$$\hat{\boldsymbol{\rho}}_{eq.} = \frac{e^{-\frac{\hbar}{kT}\cdot\hat{\mathcal{H}}}}{Tr\{e^{-\frac{\hbar}{kT}\cdot\hat{\mathcal{H}}}\}} \tag{2.16}$$

Applying the ZEEMAN Hamiltonian 2.5 and equation 2.16, and taking only the first-order term of a Taylor series expansion, leads to a simple BOLTZMANN distribution of populations.

### 2.1.3. Secular Approximation

One of the fundamental theorems of the quantum mechanics of angular momentum states that only a single component of the angular momentum can be measured independently, by convention the $z$-component[19]. This statement already led to the ZEEMAN Hamiltonian and the energy states depicted in figure 2.1. However, the magnetic dipole moment of a nucleus cannot be fully described by the ZEEMAN basis, since also other components contribute to the untruncated interaction Hamiltonian. The different spin interactions may be treated by means of perturbation theory with $\hat{\mathcal{H}}_Z$ being the unperturbed system. In this context only those components that are diagonal in the basis of the ZEEMAN Hamiltonian contribute to the total energy of the system, i.e., all parts not commuting with $\mathcal{H}_Z$ vanish. This can be illustrated by a perturbation field added to the external $z$-field, as shown in figure 2.3. In case of a small perturbation, the increment of the effective field is still governed by the component aligned with the $z$-field, whereas the perpendicular component is negligible. The perpendicular component vanishes over time and as it is moreover subject to fast oscillations average to zero, indicated by equation 2.17.

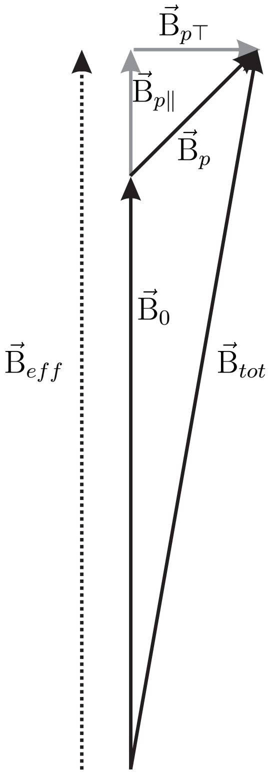

$$\vec{\mathrm{B}}_{tot} = \vec{\mathrm{B}}_0 + \vec{\mathrm{B}}_{p\|}\sqrt{1 + \frac{|\vec{\mathrm{B}}_{p\top}|}{|\vec{\mathrm{B}}_{p\|}| + |\vec{\mathrm{B}}_0|}}\vec{\mathrm{e}}_p \qquad (2.17)$$

$$\vec{\mathrm{B}}_{eff} \approx \vec{\mathrm{B}}_{tot}$$

$$\vec{\mathrm{B}}_p = f_{(t)}$$

$$\langle\vec{\mathrm{B}}_{p\|}\rangle_{r.f.} \neq 0$$

$$\langle\vec{\mathrm{B}}_{p\top}\rangle_{r.f.} \approx 0$$

**Figure 2.3.** Graphical Illustration of the Secular Approximation. The parallel component of the perturbation is not time dependent and adds to the $\vec{\mathrm{B}}_0$-field. The perpendicular component is time-dependent and averages out consequently.

A common procedure usually applied when dealing with interaction Hamiltonian is the *rotating frame transformation.* According to [15] this can be written as:

$$\hat{\boldsymbol{\rho}}'_{(t)} = e^{i\hat{\mathcal{H}}_0 t}\hat{\boldsymbol{\rho}}(t)e^{-i\hat{\mathcal{H}}_0 t} \tag{2.18}$$

The virtue of this procedure is the removal of the ZEEMAN offset. After this transformation, the spins precessing with the LARMOR frequency appear static within the rotating frame, which greatly simplifies the treatment of RF pulses. Moreover, the transformation has a similar effect as the secular approximation: As it is suggested by figure 2.3, the component $\vec{\mathrm{B}}_{p\|}$ has a non-vanishing time average in contrast to $\vec{\mathrm{B}}_{p\top}$, which averages out by rotating the reference frame about the $z$-axis.

### 2.1.4. Average Hamiltonian Theory

In this work the technique of *magic angle spinning* (MAS) is applied. Using this technique, the sample is rotated rapidly about an axis being inclined at the magic angle with respect to the magnetic field. The aim and the technical aspects will be given later in section 2.2.1. Under MAS conditions, however, the Hamiltonian becomes time-dependent which means that equation 2.15 is not valid anymore. In this paragraph a short overview will be given of how to derive an appropriate Hamiltonian nonetheless by means of the so-called *Averaged Hamiltonian Theory* (AHT).

The Hamiltonian within the propagator $e^{-i\hat{\mathcal{H}}t}$ needs to be exchanged by an approximated Hamiltonian that accounts for the whole time period spin evolution is considered. This average Hamiltonian can be achieved by splitting the evolution period into $N$ small steps of duration $\tau$ in which the partial Hamilton operators are assumed to be constant in time:

$$\hat{U}_{(t)} = e^{-i\hat{\mathcal{H}}_n\tau_n}e^{-i\hat{\mathcal{H}}_{n-1}\tau_{n-1}} \ldots e^{-i\hat{\mathcal{H}}_1\tau_1} = e^{-i\overline{\hat{\mathcal{H}}}\tau} \tag{2.19}$$

The average Hamiltonian $\overline{\hat{\mathcal{H}}}$ can however not be written as the sum of the partial Hamiltonians because simple exponential algebra does not apply due to $[\hat{H}_i, \hat{H}_j] \neq 0$. The so-called BAKER-CAMPBELL-HAUSDORFF relation can be used to expand the propagators with non-commuting Hamiltonians:

$$e^{\hat{B}}e^{\hat{A}} = exp\left\{\underbrace{\hat{B}+\hat{A}}_{1^{st}} + \underbrace{\frac{1}{2}[\hat{A},\hat{B}]}_{2^{nd}} + \underbrace{\frac{1}{12}([\hat{B},[\hat{B},\hat{A}]] + [[\hat{B},\hat{A}],\hat{A}])}_{3^{rd}\ order} + \ldots\right\} \tag{2.20}$$

According to this equation the Hamiltonian can be written as a sum of different orders:

$$\overline{\hat{\mathcal{H}}} = \overline{\hat{\mathcal{H}}}^{(0)} + \overline{\hat{\mathcal{H}}}^{(1)} + \overline{\hat{\mathcal{H}}}^{(2)} \ldots \tag{2.21}$$

The first order average Hamiltonian is given as:

$$\overline{\hat{\mathcal{H}}}^{(0)} = \frac{1}{\tau_R} \sum_{i=1}^{n} \hat{\mathcal{H}}_i \tau_i \tag{2.22}$$

In the general case where the Hamiltonians $\hat{\mathcal{H}}_i$ are not constant in time they do not commute. It is obvious that the approximation improves the smaller the time increment $\tau_i$, since the commentator $[\hat{\mathcal{H}}(t), \hat{\mathcal{H}}(t) + \tau]$ vanishes for infinitely small time steps. Thus, the different orders are calculated by means of a sum integrals, the so-called MAGNUS expansion:

$$\overline{\hat{\mathcal{H}}}^{(0)} = \frac{1}{\tau_R} \int_0^{\tau_R} \hat{\mathcal{H}}(t) dt \tag{2.23}$$

$$\overline{\hat{\mathcal{H}}}^{(1)} = -\frac{i}{2\tau_R} \int_0^{\tau_R} \int_0^{t_1} [\hat{\mathcal{H}}(t_1), \hat{\mathcal{H}}(t_2)] dt_2 dt_1 \tag{2.24}$$

$$\overline{\hat{\mathcal{H}}}^{(2)} = -\frac{1}{6\tau_R} \int_0^{\tau_R} \int_0^{t_1} \int_0^{t_2} [\hat{\mathcal{H}}(t_1), [\hat{\mathcal{H}}(t_2), \hat{\mathcal{H}}(t_3)]] + [\hat{\mathcal{H}}(t_3), [\hat{\mathcal{H}}(t_2), \hat{\mathcal{H}}(t_1)]] dt_3 dt_2 dt_1 \tag{2.25}$$

$$\overline{\hat{\mathcal{H}}}^{(3)} = \quad \dots \quad \dots \quad \dots \tag{2.26}$$

If the commutator $[\hat{\mathcal{H}}(t_1), \hat{\mathcal{H}}(t_2)]$ vanishes the represented interaction is termed *inhomogeneous*[20]. In contrast to *homogeneous* interactions, these can be treated in a much easier manner formally, but also experimentally, as will be seen for example in the performance of line narrowing methods (see section 2.2.1) or decoupling techniques (see section 2.2.6). It will be shown that homonuclear broadening in proton containing samples is a very intricate task. For inhomogeneous interactions, higher order terms of the MAGNUS expansion all vanish leaving only the first order term $\overline{\hat{\mathcal{H}}}^{(0)}$. Basically, with this knowledge general expressions of various time-dependent NMR interactions with respect to a lab-fixed coordinate system can be derived. The most important *internal* NMR interactions, i.e. interactions being intrinsically associated with the material itself, will be discussed in section 2.1.6. Prior to their one-by-one introduction, a more general approach using spherical tensor representation will be covered, greatly simplifying the treatment of time-dependent NMR Hamiltonians.

## 2.1.5. External Spin Interactions

### 2.1.5.1. *External Interactions I*: The ZEEMAN Interaction

Before continuing with *internal spin interactions* in section 2.1.6, the *external spin interaction* will be examined in this and the following section. The most important term in

Magnetic Resonance is the ZEEMAN interaction introduced in section 2.1.1. For the sake of completeness it is given here a second time:

$$\hat{\mathcal{H}}_Z = -\gamma\hbar \mathrm{B}_0 \hat{I}_z \tag{2.27}$$

The ZEEMAN interaction does not only cause energy discrimination but, provided a high magnetic field strength, it is also the biggest term which leads to important simplifications (see section 2.1.3). Apart from the quadrupolar Hamiltonian that may even exceed the ZEEMAN Hamiltonian for some nuclei, the *high-field approximation* is always fulfilled for $I = 1/2$ nuclei and the magnetic field strengths typically encountered in NMR. Compared to the thermal energy, however, the ZEEMAN term is still relatively small. The difference in the populations in $|\alpha\rangle$ and $|\beta\rangle$ levels are therefore very small as illustrated in figure 2.4.

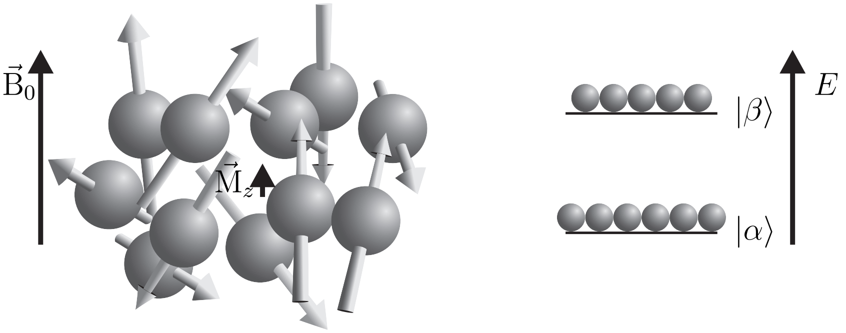

**Figure 2.4.** Illustration of the ZEEMAN interaction. In a classical picture (*left*) the spins possess almost random orientation, i.e., even in the strongest magnetic fields the induced alignment, thus the polarisation $\vec{\mathrm{M}}_z$ is very small. In a quatum-mechanical picture the disorder is replaced by the probability of finding a nucleus in the $|\alpha\rangle$ or in the $|\alpha\rangle$ state.

According to the BOLTZMANN distribution given in equation 2.16, the excess population of the lower $|\alpha\rangle$ state is only 0.00687 % higher compared to the $|\beta\rangle$ with respect to $^1$H at about 20 T magnetic field[b)]. This low polarisation is responsible for the low sensitivity of NMR, but for convenience the equilibrium population is generally not considered in the treatment of NMR methods. The equilibrium state is given defined by the operator $\hat{I}_z$ only, regardless of magnitude and dimension of the actual polarisation.

---

[b)] Corresponding to highest field available at MPIP in Mainz.

#### 2.1.5.2. *External Interactions II*: Spin Manipulation by RF Pulses

The equilibrium density matrix can be manipulated by application of *radio frequency pulses* (RF pulses). If the field oscillates at the LARMOR frequency of the nuclei, it will cause transitions between the ZEEMAN states of the spin system. In order to illustrate the effect of an RF pulse it is convenient to consider the spin precessing in the so-called *rotating frame* of reference, in which the magnetisation appears static. The presence of an RF-field $\vec{\mathrm{B}}_1 \sim \omega_{RF}$ perpendicular to the $\vec{\mathrm{B}}_0$-field causes the spins to precess about a new axis defined by the rotating $\vec{\mathrm{B}}_1$-field. Two counter rotating vectors represent the oscillating magnetic field:

$$\vec{\mathrm{B}}_{RF} = -\frac{1}{2}\gamma_j B_{RF}\{cos(\omega_L t + \phi_p)\vec{\mathrm{e}}_x + sin(\omega_L t + \phi_p)\vec{\mathrm{e}}_y\} \tag{2.28}$$

$$\vec{\mathrm{B}}_{RF} = -\frac{1}{2}\gamma_j B_{RF}\{cos(\omega_L t + \phi_p)\vec{\mathrm{e}}_x - sin(\omega_L t + \phi_p)\vec{\mathrm{e}}_y\} \tag{2.29}$$

Only one component is resonant with the LARMOR frequency and has an impact on the magnetisation in the rotating frame. By convention the term with the negative sine part is generally neglected leading to the following Hamiltonian:

$$\hat{\mathcal{H}}_{RF} = -\frac{1}{2}\gamma_j B_{RF}\{cos(\omega_L t + \phi_p)\hat{I}_x + sin(\omega_L t + \phi_p)\hat{I}_y\} \tag{2.30}$$

The prefactor of this equation $\frac{1}{2}\gamma B_{RF}$ is proportional to the field strength provided by the coil and known as as the nutation frequency $\omega_1$. Thus, by applying a certain field strength it is possible to achieve a certain flip angle by carefully choosing the duration of the pulse:

$$\alpha = \omega_1 \cdot t_{RF} \tag{2.31}$$

The behaviour of the magnetisation is quite intuitive and relates to the popular vector model of NMR. The vector model, however, is not capable of describing the time evolution of a spin system, which is subject to a more involved sequence of subsequent pulses as in a modern NMR experiment. This is rather provided by the *density matrix formalism*[18]. As an example, the evolution of the initial $z$-magnetisation during a $y$-pulse[c)] might be given by combining equations 2.15 and 2.30, leading to:

$$\hat{\boldsymbol{\rho}}_{(t)} \quad \propto \quad e^{-i\alpha_{RF}\hat{I}_y}\hat{I}_z e^{i\alpha_{RF}\hat{I}_y} \tag{2.32}$$

---

[c)] The term "$y$-pulse" means that it is formally described by the angular momentum operator $\hat{I}_y$. It does not correspond to a real spatial direction., however, all pulses and the receiver have a particular phase relation that needs to be controlled carefully by the spectrometer hardware. Generally, all pulses and the acquisition are carried out by means of a single coil with the phase being provided by the phase offset $\phi_p$, cf. equation 2.28 and 2.29.

It is not always needed to calculate the density matrix elements to estimate the impact of sequential pulses, which is quite inconvenient. In order to get easier access to the result of a pulse sequence, Ernst and co-workers have developed the so-called *product operator formalism*[21]. This formalism is based on the fact that equation 2.32 describes nothing else than a rotation in spin space, therefore in may be rewritten as:

$$\hat{I}_z \xrightarrow{\alpha\hat{I}_y} \hat{I}_z cos(\alpha) + \hat{I}_x sin(\alpha) \tag{2.33}$$

Apparently for certain flip angles such as 90° or 180° either sine or the cosine term becomes unity or zero, respectively. For these angles the formalism becomes very simple. The application of a 90° $y$-pulse turns $z$-magnetisation into $x$-magnetisation for example, whereas a 180°-pulse inverts the initial magnetisation. These rather simple rules are illustrated in figure 2.5. A summary of the effects of various pulses can be found in table 2.1.

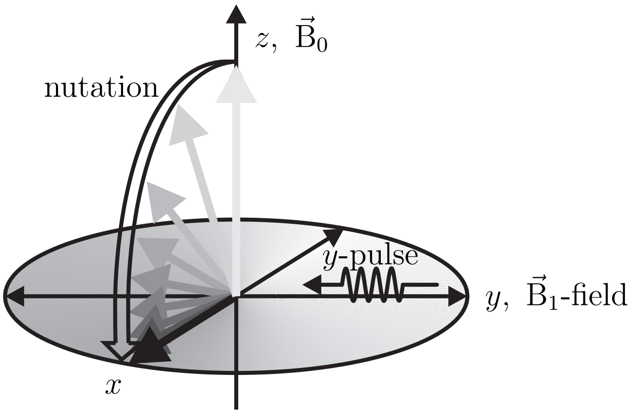

**Figure 2.5.** The effect of an RF pulse on the equilibrium magnetisation.

| | $\alpha\hat{I}_x$ | $\alpha\hat{I}_y$ | $\alpha\hat{I}_z$ |
|---|---|---|---|
| $\hat{I}_x$ | $\hat{I}_x$ | $\hat{I}_x cos(\alpha) - \hat{I}_z sin(\alpha)$ | $\hat{I}_x cos(\alpha) + \hat{I}_y sin(\alpha)$ |
| $\hat{I}_y$ | $\hat{I}_y cos(\alpha) + \hat{I}_z sin(\alpha)$ | $\hat{I}_y$ | $\hat{I}_y cos(\alpha) - \hat{I}_x sin(\alpha)$ |
| $\hat{I}_z$ | $\hat{I}_z cos(\alpha) - \hat{I}_y sin(\alpha)$ | $\hat{I}_z cos(\alpha) + \hat{I}_x sin(\alpha)$ | $\hat{I}_z$ |

**Table 2.1.** Product Operator Formalism. RF pulses and their impact on $x$-, $y$-, and $z$-magnetisation.

## 2.1.6. Internal Spin Interactions

Most interactions encountered in NMR are anisotropic, i.e. the interaction energy depends on the specific molecular orientation with respect to the magnetic field or other reference frames. In solution the anisotropic contributions of those interactions average out due to rapid molecular tumbling. In the solid-state these molecular reorientations are not present, hence anisotropic interactions have a striking effect on the appearance of resonances in the NMR spectrum and require an appropriate theoretical framework. In a systematic treatment of NMR it seems that the orientation dependence of most interactions can be represented by means of a Cartesian $2^{nd}$ rank tensor:

$$\hat{\mathcal{H}}_A \rightarrow \mathbf{A} \tag{2.34}$$

The interaction itself is written in terms of a bilinear product of the form:

$$\hat{\mathcal{H}} = \hat{\mathrm{I}} \cdot \mathbf{A} \cdot \hat{\mathrm{J}} = \begin{pmatrix} \hat{I}_x & \hat{I}_y & \hat{I}_z \end{pmatrix} \cdot \begin{pmatrix} A_{xx} & A_{xy} & A_{xz} \\ A_{yx} & A_{yy} & A_{yz} \\ A_{zx} & A_{zy} & A_{zz} \end{pmatrix} \cdot \begin{pmatrix} \hat{J}_x \\ \hat{J}_y \\ \hat{J}_z \end{pmatrix} \tag{2.35}$$

In case of the *dipolar coupling* (section 2.1.6.3), $\hat{\mathrm{I}}$ and $\hat{\mathrm{J}}$ are the angular momentum operators of two nuclei in close vicinity influencing the total energy in consequence. The angular momentum operator might also couple with the magnetic field mediated by the anisotropic electron distribution and induced ring currents (*chemical shift*, see section 2.1.6.1) or with the quadrupole momentum of a nucleus provided $I \geq 1$ (*quadrupole coupling*, see section 2.1.6.2). A comparison of these three important anisotropic interaction is given in figure 2.6. The explanation for the characteristic line shape of the different pattern can be found in the corresponding section for each particular interaction.

Any tensor describing a NMR interaction can be decomposed into three distinct tensors, namely a scalar, a symmetric, and an antisymmetric part (not shown here). Although the Cartesian representation provides some insight into the physical meaning of the interaction it is nowadays obsolete in computational simulations, since it is reducible and lacks important symmetry properties compared to a *spherical representation.* Owing to frequently changing reference frames and various rotations describing the dynamics of a spin system then becomes a tedious matter. A better suited representation is therefore based on the so-called WIGNER-ECKART *theorem* which greatly simplifies the treatment of rotations[26,27]. Moreover, it leads to a separation of a *space* (orientation dependence)

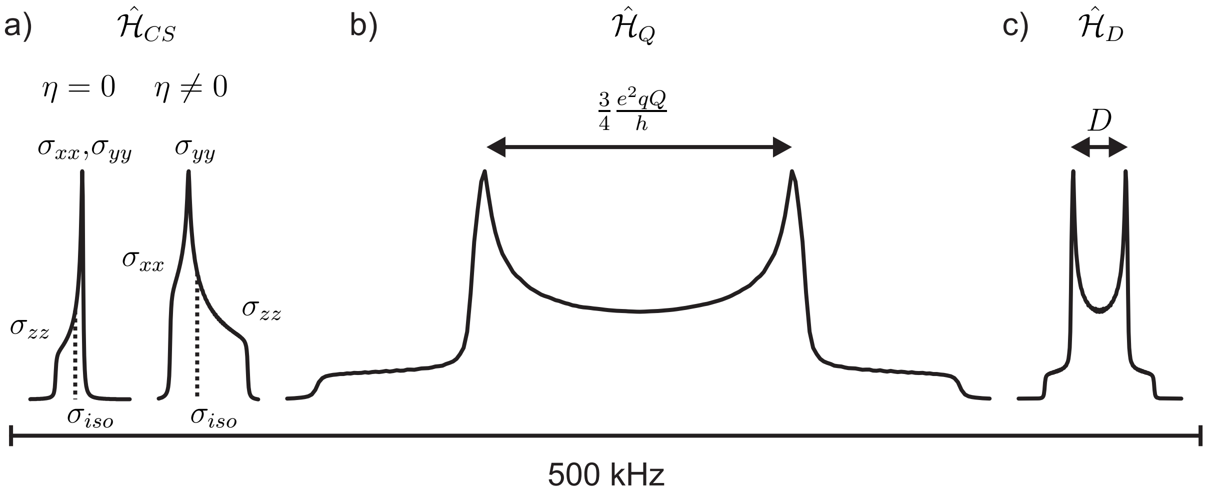

**Figure 2.6.** The plot shows a compilation typical line shapes of anisotropic interactions encountered in NMR marked by the respective Hamiltonian. The pattern have been simulated with the web based program WEBLAB[22] using reliable tensor values. The chemical shift anisotropy is field-dependent, therefore it should be noted that the simulation has been carried out assuming a field strength of 20 T. a) CSA pattern of the carbonyl $^{13}$C in poly(n-alkylmethacrylate)s (PAMAs)[23]. At high temperature (*left*) a fast rotation of the carbonyl group leads to a axial symmetry of the CSA tensor ($\sigma_{xx} = \sigma_{yy}$, $\sigma_{zz}$). The characteristic line shape follows from the higher probability of the principal tensor axis to orient perpendicular to the magnetic field than parallel to it. At lower temperature (*right*) the rotation is prevented leading to a pattern with three principal values rather than two ($\sigma_{xx}$, $\sigma_{yy}$, $\sigma_{zz}$). b) $^2$H Qudrupolar pattern of rigid benzene-$d_6$ molecules in a cyclamer at 87 K[24]. c) A feigned dipolar pattern of an isolated CH pair with a dipolar coupling constant of 22.5 kHz based on a C-H distance of 1.102 Å[25].

and a *spin part* (angular momentum operators):

$$\hat{\mathcal{H}} = \hat{\mathrm{I}} \cdot \mathbf{A} \cdot \hat{\mathrm{J}} = \sum_{k=0}^{2} \sum_{q=-k}^{+k} (-1)^q \underbrace{\Lambda^A_{k-q}}_{space} \underbrace{\hat{\mathrm{T}}^A_{kq}}_{spin} \tag{2.36}$$

In particular for solid-state NMR this separation is very meaningful, since both parts can be manipulated independently by means of fast sample rotation (manipulation of the space part, see section 2.2.1) or by application of RF pulses (manipulation of the spin part, cf. the concept of *recoupling*, in section 2.3.1). According to the secular approximation all terms with an order other than zero ($q \neq 0$) can be neglected as well as the antisymmetric component $\Lambda_{10}$ of the space part. This leads to the following reduced Hamiltonian:

$$\hat{\mathcal{H}} = \Lambda^A_{00}\hat{\mathrm{T}}^A_{00} + \Lambda^A_{20}\hat{\mathrm{T}}^A_{20} \tag{2.37}$$

There is a number of other interaction of minor importance as for example the *spin-rotation interaction*, describing the coupling between the spin angular momentum and the angular momentum of the rotating molecule itself. A small but important interaction for the interpretation of solution NMR spectra is the J-*coupling*. With the irreducible representations the first order Hamiltonian of the Magnus expansion in expression 2.23 can be rewritten as:

$$\overline{\hat{\mathcal{H}}}_A^{(0)} = \frac{1}{t}\int_0^t \hat{\mathcal{H}}_A(t)dt = \Lambda_{00}^{A,lab}\hat{\mathrm{T}}_{00}^A + \hat{\mathrm{T}}_{20}^A\frac{1}{t}\int_0^t \Lambda_{20}^{A,lab}(\omega_r t)dt \tag{2.38}$$

The derivation of the isotropic component $\Lambda_{00}^{A,lab}$ is straightforward, although the space part component $\Lambda_{20}^{A,lab}(\omega_R t)$ may lead to lengthy equations when more than one anisotropic interaction has to be taken into account.

As it will be seen later in the detailed discussion of the internal NMR interactions, any Hamiltonian can be defined within a *priciple axis frame* (PAF) in which the tensor representing the space part becomes a diagonal matrix[d]. In order to derive an expression for an arbitrary set of interactions, these have to be defined according to a common frame of reference, usually denoted the *molecular fixed frame*, which might be identical to one of the PAFs. Since the sample is rapidly rotated, the molecular fixed components need to be transformed into a rotor-fixed frame and finally transformed into the lab-fixed frame by a coherent rotation about the rotor axis. In this last step the space part becomes time-dependent.

The transformations are carried out using Wigner rotation matrices which are a convenient way of transforming spherical tensor representations. The procedure will not be shown here, but can be found elsewhere[16]. After this procedure the time integral is solved and equation 2.38 can be rewritten as:

$$\overline{\hat{\mathcal{H}}}_A^{MAS} = \Lambda_{00}^{A,lab}\hat{\mathrm{T}}_{00}^A + \hat{\mathrm{T}}_{20}^A\frac{1}{t}\sqrt{\frac{3}{2}}\Phi_A \tag{2.39}$$

The result of equation 2.38 contains $\Phi_A$, the *integrated phase* of the interaction $A$ and involves the eigenvalues of the interaction tensors. Disregarding its awkward length, it is a simple trigonometric function having two valuable properties:

$$[\Phi_A]_t^{t+\tau_R} = 0 \tag{2.40}$$

$$[\Phi_A]_t^{t+\frac{\tau_R}{2}} = -[\Phi_A]_{t+\frac{\tau_R}{2}}^{t+\tau_R} \tag{2.41}$$

Obviously, for the time of a rotor period the integrated phase just vanishes and every half rotor period it changes sign. These equations consequently lead to two obvious conclusions: Under MAS conditions any anisotropy is expected to be efficiently averaged due to

---

[d] A tensor can be diagonalised unless it is not asymmetric. As a matter of fact, there are interactions that are not originally established as symmetric. These asymmetric contributions however, can be neglected due to he secular approximation.

an acquisition time which can be thought of as 100s of rotor periods contribution a zero integral phase. Moreover, changing the symmetry of the spin part by rotor synchronised pulses may lead to *recoupling* of the spin hamiltonian as will be seen in section 2.3.3.

#### 2.1.6.1. *Internal Interactions I*: The Chemical Shift

For NMR spectroscopists the *chemical shift* (CS) is the most important interaction. Solution NMR is routinely used in structure determination and for the identification of compounds. In this method the chemical shift provides the most valuable information. It strongly depends on the chemical bonding and on the chemical environment of an atom in general. The chemical shift is based on the fact that the effective magnetic field at the position of the nucleus is not identical to the external magnetic field. This is due to a non-uniform electron distribution: A nucleus might be *shielded* more than others, hence the ZEEMAN levels and consequently the LARMOR frequency is affected and resonances eventually appear at different positions on the frequency scale.

In a classical view the magnetic field causes ring currents within the electron distribution generating an induced magnetic field. This effect is strong particularly in systems involving $\pi$-electron systems such carbonyl or aromatic structures as it is ilustrated in figure 2.7. This field is almost proportional to the external field $\vec{\mathrm{B}}_{ind} = \boldsymbol{\sigma} \cdot \vec{\mathrm{B}}_0$, where $\boldsymbol{\sigma}$ is a tensor describing the diamagnetic shielding of electrons surrounding the nucleus. It is therefore termed *shielding tensor*. The full Hamiltonian can be written as a bilinear product and since the magnetic field applies only in $z$-direction some components immediately drop out:

$$\begin{aligned} \hat{\mathcal{H}}_{CS} &= \gamma \hat{\mathrm{I}} \cdot \boldsymbol{\sigma} \cdot \vec{\mathrm{B}} \qquad \text{with } \vec{\mathrm{B}} = \begin{pmatrix} 0 \\ 0 \\ B_z \end{pmatrix} \\ &= \gamma(\hat{I}_x \sigma_{xz} + \hat{I}_y \sigma_{yz} + \hat{I}_z \sigma_{zz}) B_z \end{aligned} \tag{2.42}$$

Comparing this equation with figure 2.3 one finds that terms involving $\hat{I}_x$ and $\hat{I}_y$ are intrinsically negligible due to the secular approximation. The isotropic chemical shift as it determines the chemical shift in a solution NMR experiment, is equal to $\sigma_{zz}$ integrated over all molecular orientations. The second rank tensor $\boldsymbol{\sigma}$ describes an orientation dependent quantity. The so-called *chemical shift anisotropy* (CSA) depends on the orientation of the molecule with respect to the lab frame. As mentioned already a general second rank tensor can be decomposed into scalar, symmetric, and antisymmetric contributions, however, as

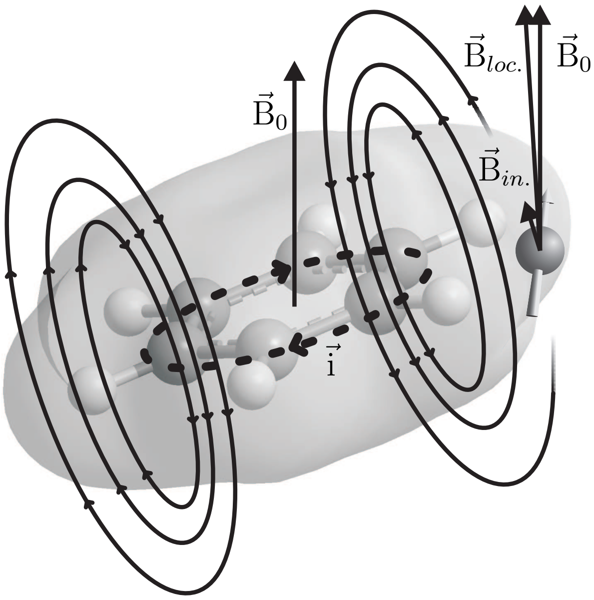

**Figure 2.7.** The origin of the chemical shift: The electron distribution and ring currents ($\vec{i}$) induce a perturbation field $\vec{B}_{in.}$ at the position of the nucleus. The local magnetic $\vec{B}_{loc.}$ and the external magnetic field therefore vary slightly.

a result of the secular approximation the antisymmetric contribution can be ignored. The CSA tensor $\boldsymbol{\sigma}$ is a symmetric tensor in a good approximation, thus it can be defined with respect to a principal axis frame making it diagonal:

$$\boldsymbol{\sigma} = \sigma_{iso} + \delta_{CS} \begin{pmatrix} -\frac{1+\eta_{CS}}{2} & 0 & 0 \\ 0 & -\frac{1-\eta_{CS}}{2} & 0 \\ 0 & 0 & 1 \end{pmatrix} \tag{2.43}$$

This notation makes use of some algebraic transformations and conventions involving

$$\delta_{CS} = \omega_L(\sigma_{zz}^{PAS} - \sigma_{iso}) \tag{2.44}$$

the anisotropy parameter and

$$\eta_{CS} = \frac{\sigma_{yy}^{PAS} - \sigma_{xx}^{PAS}}{\sigma_{zz}^{PAS} - \sigma_{iso}} \tag{2.45}$$

the asymmetry parameter. The vector orientation of the $\sigma_{zz}$ component with respect to $\vec{B}_0$ in general is defined by two angles $\theta$ and $\phi$. The frequency offset of the signal of the nucleus due to the molecular orientation is therefore given as:

$$\omega_{CS} = \frac{\delta_{CS}}{2}\left(3cos^2\theta - 1 - \eta_{CS}sin^2\theta cos(2\phi)\right) \tag{2.46}$$

This equation indicates a broad line shape observed in the solid state where preserving orientations in a crystal lattice supplant motional averaging observed in solution. The integral mean value of the line shape, however, corresponds to the isotropic chemical shift. The characteristic line shape of the CSA powder pattern is caused by the random distribution of crystallites, leading to more vectors $\vec{\mathrm{B}}_{in.}$ being perpendicular to the magnetic field as being aligned with it. The characteristic line shape can be seen in figure 2.6. Under MAS conditions the CSA powder pattern breaks up into several distinct lines indicated by the $^{13}$C carbonyl line of L-alanine in figure 2.9 being discussed in section 2.2.1.

Since the chemical shift is a relative quantity and small compared to the Larmor frequency, the *parts-per-million*-scale (*ppm*-scale) was introduced:

$$\delta = \frac{\nu - \nu_{ref}}{\nu_{ref}} \cdot 10^6 \text{ ppm} \tag{2.47}$$

In this manner the correction of the resonances with respect to a suitable reference signal $\nu_{ref}$ can be specified. In solution $^1$H NMR a widely used reference compound is tetramethylsilane (TMS). In solid-state NMR the liquid TMS is rather inconvenient for the setup of routine measurements, hence solid compounds like adamantane or tetrakis(trimethylsilyl)silane (TTSS) are used in order to *calibrate* the spectrometer hardware indirectly with respect to the TMS *reference* ($\delta_{TMS}$ =0 ppm).

#### 2.1.6.2. *Internal Interactions II*: Quadrupole Coupling

Nuclei with a spin quantum number $I \geq 1$ possesses a *nuclear quadrupolar moment eQ*. In combination with the *electric field gradient* (EFG) tensor $\mathbf{V}$ a so-called *qudrupolar interaction tensor* $\mathbf{Q}$ is defined:

$$\mathbf{Q} = \frac{eQ}{2I(2I-1)\hbar}\mathbf{V} \tag{2.48}$$

With this, the Hamiltonian describing the quadrupolar coupling can be written in terms of the familiar bilinear product:

$$\hat{\mathcal{H}}_Q = \hat{\mathrm{I}} \cdot \mathbf{Q} \cdot \hat{\mathrm{I}} \tag{2.49}$$

In case of deuterons the quadrupolar coupling is relatively small compared to the Larmor frequency, so that the secular approximation remains a valid assumption. Most other $I \geq 1$ nuclei provide a much larger quadrupolar coupling constant of several MHz, which cannot be treated by a first order Hamiltonian. For more information and detailed introduction to higher order quadrupole effects see for example [28].

In analogy to the CSA pattern the orientational dependence of the resonance frequency is given by

$$\omega_Q = \pm\frac{\delta_Q}{2}\left(3cos^2\theta - 1 - \eta_Q sin^2\theta cos(2\phi)\right) \tag{2.50}$$

leading to a related line shape. As suggested by this equation, the asymmetry and a PAS can be defined similar to the shielding tensor the anisotropy. In this work, however, the quadrupolar coupling of hydrogen-bonded deuterons is not investigated by means of exact simulations but rather incidentally as an indicator of molecular motion. A detailed description will therefore not be presented here. Note however the ± sign in equation 2.50 indicating a mirror symmetric superposition of two lines. The characteristic line shape of a typical $^2$H quadrupolar coupling pattern, with the two horns being split by $\delta_Q \approx 125$ kHz, can be seen in figure 2.6. In case of a weak quadrupolar coupling it holds $\Lambda_{00}^{Q,lab} = 0$, i.e. the first order quadrupole Hamiltonian $\vec{\mathcal{H}}_Q^{(1)}$ does not provide an isotropic contribution in contrast to the chemical shift. Under fast sample rotation the first order quadrupole pattern splits into several spinning sidebands similar to the CSA and heteronuclear dipolar coupling (see section 2.2.1).

In case of stronger quadrupolar couplings it is sometimes sufficient to include second order perturbation effects not being described by the secular approximation[e)]. For some nuclei like $^{14}$N for example, the coupling is so large that $m$ denoting the nuclear ZEEMAN eigenstates even becomes a "poor" quantum number and the ZEEMAN wave functions are not an appropriate basis anymore. Taking the quadrupole interaction as a basis leads to the field of *nuclear quadrupole resonance*[29] (NQR) also known as *zero-field NMR*.

#### 2.1.6.3. *Internal Interactions III*: Dipole-Dipole Coupling

Two magnetic dipoles in close vicinity will interact with each other and affect the total energy of the system, which is illustrated by figure 2.8. The Hamiltonian of this system is easily derived by substituting the dipole moments in the expression of the classical interaction energy by the dipole moment operator $\hat{\mu}$. The Hamiltonian can therefore be written as:

$$\hat{\mathcal{H}}_D = -\left(\frac{\mu_0}{4\pi}\right)\frac{\gamma_I\gamma_J\hbar}{r^3}\left(\frac{\hat{\mathrm{I}}\cdot\hat{\mathrm{J}}}{r^3} - 3\frac{(\hat{\mathrm{I}}\cdot\vec{\mathrm{r}}_{ij})(\hat{\mathrm{J}}\cdot\vec{\mathrm{r}}_{ij})}{r^5}\right) \tag{2.51}$$

Alternatively, the Hamiltonian can be written in bilinear form:

$$\hat{\mathcal{H}}_D = \hat{\mathrm{I}}\cdot\mathbf{D}\cdot\hat{\mathrm{J}} \tag{2.52}$$

---

e) In terms of perturbation theory all terms commuting with $\hat{\mathcal{H}}_Z$ are representations of $1^{st}$ order effects.

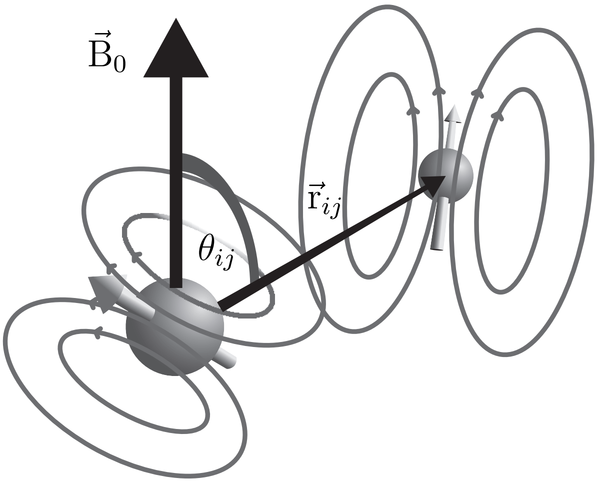

**Figure 2.8.** The dipole-dipole coupling: Two close spins interact *through-space* and thereby affect the LARMOR frequencies of the involved nuclei.

In the secular approximation the dipolar coupling tensor can be written in its PAS as:

$$\mathbf{D} = -2D_{IJ}\begin{pmatrix} -\frac{1}{2} & 0 & 0 \\ 0 & -\frac{1}{2} & 0 \\ 0 & 0 & 1 \end{pmatrix} \tag{2.53}$$

$$\text{with} \quad D_{IJ} = -\left(\frac{\mu_0}{4\pi}\right)\frac{\gamma_I\gamma_J\hbar}{r^3} \tag{2.54}$$

$D_{IJ}$ in this equation is the full dipolar coupling constant being only dependent on the distance of the nuclear spin pair. Obviously, the dipolar coupling tensor is traceless, which already implies that expressed in terms spherical tensor operators the isotropic component $\Lambda_{00}^{D,lab} = 0$ is zero just as for the quadrupole coupling. Therefore, the only non-vanishing secular component is given by $\Lambda_{20}\hat{\mathrm{T}}_{20}$, which needs to be translated into an expression defined in the lab-fixed frame. The resulting Hamiltonian reads as:

$$\hat{\mathcal{H}}_{D,\ sec} = D_{IJ}\frac{1}{2}\left(3cos^2\theta - 1\right)\left(3\hat{I}_z\hat{J}_z - \hat{\mathrm{I}}\cdot\hat{\mathrm{J}}\right) \tag{2.55}$$

As one can see, besides the full dipolar coupling constant, this equation contains the second order LEGENDRE polynomial $P_2 = \frac{1}{2}\left(cos^2\theta_{jk} - 1\right)$ as a prefactor. Both can be combined to the secular dipolar coupling constant $d_{IJ} = D_{IJ} \cdot P_2$. It contains $P_2$ which has a two zero crossings, i.e. the dipolar coupling vanishes for a spin pair being aligned at an angle of $\theta = 54.74°$, the Magic Angle, or $\theta = 125.26°$ with respect to the external magnetic field. This is the basic idea behind the magic angle spinning technique. Equation 2.55

describes the general case of a dipolar coupling including a coupling between like spins, as for example the $^1$H-$^1$H *homonuclear dipolar coupling.* In case of *heteronuclear dipolar coupling* further simplification can be applied after expanding the scalar product $\hat{\mathrm{I}} \cdot \hat{\mathrm{J}}$. The remaining expression involving $x$-and $y$-components can be rearranged to give a so-called *flip-flop term* $\hat{I}_+\hat{J}_- + \hat{J}_+\hat{I}_-$, consisting of ladder operators being briefly introduced in section 2.2.2. In case of different LARMOR frequencies this term is rather small and can be ignored, leading to the heteronuclear dipolar coupling Hamiltonian:

$$\hat{\mathcal{H}}_{D,hetero} = D_{IJ}\frac{1}{2}\left(3cos^2\theta - 1\right) 2\hat{I}_z\hat{J}_z \tag{2.56}$$

*Homonuclear dipolar couplings* in contrast need to be treated with the full secular Hamiltonian given in equation 2.55. The distinction of homo- and heteronuclear dipolar coupling is not only formal but also manifests itself in the performance of line narrowing methods for solids, being discussed in section 2.2.1. The static line shape of the heteronuclear dipolar coupling is known as PAKE-pattern[30], resembling the quadrupolar as can be seen in figure 2.6. In principle the $^1$H-$^1$H homonuclear dipolar coupling of an isolated spin pair gives rise to the same kind of pattern, however, those are hardly encountered in a real sample. For this reason, the distinct features of the dipolar coupling pattern suffers from spin diffusion in proton containing samples, making the pattern broad and featureless.

#### 2.1.6.4. *Internal Interactions IV*: J-Coupling

The second most valuable source of information in routine solution NMR is the J-coupling, predominantly observed in $^1$H NMR. In case of nearby protons connected by one or more carbon atoms the proton resonance breaks up into a multiplet of distinct lines. The number of lines and their amplitude depend on the number of coupled protons, hence J-coupling in combination with the chemical shift provides meaningful information about the connectivity and enables structure elucidation for moderately large molecules. However, an introduction to the interpretation of routine NMR spectra is beyond the scope of this work and can be found elsewhere, for example in references [31] or [32]. J-coupling is also referred to as *indirect spin-spin coupling*, which is suggestive with respect to the mechanism being electron mediated. The electrons around the nucleus thereby have a slight tendency to be polarised parallel to the nuclear spin. From the classical physics point of view this is surprising, though it is the result of the negative *hyperfine coupling* between electrons and protons. If a second proton comes into play there are two possibilities: Either both nuclear spins are parallel or antiparallel. The parallel state is energetically unfavourable, since the second proton transfers the same polarisation to the electrons. The electron polarisation, however, is mainly governed by the Pauli *principle*, thus a parallel spin orientation leads to higher "tension" within the exchange term. The Zeeman levels of the protons are therefore slightly shifted, depending on the spin polarisation of the coupled protons.

Since the J-coupling is very weak[f)] it is usually not observed in solids and superimposed by stronger anisotropic interactions as the discussed dipolar coupling for example. As any other NMR interaction it can be represented as a bilinear product:

$$\hat{\mathcal{H}}_J = \hat{\mathrm{I}} \cdot \mathbf{J} \cdot \hat{\mathrm{J}} \tag{2.57}$$

In solution the anisotropic part is averaged out but also in a solid the isotropic part is dominating, thus J-coupling is commonly treated as a scalar quantity being more simply written as:

$$\hat{\mathcal{H}}_J \approx J\, \hat{\mathrm{I}} \cdot \hat{\mathrm{J}} \tag{2.58}$$

This equation seems notably simple, however, it is sufficient to describe most NMR experiments based on J-couplings .

## 2.2. Basic Methods in Solid-State NMR

In the previous section the theoretical background of NMR with the most important internal interactions, AHT, and the secular approximation have been discussed. The present section will focus on more practical aspects of solid-state NMR. Some of the techniques are analogously applied in known solution NMR methods as for example the single pulse experiment or exchange spectroscopy. Others, like proton decoupling, require specific modification in order to operate in the bulk, whereas some techniques, such as cross polarisation, solely work in the solid state. Magic angle spinning is by far the most important technique in solid-state NMR and will be discussed in the first section. The theoretical treatment by means of AHT has already been given in section 2.1.4.

### 2.2.1. Magic Angle Spinning

*Magic angle spinning* (MAS) was independently invented by Andrew[33] and Lowe[34] in the late 1950s. It is based on the orientation dependence of anisotropic interactions relative to the magnetic field. The amplitude of these anisotropies is defined by a second

---

f) $J_{^{13}C^{13}C} \approx 35$ Hz for adjacent carbon atoms in an aliphatic chain.

rank tensor representation as given for example in the second part of equation 2.37. It scales with the second LEGENDRE Polynomial, which has a zero crossing at the so-called *magic angle* at 54.74°. It is based on the fact that arbitrary tensor orientations of randomly aligned crystallites in a macroscopic sample can be averaged by a sample rotation to give another symmetric tensor with its symmetry axis being aligned at the sample spinning axis. Thus, spun rapidly about an axis being inclined at the magic angle with respect to $\vec{\mathrm{B}}_0$ (see Fig. 2.9) efficient line narrowing in the spectra of solid samples is achieved provided the rotation is fast enough.

However, line narrowing is not equally accomplished in all spin systems. In general only the so-called *inhomogeneous* interactions as the CSA or the heteronuclear dipolar coupling are fully averaged over one rotor period, whereas *homogenous* interactions, like the homonuclear dipolar coupling, still contribute to severe line broadening. The latter is the most dominant broadening mechanism in $^1$H solid-state NMR spectra of organic compounds and requires NMR hardware capable of fast spinning >20 kHz. Recently spinning frequencies up to 70 kHz became possible[35] being nowadays routinely applied using commercially available probe heads and MAS rotors with an outer diameter of 1.3 mm.

The reason for the high effort put into the line narrowing techniques is that the $^1$H chemical shift contains valuable information about the supramolecular organisation, in particular the strength of the hydrogen bonds[36,37] as well as the magnetic shielding of neighbouring molecules. Here, $^1$H MAS NMR spectra provide valuable information by comparing observed and predicted chemical shifts of a computational study[38]. In this regard so-called *Nucleus Independent Chemical Shift maps*[39] (NICS maps), illustrating the impact of a molecule on the chemical shift of a nucleus turned out to be extremely useful in all experimental chapters of this theses.

According to MARICQ and WAUGH[20] interactions are called *inhomogeneous* if the Hamiltonian describing it commutes with itself at different times. The evolution of the density matrix is then refocused over a rotation period. Under MAS conditions, the static pattern of inhomogeneous interactions, such as the CSA or heteronuclear dipolar interactions, therefore breaks up into a sideband pattern due to the *evolution rotor modulation* (ERM). The pattern consists of sharp spectral features, which can be seen on the left-hand side in figure 2.9. In contrast to that, *homogeneous* interactions such as the homonuclear dipolar coupling behave differently. The homogenously broadened line behaves as a single entity and cannot be refocused, whereas inhomogeneous interactions can be refocused by

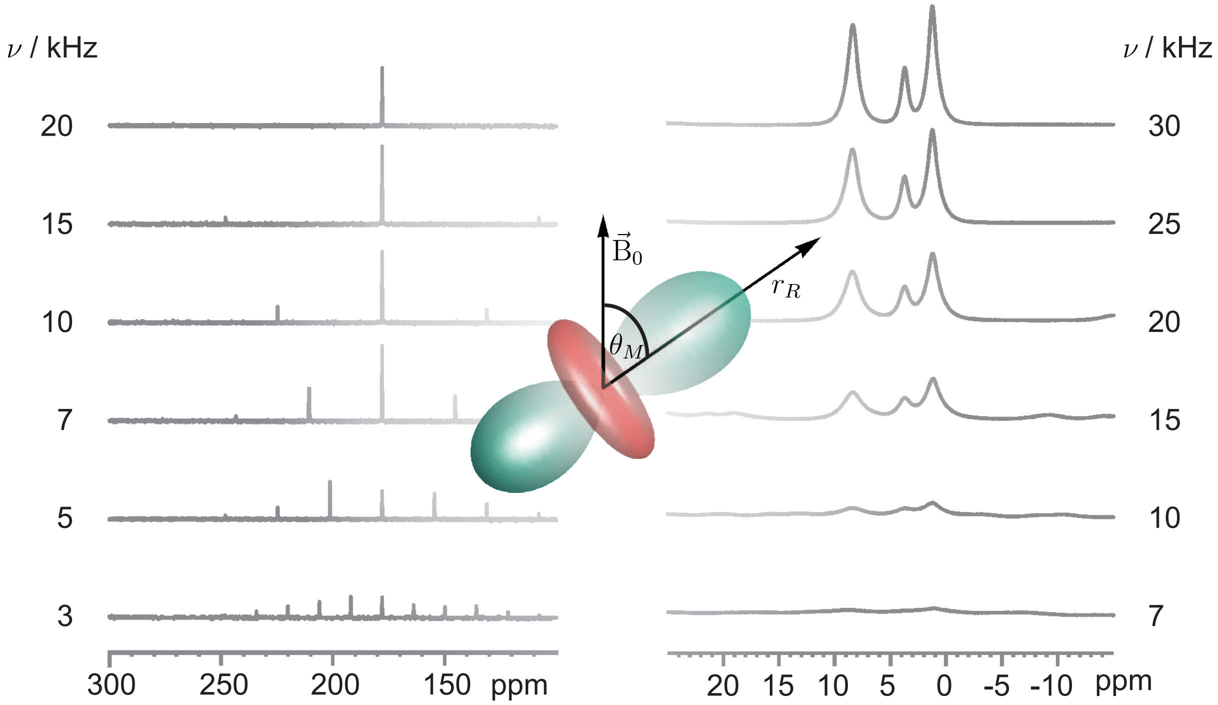

**Figure 2.9.** Effect of MAS on $^{13}C$ (*left*) and $^{1}H$ (*right*) spectra. The pattern demonstrates the different behaviour of the CSA and heteronuclear coupling on the one hand and the homonuclear dipolar coupling on the other. In the middle, a spherical 3D plot illustrates the rotational averaged second rank tensor representation of an arbitrary anisotropic interaction. As the amplitude of the tensor in the direction of $\vec{B}_0$ is just zero, the impact of the anisotropy is removed from the spectrum.

application of different echo techniques[g]. In the MAS pattern the homonuclear dipolar coupling manifests in a broad spectral line shape, which can be seen in figure 2.9.

Line narrowing under MAS is achieved by averaging the space part of anisotropic NMR interactions. For the sake of completeness it should be noted that averaging can also be done by RF pulses manipulating the spin part of the interaction in a suitable manner, which is used in the LEE-GOLDBURG technique described in section 2.2.6.2. Another approach uses both MAS in combination with RF pulses and is therefore called *Combined Rotation and Multiple Pulses* (CRAMPS)[41].

## 2.2.2. Single Pulse Excitation

The simplest NMR experiment is the *Single Pulse Excitation* (SPE), i.e., excitation by a single pulse and subsequent data acquisition. The effect of an RF pulse with a distinct

---

[g] Coherent, dipolar multispin interactions are generally accounted to homogeneous broadenings, however, they can be refocused by a so-called *magic-sandwhich echo*[40].

phase, amplitude and duration can be explained by means of the vector model or the product operator formalism (see table 2.1). In order to calculate the effect of a hard RF pulse, *ladder operators* are used to access the impact on the density matrix. These ladder operators, $\hat{I}_+ = 2^{-\frac{1}{2}}\left(\langle \hat{I}_x + i\hat{I}_y \rangle\right)$ and $\hat{I}_- = 2^{-\frac{1}{2}}\left(\langle \hat{I}_x - i\hat{I}_y \rangle\right)$, are commonly used to calculate the eigenvalues of a Hamiltonian in its given basis. In NMR these *raising* and *lowering operators* are used to describe the coherences between the ZEEMAN eigenstates, involving a change of the azimuthal quantum number $m$ by $\pm 1$.

A 90° x-pulse applied on a spin system in equilibrium generates transverse magnetisation of the phase $-y$. This transverse magnetisation induces an electric current and thus a detectable signal in coil of the NMR probe. Since the fast oscillating signal needs to be digitised for further processing, it usually passes an RF mixer. This component generates a low frequency signal, sampled with a rate of several 100 MHz. The mixing process can be seen as the technical aspect of the *rotating frame transformation* and may re-emphasise the fact that in NMR only relative changes of the LARMOR frequency are relevant$^{h)}$. Analogues to the argumentation in section 2.1.5.2, a pulse on a single spin system generates coherences of the order +1 and -1 at the same time, but only the latter is detected. Therefore the pulse in the SPE experiment is assumed to change the coherence order from 0 to -1 for the detection. The experiment and the corresponding *Coherence Transfer Pathway diagram* (CTP diagram) is given in figure 2.10. The pulse program SPE is given in appendix A.1.1 as all other pulse programs used in this thesis. By regarding the SPE pulse program one finds the same experiment is repeated with four different phases. The sequence may start with an $x$-pulse and the receiver phase of -$y$. The second experiment

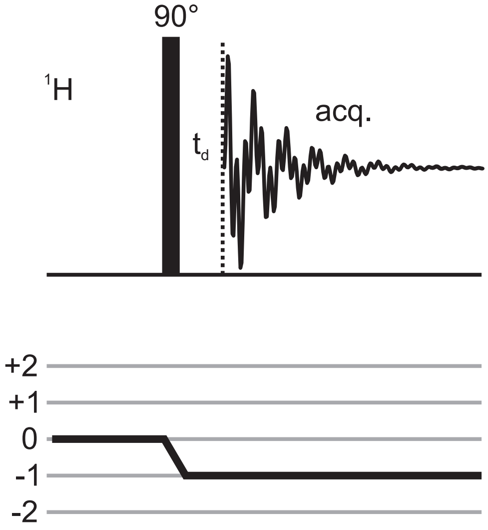

**Figure 2.10.** The Single Pulse Excitation (SPE) experiment.

---

h) In NMR transition frequencies are dominated by the gyromagnetic ratio of the nuclei which does not provide chemical information. On the contrary, in microwave spectroscopy rotational transitions of molecules may occur in the whole microwave range. For the this reason a *direct sampling* of the fast oscillating response signal is desirable, because frequency downconversion of the signal always implies a restriction to a frequency band. In the field of microwave spectroscopy devices capable of sampling and processing signals in the X-band (7-11.2 GHz) are on the cusp of being routinely used[42]. In NMR faster digitisation rather leads to higher oversampling rates improving the signal to noise ratio of the spectrum.

then starts with an -$x$-pulse and the receiver phase would change accordingly to $y$. In case of SPE and other experiments, two so-called *phase cycling schemes* are commonly applied, i.e. CYCLOPS[43] changing the excitation pulse in the sequence $x$, $y$, -$x$, -$y$ and EXOCYCLE[44], employing the order $x$, -$x$, $y$, -$y$. The reason for phase cycling in SPE is to remove effects of pulse inhomogeneities and frequency offsets that hold for resonances remote from the irradiation point in the spectrum. In various advanced NMR experiments the aim of phase cycling, however, has a more vital importance, that is, to suppress certain product operator terms. For DQ NMR for example it prevents the detection of coherences that did not evolve as DQ magnetisation during an evolution time. The aspect of phase cycling will not be explained further in this thesis, however, a good introduction can be found in the book of KEELER[9].

It should be noted that the term receiver phase is not well defined so far. In section 2.1.5.2 it was only stated that the pulse and receiver phase must be consistent at least for the length of the whole experiment. A pure absorption line shape is merely achieved by multiplication of the signal with an arbitrary digital phasor $e^{i\phi}$, which needs to be set by the operator[i)].

## 2.2.3. Relaxation of NMR signals

The NMR signal to be detected is not persisting. It dwindles exponentially in time and is therefore known as *free induction decay* (FID). The rate of this decay, i.e. the *relaxation* of the coherences is governed by dynamic properties of the investigated material. Generally it can be categorised into two different phenomena. The length of the FID is mostly determined by the *spin-spin relaxation* time $T_2$. It determines how fast the spin ensemble sustains loss of its coherent phase relation. In this manner, the macroscopic magnetisation decreases and the signal intensity goes down subsequently, although the spins may not have returned to equilibrium yet.

The second relaxation phenomenon is the *spin lattice relaxation*, specified by the $T_1$ relaxation time. This quantity determines how fast the magnetisation recovers from non-equilibrium to the equilibrium state, i.e. it describes the build-up of $z$-magnetisation after the experiment.

In general, the length of the FID determines the line width of an NMR resonance. A short FID in the time domain gives rise to a broad signal in the frequency domain after Fourier transformation. The full *line width at half maximum* (FWHM) and the apparent

---

[i)] Even the usage of an offset dependent phase factor is commonly applied and known as first order phase correction, applied after Fourier transformation.

relaxation time, therefore have an inverse relation FWHM=$1/\pi T_2^*$. The asterisk indicates that the line width may not only depend on the spin-spin relaxation exclusively. Field inhomogeneities for example also contribute to the apparent relaxation time having both *inhomogeneous* and *homogeneous* contributions which add up in a simple inverse relation: $T_2^{*-1} = T_2^{-1} + T_2^{\dagger -1}$. The *homogeneous* part refers to the actual spin-spin relaxation time being the actual limiting factor for a number of experiments possessing internal spin echos as the INADEQUATE technique, discussed in section 2.3.4.

### 2.2.4. On 2D NMR

The interpretability of one-dimensional (1D) experiments depends on the number and distribution of resonances. In principle, various information are at hand, however, if the molecule becomes larger the complexity of the 1D spectrum will increase and different contributions cannot be distinguished easily. Introducing another axis and recording a two-dimensional (2D) spectrum often prevents spectral crowding. Most 2D experiments correlate the chemical shift with either the chemical shift of another nucleus or with a another property as for example the J-coupling as in a J-*resolved* $^{13}$C spectrum[45]. A correlation pattern with two chemical shift axes greatly simplifies the spectral assignment. Technically a 2D NMR experiment is accomplished by introducing an evolution time, incremented in sequential single experiments[13, 46]. The general structure of a 2D NMR experiment is shown in figure 2.11. The experiment starts with an *excitation time*, which might be a single pulse or a sequence of pulses. In this period distinct coherences are generated, evolving during the variable *evolution time* commonly denoted $t_1$. The last preparation pulse before the $t_1$ time determines the phase of the coherence present in the evolution time which is an important point with regard to the detection scheme in 2D NMR. The third part is the *mixing* period generating detectable magnetisation (the FID) recorded in the last section, the acquisition time ($t_2$).

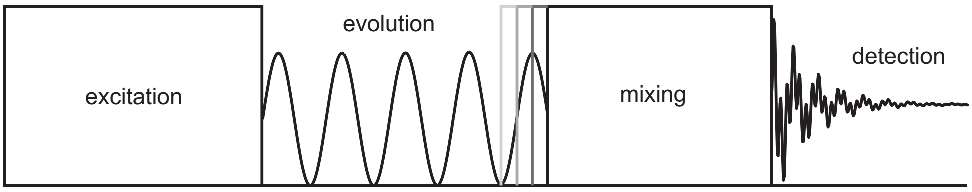

**Figure 2.11.** General Scheme of a 2D NMR experiment. The evolution time and the detection period are commonly denoted $t_1$ and $t_2$ according to their temporal order.

It should be noted that more sophisticated 1D NMR experiments other than SPE have been designed, however, a great number of those have an intrinsic 2D character and can be regarded as a projection of a certain property on a single frequency dimension[j)].

A 2D NMR spectrum is obtained by Fourier transformation in both dimensions. In contrast to 1D NMR pure absorption line shape is not so easily achieved because the spectrum cannot be phased independently in $F_1$ and $F_2$. Due to these circumstances Fourier transformation of the raw data leads to distorted peaks not having absorption line shapes in both dimensions. In the early times of 2D NMR the envelopes of these phase twisted peaks have been used which meant a severe loss of resolution. In order to avoid these unpleasant phase artefacts right away a couple of phase-sensitive 2D detection schemes have been developed. The first one, the so-called **STATES**-method, will be presented in the following paragraph.

Depending on the phase of the preparation pulse prior to the evolution, *cosine* or *sine* data sets are recorded separately for each $t_1$ increment. This allows for an artificial construction of a complex dataset by neglecting the imaginary part of the Fourier transforms of both, the *sine* and the *cosine* modulated FIDs and using only their real part. After recording two data sets, $t_1$ is prolongated by an increment $\Delta$. The **STATES**-method[47] provides absorption line shape and sign discrimination, i.e. the spectrum is not reflected at the centre of the spectrum. The scheme has a major drawback however, which is the fact that magnetisation not evolving during the evolution time gives rise to distracting signals at the $t_1 = 0$ axis of the spectrum. The next milestone in the development of phase sensitive detection came in with the ***Time Proportional Phase Incrementation*** or (**TPPI**)-method[48]. This scheme retains the goals of the STATES detection, that is, sign discriminated absorption lines, but it also relocates axial peaks to the edge of the spectrum. As the name suggests *sine* and *cosine* modulated data sets are not recorded at a constant $t_1$, but phase and time are incremented simultaneously. Since only every second data set is cosine modulated the spectral width is $1/2\Delta$. The appropriate phase increment is given by the following phase relation which is based on the consideration that half of the spectral width, i.e. $1/4\Delta$, must be added to all signals in order to shift

---

j) See for example the difference of the Double Quantum Filtered experiment (cf. section 2.3.3.2), which is a 1D method, whereas the 2D double quantum-single quantum correlation experiment is a 2D experiment, which has even been developed earlier.

all axial peaks to the edge of the spectrum:

$$\begin{aligned}\phi_i &= 2\pi\frac{1}{4\Delta}\cdot \mathrm{t}_1\\ &= 2\pi\frac{1}{4\Delta}\cdot(i-1)\frac{\Delta}{2}\\ &= 2\pi\frac{1}{4\Delta}\cdot(i-1)\frac{\pi}{2}\end{aligned} \tag{2.59}$$

As suggested by equation 2.59, changing the phase of the preparation pulse by 90° facilitates phase sensitive detection, with axial peaks being removed from the spectrum.

The described scheme is a commonly used standard method for 2D detection. For some particular purposes it still suffers from unfavourable properties. Due to its incrementation concept, TPPI the spectral width is half compared to that of the States method. Basically this can be overcome by simply reducing the increment which then only increases the experimental time. For many applications, however, the acquisition has to be done in a rotor-synchronised manner, hence the minimum increment is determined by the rotor period. This is problematic for experiments involving a large chemical shift distribution in $\mathrm{F}_1$ and the MAS frequency cannot be increased due to experimental requirements. A solution to this problem is given by the **States-TPPI** method[49], which can be seen as a combination of both discussed schemes. As in the States method, *sine* and *cosine* modulated data sets are recorded at a constant $\mathrm{t}_1$ and rearranged to construct a complex data set. The phase incrementation scheme of TPPI is retained, though. The resulting spectrum is comparable to the TPPI-processed data apart from a doubled spectral width. Due to these advantages the States-TPPI method is used throughout for 2D detection in this thesis.

## 2.2.5. Cross Polarisation

SPE is the most simple experiment and commonly used to record 1D $^1$H NMR spectra, however, for $^{13}$C NMR two problems may arise. First of all, the low natural abundance of the $^{13}$C and its low geomagnetic ratio ($\gamma_{^1H}/\gamma_{^1H} \approx 4$) lead to low sensitivity of $^{13}$C compared to $^1$H NMR. Additionally, the $^{13}$C spin-lattice relaxation time is usually much larger compared to the $^1$H relaxation. In solution NMR the INEPT[k)] experiment enables significant signal enhancement, whereas in the solid-state *cross polarisation*[51] (CP) is the method of choice for recording $^{13}$C or $^{15}$N NMR spectra since these nuclei have directly bound protons. As in INEPT, the maximum enhancement is given by $\gamma_{^1H}/\gamma_{^{13}C}$, whereas

---

[k)] Insensitive Nuclei Enhancement by Polarisation Transfer[50] the mechanism is different as well as the implementation depicted in figure 2.12 a).

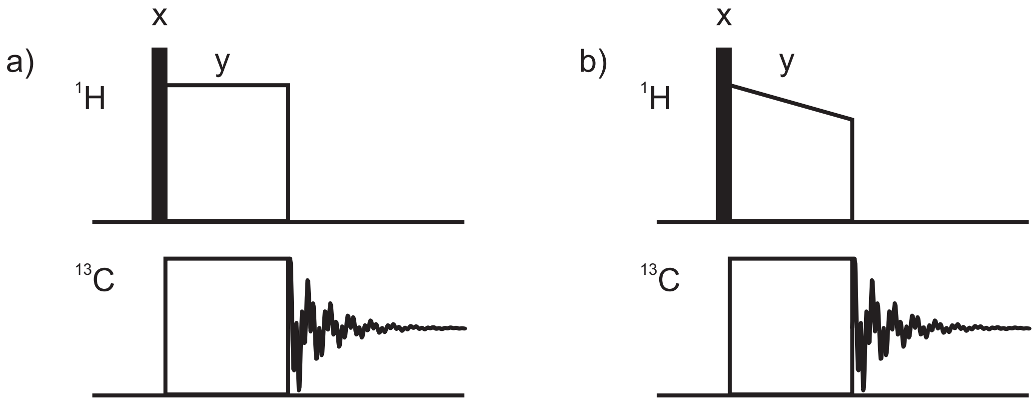

**Figure 2.12.** cross polarisation (CP): a) usual Hartmann-Hahn CP, b) ramp-CP using a linearly increasing amplitude on $^1$H channel.

The sequence starts with a 90°-pulse on the channel of the high-$\gamma$ nuclei, being mostly protons, which are abundant in most organic samples. In the subsequent *contact time* the polarisation of the protons is transferred to the low-$\gamma$ nuclei. This is accomplished by a simultaneous on-resonant irradiation at the Larmor frequency of both channels for typically 0.5 to 3.0 ms. The magnetisation of each channel is thereby *locked* to the RF field and the nutation is regarded as a precession in the two separate rotating frames. The field amplitudes are adjusted to match these nutation frequencies of both nuclei, for example $^{13}$C and $^1$H, in order to fulfil the established Hartmann-Hahn condition[52]:

$$-\gamma^{^{13}C} B_1^{^{13}C} = -\gamma^{^{1}H} B_1^{^{1}H} \tag{2.60}$$

$$\nu^{^{13}C} = \nu^{^{1}H} \tag{2.61}$$

Having the same nutation frequency, polarisation transfer occurs via a heteronuclear coupling mechanism. The enhancement depends on the strength of the dipolar coupling and may reach a saturation limit depending on the duration of the contact. Common contact times allow for an efficient distribution of polarisation, therefore also quaternary carbons can be detected.

Longer transfer times, however, may not always improve the enhancement to the theoretical limit, but may cause relaxation losses, since the locked magnetisation of both nuclei is affected by the *rotating frame relaxation* $T_{1\rho}$. Relaxation and the build-up behaviour need to be compromised for the best signal enhancement and ought to be checked for each particular sample.

Under MAS conditions the HARTMANN-HAHN condition is modulated by the rotor frequency[53], giving:

$$\nu_{^{13}C} = \nu_{^{1}H} \pm n\nu_R \tag{2.62}$$

For this reason the usual HARTMANN-HAHN CP strongly depends on the MAS frequency, i.e. for a standard experiment three parameters, the 90°-pulse on protons, the contact power of either channel, and the contact time needs to be optimised. However, a spectrum involving carbonyl groups and aliphatic signals for example, the spectral range is very broad and thus the matching condition in not equally met for all signals. In order to improve off-resonance performance linearly (ramp-CP[54]) or stepwise increasing variable amplitude pulses (VACP[55]) are used. In this way also the MAS dependence is tempered (see figure 2.12 b)).

## 2.2.6. Dipolar Decoupling

One of the most vital topics of solid-state NMR is dipolar decoupling. In case of abundant spins, such as protons, the homonuclear coupling leads to homogeneously broadened lines in a NMR spectrum of a solid sample under MAS conditions. With respect to the already low chemical shift dispersion, $^{1}$H spectra often suffer from broad and indistinct resonances. For diluted spins such as $^{13}$C whose natural abundance is about 1.1 %, the homonuclear coupling is not significant, however the heteronuclear coupling to the abundant protons takes effect. In section 2.1.6.3 it was shown that homo- and heteronuclear coupling have a different character, leading to different MAS pattern, presented in section 2.2.1. Consequently, also different decoupling concepts have been developed in order to achieve line narrowing. These will be briefly introduced in the following two paragraphs.

### 2.2.6.1. Heteronuclear Decoupling Schemes

The Hamiltonian of a carbon spin coupled to a network of protons can be written as:

$$\hat{\mathcal{H}} = \hat{\mathcal{H}}_{^{13}C} + \hat{\mathcal{H}}_{^{1}H^{13}C} + \hat{\mathcal{H}}_{^{1}H} + \hat{\mathcal{H}}_{^{1}H^{1}H} + \hat{\mathcal{H}}_{RF}(t) \tag{2.63}$$

As can be seen, several terms other than $\hat{\mathcal{H}}_{^{13}C}$ and $\hat{\mathcal{H}}_{RF}$ appear. Since we are looking at the effect on a carbon spectrum the term $\hat{\mathcal{H}}_{^{1}H}$ can be neglected. Homonuclear interactions of protons represented by $\hat{\mathcal{H}}_{^{1}H^{1}H}$ are not removed by a heteronuclear decoupling technique and may contribute to the excitation of heteronuclear DQ magnetisation for example. For most simple applications this term does not need to be considered. In this regard, efficient heteronuclear decoupling is achieved by eliminating the term $\hat{\mathcal{H}}_{^{1}H^{13}C}$ by appropriate

RF field irradiation. The most simple method is to apply *continuous wave* (*cw*) irradiation to the proton spins. The corresponding experiment is depicted in figure 2.13 a). Somewhat loosely explained, the irradiation continuously inverts the proton spins, hence averaging $\hat{\mathcal{H}}_{^1H^{13}C}$ to zero. A more sophisticated treatment of heteronuclear decoupling is demanding. AHT for example fails, since the target is not an effective average Hamiltonian because this in particular needs to become as small as possible. Although an average Hamiltonian of size zero can easily be derived, however, it is of course inappropriate for describing the performance of a heteronuclear decoupling sequence. Nevertheless, a theoretical treatment is possible by a direct approach of WAUGH[56].

One of the pitfalls of the *cw* decoupling is that the efficiency drops with the irradiation offset. Furthermore, with increasing MAS frequency the line width of the $^{13}$C resonances increases in contrary to the expected line narrowing. This might be explained by the suppression of proton homonuclear couplings, preventing fast mixing of proton states that lead to efficient *self-decoupling*. In order to increase the broadband performance and to enable efficient decoupling under fast MAS, a number of high power decoupling schemes have been developed, with the most important being discussed next.

- *Two Pulse Phase Modulation* (TPPM) decoupling[57] is the most widely used heteronuclear high power decoupling sequence. The sequence consists of a series of pulses with identical nutation angles but alternating phases. Viable parameters are given in figure 2.13 b), i.e. nutation angle of 170° and phase alternating between ±7.5° for TPPM15. For best experimental performance the values have to be fine-tuned.

- *Small Phase Incremental Alternation Decoupling* (SPINAL)[58] is a commonly used heteronuclear decoupling sequence consisting of a series of pulses having the same nutation angle and alternating phases. In contrast to TPPM the phase angle is incremented as shown in figure 2.13 c). The eight pulses of the SPINAL sequence can be summarised in an element $Q$. After the first pulse element was applied, the sequence is repeated with inverted phases ($\overline{Q}$). A continuous repetition of the two blocks ($Q\overline{Q}$) refers to SPINAL-16, whereas the four blocks of the order $Q\overline{Q}\overline{Q}Q$ refer to SPINAL-32. In this thesis the supercycled form SPINLA-64 ($Q\overline{Q}\overline{Q}Q\overline{Q}QQ\overline{Q}$) has been used for most experiments with $^{13}$C detection. The sequence can be used for solids but shows a good performance in particular for soft matter compounds such as liquid crystals.

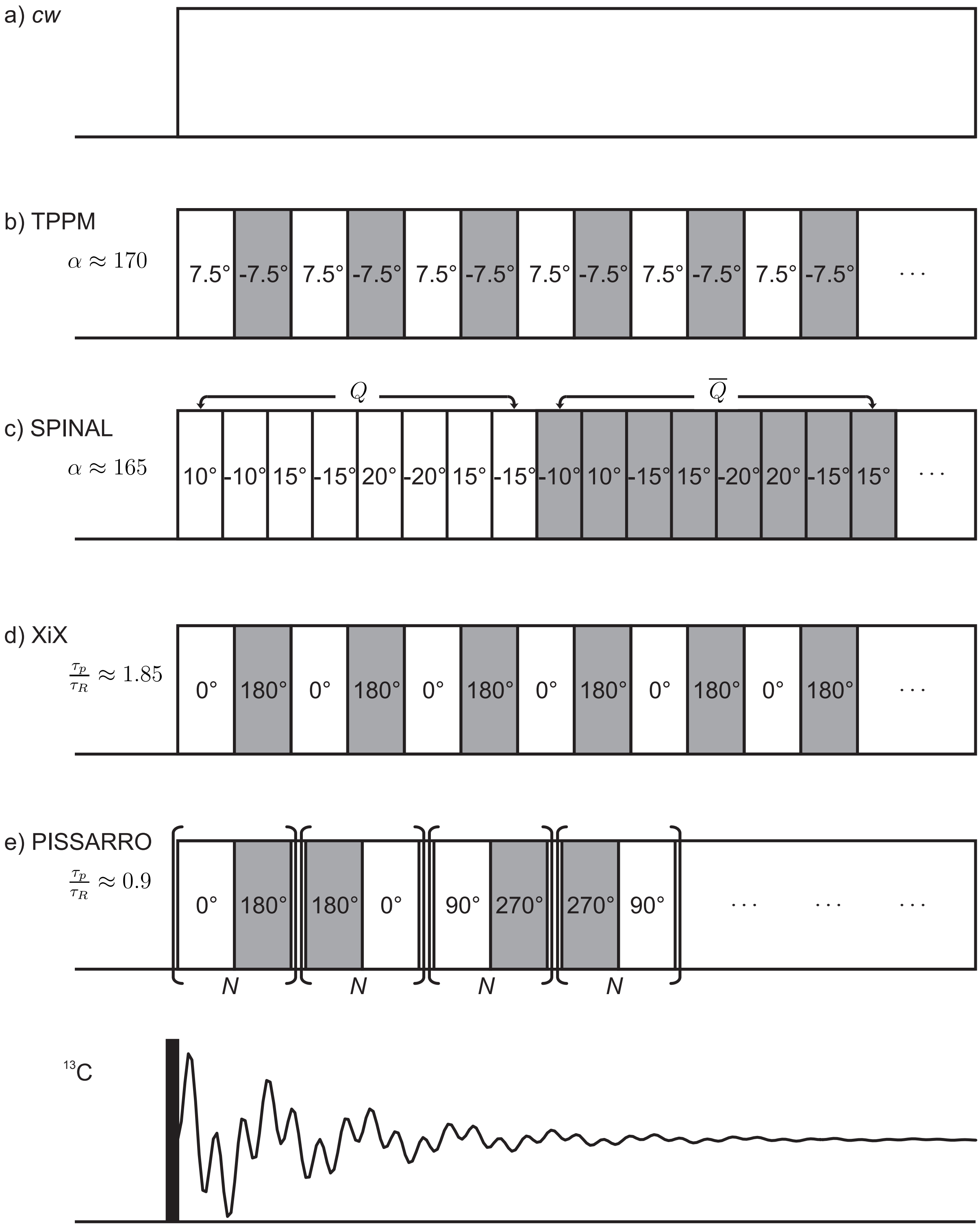

**Figure 2.13.** Heteronuclear decoupling schemes: a) *cw* decoupling, b) TPPM, c) SPINAL, d) XiX, e) PISSARRO

- Another important scheme is called *X inverse-X* (XiX)[59] which is considered to be superior to TPPM or SPINAL for MAS frequencies higher than 30 kHz. It consists of sequential pulses with alternating phases of 0° and 180° as seen in figure 2.13 d). It does not impose a certain nutation angle but the ratio of MAS period and pulse length needs to be optimised carefully at around $\tau_p/\tau_R \approx 1.85$. Since the pulse length depends on the MAS frequency, it is clear that in the limit of slow MAS, XiX shows a poor decoupling efficiency comparable to *cw* decoupling.

- *Phase-Inverted Supercycled Sequence for Attenuation of Rotary Resonance* (PISSARRO)[60] is a rather new heteronuclear decoupling sequence. Under MAS conditions several phenomena need to be considered, which might impair the quality of the obtained carbon spectrum. One of these is the so-called *rotary resonance* problem[61] taking effect when the nutation frequency $\nu_1$ matches a multiple of the rotor period:

  $$\nu_1 = n\ \nu_{rot} \qquad \text{with } n = \frac{1}{2},\ 1,\ 2,\ (3,\ \ldots) \tag{2.64}$$

  Rotary resonance is known to cause a drop of the decoupling efficiency, therefore it is advisable to use high RF amplitudes in order to meet $\nu_1 > 4\ \nu_{rot}$. For very fast MAS conditions frequencies possible nowadays, this requirement is not always fulfilled. One strategy to overcome this pitfall is the PISSARRO sequence, which partially quenches the effect of rotary resonance and moreover shows a good general performance under very fast MAS. The sequence was successfully implemented at a *Bruker* AVANCE III console in the course of this thesis. It is based on sequential pulses having opposite phase. In contrast to XiX, however, the $x\overline{x}$ pairs are only repeated $N$ times, where $N$ is typically 5. Afterwards the phase is changed in a supercycled manner which can be seen in figure 2.13 e). PISSARRO shows a good performance at $\tau_p \approx 0.9\ \tau_R$

#### 2.2.6.2. Homonuclear Decoupling

The most commonly used way to obtain high resolution $^1$H NMR spectra in the solid state is to apply fast MAS, however, sometimes the narrowing effect of MAS in the proton spectrum is not satisfactory. The homonuclear dipolar coupling might be scaled but is not sufficiently removed, thus a decoupling technique as in case of the heteronuclear coupling is desired. The homonuclear dipolar coupling must be treated differently compared to heteronuclear coupling, due to its more complex Hamiltonian. Unlike a $^1$H-$^{13}$C spin pair, for coupled protons the LARMOR-frequencies are similar, hence the spins cannot be manipulated independently. Modern homonuclear decoupling technique based on MAS and simultaneous application of RF pulses are commonly denoted *Combined Rotation And Multiple Pulse Sequence* (CRAMPS). CRAMPS techniques have been implemented during the acquisition time, i.e. in parallel to the FID in a windowed acquisition mode. In this method, multiple rotor-synchronised pulses are applied interrupted by periods in which the NMR signal is recorded. The method is very hardware demanding since it requires fast switching between pulse application and acquisition.

With the so-called LEE-GOLDBURG[62] (LG) scheme it is possible to remove the homonuclear dipolar coupling effects in the $F_1$ dimension of a 2D experiment replacing the redundant windowed acquisition scheme by an evolution period that allows continuous application of RF pulses in $F_1$ and a normal acquisition in $F_2$. A common application of LG decoupling is *Frequency Switched* LEE-GOLDBURG[63] (FSLG). The technique is based on a continuous application of off-resonant 360°-pulses, at the magic angle. Off-resonance acts as a distortion of the $B_1$-field defining the new reference axis of the *rotating frame*. An effective field is present whose direction depends on the amplitude of $B_1$ and on the magnitude of the frequency offset, as depicted in figure 2.2.6.2. If the frequency offset is carefully adjusted to match the condition

$$\Delta\nu_{off} = \frac{\nu_1}{\sqrt{2}} \tag{2.65}$$

the effective field will be aligned at the magic angle and the magnetisation precesses within a tilted rotating frame, the so-called *toggling frame*.

In this frame the dipolar Hamiltonian averages to zero over one precession period. By the geometrical constraint of matching the magic angle this period has a defined length, given by:

$$\tau_{LG} = \sqrt{\frac{2}{3}}\frac{1}{\nu_1} \tag{2.66}$$

Simultaneous switching of the sign of the frequency offset $\Delta\nu_{off}$ leads to error compensation of the magnetisation trajectories.

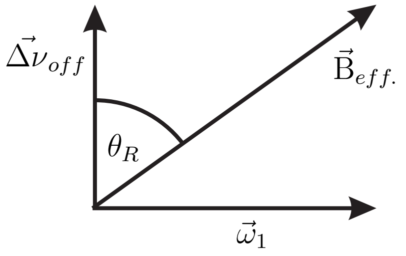

**Figure 2.14.** The principle of FSLG Decoupling

FSLG is relatively easy to implement and shows good performance at moderately high spinning[64] as well as at higher spinning frequencies in combination with shaped pulses[65]. However, it is prone to hardware instabilities and the required fast frequency switching gives rise to spectral artefacts, even with the most modern NMR equipment.

A slightly different scheme derived afterwards is *Phase Modulated* LEE-GOLDBURG (PMLG)[66], which is suited for windowed acquisition schemes (*w*PMLG) in contrast to

FSLG. In PMLG nearly on-resonant pulses are applied whose phases are continuously varying from one pulse to another. The relation between FSLG and PMLG is seen by considering the frequency phase relation $\phi_{(t)} = 2\pi\nu_{PMLG}t$. In this regard the equation resembles the condition 2.65, yielding:

$$|\nu_{PMLG}| = \frac{\nu_1}{\sqrt{2}} \tag{2.67}$$

where the frequency offset is replaced by the frequency $\nu_{PMLG}$. As indicated by the magnitude signs, this frequency may be positive or negative referring to a positive or negative rotation of the RF field. Furthermore, the sequence either starts with the magnetisation in $x$ or in -$x$-direction, and according to [67], the full denotation of the PMLG sequence declares the number of increments, the sign of the rotation, and the starting point. The phase increment is calculated according to $\Delta\phi = \pm 271.8/n$. The first series of $n$ pulses ($x$) may start with a phase of $\Delta\phi/2$, which is subsequently increased and followed by a second series of $n$ pulses ($\overline{x}$) decreasing from $180° - \Delta\phi/2$, where $2n$ is the overall number of pulses per PMLG block. The order ($x\overline{x}$) indicates a positive rotation about the toggling frame axis (PMLG$n^+$), whereas the sequence ($\overline{x}x$) acts as a negative counterrotation (PMLG$n^-$). On inverting the order of all $2n$ pulses, the magnetisation will start from opposite direction leaving the rotation direction as it is. The PMLG term will then be overlined.

In this thesis $\overline{\text{PMLG5}}^-$ has been used in the mixing time of an exchange experiment, as depicted in figure 2.2.7 b) consists have a different sign. In should be noted that in this NOESY-type experiment, the magnetisation is either aligned with the $z$-axis or with -$z$. In order to drive the precession in the toggling frame the magnetisation has to be inclined at the magic angle.

### 2.2.7. NOESY and EXCY

Molecular rearrangement or chemical reactions are sometimes accompanied by changes in the NMR spectrum. Depending on the timescale of the molecular motion, different NMR methods can be applied for quantitatively probing the rate of a molecular process. NMR in this respect provides a quite remarkable *dynamic range* of probing motional correlation times $\tau_c$. At the fast end ($\tau_c \approx 1$ ns), measurements of the spin lattice relaxation time ($T_1$ relaxation) provide general information about the rates of molecular processes. Slightly slower motions ($\tau_c <$ ms) can be traced by measuring the spin-spin relaxation time ($T_2$ relaxation) or rotating frame relaxation ($T_{1\rho}$ relaxation). By recoupling methods as well as by simulation of static line shapes or MAS patterns, motions having correlation times of $\tau_c = \mu$s to 1 ms can be investigated. These methods directly relate spectral characteristics with properties of the involved interaction Hamiltonians; hence give insight not only into the rate but also the kind of motion. At the slow end of the dynamic range, methods are mostly based on the varying chemical shift due to a change of the environment during the so-called *mixing* time. The upper limitation to the timescale of this method is only given by the $T_1$ relaxation. The method of probing *chemical exchange* during a mixing time is called *Exchange Spectroscopy* (EXCY), being routinely used in solution NMR experiments[68]. The basic pulse sequence is shown in figure 2.15 a). The first 90°-pulse generates transverse magnetisation which evolves in $t_1$ and provides chemical shift dispersion in $F_1$. The second pulse re-aligns the magnetisation along the $z$-axis prior to the mixing time whereupon a third pulse reads-out the magnetisation. Without chemical exchange the obtained 2D pattern would consist of diagonal peaks only. However, if exchange occurred during the mixing time off-diagonal cross-peaks would appear connecting those sites undergoing chemical exchange.

EXCY is obviously simple, however, it is not sensitive to chemical exchange selectively. With the given pulse sequence basically three different phenomena may cause off-diagonal peaks, referring also to separate designations for an identical pulse sequence:

- *Exchange Spectroscopy*, EXCY:
  Cross-peaks due to chemical exchange

- *Nuclear Overhauser Effect Spectroscopy*, NOESY:
  Cross-peaks due to cross relaxation

- *Dipolar Exchange*:
  Cross-peaks due to zero quantum transfer

The Nuclear Overhauser effect (NOE) is basically ascribed to a phenomenon in solution NMR, where it is the major interaction based on non-secular dipolar couplings[69] between spatially close nuclei that are not directly linked ($J \approx 0$). In a solid it is negligible compared to the dipolar exchange also known as *spin diffusion*. In dense proton systems like most organic samples it is the strongest interaction mechanism, most often stronger than chemical exchange. In order to selectively probe chemical exchange spin diffusion has to be suppressed during the mixing time, in order to ensure that cross-peaks are due to chemical exchange. This can be achieved by PMLG decoupling during the mixing time, as indicated in figure 2.15 b).

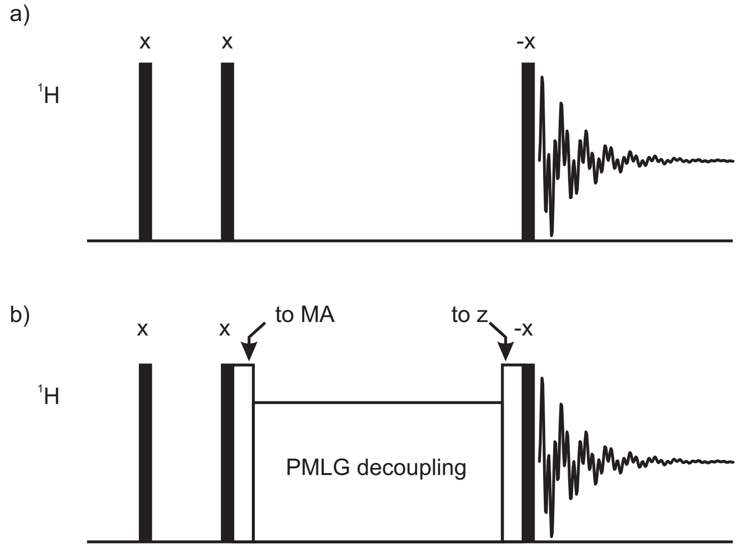

**Figure 2.15.** The EXCY sequence without (a) and with (b) suppression of spin diffusion.

## 2.3. Advanced Solid-State NMR Methods

This paragraph deals with modern recoupling methods in solid-state NMR that have been used in this work. The general concept of dipolar recoupling by means of a 2D *excitation/reconversion* scheme will be demonstrated. As seen already in the context of *de*coupling, the handling of homonuclear and heteronuclear dipolar couplings requires different concepts, hence also in dipolar *re*coupling different schemes have been developed since the late 1980s[70]. The INADEQUATE sequence, although being actually a classical solution NMR experiment, has been included in this section because *through-bond* correlation facilitated by J-couplings has lately become a important issue in solid-state NMR[71] as well as in chapter 3 of this work.

### 2.3.1. Dipolar Recoupling

As seen in section 2.2.1, the anisotropies of different NMR interactions are efficiently averaged by MAS. The achieved resolution on one side means a loss of information on the other, since the line broadening is due to interactions containing parameters such as distances or relative orientations. The dipolar coupling Hamiltonian for example exhibits a relation of $\hat{\mathcal{H}}_D \propto \frac{1}{r^3}$ with respect to the distance between the investigated spin pair. There are different ways to regain this information, as for example spinning at lower MAS frequencies[72,73] or spinning at a deviant angle not precisely inclined at the magic angle, i.e. *off-magic angle spinning*[73] (OMAS). These techniques, however, come with the price of broadening the spectral lines, whose high resolution has been achieved by elaborate MAS hardware. Moreover, the broadened spectra may only be useful in exceptional cases.

In order to retain the high resolution achieved by fast MAS *recoupling* techniques introduced by SCHAEFER and GULLION in 1989, first shown in case of *Rotational Echo Double Resonance*[70] (REDOR), are used. In REDOR and all other recoupling techniques rotor-synchronised RF pulses are used to recouple certain parts of the overall interaction Hamiltonian. That way, the achieved resolution is not diminished since the RF pulses only operate on the spin part of the Hamiltonian, leaving the line width unchanged.

In general, recoupling can be achieved using two different types of pulses. The first approach uses high power RF pulses of a very short duration, being treated as infinitely short $\delta$ pulses. This assumption is not always realistic, since the widely used pulse length of 2.5 $\mu$s has a significant length compared with the rotor period, i.e. 7 % at a common MAS frequency of 30 kHz. Luckily the effects arising from the finite duration of the RF pulse can be treated as usual pulse imperfections, hence are removed by phase cycling or compensate in other ways. The second kind of recoupling makes use of longer continuous pulses not being interrupted by delays. These pulses, matching multiples of the rotor period, cause a precession around a $\vec{\mathrm{B}}_1$-field, hence they are sometimes called *tilted frame* methods. Another more frequently used term is *symmetry sequences* introduced by LEVITT[74,75]. The expression is due to the different symmetry properties of interaction Hamiltonians, which can be used to select certain contributions. These kind of experiments are relatively prone to phase errors, require fast and precise phase switching, as well as a lot more experience. In this work recoupling is therefore only achieved by application of high power RF pulses, which are more robust and well tested. It has to be clarified, however, that if longer recoupling times are needed due to weak interactions, symmetry sequences should be preferred.

The recoupling experiments used in this thesis are the REPT-HSQC experiment, a heteronuclear recoupling method providing $^1$H-$^{13}$C *through-space* correlation. The *back-to-back* or *BABA* sequence is a homonuclear DQ recoupling technique. The conducted INADEQUATE experiment is not a recoupling technique, since it is based on the isotropic $J$-coupling which is not removed by MAS. Though small and usually not observed directly, it is still present and does not need to be recoupled.

## 2.3.2. On Double Quantum NMR

Recoupling techniques can also be used to excite multiple quantum coherences (MQCs, cf. DQ coherences in Fig. 2.2) in solids[76]. MQCs are not intuitively understood from the quantum mechanics point of view because the theory of the angular momentum actually forbids a change of the azimuthal quantum number $m$ by more than 1. This rule is even not bypassed by involving perturbation effects as in the theory of the anharmonic oscillator allowing for vibrational overtone transitions. MQCs are possible, though, because a state as $|\alpha\alpha\rangle$ is not a natural basis for a single angular momentum operator, hence the $\Delta m$ condition is softened or even meaningless. It is a redundant denotation but eligible through the density matrix formalism, in which MQCs of a particular order have a distinct position (see Fig. 2.2). An MQC does not imply a detectable field oscillating at the sum frequency of notional SQ coherences. Therefore, MQC cannot be observed directly. For this reason experiments that rely on their evolution require a 2D scheme in which MQCs are transferred into detectable SQ coherences at the end of the experiment. As a rule, an MQ experiment consists of 4 distinct steps beginning with the **excitation** of MQCs (see figure 2.16) by means of RF pulses.

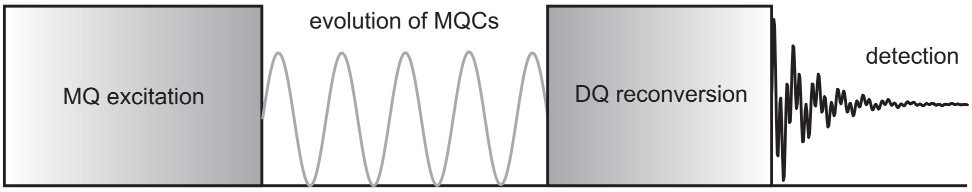

**Figure 2.16.** The illustration shows the general scheme of a *lab-frame* recoupling technique.

If the J-coupling is used to generate the MQCs the rotor synchronisation is obsolete, since the phase of the interaction is not modulated by the MAS frequency. After excitation of MQCs the variable $t_1$ time known as **evolution** period follows, in which the coherences are subjected to the chemical shift evolution in order to achieve frequency discrimination in the $F_1$ dimension. The third step is the **reconversion** of MQCs into $z$-magnetisation. The last period is the **detection** beginning with a 90°-pulse, also called *read-out pulse*, followed by the acquisition time. It should be noted that the coherence evolving during $t_1$ might not necessarily be a MQC, but may also have single quantum order. In this regard figure 2.16 can be seen as a general illustration of any *lab-frame* recoupling technique.

## 2.3.3. Heteronuclear Dipolar Recoupling

The heterononclear recoupling method presented here is based on the REDOR approach that was first used to recouple the dipolar coupling Hamiltonian of two kinds of low-$\gamma$ nuclei[70]. In equation 2.70 rotor modulation due to MAS enters the formalism and is covered by means of the integrated phase of a particular anisotropic interaction. The contribution of the anisotropic part thereby becomes antisymmetric with respect for to a time shift of half a rotor period as seen in equation 2.41, i.e. $\hat{\mathcal{H}}_D$ changes sign every $\tau_R/2$, hence vanishes over time. The REDOR-type recoupling prevents this cancellation due to the fact that the interaction is linear in $\hat{I}_z$, such as the heteronuclear coupling can be inverted by application of 180°-pulses. By application of these rotor-synchronised pulses on one of the two channels with spacings of half a rotor period, the integrated phase of the heteronuclear coupling Hamiltonian does not average out but builds-up over the length of the recoupling block. A related pulse sequence is depicted in figure 2.17, describing a *through-space* $^1$H-$^{13}$C dipolar correlation method. In order to selectively recouple the heteronuclear coupling the middle pulse of the excitation period is applied on the $^1$H channel. This does not make a difference with respect to the recoupling of the heteronuclear coupling Hamiltonian, but leads to full cancellation of the CSA integrated phase. However, REDOR-based $\pi$-pulse trains can also be used to recouple the CSA in a slightly different manner[77].

#### 2.3.3.1. REPT-HSQC

Generally, $^{13}$C has an about 20 times higher chemical shift dispersion, compared to $^1$H. Due to the large range, signals can easier be assigned, thus a sometimes crucial assignment of $^1$H resonances can only be achieved by a *heteronuclear correlation experiment* (HETCOR). The importance of these HETCOR spectra will be demonstrated in the first experimental chapter 3 in case of strongly shifted proton signals. The HETCOR spectrum was obtained using a solid-state version of the widely used *Heteronuclear Single Quantum Correlation* (HSQC) experiment[78], the so-called REPT-HSQC where REPT stands for *recoupled polarisation transfer*[79]. In contrast to the conventional HSQC, based on the heteronuclear J-coupling, the REPT-HSQC[80] is a dipolar recoupling technique, and recouples the heteronuclear dipolar coupling Hamiltonian given in equation 2.56. The pulse sequence is shown in figure 2.17.

During the excitation period so-called antiphase coherences of the order $(\hat{I}_x^{1H}\hat{J}_z^{13C})$ are created evolving under the influence of chemical shift of the protons spins in t$_1$. After the reconversion of the antiphase coherence into observable magnetisation and a final *read-out* pulse, the detected signal is given by:

$$S_x(t_1) = \langle sin(n_{exc}\Phi_{D(0)})\ sin(n_{exc}\Phi_{D(t_1)})\ cos(\omega_{CS}^{I(H)} t_1)\rangle \tag{2.68}$$

$$S_y(t_1) = \langle sin(n_{exc}\Phi_{D(0)})\ sin(n_{exc}\Phi_{D(t_1)})\ sin(\omega_{CS}^{I(H)} t_1)\rangle \tag{2.69}$$

If the t$_1$ time is incremented in units of rotor periods, the integrated phases $\Phi_{D(0)}$ and

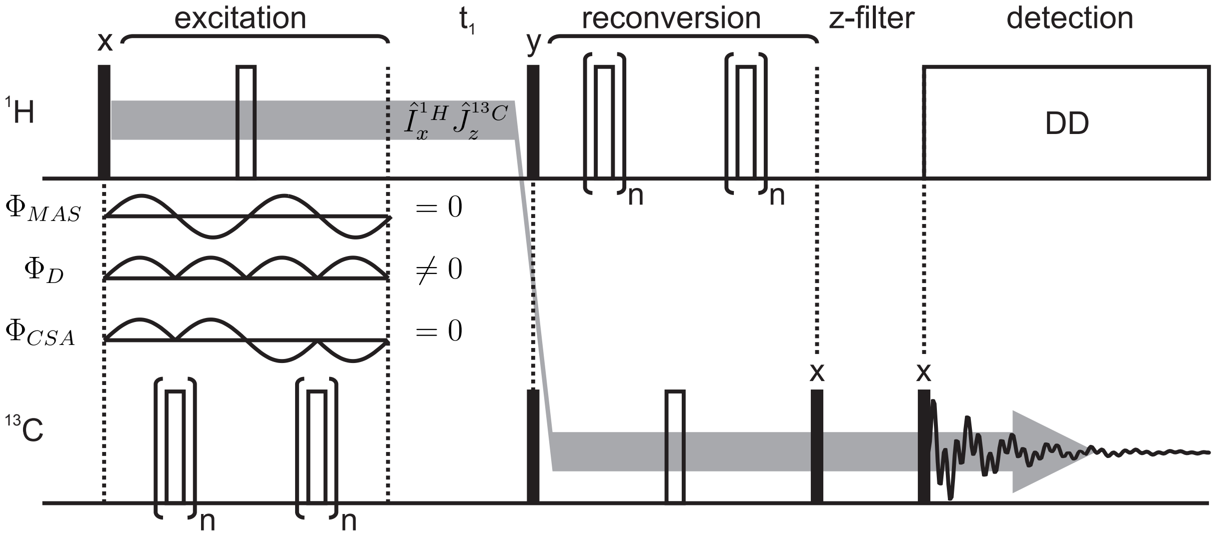

**Figure 2.17.** The REPT-HSQC pulse sequence. In order to control the overall recoupling time the length of the excitation and reconversion blocks can be changed by varying the number of $\pi$-pulses "n".

$\Phi_{D(t_1)}$, defined in equation 2.38 do not change in subsequent experiments. The magnetisation only evolves under the chemical shift of the protons and consequently, the sequence results in a carbon proton correlation spectrum. As can be seen by equations 2.68 and 2.69, appropriate data processing requires a phase sensitive detection in both dimensions, which is done by the STATES-TPPI method explained in section 2.2.4.

Using short recoupling times it is possible to probe strong heteronuclear couplings, i.e. dipolar interactions between a close and rigid carbon proton pair. Thereby setting the excitation time to one rotor period under fast MAS, only the chemically bound carbon proton pairs will be displayed, assisting the assignment considerably. More distant CH pairs can be recoupled with longer excitation/reconversion times, however, in case of a rigid methylene group, the approximation of an isolated spin pair fails. Furthermore, due to the geometrical constraint of a methylene group the intensity almost vanishes for $\tau_{exc,rec} = 2\tau_R$.

### 2.3.3.2. The Back-to-Back Sequence

Back-to-back is a homonuclear recoupling method for MQ NMR excitation[81] facilitating several different implementations in various experiments. In this thesis it was used in all experimental chapters. Back-to-back is preferably used for DQ NMR, but *triple quantum* (TQ) correlation or higher order MQCs are possible in general[82]. The method is of great use for probing proton-proton proximities, their rigidity and even for the quantisation of nuclear distances[83–85].

The major building block of back-to-back is a succession of four short 90°-pulses having distinct phases and timings. These blocks are used in the excitation and reconversion stages shown in figure 2.18 a). The rotor period is depicted in figure 2.18 b). The DQ signal arising from the excitation/reconversion blocks can be determined by considering the effects of the RF pulses on the homonuclear dipolar coupling Hamiltonian (compare with equation 2.36):

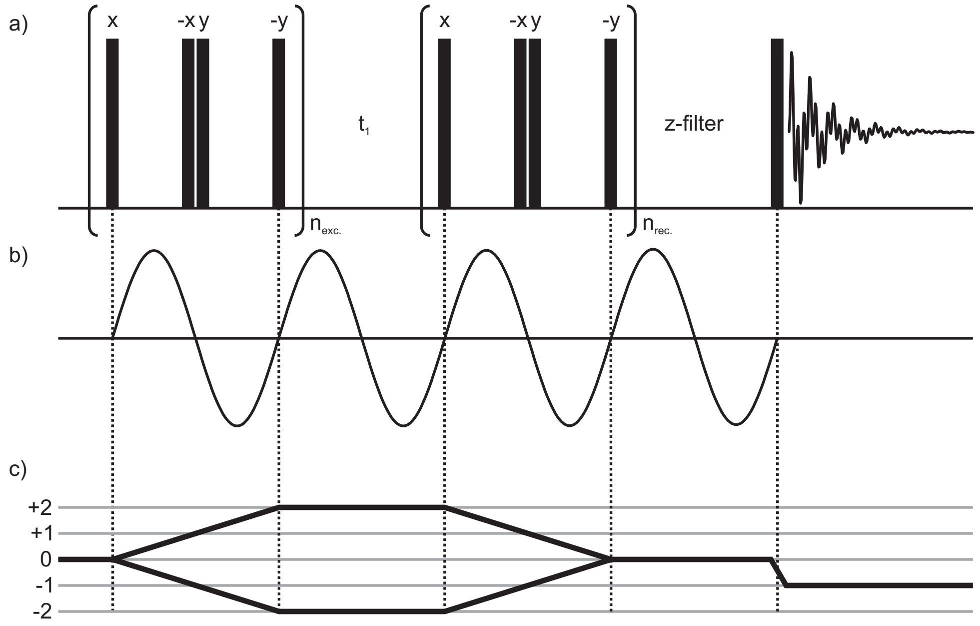

**Figure 2.18.** The back-to-back sequence. *a*) The excitation and reconversion blocks consist of rotor synchronised blocks of four 90°-pulses: $90_x - \frac{\tau_R}{2} - 90_{-x}90_y - \frac{\tau_R}{2} - 90_{-y}$. The excitation time depends on the number of blocks $n_{exc}/n_{rec}$ used. *b*) The rotor period. *c*) The coherence transfer pathway diagram of the method indicates the progression of quantum order. DQ order is selected by a 16 steps phase cycling scheme[81].

$$\overline{\hat{\mathcal{H}}}_D^{MAS} = \hat{\mathrm{T}}_{20}^{D}\frac{1}{t}\sqrt{\frac{3}{2}}\Phi_D \tag{2.70}$$

In this equation $\hat{\mathrm{T}}_{20}^{D}$ is the starting point for specific manipulation of the spin part of the Hamiltonian. According to SCHNELL in [86], the Hamiltonian describing one back-to-back segment is given by

$$\overline{\hat{\mathcal{H}}}_D = \frac{1}{\tau_R}\underbrace{[3\Phi_D^{homo}]_0^{\frac{\tau_R}{2}}}_{\Omega^{ij}}\left(\hat{\mathrm{T}}_{2,+2}^{ij} + \hat{\mathrm{T}}_{2,-2}^{ij}\right) \tag{2.71}$$

This equation only describes DQ coherences as indicated by the spin tensors of the order ±2. It is now possible to derive the DQ signal intensity of the back-to-back sequence. It is apparent that the signal is modulated by the phases of the excitation and reconversion blocks, which usually have the same length:

$$S^{ij}_{DQ}(t) \ \propto \ (d_{ij})^2 \left\langle sin\left(n_{exc}\Omega^{ij}_{exc}\right) \ \left(n_{rec}\Omega^{ij}_{rec}\right)\right\rangle \tag{2.72}$$

$$\tau_{exc} = n_{exc}\tau_R = n_{rec}\tau_R = \tau_{rec}$$

In a 2D experiment excitation and reconversion blocks are separated by the $t_1$ evolution time of the experiment as illustrated in figure 2.18 a). Back-to-back-type recoupling is a versatile method that has been implemented in a number of different experiments. The excitation/reconversion times can be increased by appending another $90_x - \frac{\tau_R}{2} - 90_{-x}90_y - \frac{\tau_R}{2} - 90_{-y}$ block. It should be noted, however, that in case of two or four rotor periods DQ excitation, the phases are set such that offset and phase imperfections are compensated.

By choosing different incrementation schemes numerous types of spectra can be obtained. Setting the increment to $\Delta t = n\ \tau_R$, i.e. by using rotor synchronised incrementation of $t_1$ leads to so-called DQ-SQ correlation pattern, with $F_1$ being the DQ dimension. The interpretation of this kind of spectra is identical to that of the 2D INADEQUATE experiment described in section 2.3.4 and is given in figure 2.19.

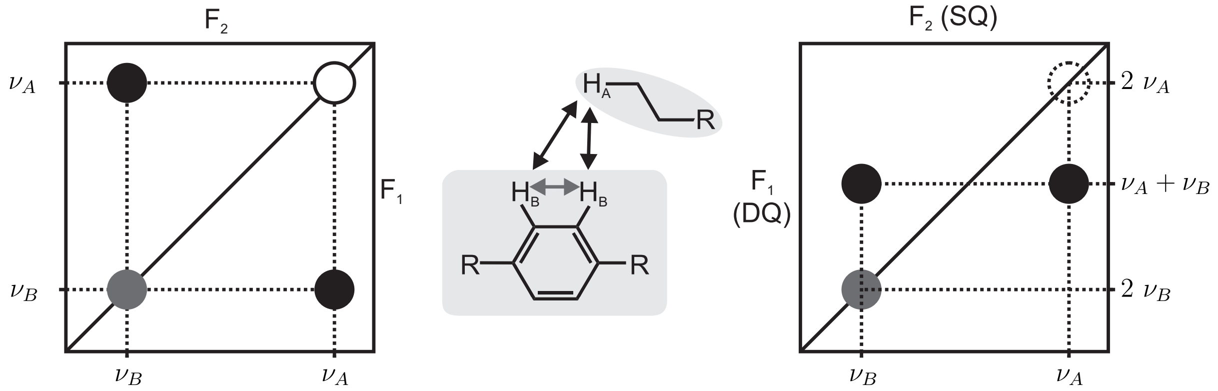

**Figure 2.19.** Interpretation of DQ-SQ correlation spectra in comparison to usual correlation pattern.

The left-hand side shows a usual 2D spectrum correlating resonances by means of their chemical shift in both dimensions. A trivial example might be the mentioned *dipolar exchange* experiment. In this experiment cross-peaks will appear if the corresponding sites exchange or are affected by any kind of polarisation transfer (see section 2.2.7 for more information). Without any of these effects present only diagonal peaks are observed. However, in case of coupled non-equivalent protons $H_A$ and $H_B$, cross-peaks arise at positions ($\nu_A$, $\nu_B$) and ($\nu_B$, $\nu_A$).

The meaning of the $F_1$ dimension in a DQ-SQ correlation pattern is different. In back-to-back-type DQ-SQ correlation pattern peaks will arise only if the corresponding $^1$H-$^1$H sites are dipolar coupled with each other. Here, the correlation peak is defined by the chemical shift of both peaks in the SQ dimension, whereas the position along the double quantum dimension is given by the sum of both SQ chemical shifts. On the right-hand side in figure 2.19 one can distinguish two cases. If two like protons are coupled ($H_A$), the pattern will show a single *autocorrelation peak* located at the diagonal ($\nu_A$, $\nu_A$). However, in case of a coupling between chemically different sites ($H_A$ and $H_B$) the method will give rise to cross-peaks located at ($\nu_A$, $\nu_A + \nu_B$) and ($\nu_B$, $\nu_A + \nu_B$). In this manner valuable information about the molecular organisation of the sample is obtained. On the one hand it can be probed which sites are dipolar coupling with each other and on the other hand the amplitude of the peaks allows for an estimation of relative distances or the dynamics of the coupled nuclei in a qualitative way.

Coming back to the BABA excitation scheme, it was shown that disaggregating the rotor period into smaller increments leads to a greater bandwidth in the $F_1$ dimension after Fourier transformation and to a DQ sideband pattern that can be analysed in order to determine the dipolar coupling constant $d_{IJ}$[87–89]. The back-to-back sequence may also be used in a 1D fashion by simply setting $\Delta t_1 = 0$. In these experiments the pulse sequence acts as a *Double Quantum Filter* (DQF), only permitting DQ magnetisation to pass through. Finally, it is possible to change the length of the excitation/reconversion blocks themselves, leading to so-called DQ build-up curves. The DQ signal intensity (equation 2.72) contains the square of the dipolar coupling constant $d_{IJ}$, thus a total distance dependence of $\propto \frac{1}{r^{-6}}$[83]. Especially at the onset with few increments the build-up curve provides precise distance information[90]. For an isolated two spin pair, longer excitation/reconversion times lead to a saturation at a certain level and characteristic oscillations of $S_{DQ}(\tau_{exc/rec})$. However, under real conditions the assumption of an unperturbed spin pair is not valid anymore and multispin effects, mainly spin diffusion, impair the build-up behaviour and cause relaxation. The analysis of DQ build-up curves is therefore limited to weakly coupled systems as liquid crystals[91] or polymer melts[92]. For this reason, the proton dense samples investigated in this thesis did not allow to record meaningful build-up curves, not to mention DQ sideband patterns. $^1$H-$^1$H DQ-SQ correlation pattern and $^1$H DQF MAS spectra, however, have been of vital importance, enabling valuable insight into the organisation of all three supramolecular systems investigated herein.

### 2.3.4. The INADEQUATE Experiment

Another DQ-SQ correlation experiment applied in this work is a J-mediated $^{13}$C-$^{13}$C *through-bond* correlation experiment widely used for structure elucidation in solution NMR. The experiment is named *Incredible Natural Abundance Double Quantum Transfer*, leading to the peculiar acronym INADEQAUTE[93]. In general, using J-couplings in solids is exceptional simple since they are isotropic, i.e., there is no orientation dependence. Consequently, J-couplings are insensitive to molecular motion and do not pose a limitation to the MAS frequency. However, there is a severe drawback related to the low sensitivity of $^{13}$C-$^{13}$C through-bond correlation at the natural abundance level being about 1.1 %. The probability of finding a connected pair of $^{13}$C atoms is therefore only about $10^{-5}$, causing very long experiment times even in the solution NMR, where carbon lines are intrinsically narrow. The pulse sequence and the corresponding CTP are given in figure 2.20.

The pulse program may sufficiently be explained by considering only the first part until the 90°-pulse after the $t_1$ time. The sequence starts with the generation of transverse magnetisation (-$\hat{I}_y$) either by a single $x$-pulse or by a CP step prior to the experiment. The following 180°-pulse in the middle of the first echo refocuses the chemical shift, hence it does not need to be considered and the magnetisation just before the 90° preparation pulse is only modulated by the J-coupling:

$$2\hat{I}_x\hat{I}_z sin(\pi J\tau) - \hat{I}_y cos(\pi J\tau) \tag{2.73}$$

Equation 2.73 is in accordance with the product operator transformations for evolution under J-couplings[10]. If the delay $\tau$ is chosen to fulfil the condition $2\tau = \frac{1}{2J_{CC}}$ the cosine term vanishes, whereas the antiphase magnetisation term $2\hat{I}_x\hat{I}_z$ is maximised. A 90° $x$-pulse transforms the antiphase magnetisation into DQ coherences. Here, it shall be pointed out that the INADEQUATE sequence gives rise to a number of different experiments starting with the first 1D experiment proposed by Bax and coworkers in 1980[93]. In this simple experiment the DQ magnetisation is immediately transferred into antiphase magnetisation by another 90° $x$-pulse, which is directly recorded giving rise to a 1D pattern containing antiphase signals. This basic experiment can be divided into two parts, illustrating its working principle, i.e. a simple spin echo combined with a homonuclear DQ filter allowing only signals to pass through that are J-modulated by the spin of a neighbouring $^{13}$C atom.

By enabling DQ evolution after the last preparation pulse by introducing a $t_1$ time the 2D INADEQUATE experiment is obtained[94,95], giving rise to the same kind of 2D DQ-SQ correlation pattern as given in figure 2.19. The $t_1$ time in this experiment can be seen as a $z$-filter of variable length. A disadvantage of the raw 2D sequence is the detection of antiphase signals meaning a loss of resolution and sensitivity. Therefore, the so called 2D *refocused* INADEQUATE is usually applied to record $^{13}$C-$^{13}$C correlation pattern. To the best of knowledge it was first introduced by Benn *et al.* in 1983[96]. The refocusing is enabled by a second echo sequence in succession to the evolution time as shown in figure 2.20. In solid-state NMR these kind of *through-bond* correlation experiments are not commonly employed, mainly because J-coupling is a relatively small quantity compared to heteronuclear dipolar interactions. In the context of recoupling methods in section 2.3.1, the *tilted frame* methods have been mentioned, filtering interactions by means of symmetry properties of the underlying Hamiltonian. The so-called *Total Through-Bond Correlation Spectroscopy* (TOBSY) belongs to this kind of symmetry sequences, enabling $^{13}$C- $^{13}$C and $^{31}$P- $^{31}$P correlation[97–99].

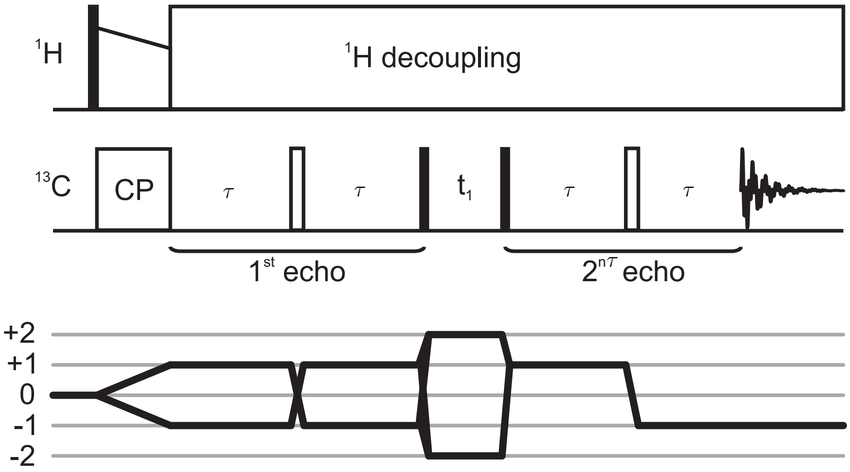

**Figure 2.20.** The pulse sequence of the refocused 2D INADEQUATE experiment.

Early experiments by Emsley and co-workers showed that dipolar contributions to the spectrum are negligible[100] and INADEQUATE is feasible also in the solid state, albeit $^{29}$Si- $^{29}$Si 2D INADEQUATE was applied even before in order to reveal the connectivity in zeolites[101]. By means of the refocused INADEQUATE it was shown that correlation spectra can be obtained in a reasonable experimental time[102].

In search of the appropriate INADEQUATE sequence another aspect should be considered relating to the distinction of homogeneously and inhomogeneously broadened line widths: In case of the non-refocused INADEQUATE the sensitivity is diminished by cancelation of positive and negative lobes of the antiphase signal leaving only smaller "wavelets" at the edge of the resonance, the sensitivity of the refocused INADEQUATE depends on the non-refocusable *homogenous* line width[102]. In this manner the refocused INADEQUATE seems to be the better choice but has to be compromised with inevitable signal losses during the second echo1).

It has been tried to improve the refocused INADEQUATE sequence in several ways for example by implementation of an additional $z$-filter avoiding spectral artefacts due to ZQ contribution during the acquisition time. A remarkable sensitivity loss is based on the splitting into antiphase magnetisation after the DQ evolution. It was shown that the sensitivity can be enhanced by a factor of $\sqrt{2}$ by using the more involved INADEQUATE-CR method[103, 104], where CR stands for *composite refocusing*. The basic concept relies on the channelling of the whole magnetisation into a single antiphase line. INADEQUATE-CR thereby avoids cancelation of magnetisation imposed by the DQ reconversion pulse after the $t_1$ time. The method is demonstrated in two tutorials by PODKORYTOV[105] and MEISSNER[106] in great detail.

As in all MQ techniques, DQ selection in INADEQUATE is provided by a 4-step phase cycling scheme, being repeated with four different receiver phases giving rise to a total minimum number of 16 steps. Another strategy serving to improve the sensitivity therefore works rather indirectly, i.e. performing the DQ selection by means of pulsed field gradients rather than by phase cycling. That way, a reduction of the experimental time by a factor of four is theoretically possible.

The usual refocused 2D INADEQUATE experiment suffers from several artefacts such as the so-called relayed peak between two non-bonded nuclei that have a common coupling partner. Besides these unwanted peaks, the spectrum slices of the 2D pattern indicate severe line shape distortions in both dimensions, in particular the double quantum dimension. All of these effects can be described by product operator formalism of a three spin system as demonstrated by CADARS and co-workers[107], suggesting that theses artefacts are mostly related to multispin effects in $^{13}$C enriched compounds. Since the herein measured samples were natural abundance compounds, multispin effects have not been considered. Due to its robustness, the usual refocused INADEQUATE sequence given in [102] has been used for all experiments apart from the incorporation of different polarisation methods (Hartmann-Hahn CP, ramp-CP and SPE), various decoupling schemes, and 2D detection methods, that have been carefully adjusted to obtain distinct correlation peaks. In order to demonstrate the power of the refocused 2D INADEQUATE, the setup

---

1) In case of $1/\pi T_2^* \approx 1/\pi T_2$ (see section2.2.3), the non-refocused version is clearly the better choice since the second echo only contributes to relaxation.

has been carried out for uniformly labled L-tyrosine·HCl shown in figure 2.21.

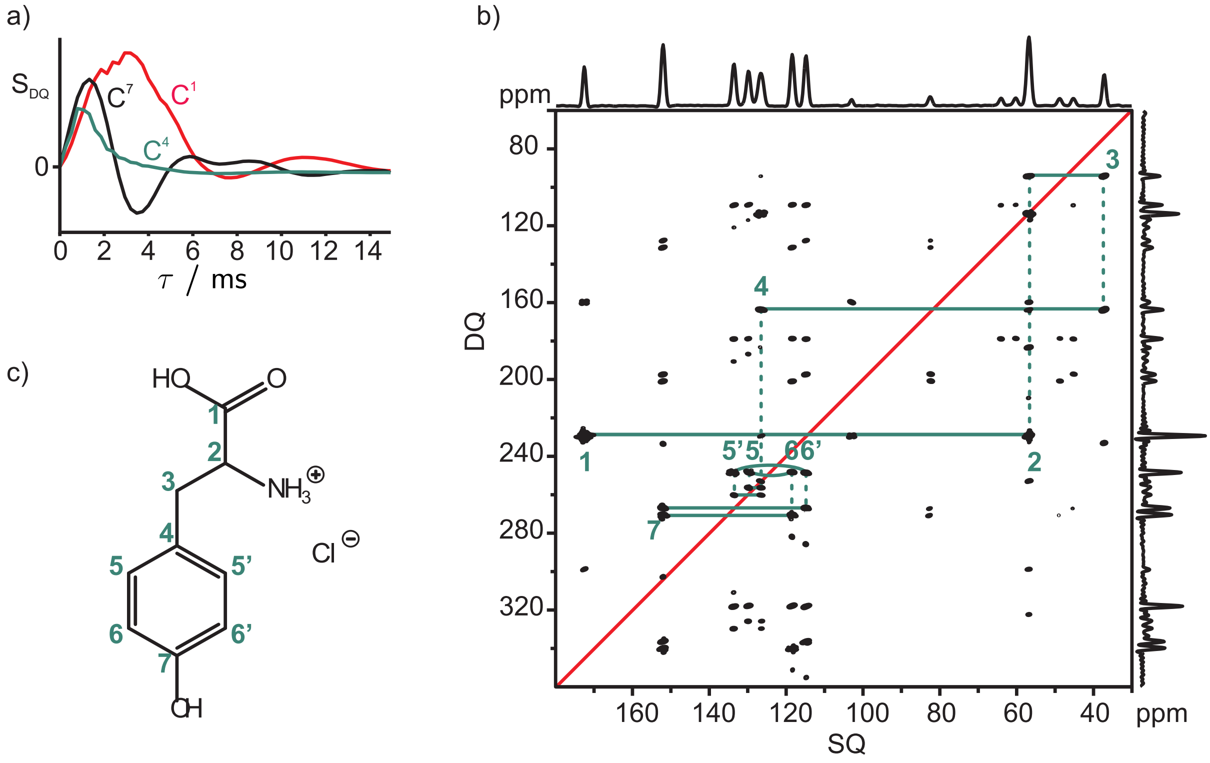

**Figure 2.21.** a) DQ build-up of selected carbon atoms in uniformly labeled L-tyrosine·HCl as a function of the delay time $\tau$ (cf. Fig. 2.20). The build-up is superimposed by ill-defined relaxation effect suppressing oscillations of the DQ intensity. These relaxations also shift the maximum of the build-up to very short delay times. b) Refocused 2D INADEQUATE of L-tyrosine·HCl using a delay of 1.4 ms. c) Connectivity of L-tyrosine·HCl as indicated by the 2D pattern.

Figure 2.21 a) shows the DQ build-up behaviour for three specific carbon sites in L-tyrosine·HCl. In this experiment, performed prior to the actual through-bond correlation run, the echo delay $\tau$ is varied with zero $t_1$ time. The $^{13}$C-$^{13}$C J-coupling in aliphatic $sp^3$ carbons is commonly known to have $J_{CC} \approx 35$ Hz. In theory this value leads to an optimal delay of about 7 ms, whereas the highest DQ intensity $S_{DQ}$ is reached already for delays slightly longer than 1 ms. Clearly, the $J_{CC}$ constant in case of a aromatic carbon sites is larger, however, it does not shift the maximum of the curve to such low values. The build-up is apparently superimposed by severe relaxation losses, shifting the relaxation to shorter delay times. For this reason the 2D $^{13}$C-$^{13}$C correlation pattern presented in figure 2.21 b) has been recorded with only $\tau$ =1.4 ms. The interpretation may start with the carbonyl peak (C$^1$) which is easily assigned due to its rather outstanding chemical shift of 173 ppm. By pointing in horizontal direction the peak of the coupled site C$^2$, having same chemical shift in $F_1$ is found. This peak is coupled to the site $C^3$ indicated by a pair of cross-peaks located at (57 ppm, 95 ppm) and (38 ppm, 95 ppm). In this manner it is possible to trace the connectivity of the whole L-tyrosine·HCl given in figure 2.21 c).

In this work the refocused 2D INADEQUATE sequence has been of great value in order to reveal conformational changes in the side chains of $C_3$-symmetrical tricarboxamides which will be presented in the following chapter.

# 3. The Bulk Organisation of $C_3$-Symmetrical Tricarboxamides

Solid-State NMR is a powerful tool to reveal the microscopic organisation of a material. Disc-shaped symmetrical molecules are a particularly rewarding class of materials to be covered in a supramolecular study, since the oblate shape *a priori* suggests a stacking or at least a coplanar arrangement of molecules, a fact that leads to discotic liquid crystalline behaviour. Disc-shaped compounds often possess further symmetry elements like centres of inversion or mirror planes perpendicular to the molecular backbone. This has two obvious advantages with respect to NMR: On the one hand, even moderately large molecules provide a limited number of sites, thus avoid spectral crowding. On the other hand, a more complex solid-state NMR spectrum, *i.e.*, more signals than the pure number of non-equivalent atoms would suggest, points to a symmetry breaking due to the environment of the molecule. The symmetry breaking is mostly induced by an asymmetric packing of molecules which often enables an elucidation of the type of the arrangement. This has been shown for example in case of hexabenzocoronenes[108].

In this chapter small $C_3$-symmetrical molecules will be presented, revealing a large number of structure-related properties in the solid state, although their chemical structure is staggeringly simple. This first experimental chapter deals with the organisation of benzene-1,3,5-tricarboxamides (BTAs), which where intensely investigated by MEIJER and co-workers since the late 1990ies[109–111]. The common building block of these compounds is a benzene ring, which is substituted by different amide groups in 1, 3, and 5-position of the ring. Early results on these materials have been obtained for relatively large systems, for example including a 3,3'-diamino-2,2'bipyridine unit capped with gallic moieties located at each arm, thus for compounds with a considerably larger blade compared to the samples investigated in this study (see below). The structure of one of these complex molecules is given in figure 3.1, also illustrating their obvious helical supramolecular arrangement. These previously studied materials had been explored by various techniques, including a solid-state NMR investigation carried out by HOFFMANN[112]. The

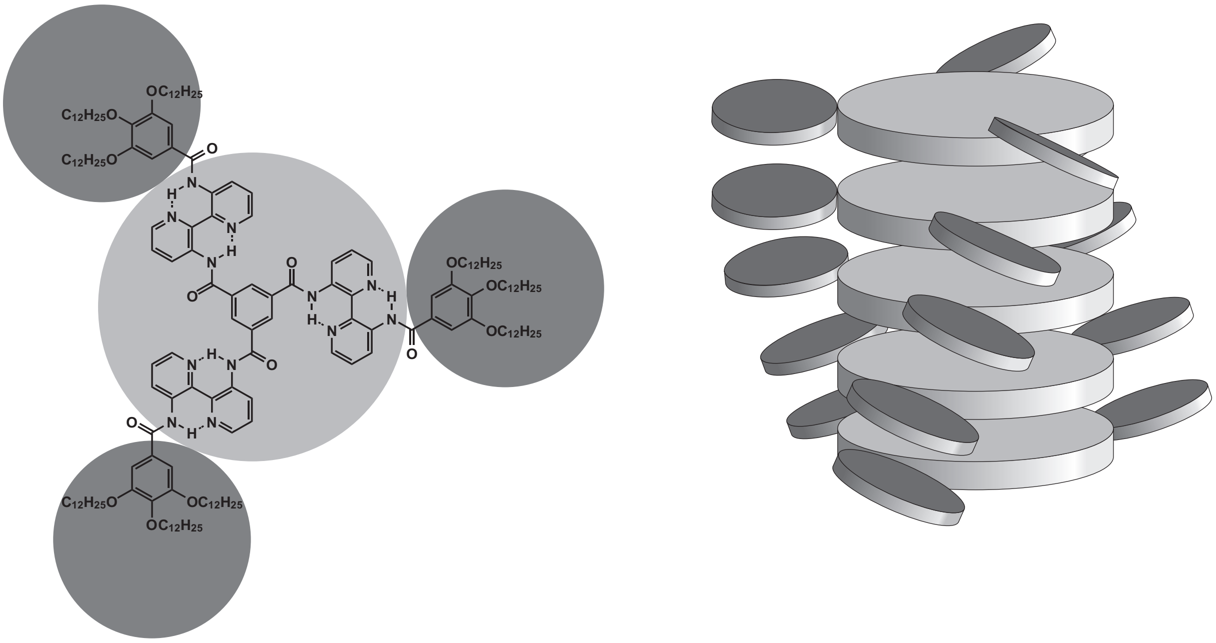

**Figure 3.1.** Formerly investigated BTAs. The inter-disc distance within the stack was determined to be 3.4 Å and the intercolumnar distance to 40 Å[112].

studied compounds exhibited a hexagonally ordered thermotropic liquid-crystalline $D_{ho}$ phase over a wide temperature range and enabled valuable insight into mechanisms of aggregation[111]. In dilute solution these compounds constituted a helical arrangement[113] with certain spacing between adjacent discs and a defined pitch angle but indefinite helical sense in case of achiral linear side chains at the gallic moieties. Species having chiral branched side chains, revealed a pronounced COTTON effect that could rather be attributed to the supramolecular aggregate than to the net effect of the individual chiral monomers. Moreover in a mixture of both species, few chiral molecules tended to transfer their chirality to the whole aggregate and therefore led to an enhanced COTTON effect[114]. It should be stated that also achiral molecules lead to a helical arrangement. However, the absence of chiral centres causes equivalence of both screw senses, hence equal populations and in consequence the mixture lacks any optical anisotropy effect. The capability of a *chiral director* to impose a certain helical sense can be studied in the so-called *sergeant and soldier* experiments[115]. These provide knowledge about the mechanisms of the widely investigated phenomenon of *chiral amplification* in dynamic aggregates and can be used to study the kinetics of organisation processes in dilute solution. This kind of nonlinear response does not only apply for chiral sergeant and its achiral analogue. It also holds for a small excess of one enatiomer within an almost racemic solution, which can be probed in *majority rule* experiments[116].

Due to the complexity and the large extension of the BTA system containing diaminobipyridine and gallic moieties, important aspects about the impact of the hydrogen bonding could not be conceived. Indeed, solid-state NMR was able to confirm the helical stacking of molecules proposed by X-ray investigations[112]. However, the helical arrangement of this compound was most likely not induced by intermolecular hydrogen bonds, but rather the propeller-like geometry of the core led to the observed helicity. The role of the hydrogen bond, besides other features of these materials, consequently remained unclear.

For this reason, the complexity of the structure was reduced, sparing only the inner part, *i.e.*, the BTA core, equipped with different chiral or achiral aliphatic alkyl chains. Figure 3.2 provides a survey of the compounds, that have been studied in this work. The remarkably simplified structures eventually enable deeper insight into the supramolecular arrangement of the $C_3$-symmetrical discs.

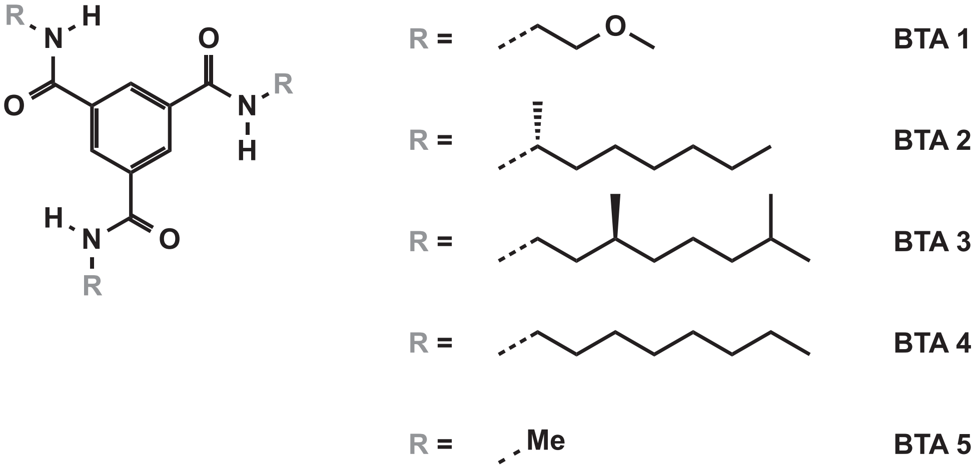

**Figure 3.2.** A compilation of the five investigated compounds. All exhibit a $C_3$-symmetrical basic element, namely the benzene-1,3,5-tricarboxamide core, which is equipped with different aliphatic side chains. The given nomenclature is used throughout this thesis.

Due to their size and symmetry, the depicted BTAs are suitable model compounds for a profound solid-state NMR investigation. The compilation of molecules served to examine fundamental aspects of supramolecular arrangements, such as symmetry and symmetry breaking, hydrogen bonding, $\pi$-$\pi$-interaction, and the disorder introducing effects of side chains.

The first part of this chapter gives an overview on recent research on BTAs in solution, as bulk material or as gel former, qualifying them as a key component for numerous applications, that will be briefly introduced in section . CO-centred BTAs as depicted in figure 3.2 will be thoroughly discussed in section 3.2. Afterwards, in section 3.3, an N-centred derivative, will be examined, having an inverted amide group.

## 3.1. Previous Research on BTAs

### 3.1.1. Structure of BTAs in the Solid State

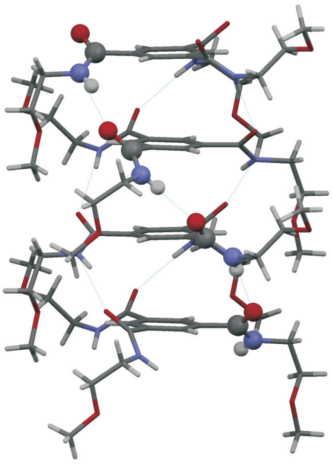

**Figure 3.3.** Crystal structure of BTA 1. Four molecules are shown in *capped-stick* mode. In order to clarify the helicity of the self-complementary hydrogen bonding units, one arm per molecules is emphasised by *ball representation* of the corresponding amide groups.

The crystal structure of BTA 1, containing three ethylmethoxy side chains (see Fig. 3.2), was published in a single crystal X-ray diffraction (XRD) study by LIGHTFOOT *et al.*[117], revealing a triple hydrogen-bonded columnar arrangement of BTA molecules. The monoclinic $P2_1$ structure can be visualised, by an asymmetric unit containing only two molecules. The stack is virtually generated by a quasi six-fold screw operation ($6_3$) perpendicular to the ring plane by 1/2 of the unit cell length in the columnar direction (*i.e.*, the crystallographic $b$-axis). This operation almost perfectly transforms one molecule into another, irrespective of a marginal displacement of adjacent rings. The stacking leads to a centroid distance of 3.62 Å along the crystallographic $b$-axis, which is in good agreement with other $\pi$-conjugated stacked systems (cf. graphite 3.35 Å[118], benzene dimer ~3.7 Å[119]). As can be seen in figure 3.3 the self-complementary CONH-motif, highlighted by ball representation of involved atoms, can be imagined as a helical chain of repeated hydrogen bonds. The whole backbone contains three of these helices. In the assembly, the amide groups are tilted by angles of 37°, 42° and 46° between the CO bond and the aryl plane, thus are not in full conjugation with the ring. The O-N distances were determined to 3.0 Å indicating moderately strong hydrogen bonds between the molecules. All amide groups of this structure are consequently tilted by 50° off the columnar axis, unlike another system containing a cyclohexane ring instead of benzene, in which the hydrogen bonds are parallel to the columnar axis[120].

XRD measurements have been carried out first by MATSUNAGA *et al.*, who investigated symmetric linear chain homologues from 4 to 18 carbon atoms, such as BTA 4 (cf. figure 3.2)[121]. The XRD patterns he obtained, however, indicated a lamellar-like type of arrangement, rather than a columnar stacking, which might possibly relate to the phase behaviour of BTA 4 being discussed in section 3.2.6. A second[122] study found evidence for a hexagonal columnar arrangement with an inter-disc distance of 3.5 Å, which could be verified by recent XRD investigations as well[123]. Moreover, XRD patterns on aligned samples of liquid-crystalline BTA 3 also suggested a $6_3$ screw axis[a)]. The intercolumnar distance could be estimated to 19.9 Å[124].

### 3.1.2. Structure and Dynamics of BTA Gels

Some tricarboxamides form gels in apolar solvents. For the investigated small BTAs the dynamics of the NH proton seems to play a more critical role for the columnar arrangement than for larger bipyridine containing BTAs, which do not show evidence for a director function of the hydrogen bond. The importance of the hydrogen bond was first shown by Yasuda *et al.*, who investigated the temperature dependent transition between BTA gels and their solution in dichloroethan[125]. By replacing the amide proton by a methyl group, *i.e.*, by creating an imide, a gelation of the mixture was no longer observed, leading to the conclusion that hydrogen bonding plays a key role in the aggregation of BTA molecules. However, the approach of exchanging the proton by a methyl group is rather crude, since an additional group means an additional spatial demand. Thus, a method like solid-state NMR, capable of probing hydrogen bonds directly, is very desirable.

The BTA gels demonstrate remarkable mechanical properties. Dynamic viscoelastic measurements revealed a mechanical behaviour, that can sufficiently be described by a simple Maxwell *model*, *i.e.*, a combination of a single viscous damper and a single elastic spring in series. The gel showed a fast relaxation mode, whose rate ($\tau_c \approx 1$ s) was nearly concentration independent, a fact that could neither be described by the common *reptation model*, nor the *living polymer model*[126, 127]. Since single molecules are not covalently bound as in a conventional polymer, the so-called *phantom crossing model* was proposed, which had been applied to other threadlike supramolecular systems before[128]. The model is based on a certain numbers of defects in the columnar chain, accounting for the flexibility of the strands. In this context "defect", describes a position within the column, where one or more hydrogen bond donor or acceptor groups are not bound in the regular triple

---

a) The XRD results could also be interpreted as a 45° tilting of the aliphatic chains with respect to the columnar axis, though, this would be a very uncommon behaviour for discotic liquid crystals.

symmetrical way. The origin of such a defect might either be an acute angle of the column, which prevents simultaneous formation of all three hydrogen bonds at the same time or a reversal of the helical sense within the column. In the *phantom crossing* model of BTA gels a regular tripel-bonded section is regarded as relatively rigid compared to an irregular defect position. Two stands can cross each other in a two step process. A breaking of a regular section is unlikely, therefore it is assumed that in a first step an entanglement point of two defects is formed. Due to steric hindrance, this unfavourable state rapidly reacts by rearrangement of hydrogen bonds leading to two new strands that will move apart subsequently.

### 3.1.3. Organisation of BTAs in Dilute Solutions

The formation of gel-like structures in solutions depends on the concentration of BTAs. In dilute solution gel formation is not possible, however, BTAs are known to assemble to oligomers, having a similar helical structure as the columns found in the solid state. By introducing chiral centres into the side chains of the BTAs (cf. BTA 2 and 3 in figure 3.2) a certain helical sense of the columns is preferred, leading to the phenomenon of different absorption coefficients of right- and left-handed circularly polarised light, known as *circular dichroism* (CD). The assembling process of BTAs in dilute solution has been investigated by application of a modified nucleation growth model[129]. This model allowed an estimation of the stack length of $10^3$ to $10^4$ molecules per stack[130] for BTA 4 with a concentration of $10^{-5}$ M in heptane. The observation of a sharp transition between isotropic solution and a pronounced CD effect on cooling the sample to the onset temperature of the molecular aggregation made a non-isodesmic mechanism highly probable, *i.e.*, a cooperative process exists, facilitating growth after an aggregate is formed. CD spectroscopy and *ultraviolet* (UV) absorption spectroscopy revealed a free enthalpy in the range of ~60 kJ mol$^{-1}$ for the chiral sample BTA 3 and ~70 kJ mol$^{-1}$ for BTA 4 with linear octyl side chains[130]. The slightly smaller value in case of BTA 3 is most likely due to the branched side chains exerting a slightly higher steric hindrance. A mixture of the chiral BTA 3 and the achiral BTA 4 in an apolar solvent resulted in a high degree of chiral amplification. A remarkable COTTON effect could be assigned to a right-handed helical conformation of the enatiopure chiral counterpart of BTA 3[b)]. Addition of only 4 % of the chiral BTA resulted in a random incorporation of chiral molecules into the stacks and caused a saturated CD effect, *i.e.*, most columns exhibited a uniform helicity.

---

b) The compound used in [130] had *R*-symmetry instead of *S*-symmetry

It is worth noting that a helical orientation is generated by the chirality of the side chains, but a *helical reversal* is primarily hindered by entropically unfavourable reorientation of the amide groups and alkyl moieties. Therefore, two distinct energetic terms were introduced, namely the *helical reversal energy*, referring to the reversal of the helical sense of a columnar section and the so-called *mismatch penalty*, which describes the incorporation of molecules into a column with their non-preferred helicity. Based on *Majority Rule* and *Sergeant and Soldier* experiments, statements concerning the thermodynamics of these processes could be made using a previously published model proposed by VAN GESTEL *et al.*[131]. The experiments were performed in cyclohexane with an asymmetrically substituted, achiral molecule and BTA 3 as a chiral sergeant. According to this approach, a helical reversal energy of 13.5 kJ mol$^{-1}$ and a mismatch penalty of 1.2 kJ mol$^{-1}$ could be obtained[132].

The large BTA containing 2,2'-bipyridine-3,3'-diamine moieties (shown in figure 3.1), has been investigated by CD spectroscopy as well, resulting in a mismatch penalty of only 0.92 kJ mol$^{-1}$ and a helical reversal energy of 7.8 kJ mol$^{-1}$, *i.e.*, in case of a considerably larger molecule, a similar value was found[133]. This can be seen as an additional support for the viability of small BTAs to serve as model compounds for systems involving hydrogen bonds and $\pi\pi$-mediated stacking.

With regard to the gels discussed in section 3.1.2, it was found that the relaxation process after a mechanical stimulation is mostly governed by phantom crossing mechanism[126], since defect positions in BTA systems are more likely situated between sections of mismatching helicity. The number of defects depended on the ratio of enatiomers, which therefore had a direct impact on the structure of the gel. For example, an excess of 30 % of one enatiomer pushed the number of hydrogen atoms involved in hydrogen bonds from 60 to 90 %, which means that only ~10 % of the amide protons were not involved in hydrogen bonds. In this sense it appears reasonable that a different motif with non-tilted parallel amide groups, using an 1,3,5-substituted cyclohexane core instead of benzene[120], exhibits a completely different relaxation behaviour, which is best described by a sum of two MAXWELL models[134].

For BTA materials the columnar assembly is not the only kind of supramolecular organisation, but it is the required step for further aggregation. In case of a slightly different molecular structure BOSE *et al.* reported a remarkably hierarchal organisation in methanol water mixtures[135]. In a first step the BTA molecules (primary structural unit) formed the known triple hydrogen-bonded columnar stack (secondary structure). These columns further assembled to a bundle of columns, whose envelope was helically undulated due to supramolecular forces and named the ternary structure. Even a quaternary structure existed, enabling the direct observation of triple helical rods, which consisted of three bundles yielding a diameter of less than 200 nm. As a matter of fact, the helical sense of this quaternary structure was determined by the chirality of the side chains of the primary unit, that is, the comparatively small BTA.

### 3.1.4. Applications of BTAs and BTA-Copolymers

3 The capability to efficiently form helical columnar structures has been used to “freeze” chiral information within a polymer[136]. The chiral structure-directing compound or the *sergeant* in terms of GREEN *et al.*[115], forces the column to adopt a certain helicity. In a second step a photopolymerisation of the assembled soldier molecules occurs, resulting in a permanent chiral backbone structure. Even after purification and dissolution in a polar solvent usually known to prevent chiral assemblies[137], the chiral information can be restored by crystallisation, since it is now inherently associated with the covalently bound backbone structure. By this so-called covalent fixation of the chiral assembly kinetically robust nanoscaled structures are accessible[132]. A slightly different approach uses a telechelic polymer, endcapped with BTA molecules or copolymerisation with BTAs to obtain supramolecular materials, that exhibit improved mechanical properties[138]. Furthermore, symmetric BTAs with different branched alkyl chains are used as efficient nucleating agents for the $\alpha$-crystal structure of isotactic polypropylene[139]. Apart from the low concentration of $2 \cdot 10^{-4}$ $w\%$ at which these agents operate, excellent thermal stability and colourlessness are further advantages of BTAs.

## 3.2. Side Chain Impact on the Assembly of CO-Centred BTAs

### 3.2.1. Thermal Analysis

All BTAs investigated in this section, namely BTA 1 to BTA 5 (see Fig. 3.2) were probed by *differential scanning calorimetry* (DSC) prior to the NMR experiments in order to assess their thermal behaviour. The DSC curves are given in figure 3.4. For BTA 1 to 3 the first heating run showed a good agreement with the subsequent runs indicating that the samples were little affected by the prior processing. BTA 1 provided a crystallisation point at about 120 °C on cooling and a melting point of 150 °C on heating the sample (see Fig. 3.4 a). The high temperature phase is an isotropic melting in case of BTA 1, whereas

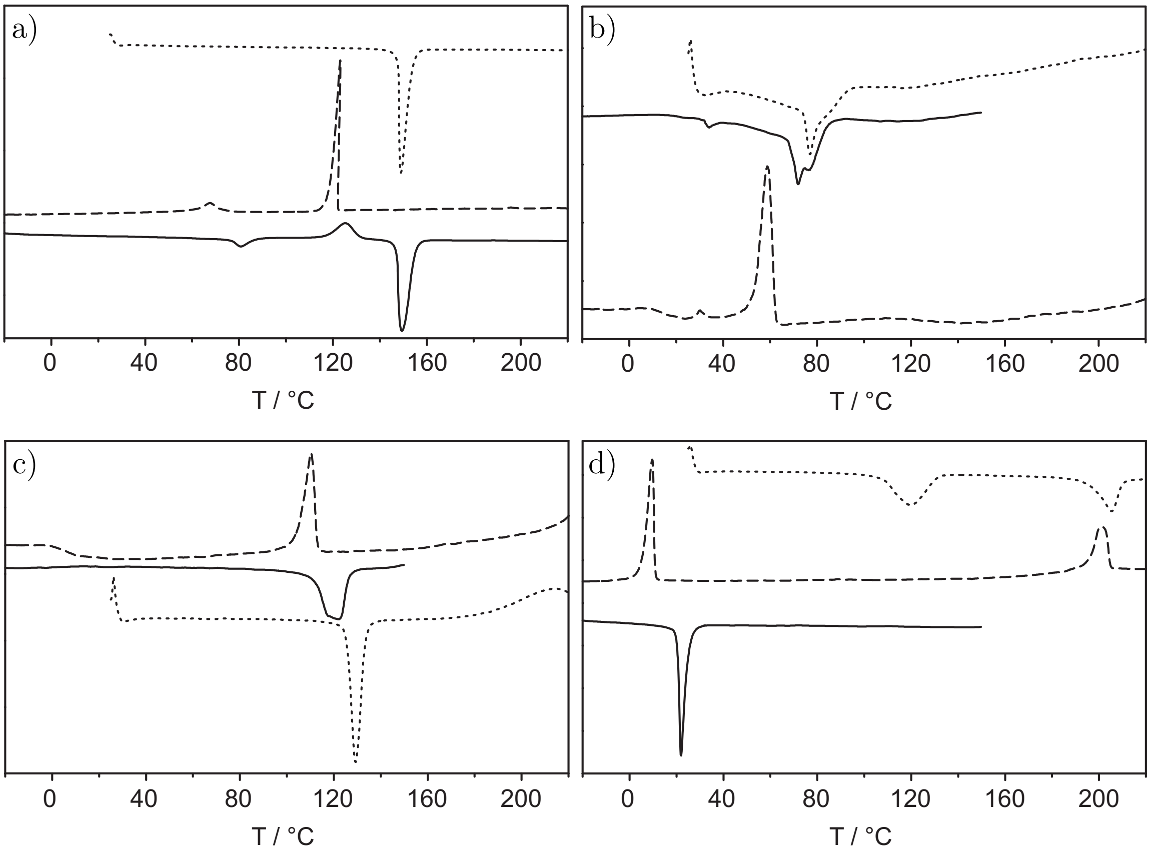

**Figure 3.4.** DSC curves of all investigated BTAs: *a*) BTA 1, *b*) BTA 2, *c*) BTA 3, *d*) BTA 4.

for the chiral compound BTA 2 a phase transition occurred between two solid crystalline phases slightly above 60 °C (see Fig. 3.4 b). It should be noted that the smaller enthalpy changes at 80 °C (BTA 1) and at 40 °C (BTA 2) could not be related to any change of the supramolecular assembly by any of the applied methods. These features are of minor importance and will not be considered in this work. The second chiral compound BTA 3 has recently been investigated by DSC and *polarised optical microscopy* (POM)[123,137]. It provided a known liquid-crystalline mesophase above the transition temperature of about 120 °C (see Fig. 3.4 c). Figure 3.4 d)) shows the DSC of BTA 4 revealing an endothermic process at about 110 °C of the first heating run, which could not be reproduced in the second heating run. The cooling as well as the heating curve clearly indicated a phase transition at 0 °C on cooling and at 20 °C on heating the sample a second time. BTA 5 did not show any transition in the accessible temperature range of the solid-state NMR probes. Therefore, its DSC curves are not presented here.

The linear chain compound BTA 4 was one of the first investigated 1,3,5-substituted BTAs. Matsunaga *et al.* analysed the thermal properties of di- and tribcarboxamide derivatives with linear alkyl chains[121] of varying length. It was found that some trisubstituted compounds showed one or two solid phases but all, except the smallest compound, having only an n-butyl chain, provided a thermotropic mesophase. Besides this, a remarkably small melting enthalpy of 19 kJ $\mathrm{mol}^{-1}$ was found for the solid-mesophase transition and 17 kJ $\mathrm{mol}^{-1}$ for the isotropisation of compound BTA 4. Moreover, the DSC measurements revealed an odd-even alternating behaviour of the isotropisation temperature by subsequently increasing the alkyl chain length. As expected, the temperature of the solid-mesophase transition was generally lowered. Specifically, for BTA 4 the study found one phase transition at 102 °C, which disagreed with the DSC results depicted in figure 3.4 d). If anything, this transition corresponds to the onset of the small hump in the first heating curve given in figure 3.4 d), which is actually omitted in the discussion. However, the significant incidents at about 0 °C (cooling) and 20 °C (second heating) have not been reported, although the corresponding temperature range has clearly been investigated, since low temperature phases of short chain homologues of BTA 4 have been explicitly recited[121].

In the following section the thermal behaviour of BTAs will be examined. Due to the discrepancy in literature concerning BTA 4 a solid-state NMR study of this compound is of particular interest.

## 3.2.2. Standard NMR Approach of BTAs

**Solid-State $^1$H NMR Spectra** The $^1$H MAS NMR spectra of BTAs at room temperature revealed three to four peaks arising from the amide protons, aryl protons, and protons from the interior methylene group, linking the backbone and the side chain. The side chain protons gave rise to a bulky high field peak. Two compounds provided only three peaks because the side chain consisted either of only a methyl group (BTA 5) or a methoxyethyl side chain, which was no resolved (BTA 1). Since the basic features of the studied proton spectra were very similar for the different BTAs, they are sufficiently explained by means of BTA 1, whose $^1$H MAS NMR spectra is presented in figure 3.5.

The low field region consisted of two peaks, at 9.0 ppm (FWHM: 1200 Hz) and 6.8 ppm (FWHM: 600 Hz). The side chain signal was located at 3.3 ppm. In addition to the solid-state NMR methods, solution NMR spectra were recorded for comparison of the chemical shift in both phases. The obtained spectrum, given in the lower part of figure 3.5, possessed two low field resonances at 8.2 and 7.1 ppm as well as two aliphatic signals at 3.6 and 3.4 ppm, resulting from the ethylene and methyl side chain.

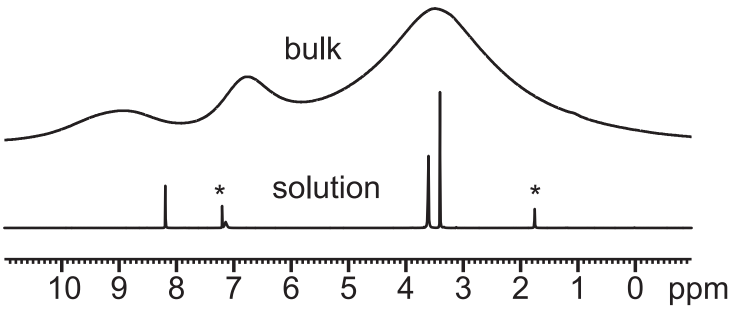

**Figure 3.5.** $^1$H MAS NMR spectrum of BTA 1 at 23 °C recorded at 30 kHz MAS and a $^1$H spectrum of BTA 1 in chloroform-*d* solution. Solvent peaks and impurities are marked with an asterisk.

**Solid-State $^{13}$C NMR Spectra** The $^{13}$C spectra of the investigated BTAs were easily assigned due to the broad chemical shift dispersion of the three backbone atoms. The carbonyl peak was located at the low field end of the spectrum at around 168 ppm. It is connected to the quaternary ring carbon, giving rise to the signal at around 138 ppm, whereas the signal at 127 ppm was assigned to the ternary ring carbon atom. Examined in more detail, some resonances were split or broadened due subtle differences in the dihedral angles of the amide groups or packing effects. Hence $^{13}$C NMR served as sensitive monitor of symmetry in the current system. As an example, the $^{13}$C {$^1$H} CP/MAS NMR spectrum of BTA 1 is depicted in figure 3.6, showing a split signal of the ternary ring carbon.

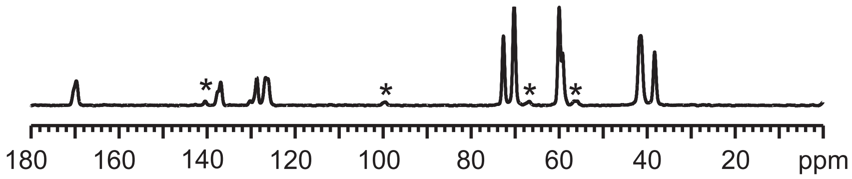

**Figure 3.6.** $^{13}$C {$^1$H} CP/MAS NMR spectrum of BTA 1 recorded at a LARMOR frequency of 212 MHz at at ambient conditions and 15 kHz MAS. Spinning sidebands are marked by asterisks.

### 3.2.3. $^1$H Chemical Shift Assignment

The $^1$H MAS NMR spectrum of BTA 1 showed a seemingly good agreement to the solution NMR data, which is misleading, though, since it implied a wrong assignment. Inspired by the known crystal structure of BTA 1 the amide protons were expected to experience a substantial low-field shift due to hydrogen bonding to the carbonyl groups of adjacent rings. Specifically, the NH resonance in the spectrum of BTA 1 was found at 7.1 ppm in solution, whereas in the $^1$H MAS NMR spectrum the backbone peaks arose at 6.8 ppm and 9.0 ppm. With respect to the hydrogen-bonded structure of the material, the 9.0 ppm was more likely assigned to the amide protons, though, this implies a drastic high-field shift of the aryl protons from 8.2 ppm in solution to 6.8 ppm in the bulk.

#### 3.2.3.1. 2D $^1$H-$^{13}$C Through-Space Correlation: $^1$*H Assignment*

Since the assumption of high-field shifted aryl protons could not be confirmed by simple $^1$H MAS NMR spectra, $^1$H-$^{13}$C HETCOR spectroscopy was employed, making use of the more definite assignment of the $^{13}$C spectrum.

The solid-state NMR version of the popular HSQC method, the so-called REPT-HSQC, was used to this end. For short recoupling times only the strongest heteronuclear dipolar couplings can be observed, hence only coherence involving directly bound CH pairs appear in the spectrum. In this manner the REPT-HSQC, actually a *through-space* correlation method, could be used for *through-bond* spectral assignment. The method is based on a coherent polarisation transfer from protons to carbon atoms, which is established by $\pi$-pulses applied on both channels. Since the RF pulses have to be applied in a rotor-synchronised manner (see section 2.17 for details) the method requires a recoupling time of multiples of one rotor period. With respect to the MAS frequency of 25000 Hz the shortest recoupling time was 40 $\mu$s.

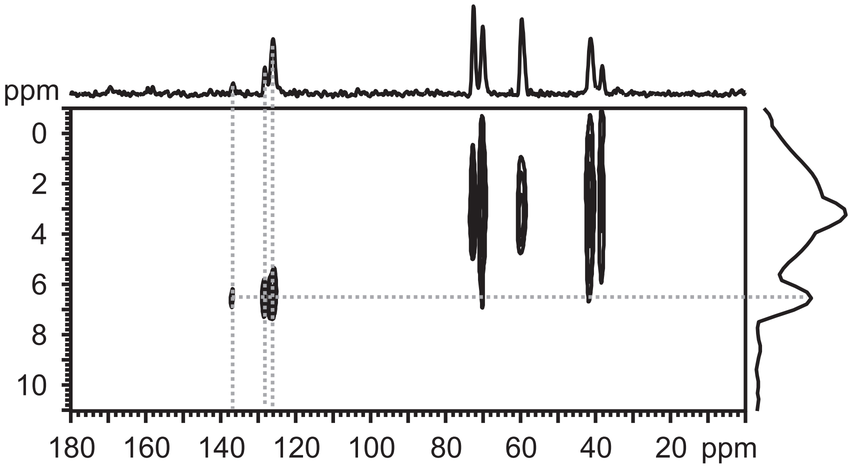

**Figure 3.7.** $^1$H-$^{13}$C REPT-HSQC correlation spectrum of BTA 1.

Figure 3.7 shows the REPT-HSQC spectrum of compound BTA 1 with a recoupling time of 40 $\mu$s. The skyline projection of the carbon dimension matched well with the carbon spectrum given in figure 3.6 regarding the signals of the ternary carbon and the side chains. Due to the short recoupling time the carbonyl signal could not be seen, since it is not bound to a proton. The quaternary ring carbon gave rise to a relatively small signal. The most informative feature therefore was the correlation between the aromatic ring carbons (three signals at approximately 127 ppm) with the attached protons at 6.8 ppm.

That way, the $^1$H-$^{13}$C correlation pattern unambiguously assigned the proton peak at 6.8 ppm to the aryl proton (located at 8.2 ppm in chloroform-*d* solution). A coherence involving the amide protons could not be observed, because no carbon atoms are located in proximity of those protons. Since the origin of the proton signal at 6.8 ppm was verified, the remaining signal at 9.0 ppm, could be assigned to the amide protons. Accordingly, they were shifted by +1.9 ppm to low field caused by the moderately strong hydrogen bonds.

In conclusion, the assignment of the proton spectrum has been achieved. Remarkably, the aryl protons were found to be shifted by -1.4 ppm to high field. This shift was even larger in magnitude than the low-field shift caused by the moderately strong hydrogen bonds. Therefore, the shielding impact of the neighbouring molecules on the aryl protons required a more detailed examination. The study was therefore supported by CAR-PARINELLO *Molecular Dynamics* (CPMD) simulation, focussing on the shielding effects of molecules within the columnar assembly.

#### 3.2.3.2. A Nucleus Independent Chemical Shift Map: *Packing*

As proven by the REPT-HSQC in the last section, the two low-field signals of the backbone protons reversed order in comparison to the solution spectrum. The origin of the remarkable shifts of the aryl and amide protons was further examined by a supporting *density functional theory* (DFT) study on compound BTA 1. The study included a chemical shift calculation of an isolated molecule (monomer) representing the compound in solution. The impact of the stacking of molecules was incorporated in different steps: Firstly, small oligomers were investigated, *i.e.*, stacks of three or five molecules. Since the calculation time increased rapidly with the system size, due to the scaling of $N^2$, it was desisted from simulating the chemical shifts of larger stacks. That way, by simulating the chemical shifts of a trimer and a pentamer, the local influence of neighbouring molecules within a column has been investigated. It should be noted that only the inner molecule of the stack was considered. Terminal molecules at the end of the column do not provide reliable insight into the shielding effects. Secondly, the bulk was simulated with full periodicity along the columnar axis, thereby generating an infinitely long column of triple hydrogen-bonded molecules. In this manner, the procedure described the effect of the stacking, but still did not account for any impact of neighbouring columns or additional bulk effects. Thirdly, since the known crystal structure of compound BTA 1 could be used as a starting geometry, a simulation of the whole crystal was done by applying a full periodicity in all three dimensions. Figure 3.8 shows the observed spectra in bulk (top) and in solution (bottom) as well as the resulting spectra of the CPMD simulation for the monomer, the pentamer, and the whole crystal.

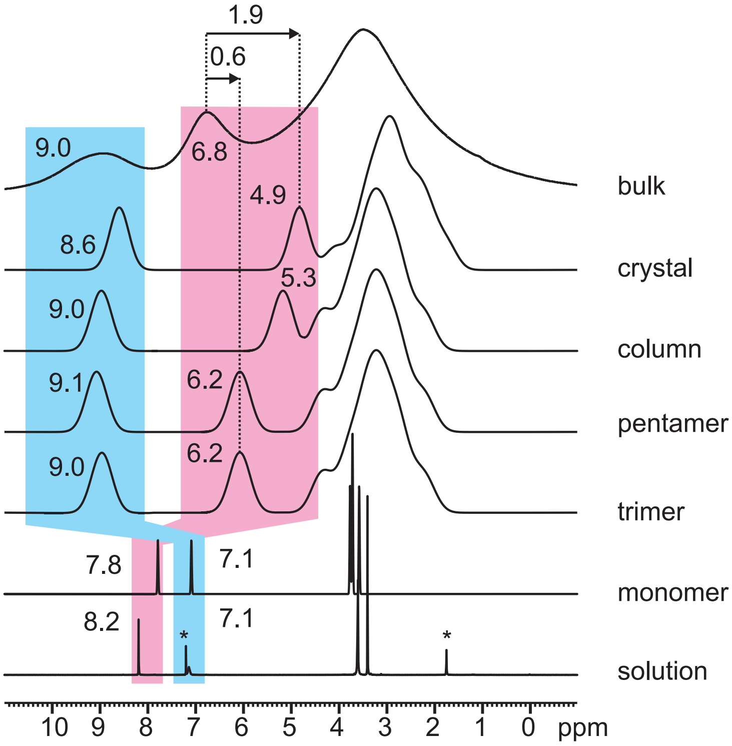

**Figure 3.8.** Comparison of observed and simulated chemical shifts in BTA 1.

The observed low-field shift of the three equivalent amide protons could be explained by hydrogen bonding to the carbonyl groups of the adjacent layer. These protons were found at 7.1 ppm in chloroform-*d* solution, whereas in the solid the same resonance was found at 9.0 ppm (figure 3.8). The corresponding calculation of the isolated molecule matched exactly the chemical shift value of the molecule in solution, *i.e.*, 7.1 ppm. The chemical shifts of the amide protons were 9.0 ppm and 9.1 ppm in the trimer and pentamer, respectively. No significant change was found in case of the 1D column (9.0 ppm, not shown). The simulation of the whole crystal in contrast resulted in 8.6 ppm (*i.e.*, 0.4 ppm less), which might be ascribed to slightly different conditions. In case of the trimer, the pentamer, and the infinite chain, no neighbouring columns were present, whereas the simulation of the entire crystal was based on a dense packing of molecules. It is commonly known that both models therefore differ in the global susceptibility of the space in which the simulation is carried out.

It is obvious that the experimental chemical shifts of the amide protons were well reproduced by the calculation. The amide peak of the bulk material at ambient conditions was located at 9.0 ppm. The calculations of the infinite column or the small oligomers exactly hit the observed shift. However, since it is the more genuine way of simulating the properties of a material, the simulation of the entire crystal has a superior significance. Nevertheless, a difference of 0.4 ppm is a very good agreement between experiment and simulation. The reason for the high-field shift of the aromatic proton is the remarkable shielding impact of adjacent molecules in the columnar assembly, which can be seen with the aid of the *nucleus independent chemical shift map* map (NICS map) in figure 3.9. The effect is predominantly due to the ring current effect of neighbouring benzene rings$^{c)}$. The effect even influences the protons located outside the cylindrical envelope of the benzene core, probably due to a widening of the shielding cone by the attached carbonyl groups. The colour code illustrates the impact of the chemical shift of the upper molecule on the in-plane molecule underneath it. For the sake of clarity, this lower molecule is shown without the side chains. As indicated by the blue colour, the ring protons were found to be shifted by about -0.75 ppm to high field. The molecule situated below the plane is not displayed,

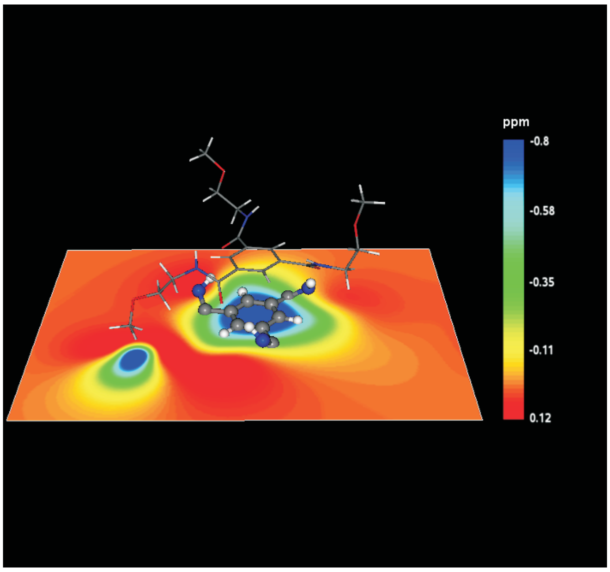

**Figure 3.9.** NICS map of BTA 1.

---

c) For a graphical illustration of this phenomenon see figure 2.7 in section 2.1.6.1.

but naturally it gives rise to the same effect. Thus, by addition of both contributions a net shift of about -1.4 ppm was expected, which corresponds well with the observations, *i.e.*, the high-field shift of -1.4 ppm of the aryl protons in the bulk (6.8 ppm) compared to solution (8.2 ppm). Accordingly, the trimer calculation (6.14 ppm) in comparison with the monomer calculation (7.8 ppm) results in a high-field shift of -1.7 ppm, which is in good agreement with the -1.4 ppm implied by the NICS map.

Surprisingly, the study did not reveal a significant difference in the chemical shift of the pentamer or the trimer. An interesting finding of this study is therefore the mismatch between the infinite column (5.3 ppm, not shown) or the crystal (4.9 ppm) compared to the trimer and pentamer calculations of -1.3 ppm and -1.7 ppm, respectively. A possible explanation might involve a very slow convergence of the chemical shift upon elongation of the columnar scaffold, which becomes evident only for very long columns as has been found for hexabenzocorones systems[140]. Apparently, the experimental spectrum is more accurately described by the results of the trimer and pentamer calculations (mismatch only 0.6 ppm) than by those of the infinite column or the crystal. This points towards certain imperfections existent in the bulk material, *e.g.*, of smaller columns, a high number of defects, or a deformed or slightly bended structure.

## 3.2.4. 1D Proton NMR Techniques

### 3.2.4.1. VT $^1$H MAS NMR: *Assembly*

*Variable temperature* (VT) $^1$H MAS NMR has been carried out for compounds BTA 1 to BTA 4 in a temperature range from -15 °C to 146 °C. As shown in this section, $^1$H NMR is very sensitive to changes in the hydrogen bonds and the local organisation of molecules, hence it is an appropriate method for studying the temperature dependent behaviour of these materials. $^1$H MAS NMR provides more detailed information than thermal analysis because it not only detects transitions, but it also points out the most affected molecular parts.

**BTA 1** At a temperature of -15 °C BTA 1 is in the crystalline state. Upon heating to 146 °C the amide proton peak shifted from 9.1 to 8.4 ppm as shown in figure 3.10, thus reflecting a weakening of hydrogen bonds. In contrast to the amide proton, the aryl protons did not even show a small drift of the chemical shift. Its signal was virtually located at 6.8 ppm over the whole temperature range. The most remarkable feature of the $^1$H MAS NMR stack is the appearance of isotropic components which were first recognised at a temperature of 99 °C and quickly gained intensity with increasing temperature at

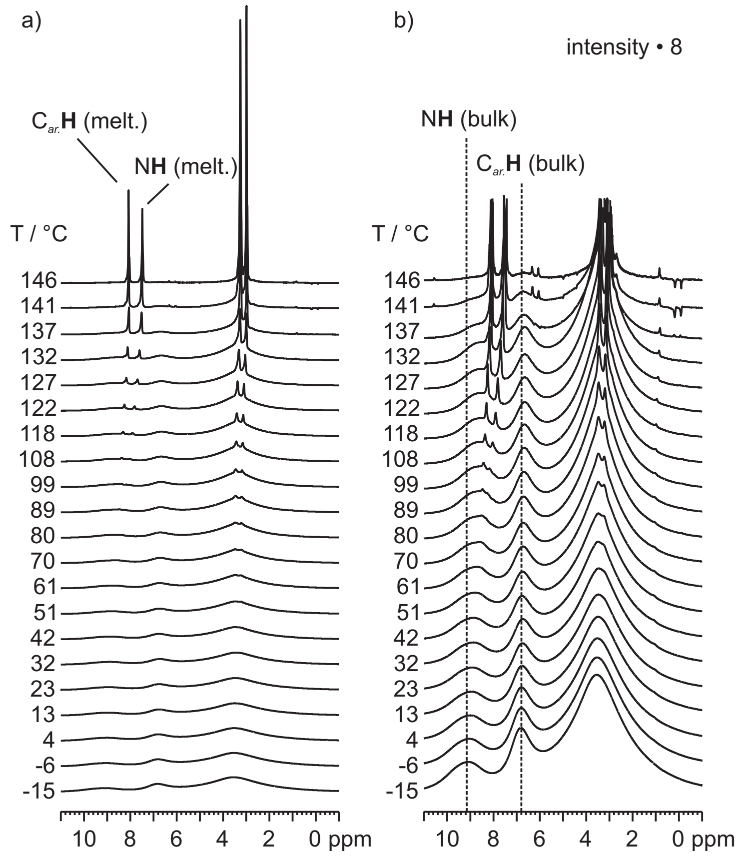

**Figure 3.10.** *a*) VT $^1$H MAS NMR of BTA 1 in a temperature range between -15 and +146 °C. *b*) Same pattern but eight times enlarged for a better visualisation of the broader bulk signals.

cost of the broader peaks of the solid phase. The rise of intensity was accompanied by a small drift of these components. The low field signal shifted from 8.3 ppm to 8.0 ppm, the high-field peak from 8.0 to 7.5 ppm. Especially at higher temperature, these narrow peaks showed good agreement with the solution NMR spectrum and therefore could be ascribed to the melting of BTA 1. Additionally, the melting temperature of BTA 1 of 150 °C (120 °C upon cooling) obtained by DSC, showed good agreement with the appearance of the narrow lines, hence gave further evidence for the ongoing melting of the sample.

No thermotropic phase of BTA 1 has been reported, therefore a regular melting behaviour can be assumed, which is in line with the double quantum filtered (DQF, not shown here) experiment as well. The observation of a widely blurred melting point and its onset at low temperature at least 20 K before the DSC indicated melting point is surprising though. Apparently, a certain fraction of the material seems to be molten before the actual melting process started. This might be related to the tendency of longer alkyl chain containing BTAs to form thermotropic liquid-crystalline phases[123, 137]. The temperature range of a notional columnar mesophase of BTA 1 is therefore smaller compared to

BTAs with longer alkyl chains. Moreover, the oxygen in the methoxyethyl side chains can create hydrogen bonds to the amide protons. This "backbonding" can efficiently stabilise the single molecule in the melting, hence prevent a liquid-crystalline phase[124,141].

**BTA 2** All investigated BTAs, other than BTA 1, possess purely apolar aliphatic side chains. BTA 2 for example is equipped with an (*R*)-1-methylheptane chain, being branched at the carbon next to the amide group (see figure 3.2). The VT $^1$H MAS NMR in figure 3.11 *a*) revealed a distinct behaviour, without appearance of isotropic lines or at least narrow lines as commonly observed in LC phases. The phase transition temperature of BTA 2 is considerably higher than those of all other BTAs herein presented[d)]. At -15 °C the amide proton peak was located at 9.6 ppm and the ring proton signal at 6.6 ppm. At this temperature the methyl and methylene protons were not resolved and the CH group next to the amide appeared as a small shoulder at approximately 4.0 ppm. On heating the sample, the amide proton drifted to a value of 8.5 ppm at 146 °C, re-

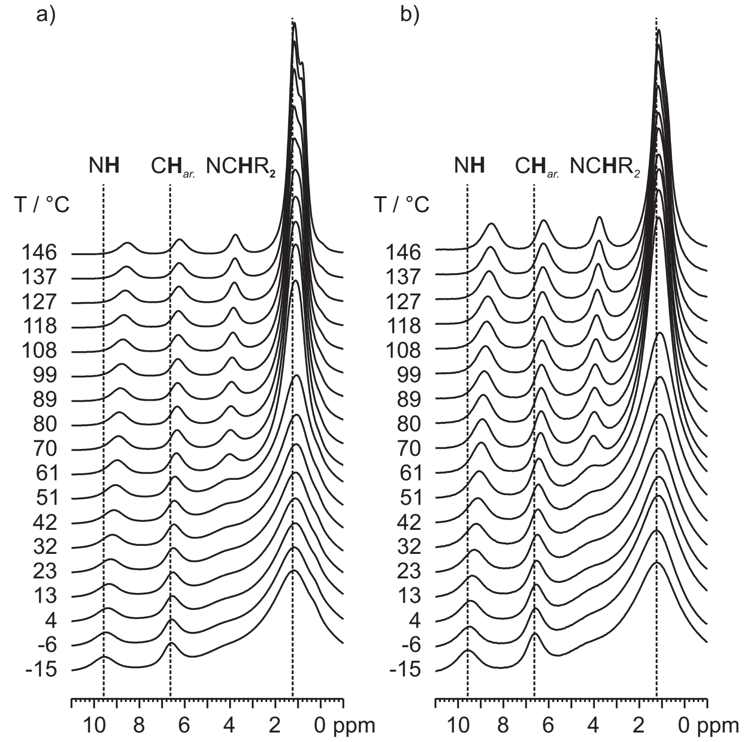

**Figure 3.11.** *a*) VT $^1$H MAS NMR spectra of BTA 2 within a temperature range between -15 and +146 °C. *b*) VT $^1$H DQF NMR spectra of BTA 2, recorded with a recoupling time of 33.6 μs. The spectra in *b*) are eight times enlarged compared to *a*).

---

[d)] A stable mesophase of BTA 2 was found between 220 and 278 °C by POM measurements[142].

sembling the behaviour found for sample BTA 1. In contrast to that, the aryl peak also shifted to high field by +0.3 ppm to 6.2 ppm. Apparently, the effect inducing the already remarkable chemical shift value surprisingly became more intensive with increasing temperature. Generally, it should be noted that the high and low-field shifts of the two backbone resonances mediated by the packing were more pronounced in case of BTA 2 compared to BTA 1.

In the DSC a minor important enthalpy change was found at a temperature of ∼60 °C, which can be identified in the stack of VT $^1$H MAS NMR spectra. Above this temperature the side chain peak narrows remarkably and the NCH peak became much more resolved. At the same time the gradual shifts of amide and aryl resonances were hardly affected. Therefore it may be concluded that the effect basically addressed the side chains or BTA 2.

Further knowledge about this phase transition at 60 °C could be obtained from double quantum filtered $^1$H NMR spectra, which have been recorded within the considered temperature range (see Fig. 3.11 *b*)), since these spectra are more sensitive to the mobility of the sample. At first sight no striking difference between SPE and DQF spectra can be detected, however, the intensity ratio between side chain peak and the backbone peaks (aryl H, and amide H, NCH) changed. This observation is commonly observed in systems comprising a mobile side chain part and a rigid scaffold. Due to increasing dynamics at higher temperature dipolar interactions partially average and along with this, the efficiency of double quantum excitation is reduced. Regarding the integrals of the backbone peaks of BTA 2, relatively constant intensities were found in the whole temperature range. The phase transition, however, took significantly more effect in the DQF spectra, compared to the MAS spectra, which is best seen at 51 °C and 61 °C. The line width of the side chain peak dropped noticeable, leading to a higher relative intensity of this peak. Above the phase transition, a linearly decreasing DQF intensity of the side chain signal was found on heating the sample.

**BTA 3** The tricarboxamide core of BTA 3 is equipped with (*S*)-3,7-dimethyloctyl side chains, *i.e.*, twice branched with the inner methyl group at position 3 in contrast to position 1 in BTA 2 (cf. Fig. 3.2). This compound was intensively studied in solution[130], as well as in the solid state[123]. VT $^1$H MAS NMR spectra are given in figure 3.12 a). The spectrum at -15 °C exhibited the same basic features as the previously covered compounds, *i.e.*, an amide proton peak at 9.9 ppm, the aryl proton peak at 6.6 ppm and a broad peak of the alkyl chain protons at 1.1 ppm. The hydrogen bond induced shift of the NH protons was slightly stronger than for BTA 2. Moreover, the line width of BTA 3 and 2 suggested a similar degree of organisation in contrast to BTA 1. Upon heating, the expected high-field shift of the NH signal also persited for BTA 3, however, the position of the aryl proton did not change significantly.

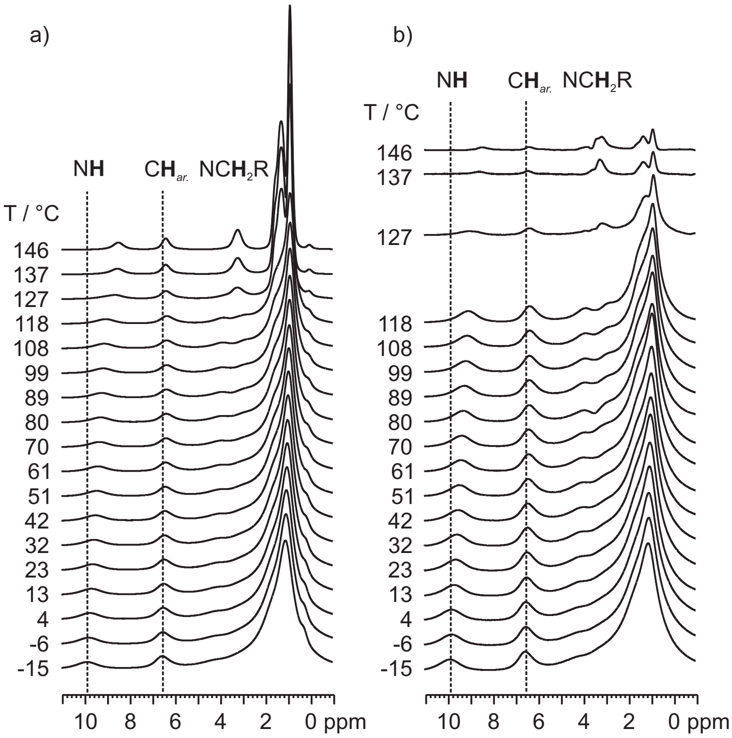

**Figure 3.12.** *a*) VT $^1$H MAS NMR spectra of BTA 3 within a temperature range from -15 to +146 °C. *b*) VT $^1$H DQF NMR spectra of BTA 3, recorded with a recoupling time of 33.6 $\mu$s. The spectra in *b* are eight times enlarged.

Above 125 °C a tremendous line narrowing occured, being most clearly seen for the side chain region of the spectrum. The temperature coincided with the transition phase temperature in the shown DSC plot 3.4 c). Preceding DSC and POM studies already indicated the existence of a thermotropic mesophase above the phase transition temperature[123, 137].

At 146 °C, the NCH$_2$ protons could clearly be identified, as well as two distinct side chain peaks arising from the three methyl protons at 0.9 ppm and the rest of the side chain protons at 1.4 ppm. The significant width (150 Hz for the three methyl groups) of these peaks affirmed the finding of a mesophase and precluded an ordinary melting as found in case of sample BTA 1. Here, a partial averaging of the anisotropic line width was indicated, whereas for BTA 1 total isotropisation was observed. In this context it has to be pointed out that the temperature dependent drift of the amide resonance was not only gradual, but varied abruptly upon the phase transition temperature. The signal shifted from 9.1 ppm at 118 °C to 8.5 ppm at 137 °C, which means a jump of -0.6 ppm to high field. In fact, this indicated an immediate weakening of the hydrogen bonds. Nonetheless, preservation of the columnar arrangement could be assumed, since the aryl peak was unaffected by the transition. As a matter fact, both chemical shifts of 8.5 ppm in the mesophase and 7.1 ppm in solution still indicated a hydrogen-bonded column arrangement.

Another interesting feature of the single pulse spectra was the structure of the $NCH_2$ signal. Just below the transition temperature it appeared to be split into two distinct peaks with different chemical shifts. This observation will be discussed in detail in section 3.2.9.

Further knowledge about the characteristics of the phase transition could be obtained from VT $^1$H DQF NMR spectra given in figure 3.12 b). Below 120 °C the stack showed basically the same features as the usual MAS NMR spectra, except for the expected lower intensity of side chain peaks in comparison to the backbone peaks. In the proximity of the phase transition temperature the intensity decreased rapidly, but did not disappear completely. This is contrary to BTA 1, for which a total breakdown of DQF intensity above the transition temperature proved the melting of the sample (not shown). The remaining DQF intensity is a strong indication for an persisting orientational order, as it is particularly found in liquid crystalline phases.

**BTA 4** The linear octyl side chain derivative BTA 4 has been studied before, together with other linear chain homologues with regard to their thermal and optical properties using DSC, amongst other methods. The DSC results of different investigations were not unambiguous. The first time reported by MATSUNAGA *et al.*, a phase transition temperature of 102 °C but no further information about other transitions at temperatures below[121]. Other studies proposed different transitions as for example a glass transition at approximately 70 °C[142]. A DSC of BTA 4 obtained during this study is shown in figure 3.4 d).

The first heating run of the DSC is usually governed by ill-defined reorganisation processes of the material, because its arrangement in solution- and melting-crystallised samples may differ. Surprisingly, the endothermic peak of the first heating run coincided with the phase transition at 102 °C, found by MATSUNAGA. For this reason, the solid-state NMR investigations on the BTA compounds were supposed to be especially fruitful in

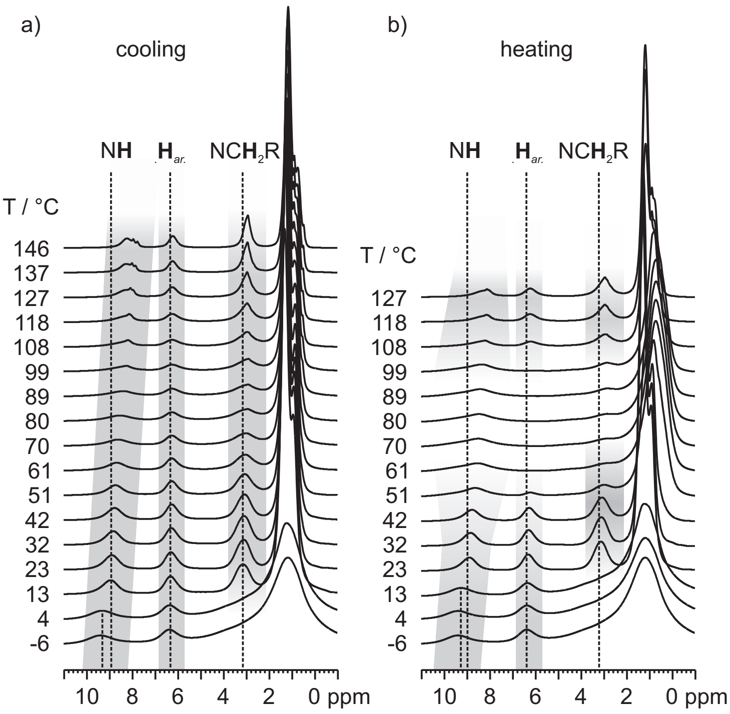

**Figure 3.13.** *a*) VT $^1$H MAS NMR spectra of BTA 4 on cooling the compound from -15 to +146 °C in steps of approximately 10 °C. The delays between consecutive measurements were about 10 min. *b* VT $^1$H MAS spectra of BTA 4 on stepwise heating the sample under identical conditions subsequent to the cooling run.

case of BTA 4. In order to elucidate the thermal behaviour of BTA 4, it seemed worthwhile to mimic the temperature profile of the DSC experiment by VT $^1$H MAS NMR measurements. To exclude reorganisation effects of the solution-crystallised compound, that may impair the reliability of the spectra, the sample was carefully heated to the maximum accessible temperature of 146 °C and cooled down subsequently in a stepwise manner.

At 146 °C the spectrum appeared like the well-known pattern indicating a helical arrangement by the down field shifted amide protons at 8.2 ppm, the high-field shifted aryl protons 6.2 ppm, the $NCH_2$ signal at 3.0 ppm, and the partially resolved side chain signals with a major component at 1.2 ppm. On top of the amide proton peak two very narrow peaks could be recognised, announcing the onset of a partial isotropisation as seen before for BTA 1. As BTA 4 exhibits liquid-crystalline behaviour at elevated temperatures, the proton NMR spectrum resembled the spectrum of the liquid-crystalline compound BTA 3. Even for this sample a continuous strengthening of the hydrogen bonds during stepwise cooling could be found, indicated by the gradual low-field shift of the amide protons. All other peaks, including the aryl proton peak were not significantly affected, *i.e.*, did not change their position. However, the three well resolved backbone peaks seemed to flatten between 100 °C and 60 °C. A more detailed examination in this temperature range revealed that the backbone peak integrals diminished, indeed. It is well known that intensity decreases when the correlation time of a dynamic process enters the time scale of the MAS frequency[143]. This phenomenon might have taken effect here, however, the characteristic of the dynamic process remains unclear. The effect is possibly related to several processes, *e.g.*, the rotation of single amide groups within the columnar assembly. Such processes have been determined for other linear chain BTAs[144].

With respect to this intensity minimum of the backbone resonances, it has to be clarified that for all proton measurements a recycle delay of 2 s was used, unless other values are explicitly given. Additionally, saturation recovery-type experiments[e)] have been carried out at different temperatures in order to probe the temperature dependence of the $T_1$ relaxation time on cooling and heating. According to these measurements the $T_1$ time decreased continuously on cooling the material and did not show a maximum between 60 °C and 100 °C. The slightly lowered signal intensities of the backbone peaks within this temperature range could therefore not be explained by relaxation losses due to a too short recycle delay, but rather by an undefined dynamic process in the material. This effect was not investigated in detail, since it appeared to be of minor importance with regard to various phase transitions of the sample.

Corresponding to the crystallisation point in the DSC depicted in figure 3.4 d), the material passed another transition between 13 °C and 4 °C. The proton spectrum at this temperature changed dramatically, most clearly seen in the remarkable broadening of the side chain peak. In comparison to other BTAs, the side chain peak of BTA 4 prior to the transition at 4 °C seemed to be rather narrow, pointing to a relatively high degree of mobility in the side chains. Upon the transition, the line width increased from 260 Hz to more than 1000 Hz after the transition. Apart from the side chain effect the jump of the amide peak from 8.9 ppm to 9.3 ppm indicated a strengthening of the hydrogen bonding of adjacent molecules.

Upon heating the sample again, the $^1$H MAS NMR spectra first showed the expected reversal of the observed transition at a slightly elevated temperature due to a minor hysteresis, *i.e.*, between 13 °C and 23 °C. Further heating resulted in a strongly deviant behaviour, most significantly seen for the signal of the aryl proton, which suddenly disappeared above ~50 °C. At the same time the amide peak became broad and more indistinct.

---

[e)] The pulse program is given in appendix A.3.

The same holds for the $NCH_2$ peak, whereas the side chain peak did not only broaden, but also shifted by -0.4 ppm to high field (-0.7 ppm at 70 °C). In conclusion, a tremendous discrepancy of spectra of the cooling and the subsequent heating run of BTA 4 could be ascertained in the temperature range from about 50 to 100 °C.

Further rise of the temperature above 100 °C recovered the original high temperature pattern, including a high-field shifted aryl proton peak, found for all investigated BTAs. The temperature related to this event corresponded to the literature-known transition at 102 °C and moreover to the transition observed in the first heating run of the DSC, as illustrated in figure 3.4 d).

Between 50 and 100 °C the proton spectrum appeared different in all aspects, that is, the broadened line width of the alkyl chain peak, the flattened amide resonance, and most significantly the disappearance of the aryl signal. Apparently, the sample underwent another phase transition during the stepwise heating of the sample. $^1$H MAS NMR, though, could not provide a deeper insight into the characteristics of the transition, *i.e.*, it did not distinguish between a change in the structure or in the time scale of an unknown dynamic process. However, the latter approach is rather unlikely since the effect was exclusively observed for the aryl protons. Furthermore, it neither explains the change of line width nor the remarkable high-field shift of the side chain peak.

#### 3.2.4.2. VT $^1$H DQF NMR: *Mobility*

Further insight into the processes taking place in BTA 4 could be provided by VT $^1$H DQF NMR. Decreasing the temperature from 146 °C on led to chemical shifts as seen in the SPE experiments discussed in section 3.2.4.1. The low DQF intensity at high temperature from 146 to 90 °C clearly indicated a mesophase with almost liquid-like behaviour of the side chains, but also a high overall dynamic, suggested by the small backbone peaks in figure 3.14 a). It is worth noting that at 146 °C the intensity of the signal of the $NCH_2$ protons was as large as the signal of the remaining side chain (*i.e.*, 15 protons). On cooling beyond 90 °C a gradual amplification of double quantum filtered intensity was determined. Apparently, the backbone became more rigid and more coupled in consequence. Normalised to the intensity of the single pulse experiment, the double quantum filtered intensity of the $NCH_2$ protons increased from a level of 3.5 % at 90 °C to 22 % at 30 °C in a nearly linear manner. The side chain signal showed the same tendency rising from about 1 % to 5 % between 100 °C and 10 °C. The following crystallisation showed up in a strong broadening of the alkyl chain peak, but since the signal amplitude did not

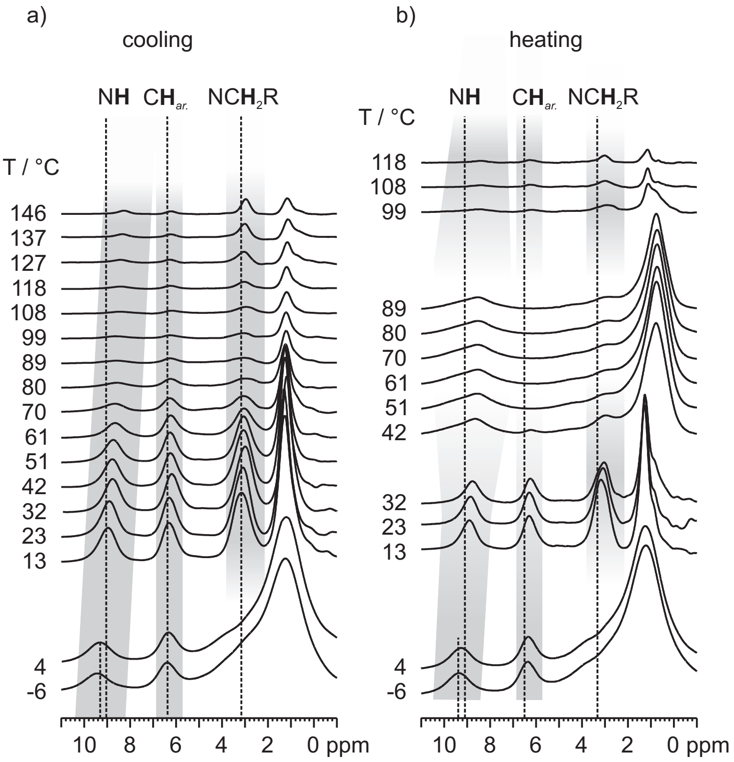

**Figure 3.14.** VT $^1$H DQF NMR spectra of BTA 4 recorded at 30 kHz MAS with an excitation time of 33.6 $\mu$ s. The used temperature profile was the same as described for VT $^1$H MAS NMR, *i.e.*, *a*) cooling, *b*) heating.

drop significantly, the overall integral of the peaks rose by a factor of three with respect to the value at 13 °C. Interestingly, the DQF intensity of the backbone protons did not change significantly. It can be assumed that the rigidity of the hydrogen-bonded scaffold just before the crystallisation was already at its maximum. Hence, the transition at about 10 °C can be attributed primarily to the side chains, albeit an obvious low-field shift of the amide peak.

The resulting spectra of the heating run of the $^1$H DQF NMR measurements in figure 3.14 b) revealed the disappearance of the signal of the aryl protons and the -0.4 ppm high-field shift of the side chain signal. Therefore, the behaviour was in accordance with $^1$H MAS NMR spectra in a temperature range from 42 to 89 °C. However, in contrast to SPE, DQF is capable of probing the local dynamics of the molecular parts. By this means, $^1$H DQF NMR discovered a remarkable increase of the DQF intensity of the side chains, pointing to considerably improved packing of side chains in the intermediate temperature range. Since the side chain signal appeared to be frozen, a vanishing of the aryl protons on grounds of dynamic processes could be ruled out. It rather seemed that the material underwent a retarded phase transition, which have not been observed during the cooling run of the experiment because of its extremely slow kinetics. The transition could preliminarily be assigned to a slow conversion between a supercooled mesophase to a crystalline phase of BRA 4.

### 3.2.5. Carbon NMR Techniques

As a second standard experiment $^{13}$C spectra of invetigated BTAs have been recorded. Other than protons lines, carbon resonances are not homogeneously broadened; hence they have a comparatively narrow line width, while providing a much higher chemical shift distribution. For this reason $^{13}$C MAS NMR and the $^{13}$C {$^{1}$H} CP/MAS spectra clearly demonstrated the sensitivity of carbon resonances with respect to the spatial symmetry.

#### 3.2.5.1. VT $^{13}$C {$^{1}$H} CP/MAS NMR: *Symmetry*

The unit cell of BTA 1 contains two molecules and the space group was found to be $P2_1$, resulting in 6/2=3 magnetically non-equivalent sites (cf. Fig. 3.3)[117]. The side chains are more affected by the asymmetry of the space group because of different side chain conformations. This leads to more complex high field region of the spectrum. The side chain positions 1, 2 and 4 (see Fig. 3.2) gave rise to signals centred at 40, 72 and 60 ppm being split into discrete lines separated by 3.4, 2.6 and 0.7 ppm, respectively. The conformational effect apparently dwindled with increasing distance to the carbonyl group. As can be seen in figure 3.15 a) two out of three signals provided similar chemical shifts, whereas one was quite different. Notably, the backbone carbon atoms showed a splitting, too, despite a rather high symmetry within the inner hydrogen-bonded scaffold as indicated by the crystal structure given in figure 3.3. This symmetry breaking was most pronounced for the tertiary ring carbon at 128.6 ppm, 126.7 ppm and 126.1 ppm. The remaining two signals could be addressed to the carbonyl resonance at 169.7 ppm (not resolved) and the quaternary carbon at 136.8 ppm and 137.5 ppm.

VT $^{13}$C {$^{1}$H} CP/MAS measurements at increasing temperature for BTA 1 did not reveal any remarkable effect apart from the expected loss of CP signal above the melting point.

The carbon spectrum of BTA 2 in figure 3.15 b) showed important differences compared to that of BTA 1 (Fig. 3.15 a)). Only three low field peaks with rather narrow line width could be observed at 168.7 ppm (FWHM: 66 Hz), 137.4 ppm (45 Hz), and 126.7 ppm (58 Hz). As for BTA 1, these lines could be ascribed to CO, the quaternary carbon and CH. Notwithstanding the absence of X-ray data, a high degree of organisation could be

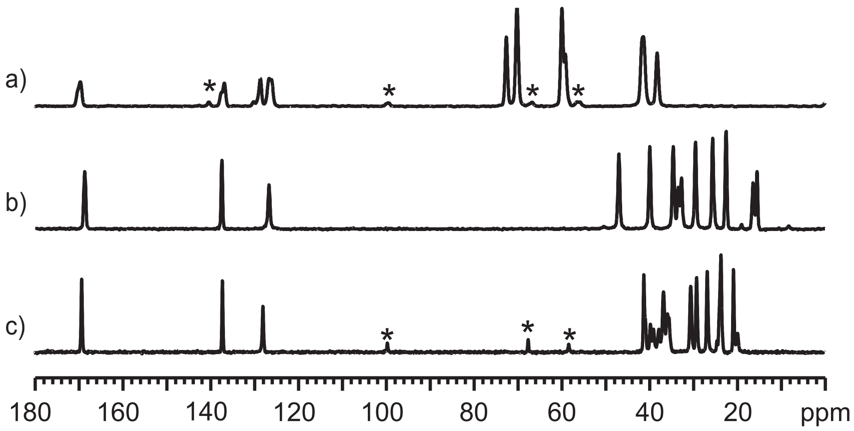

**Figure 3.15.** $^{13}$C {$^{1}$H} CP/MAS spectra of the investigated compounds BTA 1 *a*), BTA 2 *b*), BTA 3 *c*). *a*) and *c*) were recorded at a Larmor frequency of 212 MHz, *b*) at 126 MHz. Due to the larger spectral width in spectra *a*) and *c*), spinning sidebands appeared (marked with an asterisk).

deduced accounting for such narrow lines in the peak pattern of BTA 2. Similar results were obtained for BTA 3, namely signals at 169.1 ppm (64 Hz), 137.1 ppm (45 Hz), 127.9 ppm (66 Hz) in the same order (see Fig. 3.15 c).

As for BTA 1, VT carbon NMR measurements of BTA 3 did not provide additional information about the system. Above the mesophase transition the aliphatic region showed an isotropic character of carbon resonances, indicating a liquid like behaviour of the side chains as expected for liquid-crystalline phases. $^{13}$C {$^{1}$H} CP/MAS measurements of BTA 2 in contrast to BTA 1, showed a quite remarkable temperature dependence of the side chain signals upon the phase transition at about 60 °C. The observed behaviour was such extraordinary that an independent study on that issue will be presented in section 3.2.8.

### 3.2.5.2. Carbon Spectra of BTA 4

As stated at the end of section 3.2.4.2, the peculiar observation upon heating of BTA 4 were related to a very slow phase transition of this compound. Therefore, in order to probe the symmetry of the packing in different possible arrangements, a separate VT $^{13}$C {$^{1}$H} CP/MAS study on BTA 4 has been carried out, beginning with the liquid-crystalline phase above 102 °C. It should be clarified that the relaxation from the supercooled mesophase to the crystalline phase proceeded within hours, as suggested by the $^{1}$H NMR measurements. Due to the limited number of sites in BTA 4, $^{13}$C NMR spectra could be obtained in a relatively short time, thus with a negligible contribution of the supercooled phase.

Because hetero- and homonuclear couplings were almost completely averaged under these conditions, CP was not efficient any longer. The spectrum of the BTA 4 mesophase at 126 °C, given in figure 3.16 a), was therefore recorded by means of $^{13}$C SPE. The side chain region of the spectrum showed a number of relatively narrow lines indicating fast motion in this part of the molecule. The three backbone carbon signals were broader than those of the side chains suggesting a non-uniform distribution of chemical shifts and a relatively slow dynamic. A moderate dynamics in the centre and faster motion in the peripheral part of the stacked molecules was in line with the assumption of an intact triple-bonded helical arrangement implied by $^{1}$H MAS NMR in section 3.2.4.1. On a microscopic level, the high temperature mesophase of BTA 4, therefore resembled that of all other investigated BTAs.

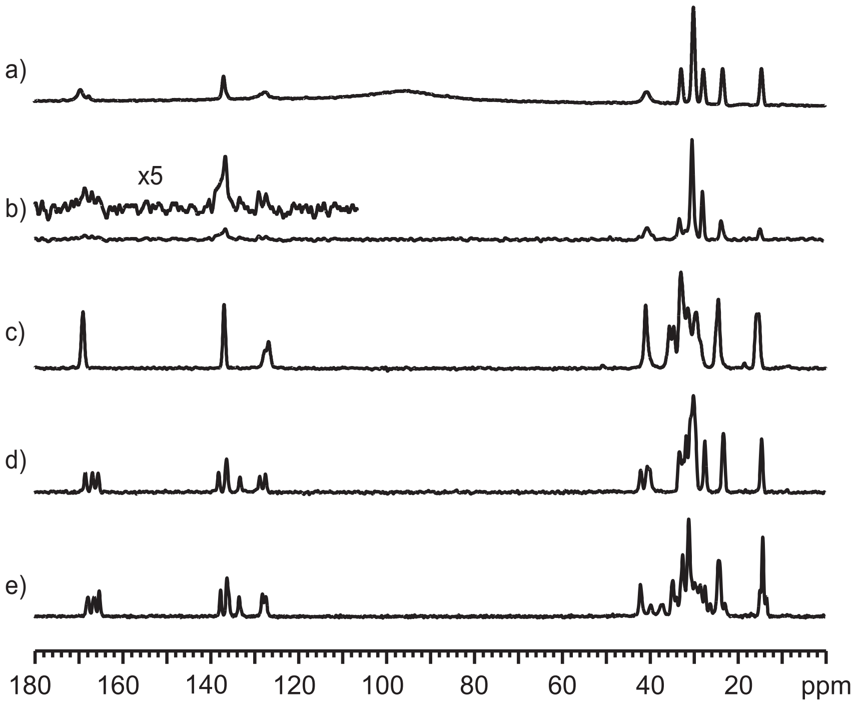

**Figure 3.16.** $^{13}$C NMR spectra of BTA 4 at different temperatures: *a*) $^{13}$C MAS NMR (SPE) of the BTA 4 mesophase at 126 °C, *b*) $^{13}$C $\{^{1}$H$\}$ CP/MAS spectra of BTA 4 rapidly cooled from 140 °C to 67 °C, *c*) $^{13}$C $\{^{1}$H$\}$ CP/MAS spectra of BTA 4 rapidly cooled from 140 °C to -12 °C, *d*) $^{13}$C $\{^{1}$H$\}$ CP/MAS of the equilibrated BTA 4 at 28 °C, *e*) $^{13}$C $\{^{1}$H$\}$ CP/MAS of the equilibrated BTA 4 at -20 °C. All spectra have been obtained at a LARMOR frequency of 126 MHz. The SPE spectrum in *a*) has been recorded with a recycle delay of 20 s. The big hump between 80 and 100 ppm in the spectrum is the carbon signal of the PTFE rotor cap, which is only seen in single pulse spectra. The CP/MAS spectra *b*)-*e*) have been recorded with a contact time of 2 or 3 ms.

The increasing DQF intensity in the $^{1}$H DQF MAS spectra discussed in section 3.2.4.2 indicated that the backbone becomes rigid on quick cooling the sample to 67 °C. Under these conditions CP became slowly operational, which is demonstrated in figure 3.16 b). This CP/MAS spectrum was recorded after rapid cooling the compound from 140 to 67 °C. Even though the signals were very weak and considerably broadened, three backbone peaks could be recognised in the fivefold magnification. Apart from the intensity, the side chain region closely resembled that of the mesophase. This observation is in line with $^1$H DQF MAS spectra as well, indicating a liquid-like behaviour of the side chains in this intermediate state of BTA 4.

As seen in the section 3.2.4.1, $^1$H MAS NMR was sensitive to a phase transition showing up in the DSC cooling curves at about 10 °C. Moreover, the phase transition was primarily ascribed to an effect occurring in the side chains. In this manner, cooling the compound quickly from above 140 °C to -12 °C and subsequently recording a spectrum yields the $^{13}$C {$^1$H} CP/MAS spectrum is given in figure 3.16 c). The spectrum resembled the mesophase spectrum at high temperature since the chemical shift values of the three backbone peaks are determined as 169.0 ppm (96 Hz), 136.9 ppm (78 Hz), and 127.6 ppm as well as 126.9 ppm (95 Hz each) for the split signal of the ternary carbon atom. The peaks were apparently broader than those of BTA 2 and 3 which, might be attributed to a minor symmetry breaking as in case of BTA 1.

Apart from the SPE spectrum recorded at 126 °C (Fig. 3.16 a)), the measurements at 67 and at -12 °C were done on an instable supramolecular assembly, because the rapid cooling prior to the measurements did not a allow a phase conversion as observed during the heating run of $^1$H NMR measurements. In another experiment the focus was on the carbon spectrum of the equilibrated compound. In order to ensure equilibration, the sample was kept at room temperature for at least 12 h prior to the measurements. The resulting spectrum is presented in figure 3.16 d). The low field region could be ascribed to the three backbone sites, being split into several distinct lines. Specifically, three distinct carbonyl peaks at 168.4, 166.7 and 165.4 ppm were observed; two peaks corresponding to the quaternary carbon atoms at 138.0 (2 carbon sites) and 136.1ppm (1 carbon site); as well as three signals arising from ternary carbons at 133.1, 128.6 and 127.3 ppm. Apparently, a phase transition occurred during the storage time, leading to a new structure under cancellation of the symmetric columnar arrangement. The new structure is not assumed to be columnar any longer. A changed connectivity of the hydrogen-bonded scaffold is obviously accompanied by a change of side chain conformation. Therefore, it is not surprising that the side chain spectra of BTA 4 in the metastable columnar low-temperature phase (see Fig. 3.16 c)) and the stable phase at ambient conditions (Fig. 3.16 d)) are also very different.

Further cooling of the equilibrated stable phase led to a another transformation in the side chain region of the molecule, which can be seen in figure 3.16 e). Apparently, the backbone peaks remained unaffected upon this transition, whereas new peaks arose in the side chain region. Many of these have an intensity lower than one third of the signals before the transition. Hence it is reasonable to assume an indefinite ratio of two side chain conformations. In fact, even the reported crystal structure of BTA 1 exhibited a source of disorder attributed to a single side chain arm with two possible conformations, that occurred randomly within the material[117]. The side chain effect is of minor importance and will not be discussed further in details, however, the fact that a relatively simple compound provides various different phases is a quite remarkable finding, which will be further examined in the next sections.

The carbon spectra of BTA 4 confirmed the different states already suggested by $^{1}$H MAS and $^{1}$H DQF NMR. At least 4 different phases of BTA 4 could be identified, all of them giving rise to clearly distinct $^{13}$C spectra. Their appearance did not only depend on the temperature, but also on the kinetics of the conversion and the thermal history of the sample.

#### 3.2.5.3. 2D $^{1}$H-$^{13}$C Through-Space Correlation: *Assignment II*

At room temperature, compound BTA 4 prefers a less symmetric arrangement as indicated by the triplet of the $^{13}$C carbonyl resonance. The sudden disappearance of the aryl peak in the $^{1}$H MAS NMR spectrum is puzzling, though. In this section the attempt is presented to resolve the $^{1}$H NMR spectrum of BTA 4 in the equilibrated room temperature phase by $^{1}$H-$^{13}$C HETCOR, or more specifically the REPT-HSQC experiment with short recoupling times. Figure 3.17 b) shows such a correlation pattern of equilibrated BTA 4 at a temperature of 51 °C. For the sake of comparability a $^{13}$C {$^{1}$H} CP/MAS spectrum of this state of BTA 4 is given in figure 3.17 b). The 2D spectrum gave rise to three peaks in the backbone region of the carbon dimension. Due to the chemical shifts these peaks could be assigned to the three ternary carbon atoms, at 133.1, 128.6, and 127.3 ppm, correlated with the single low field proton peak. According to the distribution of peak centres in the proton dimension, the aryl resonances were located between 8.4 to 9.2 ppm, hence were rather unaffected if not shifted to low field compared their chemical shift of 8.2 ppm in chloroform-$d$ solution. Obviously, the aryl protons overlapped with the amide proton peak, explaining the fact that it could not be observed before.

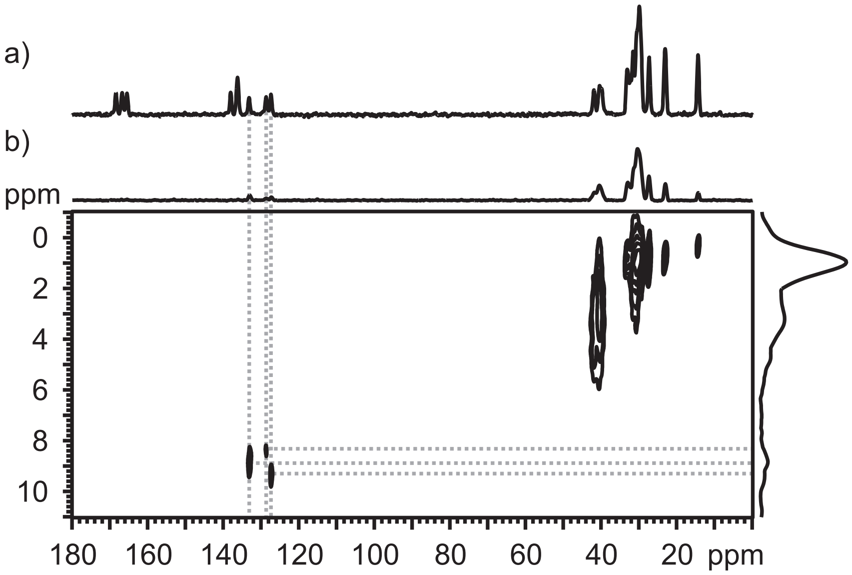

**Figure 3.17.** $^1H^{13}C$ REPT-HSQC of crystalline BTA 4.

### 3.2.6. The Distinctiveness of BTA 4

BTA 4 revealed a considerable complexity as seen in the last section. In order to probe all major states of BTA 4 and their interconversion, the previous results need to be reviewed thoroughly.

Regarding the VT $^1H$ MAS NMR spectra in section 3.2.4.1 of the heating run between 50 to 100 °C, the vanishing of the aryl peak was presumably caused by a phase conversion into a thermodynamically more stable non-columnar phase. This was indicated by the most prominent feature of the conversion, that is, the seeming disappearance of the aryl proton resonance. Surprisingly, the effect was not observed during the cooling run, thus a retarded phase transition could be assumed. Apparently, the cooling process was just too fast to reveal indications of the conversion, however, a gradual growth of DQF intensity was detected instead. This growth suggested a continuous stabilisation of the yet columnar assembly of BTA 4. As a matter of fact, a second transition was found at about 10 °C under full preservation of all columnar characteristics of the spectrum. The temperature of the transition moreover coincided with a DSC event at this temperature. This enthalpy change could fully be ascribed to the crystallisation point of the side chains, which showed remarkable dynamics above 10 °C, whereas the backbone can be assumed to be rigid already at higher temperatures.

The recovery of the liquid-crystalline mesophase on heating above 102 °C was equally determined by usual MAS and DQF NMR spectra. It was accompanied by instantaneous line narrowing, loss of DQF intensity and re-emergence of the aryl proton peak.

With the achieved knowledge about BTA 4 one more set of VT $^1$H MAS NMR measurements have been conducted. However this time, the experiments were carried out under equilibrium conditions with a sufficient waiting time before each experiment. Technically, a continuous temperature profile with stepwise changes of the temperature was impractical since the transition from the liquid-crystalline phase to the crystalline phase seemed to be temperature dependent. That means slightly below the phase transition temperature of 102 °C, the equilibration would have taken a very long time. The measurements have been recorded with increasing temperature below and decreasing temperature above the phase transition. The corresponding spectra are given on the left in figure 3.18.

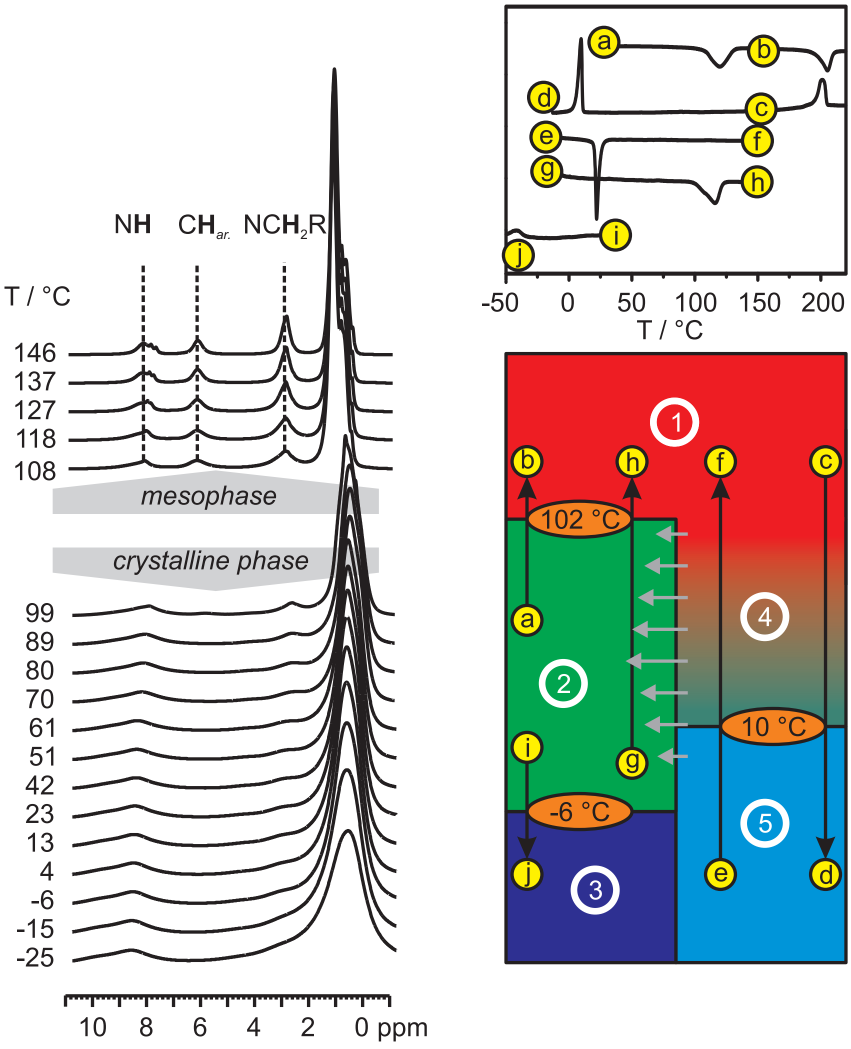

**Figure 3.18.** *left*: VT $^1$H MAS NMR of the equilibrated BTA 4. On the account of the sample characteristics, the chronological order of the experiments does not correspond to the order of the temperature scale (see text). *right*: The advanced DSC acquired after the solid-state NMR study (above) and a phase scheme of BTA 4 (below).

BTA 4 provides at least three thermodynamically stable phases. The liquid-crystalline phase above 102 °C showed the familiar features of columnar stacking, whereas the stable crystalline phase lacked a high-field shifted aryl proton and could not be assumed as properly columnar, which is in line with symmetry breaking of the carbonyl resonance observed by $^{13}$C NMR. This could be assigned to another phase transition, which confined to the side chains of the molecule.

In conclusion, several different phases of BTA 4 have been identified, which are illustrated in the phase diagram on the right in figure 3.18. These phases are the columnar mesophase above 102 °C (**1**), a crystalline phase being apparently non-columnar (**2**, -6 to 102 °C) , a supercooled mesophase preserving a columnar structure below 102 °C (**4**, 10 to 102 °C), and a supercooled mesophase with frozen side chains below 10 °C (**5**). The latter two phases were evidently metastable and transform to the stable non-columnar crystalline phase. During the precise examination of BTA 4, even a third stable phase has been discovered (**5**) with a different packing of the side chains as indicated by a subtle broadening of the side chain peak in $^{1}$H MAS NMR spectra below -6 °C. This phase corresponds to $^{13}$C spectrum given in figure 3.16 e).

The phase conversion between the supercooled mesophase (**4**) into the non-columnar crystalline phase (**2**) is apparently temperature-dependent and occurs faster at intermediate temperatures, which is clarified by the grey arrows of different length in figure 3.18. The kinetics of this transition will be more thoroughly investigated in section 3.2.7.

It needs to be pointed out that solid-state NMR is not the only method which could be applied to probe the retarded phase transition in BTA 4. Due to its high sensitivity towards the high-field shifted aryl proton resonance and the time consuming generation of VT stacks of $^{1}$H MAS NMR spectra, the slow conversion became noticeable. Generally, DSC is sensitive to all transitions found in BTA 4 (except for the conversion from the supercooled mesophase to the non-columnar phase), as shown in the advanced DSC plot on the upper right in figure 3.18. In this illustration the trajectories $a \rightarrow b$, $c \rightarrow d$, and $e \rightarrow f$ correspond to the *first heating*, *cooling*, and *second heating* curves of the DSC already presented in section 3.2 (Fig. 3.4 d). Due to the speed of the measurement the conversion from the crystalline phase to the columnar mesophase at 102 °C had only been detected in the suspect first heating run. In the two DSC measurements conducted afterwards, the annealed sample BTA 4 was stored for at least 12 h prior to the measurements, giving rise to the curves $g \rightarrow h$, reproducing the crystal-mesophase transition at 102 °C, and $i \rightarrow j$, finding evidence for the non-columnar low-temperature phase. Therefore, the reported phase transition of 102 °C has been confirmed[121].

#### 3.2.6.1. Speculations About the Non-Columnar Phase

Details about the structure apart from the evident asymmetry were unknown, since the crystalline compound lacked a single crystal X-ray structure and the full organisation could not be elucidated by solid-state NMR solely. However, BTA 4 is not the only BTA possessing non-helical crystal structure. Hanabusa *et al.* published the X-ray structure of a BTA equipped with methyl groups (see Fig. 3.19) instead of longer side chains, which is referred to as BTA 5 within this thesis[127]. The corresponding carbon and proton spectra are given in figure 3.20.

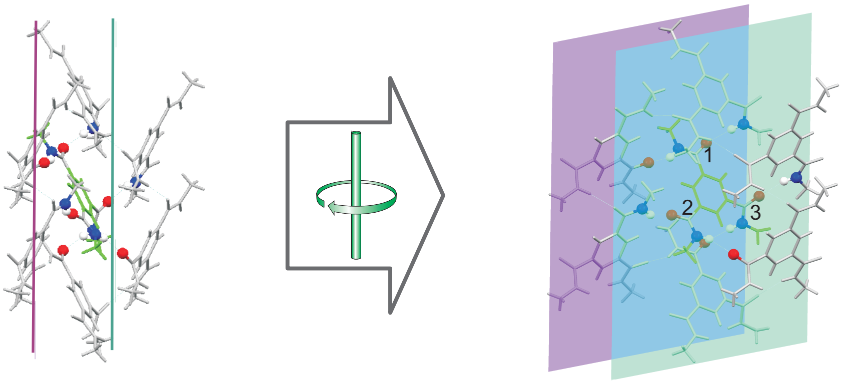

**Figure 3.19.** Crystal structure of BTA 5.

The similarity between the spectra of the compounds given in figure 3.20 b) and c) is striking, in particular the agreement of the low field carbon signals arising from the three backbone sites in figure 3.20 c). Due to its shorter side chains it was not surprising that BTA 5 is a less waxy material as compared to the other compounds. Because of the high crystallinity it provided a quite long $^1$H spin lattice relaxation time, being determined as approximately 20 s for protons. This had to be taken into account when conducting the CP/MAS experiment. For this reason and due to its missing dynamic aspect, BTA 5 only served as a reference compound for BTA 4.

The crystal structure is not as intuitively understood as the columnar arrangement, because obvious coplanar stacking is prevented. The lattice is rather based on sheets of molecules having two twisted orientations, which are seen on the left in figure 3.19. The "sheet" is best recognised by viewing along the crystallographic $c$-axis.

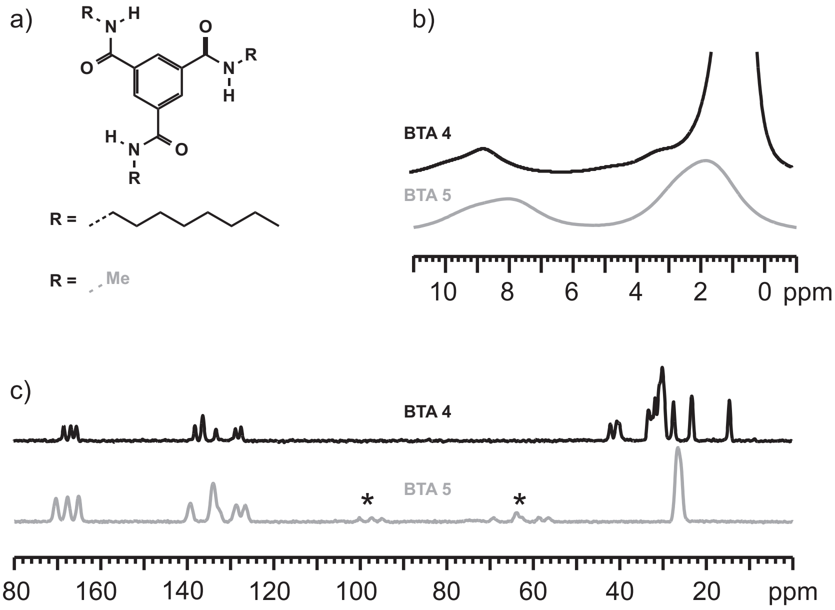

**Figure 3.20.** *a*) Structures of BTA 4 and 5. *b*) Comparison of $^1$H MAS NMR spectra of BTA 4 and 5 at ambient temperatures. *c*) $^{13}$C {$^1$H} CP/MAS spectra of crystalline BTA 4 and BTA 5 at ambient conditions. $^{13}$C NMR spectrum of BTA 4 recorded at a Larmor frequency of 126 MHz, whereas BTA 4 was measured at a frequency of 212 MHz resulting in spinning sidebands (marked with an asterisk). Both, either the $^1$H and the $^{13}$C NMR spectra of BTA 5 have been recorded with a recycle delay of 20 s due to the long $^1$H relaxation time of the compound.

Each molecule is connected to six molecules via hydrogen bonds. This is exemplarily illustrated by the green marked molecule in the middle. The purple and blue planes are parallel to the (100)-planes of the crystal lattice. The green plane can be regarded as boundary between two adjacent layers. In the arrangement, one molecule is connected to four molecules of the same layer and to two of the neighbouring layer. The amide functional group **1** is in-plane with the aryl ring, hence in conjugation with it, and forms two hydrogen bonds with neighbouring groups of the same layer. The amide group **2** is in-planar as well and binds to atoms outside the layer. For the amide group **3** the bonding state is different again. In contrast to the other two groups it is tilted about 45 ° with respect to the ring and is therefore not in conjugation with the aryl ring. Obviously, all three carbonyl groups are differently hydrogen bonded and consequently gave rise to three distinct carbonyl signals.

The affinity of the carbon and the proton spectra of BTA 4 and 5 led to the conclusion that both compounds exhibit similar hydrogen bond connectivities.

### 3.2.7. Kinetic Measurements

In this section the results of kinetic investigations of the transition between the supercooled mesophase (columnar) and the crystalline (non-columnar) phase will be presented. As indicated in section 3.2.4.1 the retarded transition on heating the sample was accompanied by a seeming disappearance of the high-field shifted aryl proton signal. Furthermore, during the heating run of the VT $^1$H MAS NMR measurement it appeared that the transition was retarded, which means it was either slow or triggered by temperature changes. In order to gain insight into the transition, time-dependent $^1$H MAS NMR measurements have been carried out at five temperatures. To this end, the sample has been heated within the NMR probe head to 146 °C, the highest possible sample temperature, and subsequently cooled to the target temperature. The starting point of each experiment was defined by the moment the heater was switched off. Due to a high cooling rate at the beginning this time approximately coincided with the time the sample temperature reached the transition temperature of 102 °C. The cooling process including a proper tuning of the NMR probehead took about 5 min on average, depending on the target temperature. Under these conditions the sample was assumed to be in the supercooled columnar mesophase when the actual NMR acquisition started. The data has been recorded with a pulse program capable of recording alternately SPE and DQF spectra in succession, thus sampling a large number of single experiments during the whole experiment time. In order to reduce possible errors due to changing $T_1$ relaxation times the recycle delay was maximised to achieve matching of a single SPE/DQF pair and the sampling rate. This was chosen to be 5 min resulting in a recycle delay of about $\sim$10 s, corresponding to 16 scans for each SPE or DQF experiment. Since the obtained dataset contains two kinds of experimental data it needed to be reconditioned after the experiment by a routine, transferring the FIDs of the SPE and DQF experiments into two separate data sets. Fourier transformation led to time-dependent data sets. In figure 3.21 a) to e) time-dependent $^1$H MAS NMR (SPE) are presented. For the sake of clarity a 1D $^1$H MAS NMR spectrum of the supercooled mesophase of BTA 4 is shown in *a*). The respective DQF experiments will be discussed afterwards.

The rate of the phase transition is apparently strongly temperature dependent. For the three intermediate temperatures 70, 51, and 23 °C the phase transition seemed to complete within the depicted experiment time of 7 h, as indicated by the fading of the high-field shifted aryl proton peak. Another characteristic feature is the transformation of the side chain resonance. The decrease of the relatively sharp side chain signal at the expense of a broader peak at higher field is well observed for all intermediate temperatures.

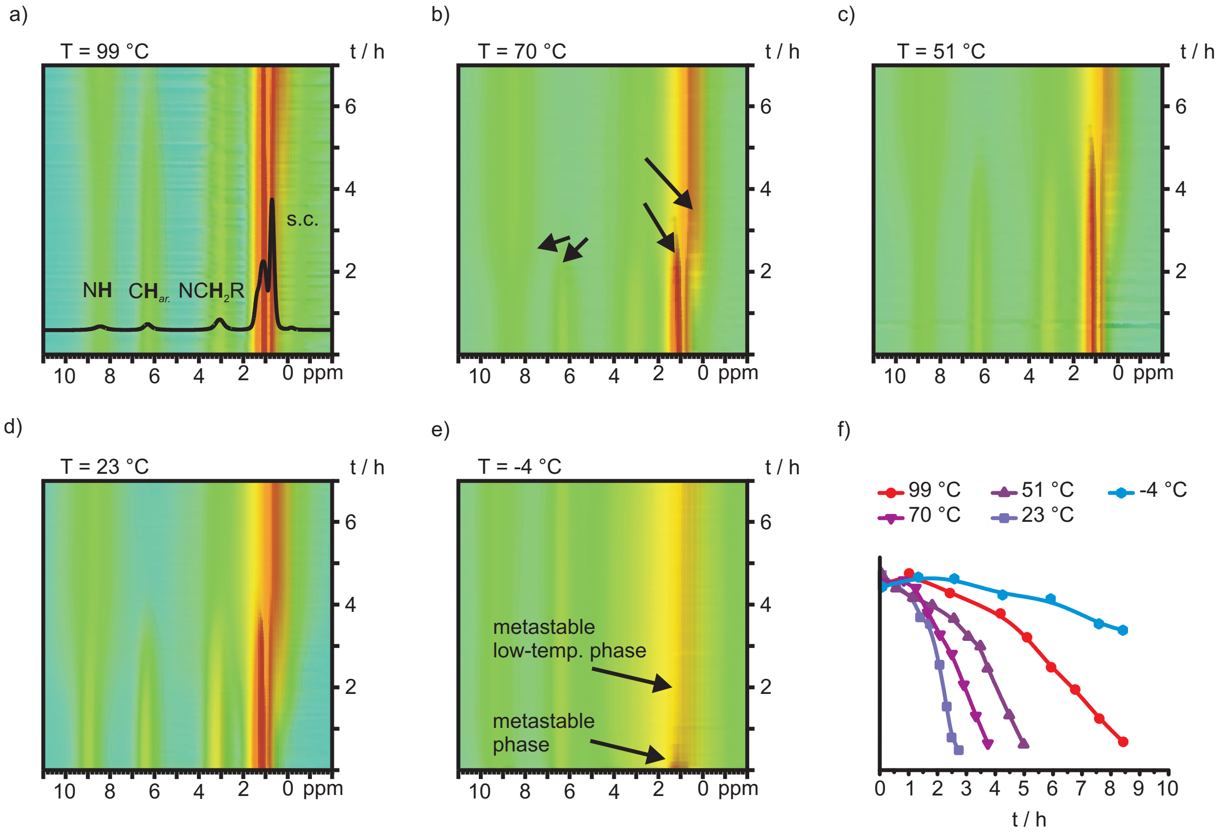

**Figure 3.21.** Kinetic measurements of the phase transition of BTA 4. The figures *a*) to *e*) trace spectral changes of $^1$H MAS NMR spectra of BTA 4 at five different temperatures within 7 h experiment time. *f*) Evolution of the area integral of the high-field shifted aryl proton signal for all investigated temperatures. The lines between the data points only serve to guide the eye.

At 99 and at -4 °C the transition is very slow, which is depicted in figure 3.21 f). The five curves indicate the decrease of the integral of the aryl proton peak, which serves as a measure of the degree of the conversion. Obviously, the experiment conducted at -4 °C indicated the slowest transition, followed by the experiment at 99 °C. The conversion into the crystalline phase was evidently faster at intermediate temperatures, with the 23 °C experiment, yielding the fastest transition completed within 3 h. The slower rate constant of the conversion at high and very low temperature can probably be assigned to a thermodynamic effect at 99 °C and to a kinetic effect at -4 °C. More specifically, the slow transition at high temperature could be explained by means of almost equal chemical potentials in both phases close to the phase transition point of 102 °C. The free formation enthalpy of the crystalline phase is therefore small and consequently the phase transition is slow. At -4 °C the free reaction enthalpy was presumably high, however, the conversion was decelerated by the slow kinetics at lower temperature. Temperatures lower than -4 °C have been checked, however, at -25 °C no noticeable spectral change could be observed within 24 h. It needs to be pointed out that at -4 and at -25 °C the metastable columnar phase of BTA 4 transformed into the metastable low-temperature phase (cf. transition **4→5** in figure 3.18). The corresponding transition is observable figure 3.22 e). It was completed within this first 20 m of the experiment as indicted by the broadening of the side chain peak (arrow in figure 3.22 e)).

The timescale of this conversion is still quite remarkable. Nevertheless, in a recent study a similar retarded phase transition from a hexagonal columnar mesophase to monoclinic crystalline phase had been found for a hexabenocoronene system[145]. The rates of the conversions at intermediate temperature were very surprising since the transitions speeded up in the order 52, 70, and 23 °C. Possibly this behaviour could be related to the several relaxation processes that occur within the temperature range reported for C6, C10, C18 homologues of BTA 4[144].

The time dependence of the DQF signal arising from the side chains upon the phase transition at 51 °C is illustrated in figure 3.22. As displayed on the left $^1$H MAS NMR signal broadened and shifted to high field. In addition to that, the time-dependent $^1$H DQF NMR spectra revealed a significantly higher DQF intensity of the side chains at the end of the conversion after approximately 4 h. This behaviour revealed a relatively poor packing of the side chains in the supercooled columnar phase, which improved upon the phase transition. The measurements therefore point to poor space filling properties of the linear side chain, being the driving force of the conversion into a non-columnar structure.

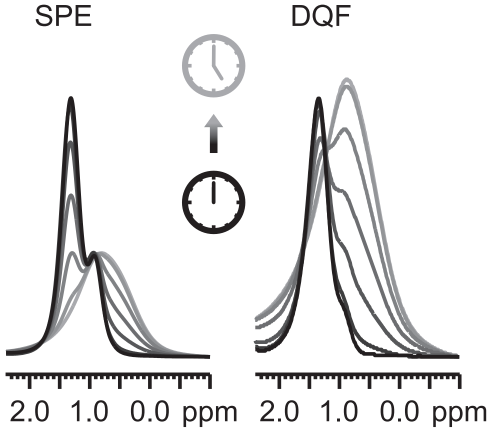

**Figure 3.22.** Time-dependent $^1$H MAS and DQF NMR spectra of the high field region of BTA 4.

It should be noted, however, that the phase behaviour of BTA 4 is rather complex and that solid-state NMR is not the method of choice to examine the gradual conversion of both phases. First, the uniformity of the supercooled mesophase and equal conditions during the cooling process is difficult to guarantee in a MAS probe. Second, rotation frequencies of 30 kHz cause a remarkable pressure gradient within the material, which may also have an impact on the phase stability and the conversion rate in consequence. In this context it should be mentioned that numerous BTAs have been probed by *infrared spectroscopy* (IR), first by Hanbusa *et al.*[127]. Independent studies on different BTAs in solution and in the solid state revealed that three characteristic amide modes could be unequivocally assigned to the helical arrangement known from preceding X-ray investigations[117,137,146]. These are the 3240 $cm^{-1}$ NH stretching band, the 1640 $cm^{-1}$ carbonyl stretching band (amide I) and the amide II band[f)] at 1550 $cm^{-1}$, which are indicative for three-fold symmetrical hydrogen bonding between the molecules. The IR spectra of the high temperature phase of BTA 4 and the supercooled mesophase were in good agreement with reported IR modes of the helical arrangement of the compound[137]. IR spectra of aged samples of heated BTA 4 were reported to change significantly, that is, 3306, 1644 and 1531 $cm^{-1}$ instead of the wave numbers of the known columnar stacking[123]. The IR spectrum of BTA 5 (*i.e.*, 3333 $cm^{-1}$, 3259 $cm^{-1}$, and 1539 $cm^{-1}$) also strongly deviated from samples providing a columnar arrangement and rather resembles the IR spectrum of the low-temperature phase of BTA 4. This can be seen as another indication for a similar hydrogen bonding conditions.

Thus, obviously IR spectroscopy is sensitive to the phase transition of BTA 4. Furthermore, it allows proper starting point and temperature control without the need of rapid sample rotation. Neverteless, the kinetic measurements of this study demonstrated the general possibility to observe a slow transition of long-lived metastable species via solid-state NMR. Though, a detailed study of the kinetics of the phase transition is beyond the scope of this work and should rather be carried out with another spectroscopic method.

### 3.2.8. 2D $^{13}$C-$^{13}$C Through-Bond Correlation: *Connectivity*

In this section the temperature dependence of the carbon resonances of BTA 2 is investigated in further details. As seen already in figure 3.15 b) at ambient conditions two side chain signals were split into two separate lines each, *i.e.*, the lines at 33.5 and 32.8 ppm

---

f) As amide I, the amide II is one of the three characteristic vibrational modes of the amide functional group. The term amide II refers to a composite vibration, but it is sometimes also described as an NH bending vibration of the amide proton.

as well as at 16.5 and 15.6 ppm. The high field component of the doublets seemed to be more intense, which was attributed to the broader line width of the low field component. Although a splitting with the intensity ratio of 2:1 would be expected with respect to the $C_3$-symmetry of the molecules, a 1:1 ratio was observed here. It has to be noted that CP/MAS in general did not provide reliable integrals.

Because of the rather exposed chemical shift at the end of the side chains the signals at 47 ppm and the split signal at about 15 ppm could safely be assigned to the innermost carbon atom $C^1$ and to the outer methyl carbon $C^7$. The resonance at about 40 ppm might barely be assigned to the second carbon atom of the chain $C^2$, whereas the origin of all other signals remained uncertain. For this reason $^{13}$C-$^{13}$C correlation spectroscopy was applied by means of the refocused 2D INADEQUATE method (see section 2.3.4 for the theoretical background). Figure 3.23 shows the resulting spectrum in combination with a simplified scheme of the BTA core and a single side chain. Similarly to the procedure applied for elucidating the connectivity of U-$^{13}$C-L-tyrosine in figure 2.21 b), horizontal correlations in the pattern pointed to a chemical bond between the corresponding sites. As an example, the terminal methyl carbon $C^7$ and the adjacent carbon $C^6$ gave rise to a very intense correlation between both frequencies at about 16 and 26 ppm. In this sense the connectivity of the whole side chain could be assessed, starting either with the terminal methyl carbon or the inner methylene. Unfortunately, not all peaks were equally intense and some were even missing (*i.e.*, three of the four expected correlation peaks of the middle carbon atom $C^4$, which is indicated by the arrow in figure 3.23). Since HARTMANN-HAHN CP was used to generate carbon magnetisation at the beginning of the experiment, the efficiency of the carbon polarisation transfer was offset dependent. The irradiation frequency was therefore set to 32 ppm, *i.e.*, the centre of the side chain region between position $C^3$ and $C^4$. On the one side, the missing $C^4$ peaks might be explained by the location of the carrier frequency close to the expected signals. On the other side, the concerning signal might also be affected by the so-called *rotational resonance*[147,148] condition induced by the MAS frequency of 15 kHz, which was about the distance between the carbonyl line and the $C^4$ signal ($2\nu_R = \Delta\nu_{CO,C^4}$)[g]. Nevertheless, it should be noted that the isolated missing correlations could be interpolated through the other coupled sites. The full elucidation of the whole connectivity of the side chain was therefore still unambiguously possible.

After the signal assignment of the side chain region was clarified, the focus was set on

---

g) The same setup was used for a similar experiment carried out later without any noticeable impact of the transmitter frequency or of the rotational resonance phenomenon.

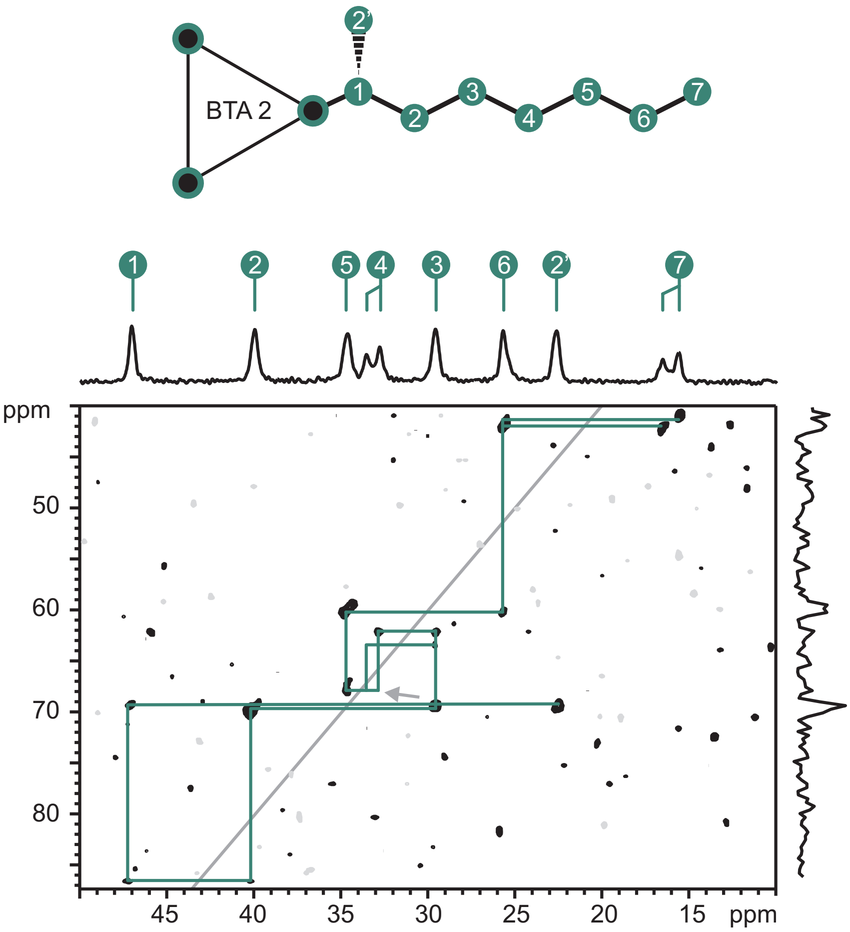

**Figure 3.23.** $^{13}$C-$^{13}$C through-bond correlation of BTA 2 at 29 °C. The horizontal 1D spectrum above the correlation pattern is a $^{13}$C {$^{1}$H} CP/MAS spectrum of BTA 2 at 29 °C. The spectrum on the right is a projection of the depicted area.

the temperature dependence of carbon lines. This is accomplished by a dense sampling of VT $^{13}$C {$^{1}$H} CP/MAS spectra ranging from -18 °C to 148 °C depicted in figure 3.24. The measurements revealed subtle spectral changes of the low temperature phase on heating between -18 °C and 57 °C. The splittings of the signals of positions $C^4$ and $C^7$ at 33 and at 15 ppm obviously increased on cooling the sample. In case of $C^4$ the order of the split signals reversed and a temporary overlap was found at approximately 40 °C, whereas the $C^7$ resonance split into three signals.

At the temperature of the phase transition at about 60 °C (~70 °C in the DSC, cf. Fig. 3.4 b)), the lines of middle side chain atoms suddenly split up in triple lines, suggesting a symmetry breaking within the assembly. This time, the peak intensities in a ratio of 1:1:1 strongly supported the assumption of a full cancellation of the $C_3$-symmetry, thus an occupation of distinct conformations for all three side chain arms. As the temperature

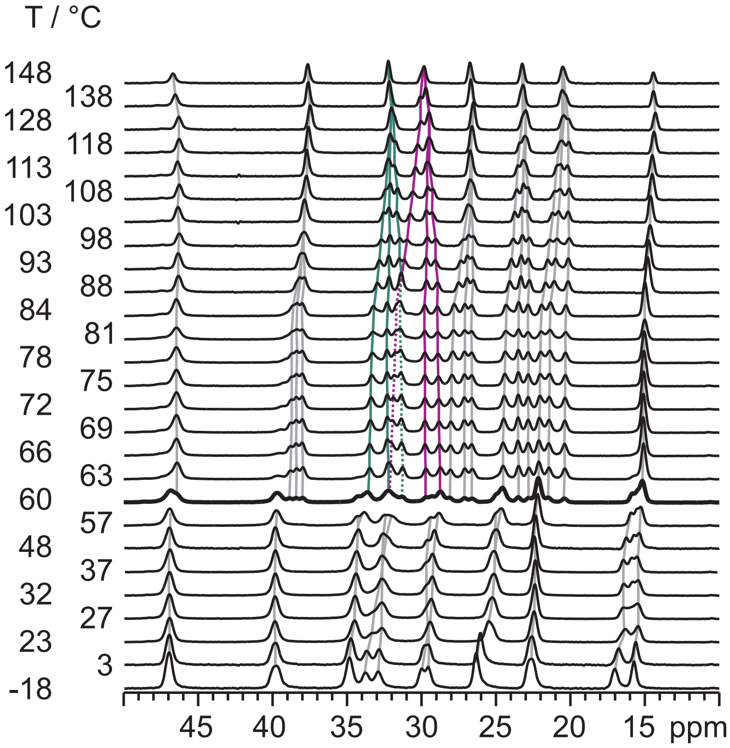

**Figure 3.24.** VT $^{13}C$ $\{^1H\}$ CP/MAS spectra of BTA 2.

increased, the splitting of signals decreased and the lines merged again. At 148 °C the spectrum resembled the spectrum before the transition, though the lines are considerably narrower and shifted high field compared to 57 °C. Position $C^2$, for example, was located at 37.7 ppm at 148 °C and at 39.8 ppm at 53 °C.

More astonishing was the splitting originating from equivalent sites itself. For the resonances of the sites $C^{2'}$ and $C^6$ at 23 and 25 ppm the temperature dependent drift can easily be traced in the stack of VT spectra. However, in the middle side chain the low field component of $C^4$ and the high field component of $C^5$ coincided at 88 °C and seemingly swapped order on further cooling. At 60 °C the $C^4$ resonances were presumably located at 28.8, 29.8 and 32.2 ppm, which would correspond to a distribution of 3.4 ppm, only based on conformation effects.

It needs to be pointed out that at about 90 °C the process of motional averaging of the carbon resonances accelerated, indicated by the slight kink in the peak trajectories, which further hampered a safe assignment of carbon resonances in the intermediate temperature range. A different assignment of the spectrum between 60 and 88 °C can therefore not be ruled out. Moreover, the separation of the $C^4$ resonances would reduce to 2.4 ppm, which is a more reliable value for a conformation effect in side chains already providing indications of dynamic averaging.

Due to this ambiguity and in order to demonstrate the validity of the method the question was brought up, whether it is possible to reveal the full side chain conformation on the basis of INADEQUATE-type $^{13}$C-$^{13}$C through-bond correlation. For this reason another refocused INADEQUATE experiment was conducted at 72 °C, that is, the temperature at which all peaks were best resolved and the succession of lines originating from sites $C^4$ and $C^5$ was rather vague. Figure 3.25 shows the result of the correlation pattern. As specified for the low temperature correlation pattern the connectivities could be deduced starting from methyl site $C^7$ or the inner carbon $C^1$. The chemical shift of these terminal carbons was not dispersed since they were only little affected by the conformational state of the neighbouring carbon atoms. On tracing the connectivity towards the interior part of the side chain two crossed-over signals assigned to sites $C^4$ and $C^5$ were found. This finally confirmed the wide splitting of clearly distinct conformational states of all side chain atoms, in particular of carbon site $C^4$.

Since the connectivities were clarified by this, it was aspired to reveal the origin of the signal splitting above 60 °C. For this purpose in figure 3.26 the chemical shift values are plotted as a function of the temperature to illustrate the gradual shift and merging of $^{13}$C lines.

The different colours on the left distinguish the pattern by the ring atoms, whereas in the right plot the signals are sorted by side chain arm. Below approximately 30 °C the two split lines corresponding to the signals of the carbon atoms $\mathrm{C}^7$ and $\mathrm{C}^4$ were separated by 0.7 and 0.9 ppm. The relatively small line width suggested a well-defined conformation effects. It appeared reasonable that the split carbon signals are due to the so-called $\gamma$-*gauche effect*[149], which describes the influence of the chemical shift on the conformational state of a carbon atom in $\gamma$-position to the observed nucleus. Specifically, the effect imposes a high-field shift of approximately -5 ppm to a $^{13}$C resonance of a nucleus having a second carbon atom in *gauche*-conformation compared to a nucleus within a full *trans*-conformation. The effect would readily explain the limitation to the two sites $\mathrm{C}^4$ and $\mathrm{C}^7$, if two distinct dihedral angle defined by the carbon atoms $\mathrm{C}^4$, $\mathrm{C}^5$, $\mathrm{C}^6$, and $\mathrm{C}^7$ were considered under otherwise identical conformations. The magnitude of the observed splitting however drastically deviated from the reported values of the $\gamma$-*gauche effect*. Therefore, the splitting could not be assigned to distinct *conformations*, but it was assumed to be due to distinct *conformational statistics*, which differed in terms of the *gauche*/*trans* ratio of $\mathrm{C}^4$ and $\mathrm{C}^7$.

Above the phase transition an abrupt net high-field shift and a symmetry breaking was

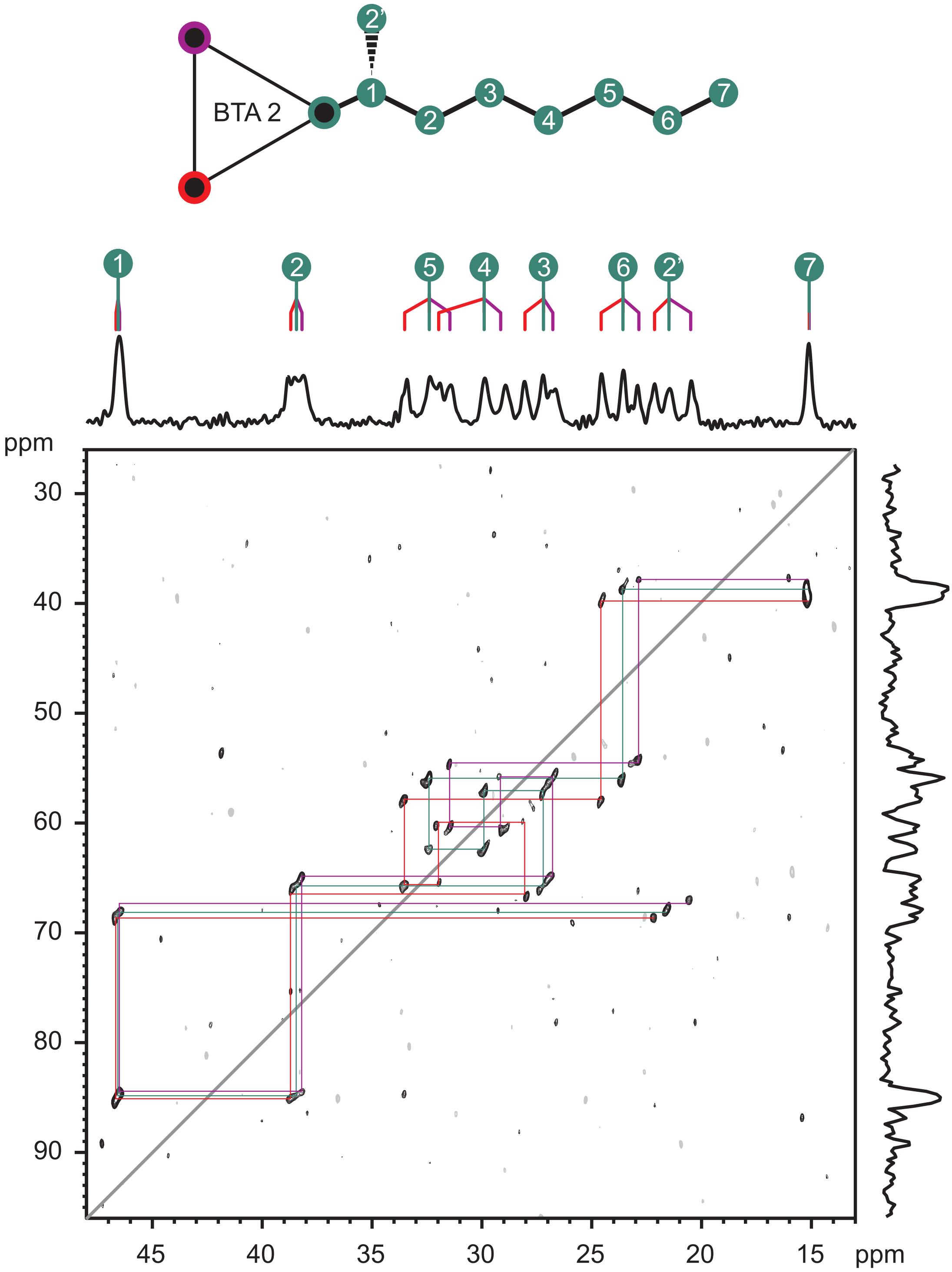

**Figure 3.25.** $^{13}$C-$^{13}$C through-bond correlation of the side chain region of BTA 2 at 72 °C. The colour code used in this graphic in combination with the denotation of the chirality actually implies a certain helical sense. The colours, however, are only used to illustrate the distinguishability of the different conformations.

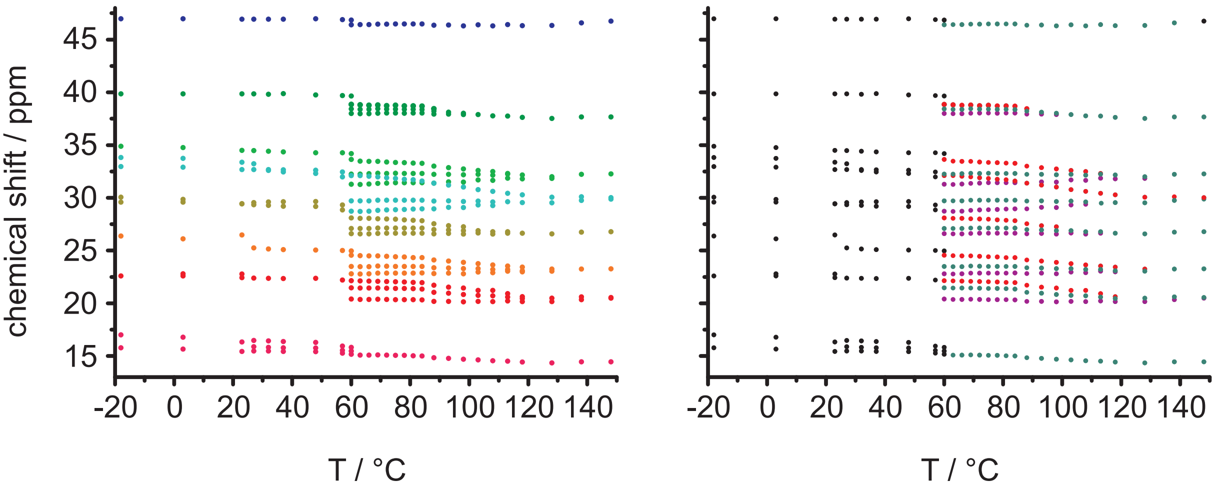

**Figure 3.26.** VT $^{13}$C chemical shift of BTA 2 as a function of temperature.

observed. Arguing by means of the $\gamma$-gauche effect, the conformational state of the chain changed from a predominant *trans*-character to a higher *gauche*-contribution.

Going into the details of the splitting, it should be clarified that it was not possible to elucitdate the complete side chain conformation (or its dynamics). This could only be achieved by elaborate NMR chemical shift calculations. Generally, the chemical shift is not only determined by the atoms in *gauche*-position. Among other impacts an important effect comes into play with the conformational state of the $\alpha$-atom[150], which is sometimes referred to as the *vicinal $\gamma$-gauche effect.* Moreover, VANDERHART found a variation of 1.3 ppm in all-*trans* alkanes depending on their crystal structure[151]. Nevertheless, it is possible to deduce conclusions about certain dihedral angles within the side chain. For example the signals of the inner carbon atom $C^1$ and the terminal position $C^7$ appeared as single lines, thus unique side chain conformations between $C^2$ and $C^3$ the outer end of the side chain could be assumed. Moreover, the non-split carbonyl line of BTA 2 (cf. Fig. 3.15 b)) indicated a single conformation between the ring and the side chain. As indicated by the split signal of the inner methyl group the *gauche*/*trans* states of the conformation are not equally populated in the different arms. The largest splitting was observed between the signals of the site $C^4$, in the centre of the side chain. Just above the transition temperature the splitting amounted to 3.4 ppm, rather close to the maximum $\gamma$-*gauche* effect. Moreover, the value was only due to a single $\gamma$-*gauche*-contribution of the carbon atom $C^1$ as indicated by the single resonance assigned to carbon atom $C^7$. Therefore, it could be deduced that the dihedral angle $C^1$, $C^2$, $C^3$, and $C^4$ has an almost pure *trans*-character in one chain, but an almost pure *gauche*-character in another. The in-between resonances were probably due to a more balanced contribution of both states.

This picture can be widened to the whole side chain, leading to the assumption that one of the three side chain arms (red) exhibited rather *trans*-conformation, whereas the other (purple) has highest *gauche*-conformations.

On raising the temperature, the carbon lines merged, yielding the spectrum depicted on top in figure 3.24. This behaviour has initially been interpreted as fast chemical exchange, hence a line shape analysis suggested itself in order to quantify the rates of the assumed averaging process. As it turned out, however, the line shapes could not be successfully fitted by means of a simple three-site exchange model[h)]. For this reason the merging of carbon lines upon heating rather indicated gradually approaching conformational statistics than a rotation of columnar sections.

### 3.2.9. 2D $^1$H-$^1$H DQ-SQ Correlation: *Proximity*

1D $^1$H DQF NMR provided information about the dipolar coupling state of the nuclei. From these measurements conclusions could be made on the rigidity of the material. The origin of the dipolar coupling, *i.e.*, the identification of dipolar coupled sites can generally be achieved by $^1$H-$^1$H DQ-SQ correlation spectroscopy. In the resulting 2D spectra the couplings are dispersed, along the double quantum dimension and sorted in accordance to the sum frequency of coupled sites. For designation of peaks the following convention is introduced, using parenthesis with the chemical shift along the single quantum dimension first followed by the shift of the double quantum dimension, *i.e.*, $(SQ, DQ)$. Consistently, couplings of like sites give rise to autocorrelation peaks, located on the diagonal and are denoted by a single pair of chemical shift values, whereas coupling between dislike sites cause pairs of off-diagonal cross-peaks, being denoted by two pairs of shift values. For a more detailed introduction to the interpretation of DQ-SQ correlation pattern see section 2.3.3.2.

In this section $^1$H-$^1$H DQ-SQ correlation pattern of BTA 3 is presented, since this compound provides a liquid-crystalline and a crystalline phase, which are both columnar as indicated by $^1$H MAS NMR and XRD measurements[123]. Moreover, it exhibits a sharp phase transition and consequently allowed the observation of a bulk phase without being

---

h) Three-site exchange in this aspect would involve the interchange between three conformations, which could in principle be triggered by a rotation of the column itself. This rotation thereby changes the environment of a side chain arm and the chain conformation (or the statistical distribution of chain conformations) adjusts accordingly.

at the risk of a material conversion during the experiment as in case of BTA 4. The experiment was conducted at two temperatures, *i.e.*, at 108 °C just below the phase transition temperature and at 146 °C above the transition.

For the pattern at 108 °C a DQ excitation time of 33.6 $\mu$s has been used. As indicated by figure 3.27 a) the side chain protons gave rise to a broad autocorrelation peak (yellow; 0.9 ppm, 1.8 ppm) of methyl and methylene protons. It appeared that the inner methyl group protons (connected to position 3) was more strongly coupled to the aryl protons, whereas the methine and methylene protons (probably position 2 and 3) were rather coupled to the amide protons, probably due to the packing of the chiral side chains. Interestingly, the distinct protons located at the inner methylene group (position 1) gave rise to an internal cross coupling of the high and the low-field shifted protons, indicated by the peaks at (2.7 ppm, 6.8 ppm) and (3.8 ppm, 6.8 ppm). Other main features of the pattern were due to the couplings of the backbone protons. The aryl proton was

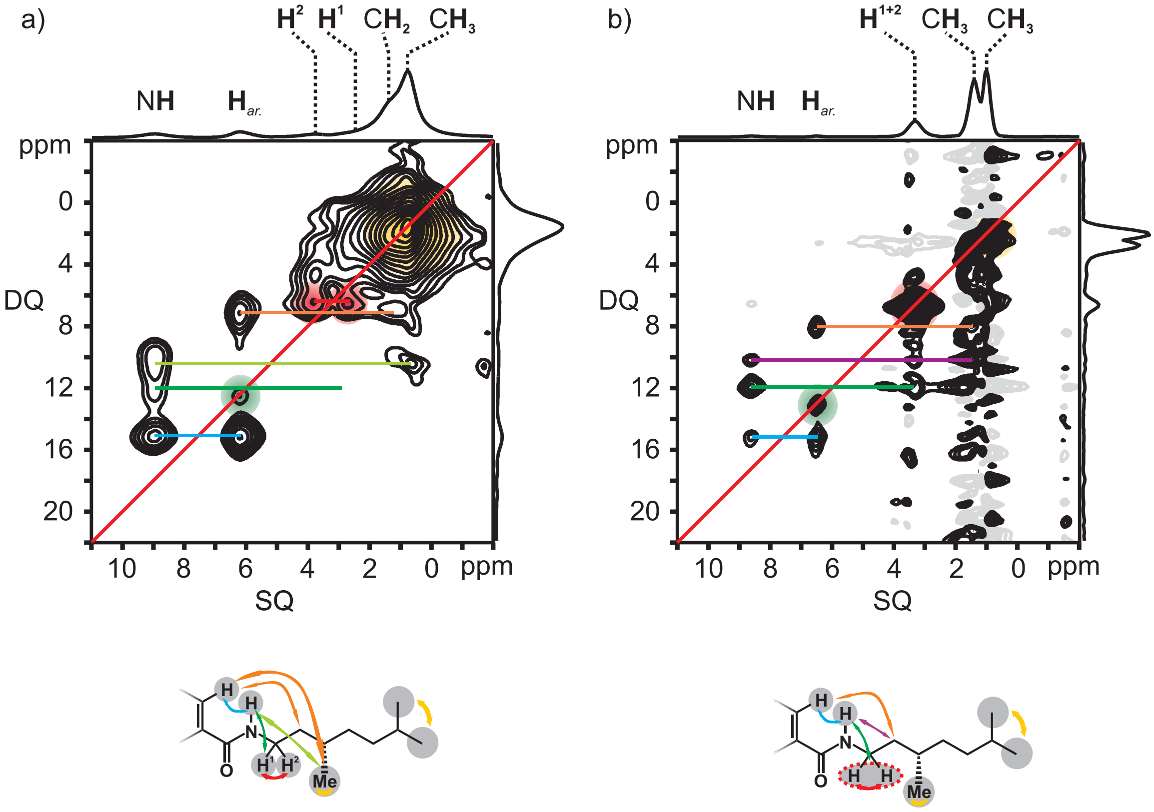

**Figure 3.27.** $^1$H-$^1$H DQ-SQ measurements of BTA 3. *a*) The spectrum was recorded at 108 °C with a recoupling time of 33.6 $\mu$s. *b*) The spectrum was recorded at 146 °C with a recoupling time of 134.4 $\mu$s.

coupled to both kinds of side chain protons (orange). At 108 °C, the amide proton signal was located at 9.0 ppm. It was dipolar coupled to the side chain (light green), to the aryl protons (blue) and to the high field proton of the $NCH_2$ group (green). Since a coherence was only established between one of the $NCH_2$ protons and the amide proton, it was assumed to be closer to the hydrogen bond. This assumption was consistent with its relative high-field shift, pointing to a more central position within the shielding cones of the adjacent molecules. The strong cross-peaks between the NH and the aryl protons were due to the proximity of both sites. The observation is in line with the short distances of 2.3 Å (intramolecular) and 2.9 Å (intermolecular) proposed by the crystal structure of BTA 1, serving as a general model for the columnar organisation of all investigated BTAs. The autopeak of aryl protons may have inter- as well as intramolecular origin since proton-proton distances are 4.2 and 4.0 Å, respectively.

The absence of auto peaks of the amide protons is in line with the crystal structure data, indicating a distance of more than 4.7 Å for these protons. This is clearly beyond the sensitivity range of DQ excitation by means of the back-to-back sequence.

At higher temperature BTA 3 was present in the thermotropic liquid-crystalline phase. As already indicated by the $^1$H DQF NMR spectra discussed in section 3.2.4.1 the material was clearly more mobile. In order to achieve a significant $^1$H-$^1$H DQ-SQ correlation pattern nonetheless, a four times longer DQ excitation time of 134.4 $\mu$s has been used yielding the pattern presented in figure 3.27 b). As can be seen in this figure, the side chain region from 4 to -2 ppm was massively affected by phase artefacts due to the very mobile side chains. A few minor differences compared to the correlation pattern of the low temperature phase could be found. The correlation of the amide proton and the methyl group was lost, although it was still coupled to the inner methylene protons of the side chain (purple). Another remarkable observation was the autocorrelation peak of the $NCH_2$ protons. Apparently, these protons were not distinguishable anymore, but still caused a significant DQF intensity. This indicated a restricted dynamics of the inner side chains leading to less distinct chemical shifts without a complete orientational averaging of the proton-proton vector. In this context, it should be noted that the double quantum filtered intensity of the $NCH_2$ protons in the high-temperature mesophase of BTA 3 was higher compared to BTA 4. This observation could be ascribed to the additional methyl group in case of BTA 3, resulting in a further restriction of the phase space of the side chain dynamics.

Conclusively, $^1$H-$^1$H DQ-SQ provided some insight into the organisation of BTA 3 in both phases. Remarkable was the distinct coupling of backbone protons to one of the $NCH_2$ protons, indicating a well-ordered arrangement and unique distance relations at low temperature.

Unfortunately, because of the high degree of symmetry within the material, the peaks could not be related to inter- intramolecular couplings. Thus, intermolecular distances could not be obtained. This is exemplified by the aryl auto peak observed in both DQ-SQ correlation pattern. The autocorrelation peak might have been due to four intermolecular couplings, as well as to two couplings across the ring, which is depicted in figure 3.28. In this manner, the high degree of symmetry impedes the investigation, in contrast to another kind of material being discussed in section 3.3.

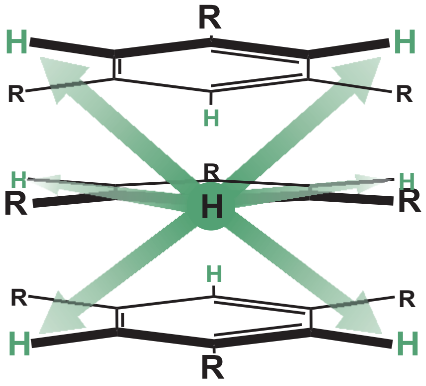

**Figure 3.28.** The illustration demonstrate the highly symmetric stacking of BTA 3.

## 3.2.10. Conclusion I

The peak assignment of $^{1}H$ MAS NMR spectra of the bulk BTAs was not straightforward as revealed by $^{1}H$-$^{13}C$ correlation spectroscopy. The amide proton of BTA 1 was found low-field shifted through hydrogen bonding by +1.9 ppm, whereas the aryl proton peak was located at 6.8 ppm, thus high-field shifted by -1.4 ppm. On the basis of CPMD simulations, the substantial high-field shift could be ascribed to the shielding effect of neighbouring molecules in the columnar stack. The characteristic shift can therefore, be related to the columnar organisation of the BTAs in general.

The thermal behaviour of the BTA 1 to 4 has been probed by DSC and VT $^{1}H$ MAS NMR measurements. The DSC curves of BTA 1, 2, and 3 showed a good agreement with reported phase transitions of these compounds, whereas the results on BTA 4 revealed a more complicated behaviour, indicating that the previous investigations on BTA 4 were incomplete.

In summary, $^{1}H$ NMR revealed an ordinary melting in case of BTA 1 upon heating. For BTA 2 a phase transition between two crystalline phases could be observed, which is related to a major change of side chain conformations as indicated by VT $^{13}C$ $\{^{1}H\}$ CP/MAS NMR. Even below the transition temperature and despite the high degree of organisation of the hydrogen-bonded scaffold, BTA 2 was affected by side chain dynamics. As a matter of fact, two slightly different side chain conformations were found, involving a different occupations of torsion states at the end of the alkyl chain, which might have been merely due to disorder within the crystal lattice. In the high temperature phase the three arms differed considerably in the middle side chain, leading to a remarkable complexity of the pattern above 60 °C. The distinct conformations could be assigned to different side chain arms by means of $^{13}$C-$^{13}$C through-bond correlation spectroscopy. The phase transition was probably related to a breaking of the $C_3$-symmetry in the high-temperature phase, being presumably related to the specific intercolumnar packing of the side chains.

For BTA 3 a transition between the crystalline low-temperature phase and the mesophase could be observed. For the low-temperature phase, the two $NCH_2$ protons of BTA 3 showed different chemical shifts, indicated by $^1$H-$^1$H DQ-SQ correlation spectroscopy. In the high-temperature phase a low but non-zero DQF intensity is in line with the reported liquid-crystallinity of the high temperature phase. The $NCH_2$ protons revealed only a single peak pointing to a higher mobility indeed, but, the location close to the ring apparently prevents full orientational averaging of the dipolar coupling between both sites. This pointed to a restricted dynamics of the inner side chains possibly due to the chiral methyl group in position 3.

Regarding BTA 4, $^1$H NMR revealed a rather complex phase behaviour explaining the ambiguous results found in literature on BTA 4. The different phases were examined by $^{13}$C NMR revealing a columnar mesophase, which is the only phase existing above 102 °C. Below this temperature the columnar organisation was found to persist in two metastable phases, *i.e.*, a supercooled columnar phase (10 °C to 102 °C) and a columnar low-temperature phase (below 10 °C). The stable phase at ambient conditions is obviously not columnar as indicated by the symmetry breaking of the backbone peaks observed by $^{13}$C $\{^1$H$\}$ CP/MAS NMR and by the absence of the high-field shift on the aryl proton peak in the $^1$H MAS NMR spectra, proven by $^1$H-$^{13}$C correlation spectroscopy. The resemblance of proton and carbon spectra of the compound with the methyl-capped compound BTA 5 strongly suggest a similar sheet-like arrangement, which could not be verified, though. In case of BTA 4 kinetic measurements have been carried out, tracing the phase transition from the supercooled mesophase to the non-columnar crystalline phase. The experiments discovered a strong temperature dependence of the conversion rate, however, the data did not allow to deduce a specific model.

The distinct behaviour of BTA 4 might relate to the space filling property of the linear alkyl chain. BTA 4 is the only linear chain BTA and it is also the only BTA with a non-columnar arrangement except for the much smaller BTA 5. In this sense it is very likely that the destabilisation of the column is induced by rapid liberation motions of the side chains, which would otherwise be hindered by the branched side chains of BTA 2 and 3.

## 3.3. Characterisation of an N-Centred BTA

After the detailed discussion of the effect of side chain modifications on the assembly of BTAs, it was obvious to raise the question how an inverted amide connectivity but otherwise similar molecule assembles in the solid state and how does such an assembly behave under identical conditions, *i.e.*, in the considered temperature range from -15 to 146 °C. Figure 3.29 shows the inverted analogue of BTA 3, namely, the molecular structure of BTAi. The compound has a similarly branched alkyl chain; however, it exhibits an inverted hydrogen-bonding motif. The amide nitrogen atom is directly attached to the ring, followed by the carbonyl group, which is now located between the nitrogen atom and the side chain. It should be noted that although the present molecule has a side chain similar to BTA 3, it contains one methylene group less per arm. In this respect the overall number of directly bound carbon atoms of each arm is the same, if the carbonyl atom of compound BTAi is taken into account.

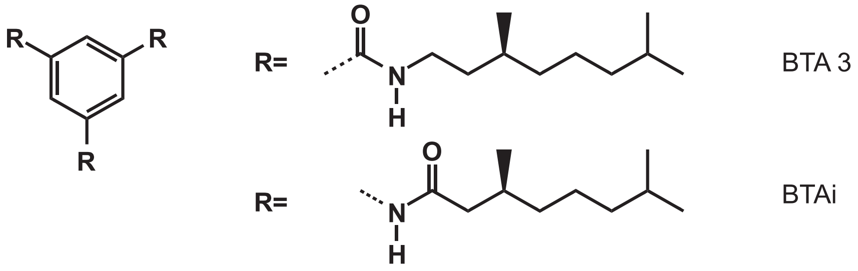

**Figure 3.29.** BTAi in comparison with the previously investigated compound BTA 3.

### 3.3.1. 1D Proton NMR Techniques

The thermal properties of BTAi had been probed by thermal analysis before. The previous DSC measurements had not indicated a phase transition, although a liquid crystalline phase had been found above ∼90 °C by POM measurements[152]. The absence of a phase transition point delimiting plastic crystalline properties at low temperature and the liquid-crystalline behaviour at higher temperature attached particular importance to the VT $^1$H NMR techniques.

#### 3.3.1.1. VT $^{1}$H MAS NMR

The compound BTAi has been investigated by VT $^{1}$H MAS NMR and VT $^{1}$H DQF NMR at various temperatures. Starting at 146 °C the temperature was successively lowered in steps of 10 °C down to a minimum temperature of -15 °C. The results are presented in figure 3.30. In good agreement with the non-inverted BTAs, two backbone peaks were observed at 8.9 and 5.7 ppm. The first signal could be assigned to the low-field shifted amide protons and the latter to the aryl protons on the basis of $^{1}$H-$^{13}$C HETCOR spectroscopy and by a supporting CPMD study (see sections 3.3.2 and 3.3.3, respectively).

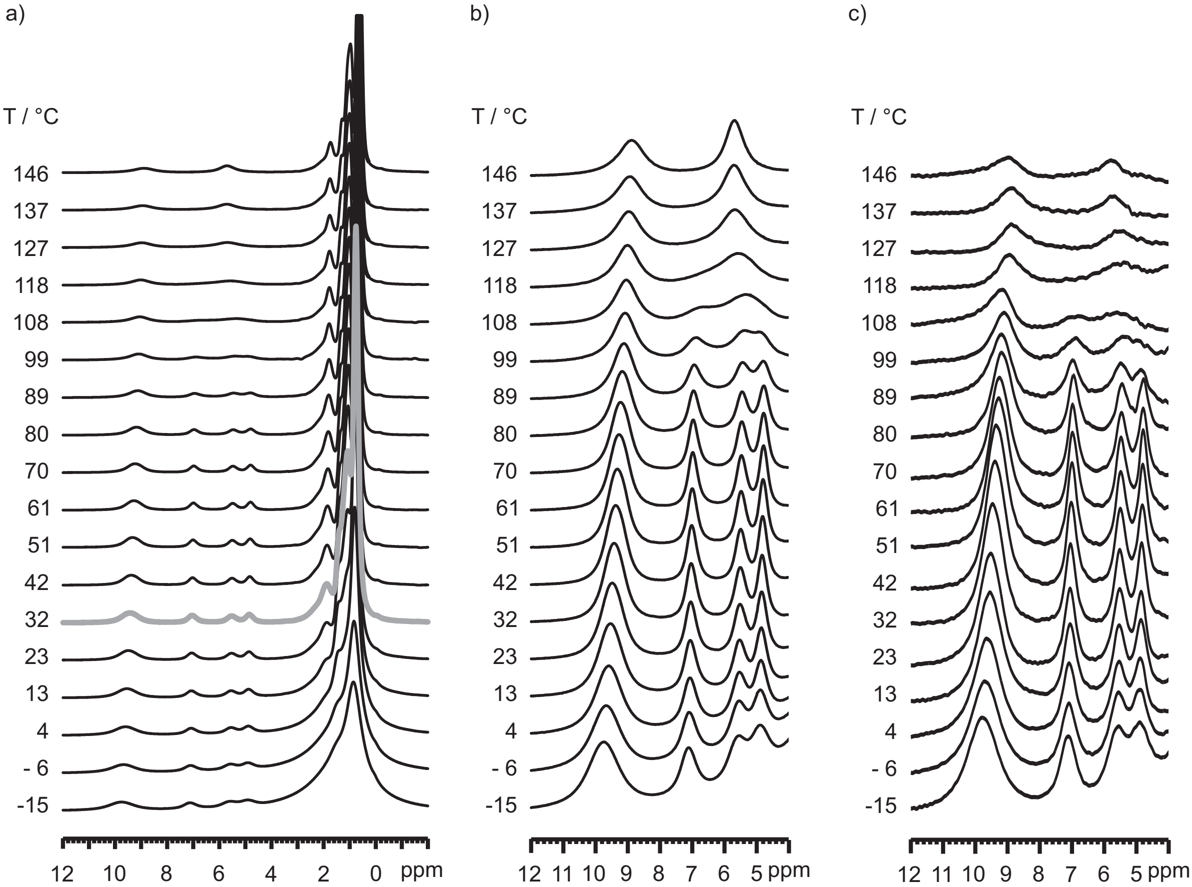

**Figure 3.30.** VT $^{1}$H NMR spectra of BTAi. *a*) VT $^{1}$H MAS NMR of BTAi. The overall range from 12 to -2 ppm. The spectrum at 32 °C is highlighted in grey. Below this temperature the side chain signals broaden. *b*) An 8 times enlarged illustration of the low field region of *a*) from 12 to 4 ppm. *c*) VT $^{1}$H DQF NMR of BTAi.

The value of 8.9 ppm indicated a moderate hydrogen bond, which is approximately as strong as found for the conventional carboxamide motif. The remarkable high-field shift was even slightly stronger, *i.e.*, 5.7 compared to 6.4 ppm in comparison to the analogue molecule BTA 3. Apart from the two backbone signals, side chain peaks could be assigned to a broad signal of the $COCH_2$ protons at 1.7 ppm, an intense peak of nine methyl protons at 0.6 ppm and two peaks arising from methine and methylene protons at 1.3 and 1.0 ppm. By lowering the temperature the NH proton resonance gradually shifted from 9.0 to 9.8 ppm at -15 °C, hence indicating a strengthening of intermolecular hydrogen bonds. The magnitude of this low-field shift was smaller compared to BTA 3, but it should be noted that BTA 3 exhibits a phase transition between both temperatures at which the chemical shift changed aprubtly by 0.8 ppm (1.4 ppm in total between 146 °C and -15 °C). The behaviour of the aryl proton peak is even more remarkable and clearly demonstrated the difference between BTAi and other non-inverted carboxamides. On cooling the sample, first a broadening of the aryl proton peak at 127 °C was observed. Further cooling led to a splitting of the aryl signal into three distinct resonances at 99 °C. At 80 °C, these three equally intense peaks reached a maximum dispersion and continued narrowing with decreasing temperature. At ambient conditions chemical shifts of the aryl proton resonances were determined as 7.1, 5.6 and 4.9 ppm with a line width of 260 Hz (FWHM). From first observation of the splitting of the CH resonance, all three peaks gradually shifted to lower field. Below room temperature, all peaks and in particular the signals of the side chains became notably broader and less resolved. This behaviour revealed a decrease of dynamics in the backbone region of the molecule without the occurrence of crystallisation point. Below 30 °C the side chain signals started broadening. Possibly this relates to the general decrease of the dynamics in the system, thus by cooling the system first the backbone began freezing, whereas the mobile side chains follow at a considerably lower temperature. In figure 3.30 c) VT $^1H$ DQF NMR spectra are shown which were recorded in the same temperature range as the single pulse spectra before. Because of strong artefacts in the side chain region the displayed spectrum was limited to the range between 12 and 4 ppm. The spectra show basically the same features. A loss of signal intensity of amide and aryl protons at higher temperature is observed, though. In this respect DQF experiments have turned out to be more sensitive to dynamic processes of an intermediate time scale compared to regular MAS experiments, since double quantum excitation and reconversion usually needs a minimum time of several 10 $\mu$s in which dynamic processes can diminish the efficiency of the double quantum excitation sequence. In simple MAS NMR experiments, the dynamic effects only apply during the acquisition time due to the excitation with a single pulse of a duration which is ideally close to zero. At 108 and 118 °C the signal almost seemed to disappear. A line shape analysis carried out afterwards (see section 3.3.6.2) indicated a correlation time of about 0.5 ms. The intensity drop in this region could not be attributed to an interference of the underlying dynamics with recoupling scheme, *i.e.*, the back-to-back sequence.

### 3.3.2. 2D $^{1}$H-$^{13}$C Correlation Spectroscopy

As yet, the assignment has been assumed to be similar to the assignment of the $^{1}$H MAS NMR spectra of the CO-centred BTAs. In order to confirm this assignment the results of $^{1}$H-$^{13}$C HETCOR spectroscopy will be presented in this section. The same method that has successfully been used to enable the assignment of compound BTA 1 was used here as well. Figure 3.31 shows a REPT-HSQC spectrum recorded with 33.6 $\mu$s recoupling time. Under these conditions only coherences between proton and carbon sites in close spatial proximity were observed and consequently only CH$_n$ groups of the side chain and the aryl CH group were detected. A split aryl correlation peak was located at 117.6 ppm in the carbon dimension, where the ternary aryl carbon was expected. The peaks provided proton chemical shifts of 4.4, 5.4, and 6.9 ppm in the proton dimension, which approximately corresponded to proton chemical shift obtained by $^{1}$H MAS NMR. In turn, the three proton resonances at 4.9, 5.5 and 7.1 ppm can unambiguously be assigned to the three distinct aryl proton sites.

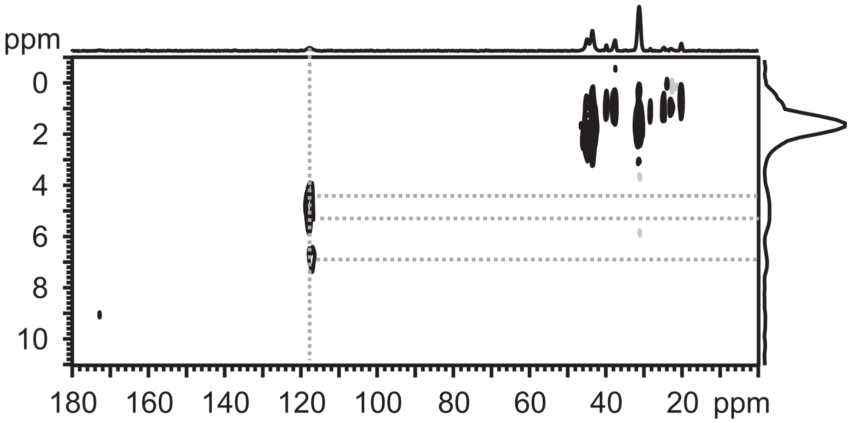

**Figure 3.31.** $^{1}$H-$^{13}$C REPT-HSQC of BTAi.

$^{1}$H MAS NMR spectra recorded below 70 °C showed chemical shifts of a rigid scaffold or at least a structure which was less affected by temperature induced dynamic processes.

The three aryl peaks were relatively narrow and corresponded to three well-defined, non-equivalent proton sites. The single proton resonance at high temperature in the liquid crystalline phase suggested a more symmetric columnar stacked arrangement or a dynamically averaged chemical shift. Remarkably, the signal in the liquid-crystalline phase was shifted to high field and all amide protons form hydrogen bonds. Furthermore, X-ray measurements of aligned samples suggested a columnar arrangement, which also demands $\pi$-facial stacking of molecules.

At this point a comparison with the CO-centred BTAs implied that their structures differ. On the one hand, a symmetric helical arrangement hardly matched the observation of three distinct aryl resonances. On the other hand, a non-symmetrical and non-columnar arrangement was lacking any explanation for the assessed considerable high-field shift of all aryl protons at the same time. In case of a non-columnar structure, a chemical shift similar to that for BTA 5 was expected, whose arrangement is proven sheet-like[127]. In consequence, a suitable model has to explain a columnar stacked packing in combination with distinct chemical shifts based on a cancelation of the $C_3$-symmetry of the molecules by means of their electronic environment.

The most likely structure is therefore a scaffold with a non-coplanar arrangement of adjacent rings but with a certain skew between them. Under these conditions not all aryl protons are located at equivalent positions of the upper and lower molecule's shielding cones, so that different chemical shifts can be expected. In case of BTAi the narrow line width already implied a high degree of intermolecular order and periodicity of the stack. For this reason, a model with molecules being slightly tilted with respect to each other was proposed, although $^1$H NMR did not provide any conclusions about the full complexity of this arrangement, *i.e.*, the number of molecules per repetition unit. Generally, two kinds of assemblies can be conceived. Firstly, the elementary unit may consist of two molecules: One molecule may bind to a tilted second molecule and the third is defined by translation of the first one along the columnar axis. Secondly, the split aryl proton signal could also be explained by a helical superstructure, *i.e.*, an envelope of the hydrogen-bonded scaffold, which is not straight columnar but bended around the columnar axis. The latter case does not involve a translational symmetry, but a screw operation transforms one molecule into another.

### 3.3.3. CPMD Study on the Assembly of BTAi

In this section the results of a CPMD study will be presented. Inspired by the CPMD simulation of BTA 1 in section 3.2.3.2 the probable arrangement of BTAi has been figured out. It should be noted that in order to enlighten the assembly within the column, BTAi had also been probed by 2D WAXS measurements on aligned samples[152]. In contrast to the high degree of organisation in the material found by solid-state NMR, the XRD pattern suggested a relatively low long-range organisation and it merely indicated a intercolumnar hexagonal arrangement with a columnar distance of 18.8 Å. At higher temperature around 160 °C an interdisc spacing of 3.5 Å could be deduced. The blurriness of the corresponding reflection at lower temperature causes speculations about the dynamics, which is elaborated in section 3.3.6.3. The partial failure of XRD at lower temperature, thus raises the importance of a supporting computational study.

The model compound used in the CPMD study was a benzene core equipped with NHCO-$CH_3$, *i.e.*, methyl groups instead of ($S$)-2,6-dimethylheptyl side chains. Prior to the simulation it had been assumed that the relocation of the NH group to the centred position at the benzene ring compared to the conventional CO-centred BTAs may have a vital effect on the symmetry of the assembly. The hydrogen bond has the same length as in CO-centred analogues, though, it is less symmetric with respect to the actual course of hydrogen bond $N\cdots H\cdots O$. In the CO-centred BTAs the donating nitrogen as well as the oxygen acceptor are not directly bound to the benzene ring, but to the carbonyl carbon atoms of adjacent BTA molecules. In case of the N-centred BTAs, however, the donor nitrogen is directly connected benzene ring, whereas the acceptor carbonyl group is separated from the ring. Therefore, BTAi lacks the perfectly matching triple-helical hydrogen bonding motif present in the CO-centred BTAs and are supposed to rearrange by a small tilt angle between stacked molecules. At first sight, it appeared reasonable to explain the remarkable splitting of the aryl proton lines in $^1H$ MAS NMR spectra with different shielding effects of the tilted molecules in the column.

However, as it turned out during the simulation, the conventional hydrogen bonding scheme following the crystal structure of BTA 1[117], (i.e., all three hydrogen bonds pointing in one direction) always led to a coplanar arrangement of adjacent rings, oriented perpendicular to the stacking axis. This arrangement would have yielded the same kind of $^1H$ MAS NMR spectra as found for the CO-centred BTAs revealing only a single aryl proton resonance. In turn, a much easier way to create non-equivalent aryl proton sites was to assume hydrogen bonds tending above and below the ring planes. Such an assembly with *antiparallel* hydrogen bonds, that is, with two carbonyl groups pointing downward and one pointing upward is given in in figure 3.32. That way, the perpendicular of the molecules in the stack exhibited a tilt of 6° with respect to the columnar axis.

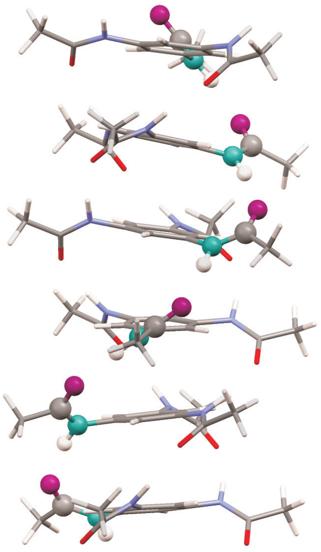

**Figure 3.32.** Stack of BTA molecules proposed by CPMD simulation. Capped stick representation of two parallel bonds: Nitrogen (*blue*), oxygen (*red*); Ball representation of hydrogen bonds pointing in the opposite direction: Nitrogen (*cyan*), oxygen (*purple*).

Obviously, the scaffold of BTAi derives from the CO-centred BTAs by rotating one of the three amide groups by 180°. The representation implies a helical chain of inverted hydrogen bonds. The CO-centred BTAs provided a quasi 6-fold screw symmetry. Due to their molecular $C_3$-symmetry and the coplanar arrangement every second molecule was equivalent at least in terms of the hydrogen-bonded backbone. In case of the N-centred BTAi the $C_3$-symmetry was broken by the conformation of the amide groups as well as by the tilt of the ring plane. The overall symmetry here reduced to the 6-fold screw axis leading to an asymmetric unit containing 6 molecules. A cell size of 21 Å corresponding to a sixfold of the interdisc distance of 3.5 Å led to full periodicity in columnar direction. The molecular stack has been formed by manual construction of a stack consisting of preoptimised molecules with dihedral angles between the benzene ring and NH-axis that allowed a proper formation of hydrogen bonds. It has first been optimised and subsequently heated to 150 K. Due to the substitution of the longer side chains by methyl groups the molecules exhibited a reduced moment of inertia which facilitated lateral sliding motions perpendicular to the stacking axis. Furthermore, since the columnar packing has not been considered, the assembly was lacking a bounding effect of the neighbouring column. Both aspects seemed to have a destabilising effect within the course of simulation. For this reason it was carried out at 150 K. After 1 ps of simulation time a copy of the simulated assembly was cooled to 0 K and a calculation of an NMR snapshot was performed. This procedure was repeated four times, thereby showing a significant convergence of molecular parameters and chemical shift values. The final structure and the NMR results of the snapshot obtained after 5 ps CPMD simulation at 150 K will be discussed in the following paragraph.

The length of the hydrogen bonds were very homogeneous for all different amide protons in the simulation, as indicated by the small standard deviation of the averaged symmetry equivalent $NH\cdots O$ bonds yielded 2.07 ± 0.02 Å, 2.03 ± 0.04 Å and 2.00 ± 0.02 Å for the three amide groups. The uniformity of the hydrogen bonds also manifested in the similarity of the chemical shift values of the three amide protons, which were determined as 10.1 ppm with almost no variation. The absolute values of the amide chemical shift, however, provided a quite large mismatch between the simulated chemical shift of 10.2 ppm and the observed shift of 9.5 ppm. Two reasons can be provided that may contribute to the mismatch. On the one hand, the short methyl group instead of the longer side chain may cause a low-field shift of approximately 0.2 ppm. On the other hand a deviation can be explained by the temperature dependence of hydrogen bonds and the temperature the simulation was conducted at. The simulation was performed at 150 K in contrast to the the experimental reference which has been recorded at 296 K. This argumentation is in line with the temperature dependent drift of amide resonances in the VT $^1$H MAS NMR spectra in figure 3.30, which showed a continuously rising chemical shift value of the amide proton resonance. By fitting the experimental $^1$H chemical shift of the amide protons by a second order polynomial and extrapolating it to 150 K a estimated chemical shift of 10.6 ppm was obtained[i)].

The agreement of CPMD results and experimental chemical shifts of the aryl proton sites provides a more significant way to estimate the reliability of the simulation, since these are split into distinct resonances. Results of simulated and experimental shifts are summarised in table 3.1. As it turned out, the protons could be separated into three groups having similar chemical shift depending on the position with respect to the antiparallel hydrogen bond. Moreover, the simulation revealed indeed a very good agreement between observed and simulated NMR parameters. The $^1$H aryl chemical shifts of 4.9, 5.5, and 7.1 ppm could be reproduced with a maximum mismatch of 0.3 ppm for aryl proton 3 ($C\mathbf{H}^3$).

It seems natural to ascribe the distinct chemical shifts to the shielding of the adjacent molecules in the ring as it readily explains the chemical shift of the aryl protons in the CO-centred BTAs (cf. section 3.2.3.2). However surprisingly, the major contribution to the additional chemical shift of the protons is not imposed by the shielding but rather

---

[i)] By using a linear fit, the extrapolation yielded a chemical shift value of 10.2 ppm, which exactly matched the simulated value, however, a curvature of the chemical shift over temperature was obvious. Therefore, a second order polynomial seemed more appropriate. The disagreement between the second order polynomial and the experimental value might be due to possible phase transitions of BTAi between 258 K and 150 K, which have not been considered.

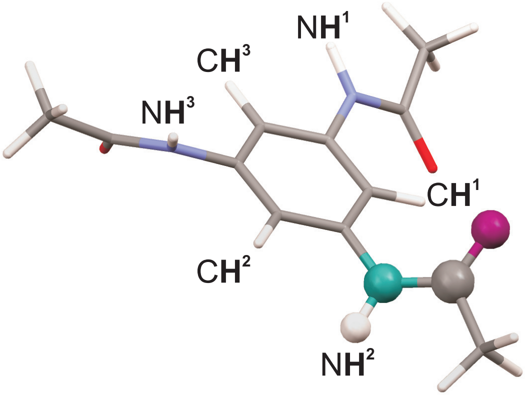

| | CPMD<br>(*sim.*) | bulk<br>(*obs.*) |
|---|---|---|
| $NH^1$ | 10.1 | **9.5** |
| $NH^2$ | 10.2 | (-) |
| $NH^3$ | 10.2 | (-) |
| $CH^1$ | 7.3 | **7.1** |
| $CH^2$ | 4.9 | **4.9** |
| $CH^3$ | 5.8 | **5.5** |

**Table 3.1.** Simulated chemical shifts of stacked BTAi.

the intramolecular electric polarisation effect generated by the amide group. This is best seen by means of a NICS map indicating the impact of two surrounding molecules on the interior molecule within a stack. The geometry of this approach is depicted in figure 3.33 a), whereas the actual affect on the aryl protons is better seen in the top view of figure 3.33 b).

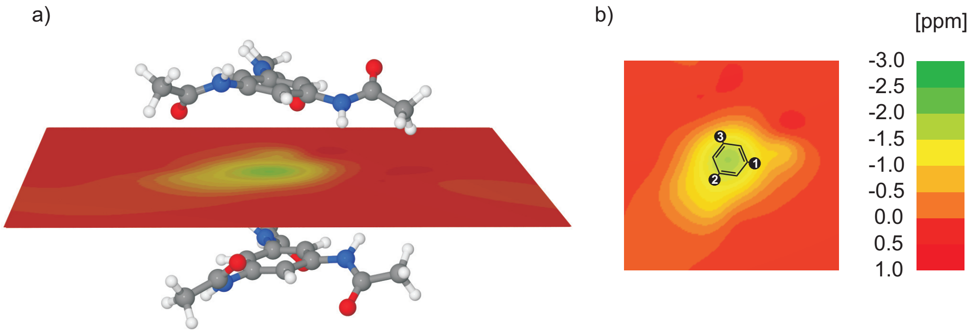

**Figure 3.33.** NICS maps of BTAi. *a*) Side view of two BTAi molecules oriented as in the stack. The third in-between molecule was omitted within the calculation and replaced by the NICS map at its appropriate position. *b*) Top view of a BTAi molecule with two CO-axes pointing towards the observer.

Two conclusion could be drawn from the NICS map. First of all, the shielding impact of adjacent molecules had about the same magnitude as for the CO-centred BTAs (cf. Fig. 3.9). Second, the given colour code implies a maximum splitting of the three aryl protons of about 0.5 ppm, which does not explain the observed dispersion of 2.2 ppm between the high and low-field shifted aryl signals. In contrast to the CO-centred BTAs, the experimental chemical shifts cannot completely be explained by the NICS map, i.e., the non-equivalence of the aryl protons is not due to an intermolecular shielding effect.

In order to elucidate the origin of the chemical shift and the wide splitting of the aryl signals, a stepwise approach of recreating the stack was conducted. In a first step the geometry of a single molecule was optimised and the chemical shifts were calculated subsequently. The next step towards the real stacking geometry in the bulk is a molecule with appropriate amide orientations. This was obtained from the optimised stack after the CPMD run. NMR parameters of this structure have been calculated without prior optimisation. All simulated values are summarised in table 3.2.

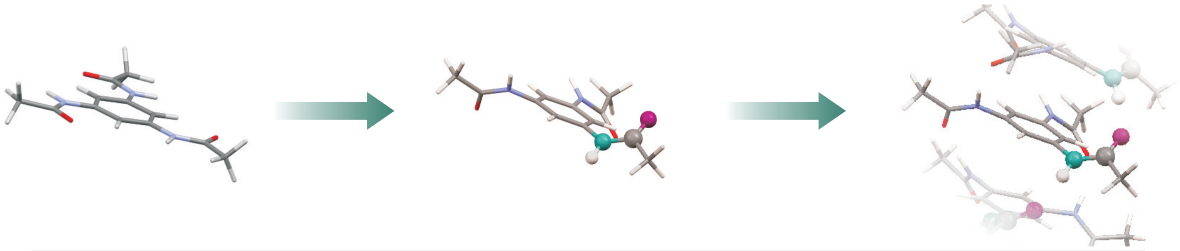

| | planar[a] (*sim.*) | solution (*obs.*) | pol.[b] | isolated[c] (*sim.*) | shield.[d] | CPMD[e] (*sim.*) | bulk (*obs.*) |
|---|---|---|---|---|---|---|---|
| N**H**$^1$ | 6.7 | 7.1 | (-) | 9.0 | +1.1 | 10.1 | **9.5** |
| N**H**$^2$ | (-) | (-) | (-) | 9.1 | +1.2 | 10.2 | (-) |
| N**H**$^3$ | (-) | (-) | (-) | 9.1 | +1.2 | 10.2 | (-) |
| C**H**$^1$ | 8.3 | 7.6 | +1.0 | 8.6 | −1.3 | 7.3 | **7.1** |
| C**H**$^2$ | (-) | (-) | −0.8 | 6.8 | −1.9 | 4.9 | **4.9** |
| C**H**$^3$ | (-) | (-) | −0.4 | 7.2 | −1.4 | 5.8 | **5.5** |

*a* Geometry optimised, $C_3$-symmetrical, planar molecule.

*b* The polarisation effect is calculated by subtracting the experimental chemical shifts obtained in solution from the simulated chemical shift values of the isolated monomer.

*c* The isolated molecule has the same conformation as in the stack.

*d* The shielding impact is calculated by subtracting the chemical shifts of the monomer (*sim.*) from the chemical shift values of a molecule within the stack.

*e* Cooled to 0 K after 5 ps of CPMD simulation at 150 K (see text).

**Table 3.2.** Intra- and intermolecular contribution to the chemical shift of aryl and amide protons

Apparently, the geometry of a single molecule itself causes the distinction of aryl protons rather than the neighbouring molecules in the stack. Thus, the distinct shifts of the aryl protons are intrinsically due to the conformation of the molecule and can be related to the environment of each aryl proton in particular. Taking, for example, the aryl resonance which was found most shifted to high field (C**H**$^2$), being located between the amide protons of a parallel and the antiparallel amide group. By comparison of the solution NMR shifts and the computational shifts of the monomer (isolated, *sim.*) a change of -0.8 ppm could be deduced being ascribed to the proximity of the two amide protons and an electrostatic polarisation effect imposed by it (cf. figure next to table 3.1). Accordingly, the least high-field shifted aryl proton (C**H**$^1$) was located between two carbonyl groups in a distance of about 2.5 Å from the oxygen atom, which imposes an opposite polarisation effect giving rise to a low-field shift of about +1.0 ppm. This shift is, however, overcompensated by the shielding impact of -1.3 ppm due to neighbouring molecules in the stack. This explains the small high-field shift of this proton of only -0.3 ppm between solution and bulk NMR data.

It should be noticed that for the amide protons a reliable polarisation effect could not be obtained, since the chemical shifts of these protons were calculated on the basis of a BTAi molecules within the hydrogen-bonded assembly. Without further optimisation, the NH bond length did not correspond to that in a free BTAi molecule explaining the low-field shift of around 2.3 ppm without an actual hydrogen bond being present. Moreover, the calculated chemical shift of the optimised, planar, and $C_3$-symmetrical structure revealed a severe mismatch of 0.7 ppm to the measured shifts in solution. Presumably, the impact of the close oxygen atoms becomes significant in the flat arrangement, thereby pointing to an average conformation in solution departing from the full planar geometry. The polarisation was therefore calculated by subtracting experimental chemical shift values obtained in solution an the calculated values of the monomer with the appropriate geometry.

To conclude, it can be assumed that the good agreement between observed and simulated chemical shifts clearly confirms the proposed antiparallel arrangement.

### 3.3.4. VT $^{13}$C {$^{1}$H} CP/MAS NMR

For the CO-centred BTAs, $^{13}$C MAS NMR proved beneficial in that it directly assesses the degree of symmetry of an assembly. Therefore, $^{13}$C $^{1}$H CP/MAS spectra have been recorded at four different temperatures (see Fig. 3.34). Compared to non-inverted BTAs the sensitivity was further reduced by a broad line shape of the three backbone signals leading to a low signal to noise ratio. At 10 °C the carbonyl, the quaternary carbon and the CH carbon resonances were located at 172.4, 136.9, and 117.5 ppm, having line widths of about 400, 300, and 600 Hz respectively. The latter value corresponded to 2.8 ppm at a Larmor frequency of 213.8 MHz. The greater line width can partially be explained by electronic effects of neighbouring molecules, which already led to a separation of the aryl proton signals of 2.2 ppm (see section 3.3.1.1). However, it has to be noted that the onset of separated peaks would have been seen, albeit strongly overlapping, if the line width of the distinct sites had been of the same size as for the analogue compound BTA 3 (130 Hz). The broad backbone resonances of BTAi may therefore indicate either disordered local packing or dynamic processes. At 10 °C the $^{13}$C signals of the side chains were very broad, apart from the narrow signal at 23.5 ppm arising from the terminal methyl groups. On heating the sample, the intensity of the backbone signals at 51 °C decreased compared to those at 10 °C and the carbon resonances of the side chains narrowed considerably. The latter might be attributed to faster dynamics of the side chains in this region. The line width of the backbone signals did not change significantly. The signal of the carbon site next to the carbonyl group split into two signals at 45.3 and 43.9 ppm with a low intensity. These two signals were much better resolved at 99 °C. The gain of intensity for this signal and peaks of the side chain region could be attributed to molecular motion, *i.e.*, the backbone was in the slow dynamic regime, whereas the side chains were in a state of higher mobility, thus better resolved. This observation is therefore in line with the broadening of side chains in VT $^{1}$H MAS NMR spectra below 30 °C. At the highest measured temperature (T=118 °C), the CP/MAS spectrum showed a merging of the two signals of the inner side chain positions and was therefore again consistent with $^{1}$H MAS NMR, which showed the same for the aryl protons at a similar temperature. The disappearance of all backbone peaks at this temperature was quite remarkable. It seems that at these conditions the dynamics of the inner core enter the timescale of the MAS frequency, which had been seen before for the carbon signal of the inner methylene group. In order to rule out a failure of the CP at 118 °C, the spectrum was recorded

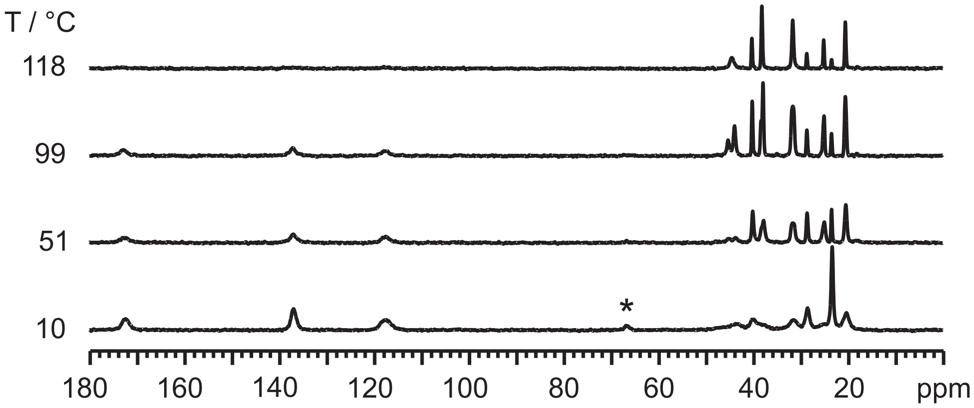

**Figure 3.34.** VT $^{13}$C {$^{1}$H} CP/MAS spectra of BTAi.

using SPE. The resulting spectrum was likewise affected by a tremendous loss of signal intensity in the backbone region. In this manner the $^{13}$C NMR supports the assumption of a temperature dependent dynamics of the whole molecule, which leads to a gradual increasing mobility during heating of the material.

### 3.3.5. $^{1}$H-$^{1}$H DQ-SQ Correlation Spectroscopy

In order to probe spatial proximities between protons of BTAi $^{1}$H-$^{1}$H DQ-SQ correlation spectroscopy was applied. Figure 3.35 a shows an $^{1}$H-$^{1}$H DQ-SQ correlation pattern measured at 47 °C with a double quantum excitation time of 33.6 $\mu$s. As already described in the discussion of the DQF spectra in section 3.3.1.1, the side chain signals were affected by strong artefacts that prevented elucidation of dynamic information from these peaks. For this reason, the right part of the spectrum below 4 ppm was not considered and dropped for clarity. The colour code used for the couplings in the pattern is illustrated in figure 3.35 b. For the sake of simplicity only intramolecular couplings are shown. Some of these couplings might be due to intra- as well as intermolecular couplings, which could not be distinguished in most cases.

The broad NH signals (9.2 ppm, 9.8 ppm)[j] arose from couplings between the amide protons with the closest side chain groups, *i.e.*, the inner methyl group (light green, only seen as a shoulder) and methylene protons next to the carbonyl (9.2 ppm, 10.6 ppm; dark green). Three very intense pairs of cross-peaks resulted from couplings of the amide protons and the aryl protons (blue). The dispersion of the three resonances into a double quantum dimension was advantageous since it revealed certain differences of the amide protons. They showed up as small chemical shift differences in the single quantum dimension, which would have remained undiscovered in simple one dimensional NMR spectroscopy. The magnitude of these variations, however, was very small. Obviously the hydrogen bonds are rather uniform, which is in line with results of the CPMD simulation.

Another group of cross-peaks arose from the three aryl proton sites, which were coupled to both spectrally resolved side chain groups. Couplings between aryl protons and methyl protons are depicted in yellow in figure 3.35 b, couplings of aryl protons and the inner methylene group in orange. The coherence at low field (orange; 6.8 ppm, 8.5 ppm) was quite remarkable, since it was obviously larger than the two other coherences at higher filed. This can be related to the closer proximity of the corresponding proton (being low-

---

[j] Note the convention (*SQ*, *DQ*).

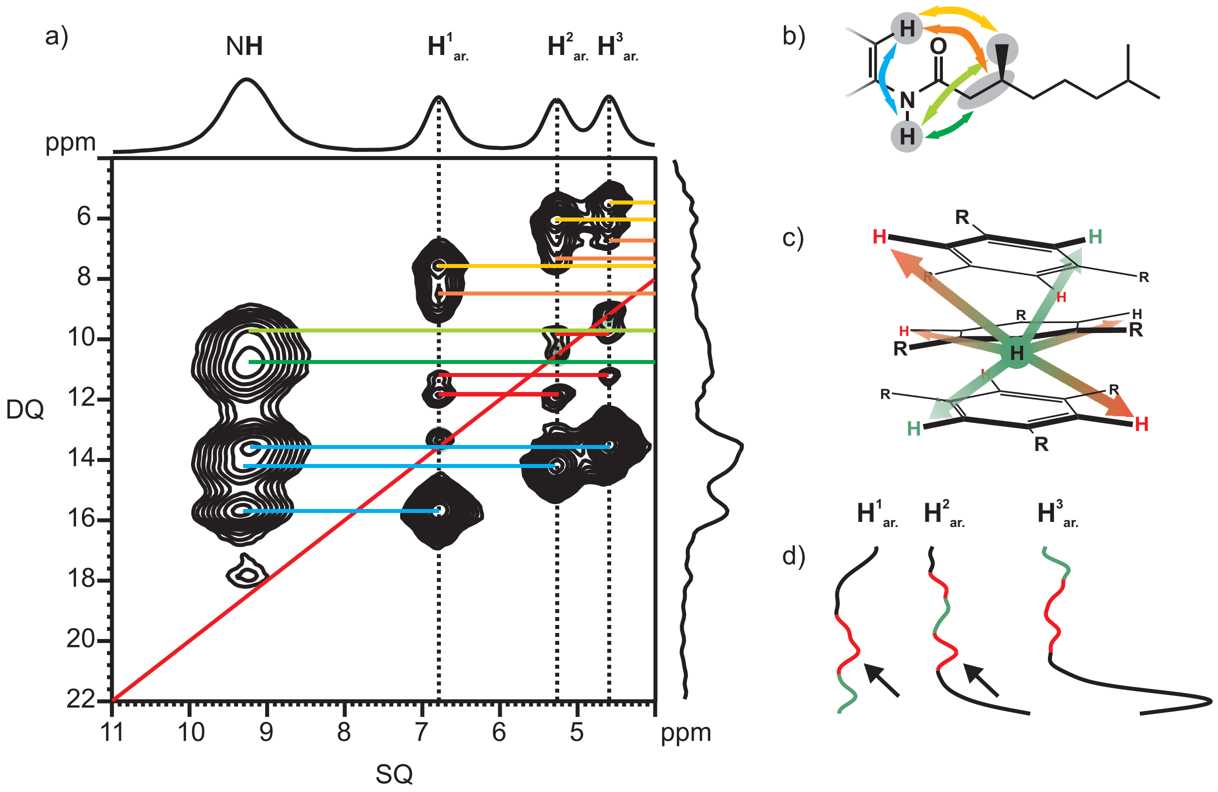

**Figure 3.35.** *a*) $^1$H-$^1$H DQ-SQ correlation pattern of BTAi recorded at 55 °C. *b*) Illustration of dipolar couplings and the colour code corresponding to the horizontal lines in *a*). For simplicity, only possible intramolecular couplings are shown. *c*) Illustration of possible dipolar couplings between aryl protons. *d*) Projections of the aryl resonances along the DQ dimension (dotted lines in *a*)). Autopeaks are coloured turquoise; off-diagonal peaks are shown in red. The peaks corresponding to the strongest cross coupling are marked with arrows.

field shifted) to the methylene group of the upper molecule[k]. Due to the tilt of the ring plane this aryl proton is located closer to the methylene group compared to the average intermolecular Ar-**H**$\cdots$CHR distance. It should be noted that intramolecular couplings contributed to the intensity of these peaks as well. However, the extra intensity of the discussed cross-coupling was more likely attributed to the relative orientation of molecules in the column, since the intramolecular Ar-**H**$\cdots$CHR turned out to be rather constant in the simulation.

A different situation held for the internal couplings of the aryl protons, which are exemplified in figure 3.35 c). Since all three aryl protons of the rings were supposed to have different chemical shifts, all autopeaks (turquoise, on the diagonal in Fig. 3.35) must have

---

[k] "Upper" refers to the molecule in direction of the CO-axis of the antiparallel amide group, *i.e.*, top of figure 3.32.

been due to intermolecular couplings. Interestingly, all these couplings showed a similar intensity, whereas the corresponding cross-peaks revealed specific intensity differences. The amplitudes of these peaks are best compared by regarding the three slices along the double quantum dimension given in figure 3.35 d). The very similar intensities of the autopeaks are apparently due to very similar distances of symmetry-equivalent protons within the simulated stack as indicated by the small standard deviation of their averaged distance (*i.e.*, by averaging all 18 intermolecular distances 4.30 ± 0.10 Å were determined with almost no difference between the three distinct groups of protons).

Cross-peaks (red) can have inter- as well as intramolecular origin. Intramolecular couplings would be due double quantum coherence between protons separated by about 4.32 Å. Since the intramolecular coupling between the protons would operate across the ring and due to the large distance the intensity of the corresponding coherences was expected to be rather weak. A certain contribution to the observed intensity of the cross-peaks could not be excluded, though. For this reason only the *relative* intensities of the cross-peaks were a significant source of information, since those can be influenced only by intermolecular couplings. The two arrows in figure 3.35 d) indicated the strongest cross coupling found among the aryl protons. It was due to dipolar interactions between the most low field and the intermediate proton. For the latter, the shortest distance to a low-field shifted proton was 3.83 ± 0.05 Å on average[l)], whereas the high field proton was more remote, *i.e.*, 4.68 ± 0.14 Å on average[m)]. The intense cross coupling is therefore another indicator of the helically tilted structure.

In conclusion it need to be said that a very close comparison of proximities deduced from a $^1$H-$^1$H DQ-SQ correlation pattern in many ways corroborates the antiparallel hydrogen bond configuration proposed by the supporting CPMD simulation.

### 3.3.6. Dynamics of BTAi

#### 3.3.6.1. $^1$H Exchange Spectroscopy

The ultimate proof that the single aryl proton line at higher temperature was due to motional averaging, could be provided by 2D Exchange Spectroscopy. In this experiment the exchange process was indicated by the occurrence of cross-peaks between the three presumably exchanging aryl proton sites. The temperature at which this experiment was carried out was chosen to be 100 °C and a short mixing time of 3 ms was used. At this

---

[l)] to the lower molecule according to the orientation in figure 3.32

[m)] to the upper molecule according to the orientation in figure 3.32

temperature the lines were already slightly broadened but still separated as can be seen in VT $^1$H MAS NMR spectra in figure 3.30. The results of the exchange experiments are presented in figure 3.36.

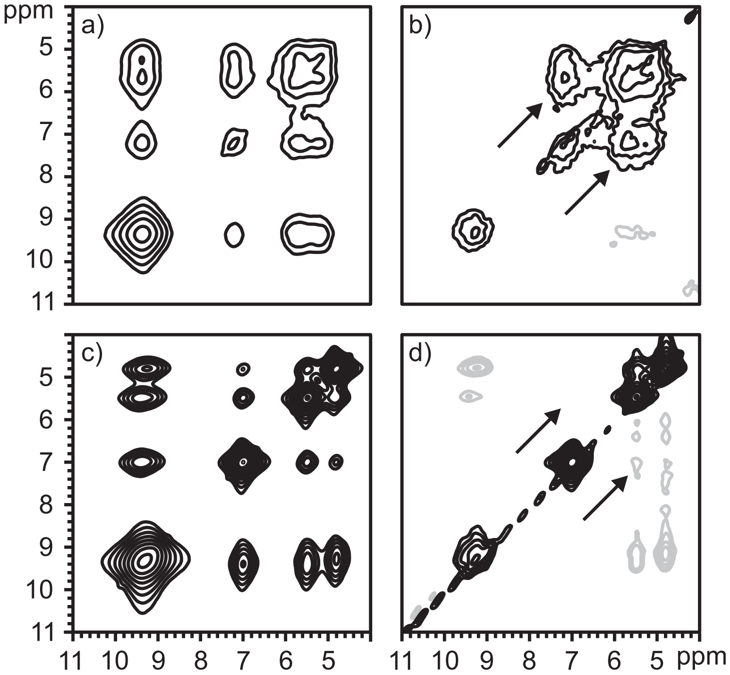

**Figure 3.36.** $^1$H NOESY NMR experiments with a mixing time of 3 ms. The experiments were recorded *a)* at 100 °C, *b)* at 100 °C with PMLG decoupling, *c)* at 55 °C and *d)* at 55 °C with PMLG decoupling.

In case of carbon sites such an experiment would directly probe exchange processes. However, since protons are affected by fast and efficient spin diffusion, cross-peaks may originate from exchange phenomena as well as from dipolar couplings between the sites. This problem is clearly encountered in figure 3.36 a), in which cross-peaks between all resolved sites are shown in the considered region. For the cross-peaks of aryl and amide protons exchange could certainly be excluded, thus the peaks originated from polarisation transfer via spin diffusion or fast cross relaxation. To avoid these ambiguities, a modified exchange experiment was performed under otherwise identical conditions. Figure 3.36 b) shows the outcome of a EXCY experiment with application of PMLG decoupling during the mixing time (see section 2.2.6.2 for details). This homonuclear decoupling sequence effectively suppressed spin diffusion and cross relaxation between protons and therefore allowed an identification of cross-peaks resulting from chemical exchange processes. Cross-peaks of amide and aryl protons were prevented, whereas those of aryl protons were still present, thus unambiguously indicating chemical exchange between these sites.

To validate the method, both experiments have been repeated at 55 °C. The result of the usual EXCY experiment is depicted in figure 3.36 c) showing basically the same pattern as given in figure 3.36 a). All peaks, especially aryl proton peaks, were better resolved, since the lines were sharper at lower temperature. By application of PMLG decoupling during the mixing time all cross-peaks were suppressed as seen in figure 3.36 d). This time the suppression also held for the aryl sites, which were not yet affected by chemical exchange, in contrast to the experiments at higher temperature.

#### 3.3.6.2. Activation Energy of the Averaging Process

Since the averaging process occurred slowly and over a relatively wide temperature range, it was possible to examine the dynamics of BTAi by lineshape analysis. The line shape was simulated according to the extended Bloch equations given on *p.* 215 in reference [13]. The time evolution of the initial transverse magnetisation is given by the *dynamic matrix* $\mathbf{L}^+$:

$$\mathbf{L}^+ = i\mathbf{\Omega} - \mathbf{\Lambda} + \mathbf{K} \tag{3.1}$$

In this equation the diagonal matrices $\mathbf{\Omega}$ and $\mathbf{\Lambda}$ contain the chemical shifts and the transverse relaxation rates $1/T_2$, respectively. The kinetic matrix $\mathbf{K}$ takes into account the effects of chemical exchange between the sites. The magnetisation at a time $t_1$ can be calculated by means of the initial magnetisation and the eigenvalues of the dynamic matrix:

$$\mathrm{M}^+_{t1} = e^{diag(\mathbf{L}^+)\cdot t_1}\mathrm{M}^+_0 \tag{3.2}$$

Diagonalisation and subsequent Fourier transformation then leads to the simulated frequency domain, in this case to the spectrum of the three proton sites $\mathrm{H}^1$, $\mathrm{H}^2$, and $\mathrm{H}^3$.

The simulation required knowledge about static chemical shifts of the three protons and the apparent $\mathrm{T}_2$ relaxation time, that is, the line width' of the aryl signals. The values were obtained by decomposing the spectrum using the program DMFIT[153] and subsequent averaging of the $\mathrm{T}_2$ relaxation times of the aryl protons. After the initial setup, the aryl part of the $^1$H MAS NMR spectrum was simulated as a function of the rate constant $k$ of the averaging process.

Plotting of $ln(k)$ *vs.* $\mathrm{T}^{-1}$ allowed to deduce an activation energy by assumption of a simple Arrhenius law describing the temperature dependence. Figure 3.37 shows the result of the fit, yielding an activation energy of 82.9 kJ mol$^{-1}$.

It needs to be clarified here that the simulation has been done in a qualitative way only, *i.e.*, by a visual comparison of simulated and experimental line shapes. In this manner, the error bars given in figure 3.37 were defined by upper or lower limiting values, which clearly over- or underestimated $k$. Thus, the errors are not based on a statistical approach and have consequently not been used as weighting factors in the fit. As indicated by the size of the error bars, the line shape simulation was more precise at high temperature, since the impact on the line shape was more pronounced when the correlation time of the motion gets closer to the timescale of the experiment.

### 3.3.6.3. An Extended Model of Dynamics

The different BTA motifs, either the CO-centred or the N-centred can apparently be associated with parallel or tilted helical stacking of benzene rings, respectively. As indicated by $^1$H MAS NMR the distinction of the aryl protons caused by the polarisation impact of the amide groups was gradually cancelled by raising the temperature, evidently due to motional averaging. An appropriate dynamics leading to this kind of averaging, would involve a rotation of amide groups in the column, which can be seen as a permutation of parallel and antiparallel hydrogen bonds. If this occurs on the time scale comparable to the MAS frequency, the merging of aryl resonances is observed as presented in section 3.3.1.1.

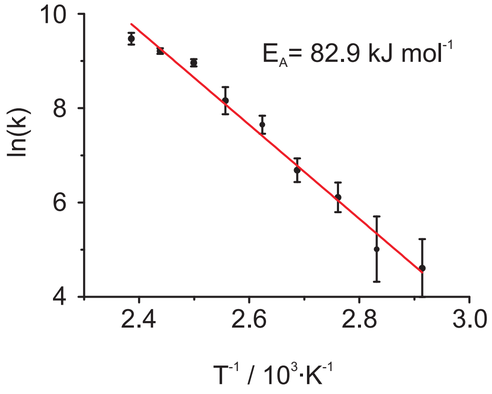

**Figure 3.37.** ARRHENIUS-plot based on simulated rate constants, extracted from line shape analysis of $^1$H MAS NMR spectra of BTAi. The fit yielded an activation energy of 82.9 ± 3.9 kJ mol$^{-1}$. The errors bars have not been included to the fit. See text for explanation.

A little discrepancy arises, however, due to the observation of reflections indicative of a parallel orientation of benzene rings at higher temperature. In NMR the motional averaging occurs, when the dynamics enters the times scale of the underlying experiment, which is the MAS frequency in case of $^1$H MAS NMR. For XRD techniques this kind of averaging is not possible, since even fast motion rather leads to diffuse reflections. Assuming the material in the antiparallel bonded state, the discs would therefore not enable the observations of X-ray reflections.

For this reason a slightly extended model is proposed in this paragraph considering two kinds of hydrogen bond configurations. At ambient conditions most molecules are predominately found in their antiparallel configuration, since this leads to the more stable assembly. The model assumes, however, a certain fraction of molecules in the columnar rod occupying the parallel bonding scheme, *i.e.*, segments within the column with hydrogen bonds pointing in only one direction.

At elevated temperature the column will break apart and reform again under dynamic conditions. Here, although it is assumed to be less stable and definitely inappropriate for describing the $^1$H MAS NMR pattern at ambient temperatures, the parallel arrangement is kinetically favourable since it is less demanding with respect to the recombination of columnar sections. A rotation of a columnar segment by about 120° along the columnar axis, for example, would leave the parallel bonded BTA pair unaffected, whereas for the antiparallel arrangement the recombination was hindered by the non-matching donor-acceptor pairs. This way, the antiparallel configuration would promote the separation of the two sections and lead to destabilisation of the system.

In this sense, it might be argued that the equilibrium between both arrangements shifts in favour of the parallel arrangement because it has the superior motif under dynamic conditions involving fast breaking and forming of hydrogen bonds. Since the parallel bonding implies also a parallel coplanar arrangement of the rings, the rearrangement would indirectly explain the high intensity of the X-ray reflection corresponding to the interdisc distance.

### 3.3.7. Conclusion II

The N-centred compound BTAi revealed several striking differences compared to the previously covered CO-centred counterparts. Although the organisation was obviously columnar, which was shown by $^1$H-$^{13}$C correlation spectroscopy and in line with X-ray results of a previous study, the assembly lacked certain symmetry properties contraray to BTA 1 to 4. At room temperature the cancellation of the $C_3$-symmetry was evident by the observation of split aryl proton resonance whose origin was revealed by a supporting CPMD simulation study. The results of the study showed a very good agreement with the experimental $^1$H chemical shifts obtained by $^1$H MAS NMR. It appeared that the distinct chemical shifts of the aryl protons could be explained by a deviant hydrogen bonding scheme in case of the N-centred BTAi. Compared to the CO-centred BTAs, one amide group is supposed to be rotated by 180°, thus giving rise to an antiparallel hydrogen bond which leads to a tilt of the ring normal by 6° off the columnar axis. Moreover, CPMD results demonstrated that the distinct chemical shifts of the amide protons can not be ascribed to a shielding effect of the adjacent molecules within the stack. Rather an intramolecular polarisation effect imposed by the amide groups caused the distinctiveness of chemical shifts. The proposed assembly was supported by $^1$H-$^1$H DQ-SQ correlation spectroscopy providing manifest evidence of a tilted ring plane in the columnar assembly of BTAi.

Solid-state NMR also facilitated insight into the dynamics of BTAi. At ambient conditions the side chains revealed an increasing mobility indicated by a changing line width in $^{1}$H MAS NMR spectra. On raising the temperature, the dynamics was transferred to the inner scaffold of the column, which is consistent with broadenings observed for VT $^{13}$C $\{^{1}$H$\}$ CP/MAS NMR spectra. The most striking observation upon heating the material, however, was the merging of the three distinct aryl resonances in the $^{1}$H MAS NMR spectra above 80 °C. Exchange spectroscopy has been used to prove motional averaging of aryl protons and consequently a fast permutation of parallel and antiparallel hydrogen bonds. A line shape analysis of the VT $^{1}$H MAS NMR spectra allowed to deduce an activation energy of $82.9 \pm 3.9$ kJ mol$^{-1}$ of the corresponding process, which is not only in accordance with NMR derived activation energies in other columnar systems[154], but also agrees with $\beta$-relaxation processes determined for CO-centred BTAs. This kind of dynamics involves a 180° rotation of single amide groups of the BTA molecules within the columnar assembly, hence matches the proposed the dynamics for BTAi. In a recent study on C6 and C10 homologues of BTA 4, activation energies of 92 kJ mol$^{-1}$ and 59 kJ mol$^{-1}$, respectively, could be deduced upon electric field stimulation[144].

Reported X-ray results might be interpreted in this context as a parallelisation of benzene rings at higher temperature. If this applies, the determined activation energy can be related to an energy barrier of a rectification of the hydrogen bonds, which may point in one direction at higher temperature. This assumption should be investigated in a prospective detailed X-ray investigation, which is, however, beyond the scope of this work.

# 4. Organisation of an Octa-substituted Phthalocyanine

## 4.1. Introduction to Phthalocyanines

The discovery of phthalocyanine (Pc) was made more than 100 years ago[155]. The molecular connectivity was elucidated by LINSTEAD and DENT in 1934[156] without using diffraction techniques, whereas the first X-ray crystal structure by ROBERTSON was published in 1936[157]. It was shown that the metal-free phthalocyanine exhibits a planar ring structure. Moreover, it was recognised as apparently not completely tetragonal, but one side is longer than the other, depending on the position of the protons inside the core[158] (see figure 4.1) and the crystal packing[159]. All phthalocyanines have a very high extinction coefficient assigned to strong $\pi$-$\pi$-transitions, called Q-band, leading to the blue-green colour of these materials. The common metal-free phthalocyanine ($H_2Pc$) has a $D_{2h}$ symmetry and a split Q-band due to two non-degenerate LUMOs in contrast to higher symmetric, metal containing phthalocyanines. Today, more than 70 elements are known that can be placed inside a phthalocyanine ring[160], mostly leading to $D_{4h}$ symmetry, *e.g.*, CuPc. The first scientists who performed research on phthalocyanines were amazed by the extraordinary stability of the compound and its manifold derivatives. The long-lived absorption explains the use of phthalocyanines as colourants in textile and packaging industry as well as for ink jet printing[161]. More research is done on phthalocyanines regarding their recent applications as catalysts[162] and chemical sensors[163].

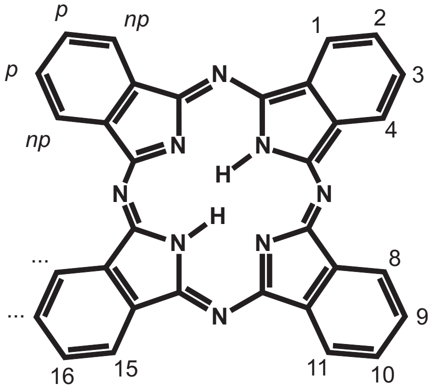

**Figure 4.1.** Structure of general metal-free $H_2Pc$ with a numbering of carbon atoms and the designations ($p$=peripheral, $np$=non-peripheral) used to specify the position.

Phthalocyanines can be categorised, depending on their structure (planar or not) or by the type of ion they accommodate inside the ring. There are many different solid-state arrangements of the planar phthalocyanine, however, three major crystal structures are most important: First of all, the $\beta$-form which belongs to the space group $P2_1/a$ with 2 molecules per unit cell. This structure is known as the thermodynamicly stable form of $H_2Pc$ and most Pcs containing transition metal ions. The bulk organisation can be imagined as a herringbone arrangement, with molecules tilted by an angle of about 45° with respect to the crystallographic $b$-axis[164a)]. The second structure is the so-called $\alpha$-form, whose X-ray validation was achieved much later[165]. The major difference with respect to the $\beta$-form is a smaller tilt angle of about 30°. It has the space group $C2/c$ and consists of four molecules per unit cell. An example of this form is the popular blue-green pigment CuPc. The third important modification is termed the X-form and was investigated intensively for its high photosensitivity which explaining its importance for xerographic applications (*e.g.*, photocopiers)[166]. It can be produced by mechanic grinding of the $\alpha$-form, but despite the enormous industrial use of this modification a reliable X-ray structure was not published before 1996[167]. It should be noted, that many phthalocyanines are polymorphous materials, thus occupy more than one crystal structure. Many other structures of minor importance can be found, described mainly in patent literature[168]. In particular discotic liquid crystalline materials have been investigated, which will be briefly introduced in the next section.

## 4.2. Liquid-Crystallinity of Phthalocyanines

Octaalkyl-substituted Pcs are of special interest because of their columnar liquid-crystalline properties. The mesogenicity of alkyl-substituted phthalocyanines was first demonstrated by PIECHOCKEI and SIMON in 1982[169] on the basis of the copper-containing compound CuPc-*op*-C1-O-C12[b)]. Unfortunately, these materials usually form fibrous solid crystals in their crystalline temperature range, which are inappropriate for single crystal X-ray analysis, barring for example the compound $H_2Pc$-*onp*-C6 which possesses a very unique orthorhombic structure[171]. The stability and the structure of the liquid-crystalline phase crucially depends on the kind of alkyl-substituent, i.e. the number of side chains, their

---

a) For an illustration of the tilt see figure 4.9 in section 4.6

b) The used synonyms are in accordance with common abbreviation rules for phthalocyanines[170] with the metal ion in front, followed by "Pc" and a designation declaring the number and position of substituents, like *op*: octa-substituted at the peripheral positions, *e.g.*, ring positions No 2 and 3 (see Fig. 4.1), or *onp*: octa-substituted at the non-peripheral, *e.g.*, position 1 and 4. The type of the side chain is given last.

position, their length, and also the linking group connecting the alkyl group with the Pc core. Elongation of the alkyl chain for example decreases the isotropisation temperature by about 13 °C per C atom[170].

The linking group connecting $H_2$Pc and the side chain has an even more striking effect than the side chain itself. Similar to the copper containing paradigm of PIECHOCKEI and SIMON other methoxy-linked compounds have been studied, having the same hexagonally disordered columnar arrangement[172,173]. The same symmetry was also found in systems with methylene-linkers, i.e. purely aliphatic side chains (C5, C6, C8, C10[174]; C12[171])[c]. If the linking group is planar such as oxy (O-C6 to O-C12[176], O-C12[177]) or carboxy[178] a hexagonally-ordered columnar phase ($D_{ho}$) is observed. This is expected, since the driving force of the stacking is a $\pi$-$\pi$-interaction leads to strong orbital overlaps and allows for charge transfer along the column. By introducing non-planar linkers like methylene, the dense packing is effectively hampered. In these materials rather a hexagonal disordered phase is observed. Another aspect relates to the electronic structure of the molecule when exchanging the oxy-linker by another atom. The oxy-group is electron donating due to its free electron pairs in conjunction with the ring, whereas a carbon atom for example has a less significant net effect on the electron density of the aromatic ring. The compound investigated in this study (see figure 4.2) is an octa-substituted phthalocyanine with eight thiododecyl-moieties connected to the peripheral carbon atoms ($H_2$Pc-*op*-S-C12). Sulphur is not the most commonly used linker, however, a study characterising the very similar compound $H_2$Pc-*op*-C-S-C12 was published in 1988[179]. Due to its focal conic texture the mesophase was assigned to $D_{hd}$-type packing, which can sufficiently be explained by the non-planar $CH_2$S-linker connected to the ring; alas it does not provide

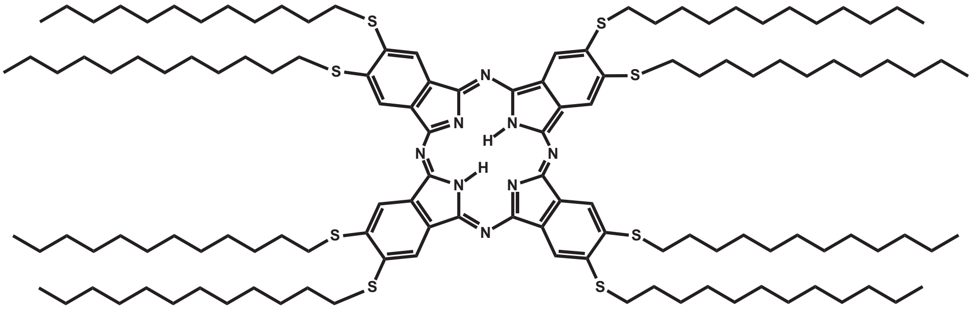

**Figure 4.2.** The structure of $H_2$Pc-*op*-S-C12.

---

[c] As reported by CLARKSON *et al.*, further extension beyond twelve carbon atoms leads to a rectangular disordered phase in case of $H_2$Pc-*op*-C16[175].

an initial guess for the arrangement of the present compound $H_2$Pc-*op*-S-C12. According to the theory of Hunter and Sanders a more electron withdrawing (or less donating) substituent like thioalkyl reduces the repulsion of close $\pi$-orbitals in a stack and leads to a stabilisation of the column[180]. A contrary effect might be the bigger Van-der-Waals radius of sulphur implying a less dense packing, hence a destabilisation.

In this work several experimental methods have been applied to study the organisation and the thermal behaviour of the compound $H_2$Pc-*op*-S-C12. Firstly, thermal analysis by means of DSC was carried out to identify the expected crystal-mesophase transition. Secondly, solid-state NMR methods were employed to study the local organisation of the compounds. $^1$H MAS NMR served to trace the initial columnar reorganisation of the freshly processed sample. Just as seen for the BTAs, the temperature profile of the thermal analysis has been emulated by VT $^1$H MAS NMR and MAS NMR to reveal changes of the supramolecular packing and the mobility. Since the extended aromatic $\pi$-system of the compound has a high impact on the $^1$H chemical shift of the protons, these measurements were supported by a computed NICS map of a smaller $SCH_3$ end-capped phthalocyanine. $^{13}$C NMR allowed to deduce statements about the symmetry of the arrangement. The assignment of the ring carbon resonances in substituted phthalocyanines with varying linker atoms is not straightforward and needed to be supported by a separate DFT calculation. Thirdly, the long-range order has been tested by 2D *wide-angle X-ray* (WAXS) diffraction, providing insight into the parameters like stacking distance and a possible tilting of the molecules.

## 4.3. Thermal Behaviour

Prior to the solid-state NMR experiments a DSC study has been carried out to probe the thermal behaviour of $H_2$Pc-*op*-S-C12. The DSC curves obtained between -80 and 130 °C using a cooling and heating rate of 10 K per minute are given in figure 4.3. The first heating run indicates several endothermic processes related to the equilibration of the sample. During these processes the material is expected to reorganise into a well-ordered columnar structure, as found for several other alkyl-substituted phthalocyanines before[170]. By cooling the sample a phase transition at 0 °C occurs corresponding to crystallisation of the compound. The reversal of this process can be observed in the second heating run at 15 °C, indicating only a small hysteresis, compared to $H_2$Pc-*op*-$CO_2$-C8 octaesters[181], which had revealed remarkably different crystallisation temperatures in the heating and

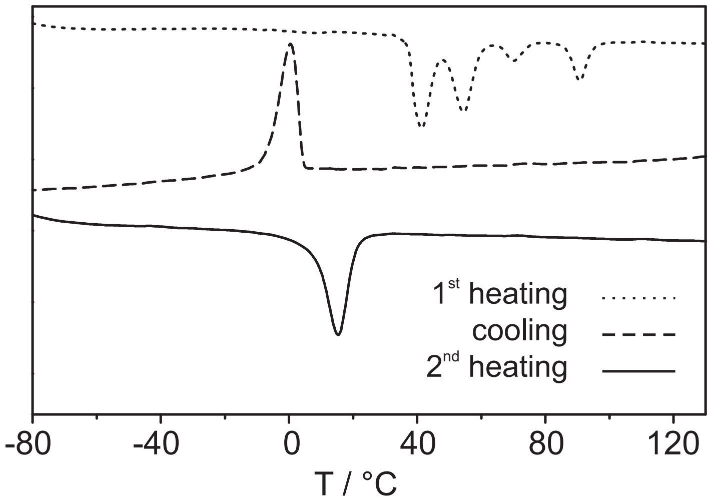

**Figure 4.3.** The DSC of $H_2Pc$-*op*-S-C12 between -80 and +130 °C. A heating and cooling rate of 10 K $min^{-1}$ was applied revealing a phase transition at 15 °C (0 °C cooling), $\Delta H_t$= 55 kJ $mol^{-1}$.

cooling run resulting in a hysteresis of 82 °C. Moreover, the measurement of $H_2Pc$-*op*-S-C12 resulted in a rather small enthalpy of 55 kJ $mol^{-1}$ compared to 87.1 kJ $mol^{-1}$ for $H_2Pc$-*op*-$CO_2$-C8. This is possibly due to the less favourable effect of a sulphur atom in contrast to carbonyl. Furthermore, the value was significantly lower than the enthalpy of 109 kJ $mol^{-1}$ found for the oxy analogue of the present compound[176]. Due to its mechanical properties and optical appearance the high temperature phase could be ascribed to a liquid crystalline mesophase and the low temperature phase to a plastic crystalline phase.

## 4.4. Proton NMR Techniques

### 4.4.1. 1D $^1H$ NMR Techniques

#### 4.4.1.1. VT $^1H$ MAS NMR

The temperature dependent behaviour of $H_2Pc$-*op*-S-C12 has been traced by $^1H$ MAS NMR between -27 °C and 99 °C in steps of approximately 5 °C (see Fig. 4.4.1.1). The spectra were recorded using the material as-synthesised. In this manner, the proton spectra corresponded to the first heating run of the DSC in figure 4.3.

The $^1H$ MAS NMR spectrum at -27 °C was dominated by a remarkably broad peak of the dodecyl side chains at 1.1 ppm. In the aromatic region two signals could be found, one relatively narrow peak at 7.6 ppm and a small shoulder 8.9 ppm. The inner core protons were not resolved but appeared as a shoulder at around -2.8 ppm, compared to -3.5 ppm in $CDCl_3$ solution. There was no remarkable change observed in the spectrum up to a temperature of 65 °C. At this temperature the signal of the inner core protons shifted instantaneously to -7.6 ppm. As known from earlier investigations on Pcs, the chemical shift of the inner core protons depends strongly on the supramolecular assembly of the molecules. Even values around -9 ppm have been reported before[181]. Due to this observation the material was now presumed to exhibit a columnar organisation, adjacent molecules providing an additional high-field shift. The sudden reorganisation was accompanied by narrowing of the side chain signal from 980 Hz at 60 °C to 300 Hz at 75 °C. Besides this, the signal of the methylene group adjacent to the sulphur atom was resolved at 2.4 ppm. Both low-field signals at 8.9 ppm and 7.6 ppm decreased dramatically to the account of a new peak at 6.2 ppm and only a small shoulder at 7.6 ppm remains.

The NMR observations between 65 and 75 °C did not correspond to any observed enthalpy change in the DSC curve of the first heating run. Therefore, it should be clarified, that studying the thermal behaviour of samples investigated as-synthesised often leads to irreproducible results. Moreover, the effective heating rate of a VT solid-state NMR measurement is usually much smaller as compared to routine DSC run. For that reason the first heating curve is not considered in most studies. In this case, however, VT $^1$H MAS NMR nicely demonstrated, that the compound was in a state of local disorder. The organisation improved as soon as the sample was heated above a certain temperature enabling the molecules to adopt a columnar structure. The signal of the inner core protons of the phthalocyanine is therefore a sensitive probe for these reorganisation processes in substituted Pcs.

By cooling the sample no abrupt phase transition around $T = 65$ °C could be observed (see figure 4.5). Only gradual changes occurred like a slight broadening of the aromatic peak and a continuous shift of the side chain signal from 1.25 ppm at 99 °C to 1.45 ppm at 4 °C. The signal of the inner core protons drifted from -6.9 ppm to -7.7 ppm within the same temperature range. Below this temperature at around 0 °C a phase transition was observed, indicated by the abrupt broadening of the side chain signal. This signal evolved from 650 Hz at 4 °C to 1350 Hz at -6 °C, i.e. it more than doubled. At the same temperature the aryl signal became blurred, meaning it was either homogeneously broadened or more likely, it split up into two strongly overlapping peaks. The latter case had already been observed for the low temperature phase of other symmetrically substituted phthalocyanines[181]. The broadening of the alkyl chain peak and the splitting of the aryl resonances were accompanied by a more subtle behaviour of the signal, arising from the

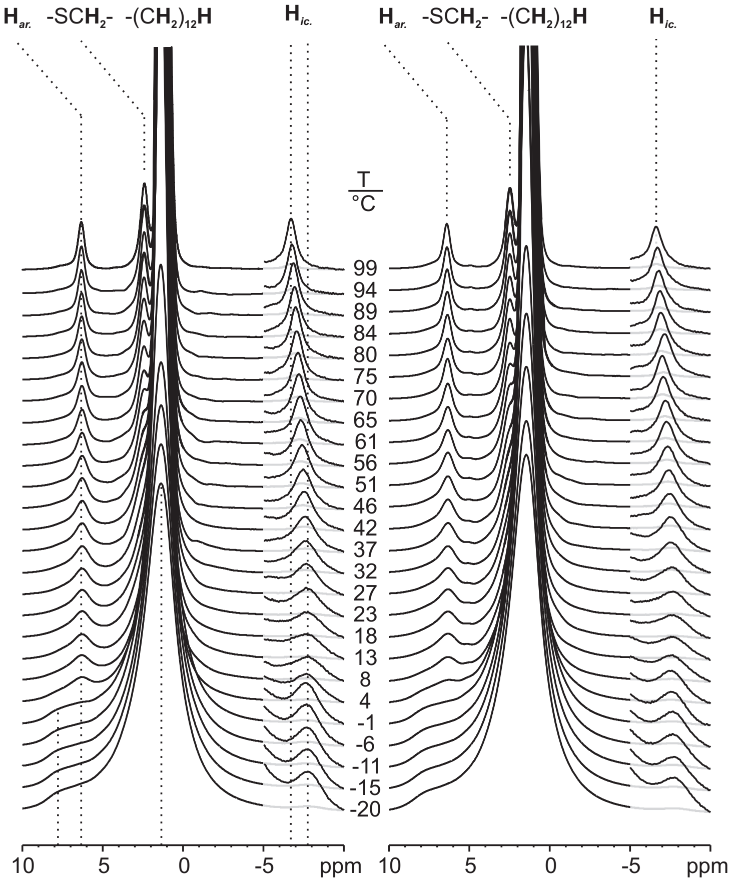

**Figure 4.5.** VT $^1$H MAS NMR spectra of the $H_2$Pc-*op*-S-C12. The compound was annealed at 150 °C before the measurements. For the sake of clarity the original spectra in the range of the inner core protons are faded and the same region is depicted 8 times enlarged. The cooling run is depicted on the left, heating on the right (*ar.*=aryl, *ic.*=inner core).

inner core protons. In contrast to the previously investigated Pc octaesters the signal of these protons remained at higher field upon cooling[181]. The jump, observed for the first time heated $H_2$Pc-*op*-S-C12, could therefore only be detected once. The generation of the columnar architecture during the annealing was apparently not reversible by cooling the sample below the transition temperature at 0 °C. Therefore, it was reasonable to assume a slightly different organisation in the low temperature phase of $H_2$Pc-*op*-S-C12 and the phthalocyanine octaesters. On heating $H_2$Pc-*op*-S-C12, all effects were reversible without indication of hysteresis in contrast to the DSC measurement, probably due to a smaller heating rate.

#### 4.4.1.2. VT $^1$H DQF NMR

In order to better trace mobility changes within the investigated temperature range $^1$H DQF MAS experiments have been performed. The raw pattern can be seen on the left side in figure 4.6. Since the investigated compound exhibited a high number of mobile side chain protons (96 in particular, compared to 8 aryl protons and only 2 inner core protons) the DQF spectra usually emphasising rigid backbone peaks were still governed by the bulky side chain signal. The spectrum at -24 °C was therefore as featureless as the $^1$H MAS NMR, apart from a little higher intensity of the two aromatic signals. The signal of the inner core protons was also missing, which might be attributed to the short excitation/reconversion time of 33.6 $\mu$s (see section 4.4.2). On heating the sample above the phase transition at around 0 °C, the compound entered the mesophase indicated by the striking loss of relative DQF intensity at this point. The onset of the transition was unfortunately accompanied by strong phase artefacts that arise from side chain parts and also impaired the low field region of the spectrum. A smaller peak between 6 and 7 ppm could safely be assigned to the aryl resonances whose intensity dropped considerably. Hence it was concluded, that the phase transition is a process that involves the whole molecules and cannot be assigned to the melting of side chains in particular. For this reason, it seemed interesting to compare DQF intensities with integrals of SPE experiments. Since a deconvolution of the spectra was impossible, the whole spectral range had to be integrated. The results are given on the right-hand side of figure 4.6. As one can see the relative DQF intensity of the as-synthesised sample was about 15 % and remained constant up to a temperature of 60 °C. At 65 °C, the onset of the phase transition, the DQF intensity decreased rapidly to 2 % (cf. DSC in Fig. 4.3). On cooling the sample to 9 °C, a small gradual growth of DQF intensity could be observed before the intensity abruptly jumped to 14 %. By storing the sample for several hours at this temperature, a slightly higher intensity of 16 % was measured, possibly due to improved

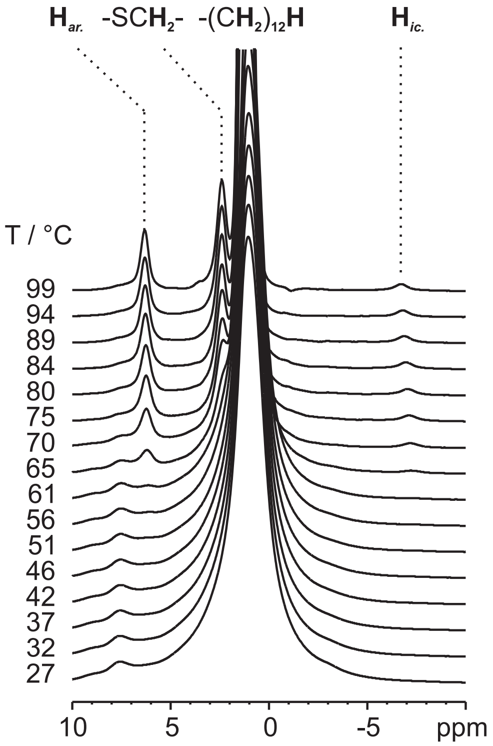

**Figure 4.4.** VT $^1$H MAS NMR spectra of the $H_2$Pc-*op*-S-C12 as-synthesised, 1$^{st}$ time heated; *ar.*=aryl, *ic.*=inner core)

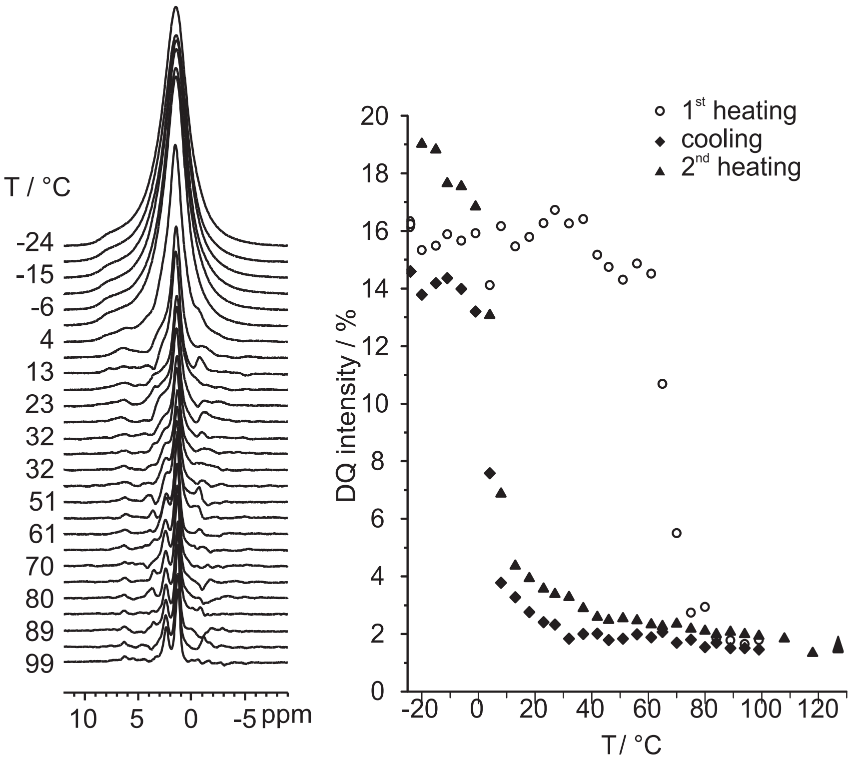

**Figure 4.6.** *left*:$^1$H DQF NMR spectra of the (annealed) compound H$_2$Pc-*op*-S-C12 between 12 and -9 ppm, recorded with a excitation time of 33.6 $\mu$s. The sample was continuously heated from -24 °C to 99 °C in steps of 5 °C. For a reasonable illustration the temperature is turned upside down. *right*: Relative DQF intensities as a function of temperature. Different symbols correspond to different heating or cooling runs.

packing. Apart from these higher values at the beginning, the second heating run of the experiment nearly overlapped with the cooling curve and showed the same sigmoidal shape of relative DQF intensity over temperature. As already indicated by the $^1$H MAS NMR spectra, no significant hysteresis could be observed.

### 4.4.2. 2D $^1$H-$^1$H DQ-SQ Correlation

Rotor-synchronised $^1$H-$^1$H DQ-SQ MAS NMR spectra with different excitation times have been recorded to further enlighten the packing of molecules in either the plastic crystalline phase as well as the liquid-crystalline phase. The results of these measurements are given in figure 4.7. Like in the 1D NMR spectra, the alkyl peak is dominating the spectrum and gave rise to the large auto peak around (1.5 ppm, 3.0 ppm), hardly providing information on the supramolecular assembly. In the low-field region however, the spectrum with a short excitation time of 33.6 $\mu$s confirmed the presence of two distinct signals in the aromatic region. In this area the spectrum consists of two pairs of cross-peaks (6.5 ppm, 9.0 ppm), (2.5 ppm, 9.0 ppm) and (7.7 ppm, 11.2 ppm), (3.5 ppm, 11.2 ppm). Both correlations

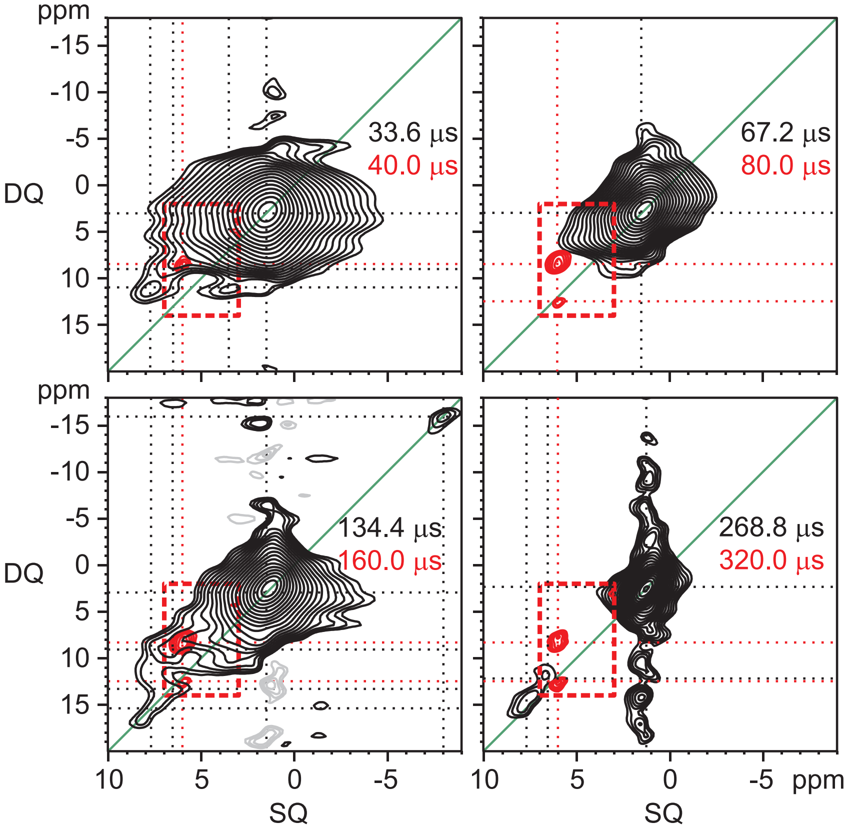

**Figure 4.7.** Rotor-synchronised $^1$H-$^1$H DQ-SQ MAS NMR of $H_2$Pc-*op*-S-C12. The spectra have been recorded with different excitation times corresponding to 1, 2, 4 and 8 rotor periods with respect to an MAS frequency of 29762 Hz. Black (positive) and grey (negative) contour levels correspond to spectra recorded at -24 °C, whereas the red spectra have been obtained at 70 °C and a lower MAS frequency of 25000 Hz. Due to the low signal to noise ratio and disruptive artefacts only small cut-outs from 2 to 14 ppm along the DQ dimension and from 3 to 7 ppm along the SQ dimension are plotted (*red*), overlying the low temperature spectra.

indicate distinct DQ coherences between two kinds of aryl protons with two aliphatic sites at 2.5 ppm and 3.5 ppm. This requires the presence of two spatially separated and distinguishable SCH$_2$-sites having different chemical shifts. It should be noted that these couplings were unique, i.e. there was neither a coupling of the sites observed at 2.5 ppm and 7.7 ppm, nor of those observed at 3.5 ppm and 6.5 ppm. This observation could be explained by two coexisting phases, though, this is very unlikely since it would imply a transformation into two low-temperature arrangements of equal size, since the integral ratio of the aromatic peaks was about 1:1. The splitting could therefore be attributed to a symmetry reduction due to the molecular arrangement, i.e. the molecules do not any longer exhibit a virtual $D_{4h}$-symmetry. This could be explained by a deformation of the ring structure, a slower tautomerism of the inner ring protons or a combination of both (for a detailed discussion see publications of LIMBACH and co-workers, for example [182]).

The correlation pattern recorded with 67.2 $\mu$s excitation time did not show any peaks in the low field region. Using 134.6 $\mu$s excitation time DQ coherences between the relatively close (2.15 Å)[183] inner core protons were established, indicated by a rather narrow peak at (-8.0 ppm, -16.0 ppm). The relatively long excitation time could be attributed to a fast tautomeric exchange of these protons[182]. Furthermore, the correlation between the 6.5 ppm and 2.5 ppm peaks reappeared in this experiment, whereas the low field pair at 7.7 ppm and 3.5 ppm was much less incisive. On the one hand, the different intensities might be explained by different mobilities of the $SCH_2$ groups. According to this assumption the coupling between 6.5 and 2.5 ppm might be stronger because of a more rigid -$SCH_2$- group. Compared to the 7.7 and 3.5 ppm signal, the different dynamics of surrounding parts may also lead to less pronounced relaxation losses during the DQ excitation/reconversion periods. On the other hand, the observed coupling pattern might be a result of well defined tilt angles of the S-$CH_2$ bond axes. If these were coplanar with the aromatic ring, the distance would be about 1.8 Å, in contrast to 4 Å if the SC axis would be perpendicular to the ring. In the latter case the longer distance between the protons implies a weaker coupling, hence a diminished DQ intensity. This way one might ascribe the high-field shifted aryl and $SCH_2$ protons to that side of the molecule that exhibits in-plane character of the side chains and the non-shifted proton sites to an out-of-plane side chain arrangement. Since both couplings seem to have the same strength in the pattern recorded with short excitation time, the argumentation in favour to the relaxation losses of the 7.7 and 3.5 ppm DQ coherence.

Moreover, at 134.6 $\mu$s excitation two autocorrelation peaks began to build-up at the plot diagonal, rising further at 269.2 $\mu$s excitation time. This either indicated an intramolecular coupling between aromatic protons across one edge of the phthalocyanine molecule or it was due to an intermolecular coupling of neighbouring molecules in the columnar assembly. Due to the intermolecular distance of slightly more than 4 Å between these protons[183] both explanations might be possible, thus no specific information about the packing could be extracted. The absence of cross-peaks between the two distinguishable aromatic proton sites was not surprising, since for the common $\beta$-form of $H_2Pc$ the periodicity of molecules is larger than 4.7 Å, preventing a detectable DQ coherence. Furthermore, due to the tetragonal distortion of the molecule in a tilted herringbone arrangement, the distances of the aryl protons were not completely equal. The splitting might be attributed to a tilting or a distortion and distinct local fields imposed by that, with the tilting having the larger impact on the chemical shift.

SQ-DQ correlation spectra have also been recorded at 70 °C. However, the quality of the spectra was significantly lower compared to those of the low-temperature phase. The high abundance and mobility of side chain protons gave rise to large artefacts affecting almost the whole spectrum. For the sake of clarity only small cut-outs from 2 to 14 ppm along the DQ dimension and from 3 to 7 ppm along the SQ dimension are given providing limited additional information after careful data processing. These patterns (red) overlie the low-temperature spectra and consist of the left correlation peak of the $SCH_2$ and aryl protons and the aryl autopeak. The DQ coherences were relatively weak at short excitation times and built up on increasing it. The same observation held for the autocorrelation peak of the aryl protons not being visible at 40 $\mu$s excitation time, but rising with longer excitation times. A minor feature was the intensity drop of the cross correlation peak whose intensity decreases by changing from 160 $\mu$s to 320 $\mu$s excitation time. This might be related to side chain induced relaxation, which does not affect coherences between backbone protons. Quite remarkable is the observation of only one aryl signal at the considered temperature. This proves a higher symmetric state above the transition temperature.

## 4.5. Carbon NMR Spectra

### 4.5.1. $^{13}$C Peak Assignment

In order to probe the symmetry properties of the molecular arrangements in both phases in more detail $^{13}$C {$^1$H} CP/MAS spectra of the low and high temperature phases have been recorded. As reported for other *op*-substituted phthalocyanines[181,184] the aromatic region of the plastic crystalline phases contained more carbon signals than the symmetry of the molecule implied. Hence it was assumed that also $H_2$Pc-*op*-S-C12 provides more than four distinct carbon lines. Since the compound had not been characterised yet by solution NMR, a $^{13}$C J-modulated spin echo experiment was conducted prior to the solid-state study to achieve a proper assignment of the solution NMR spectrum. In this widely used standard experiment carbon atoms connected to an odd number of protons (methyl and methine carbons) appear negative, whereas positive signals correspond to an even number of protons (methylene and quaternary carbons). As can be seen in figure 4.8 a), the spectrum consists of four peaks irrespective of side chain signals. A very small positive peak at the low field end of the spectrum (148.0 ppm) may easily be overlooked. This signal could be ascribed to the eight carbons of the inner ring, located between the nitrogen atoms. The low intensity of this signal had been observed in single pulse spectra of other phthalocyanines and was attributed to fast tautomerism of the imidazol nitrogen atoms and fast alternating positions of the inner core protons[185]. However, coordination by two $^{14}$N atoms, both possessing a relatively large quadrupole moment, may also contribute to the fast relaxation of this carbon atom. The only negative peak was located at 119.9 ppm and could be assigned to the only non-quaternary carbon, i.e. the aryl CH position. The two large positive peaks at 139.9 and 132.7 ppm could be ascribed to two quaternary carbons, whereas their explicit assignment remains unclear. Clarification was achieved

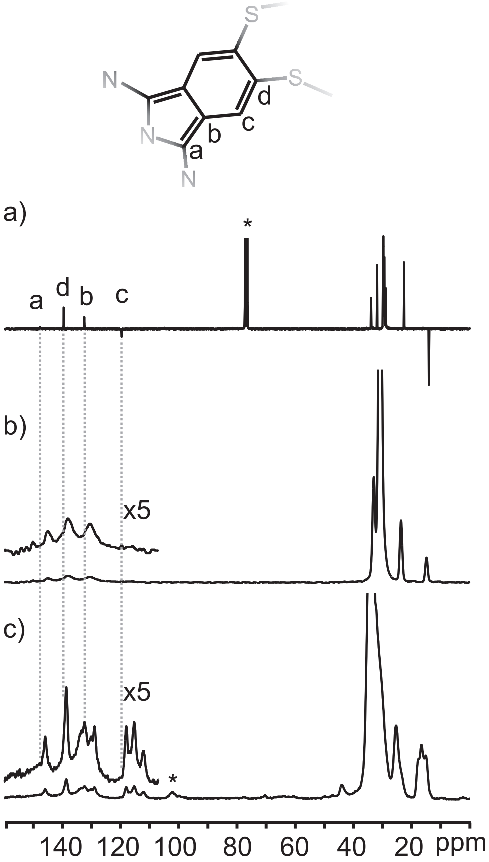

**Figure 4.8.** a) J-modulated spin echo experiment of $H_2$Pc-*op*-S-C12 in chloroform-*d* solution. The two negative peaks refer to the methyl group and the single aryl proton. The spectrum was obtained recording 21210 transients in chloroform-*d* solution. The solvent peak is marked with an asterisk. b) $^{13}$C {$^{1}$H} CP/MAS spectrum of the same compound at 25 °C (mesophase). 33792 scans have been recorded at a LARMOR frequency of 125.8 MHz and MAS speed of 15 kHz. c) $^{13}$C {$^{1}$H} CP/MAS spectrum at -43 °C (crystalline phase). 16384 scans have been recorded at a LARMOR frequency of 176.1 MHz and a MAS speed of 12 kHz.

by comparing the spectrum with NMR results of a study in which the non-peripherally substituted compound $H_2$Pc-*onp*-O-C6 had been investigated[185]. The chemical shift of carbon **b** had been found at 133.5 ppm, which best matched the signal at 132.8 ppm of the present compound. Accordingly, the remaining peak at 139.7 ppm could be assigned to the peripheral carbon **d** bound to the sulphur atom. KENTGENS *et al.* published chemical shifts of $H_2$Pc-*op*-O-C11, an oxy-analogue of the examined compound with one carbon atom less per side chain[184]. In their solid-state NMR study they had found 151.6 ppm for the outer position. The large difference could be explained by a lower electronegativity and different shielding properties of sulphur compared to oxygen atoms. Further confirmation could be obtained by a supporting DFT calculation, discussed in the next section 4.5.2.

### 4.5.2. DFT Calculations and Chemical Shift Prediction

The calculation has been carried out using the B3LYP-GIAO/6-31G level of theory. In order to reduce the computational time, the dodecyl moieties were substituted by methyl groups. The substitution was assumed to have no significant effect on the chemical shift of the ring atoms. Precedent optimisation led to a $C_i$-symmetric structure with methyl groups occupying either in-plane or out-of-plane conformations. Besides a too small basis set to accurately describe a large aromatic system binding to sulphur atoms, two more intrinsic problems in the run-up to the calculation appeared. Firstly, the tautomerism of the ring protons could not be taken into account in a simple manner. The chemical shifts of the inner carbon atoms were therefore affected by the position of these protons, thus have different chemical shifts. The impact of the proton position dwindled with the distance to the inner core, i.e. the inner protons did not affect the chemical shift of the outer carbons. The chemical shift of the outer carbon atoms, however, was partially governed by the conformational state of the terminal methyl group, referring to the first side chain atom in the experiment. The shift of position **d** therefore only depended on the tilt angle of the C-S axis with respect to the ring plane. Both of these effects had a noticeable impact on the two in-between positions. The calculated chemical shifts for the eight equivalent positions (according to the $D_{4h}$ symmetry) were averaged, thus fast exchange was taken into account in a rather simple way. Position **a** exhibited an observed chemical shift of 148.0 ppm. The calculation predicted an isotropic chemical shift of 129.1 ppm therefore differing by -18.9 ppm. A very similar deviation (-18.5 ppm) was found for position **c** (exp.: 119.9 ppm, calc.: 101.4 ppm). The accuracy did apparently not allow direct conclusions. However, regarding only the relative deviations, a rather precise prediction for the two quaternary carbons could be obtained. Assuming that the average

| *Position* | *Obs.* | *Calc.* | $\Delta$ | *Estimation* | *Error* | *Assignment* |
|---|---|---|---|---|---|---|
| **a** | 148.0 | 129.1 | 18.9 | (147.8) | +0.2 | |
| **c** | 119.9 | 101.4 | 18.5 | (120.1) | -0.2 | |
| | | average: | **18.7** | | | |
| **b** | | 113.2 | | 131.9 | +0.8 | 132.7 |
| **d** | | 128.5 | | 147.2 | -7.5 | 139.7 |
| **d’** | | 121.5 | | 139.2 | +0.5 | 139.7 |

**Table 4.1.** A comparison between calculated chemical shifts using B3LYP-GIAO/6-31G level of theory. The geometry was preoptimised before using the same method and basis set. The position numbers refer to those given in figure 4.8. All calculated values have been referenced with respect to RBLYP/GIAO/6-311++G**. The two unambiguous shifts were used to calculate the average deviation of the used method. This value, -18.7 ppm, was used to employ an empiric correction to the calculated values of position **b** and **d**. In order to validate the method, the errors of the prediction, i.e. the deviation of the prediction and the observed chemical shift, are also given. Since the agreement of the prediction and the experiment in case of the peripheral carbon was not as good as for the other sites, in the lower line (**d’**) a second prediction is included using an average of the four *in-plane* conformations only.

deviation of -18.7 ppm was a systematic mismatch, the experimentally observed signal at 132.8 ppm could be attributed to position **b**, having a calculated shift of 113.2 ppm.

The described procedure was not valid for the outer position **d**. The lack of agreement (exp.: 139.7 ppm, calc.: 128.5 ppm, corrected prediction: 147.2 ppm) between the experiment and the prediction was probably due to the proximity of the outer carbon and the sulphur atom. Here, the chemical shift depended more likely on the average mean conformation of the alkyl part and thus on the real side chain dynamics. The fast exchange was a reasonable assumption to describe tautomerism of the inner core protons, but in case of the peripheral carbons averaging would have implied a fast exchange of pure in-plane and pure out-of-plane conformations, which is not a sustainable model. At this point it appeared reasonable to take into account only the four carbon sites next to the in-plane sulphur atoms, since this is the more likely conformation for a macromolecule in solution. A thereby calculated chemical shift of 121.5 ppm (sd: 0.9 ppm) led to a corrected prediction of 140.2 ppm, which was again close to the observed chemical shift of 139.9 ppm. All observed and simulated chemical shifts are summarised in table 4.1.

In this way the given assignment in figure 4.8 was verified by literature comparison and additional DFT calculations. Furthermore, the impact of the side chain conformations was demonstrated by this method.

### 4.5.3. $^{13}$C {$^{1}$H} CP/MAS Spectra

$^{13}$C {$^{1}$H} CP/MAS spectra have been recorded at two temperatures, above (at 25 °C) and below (at -43 °C) the transition point. The results are presented in figure 4.8 b) and c). The side chain atoms in the mesophase gave rise to relatively narrow signals indicating a liquid like behaviour, see figure 4.8 b). The four aryl site signals, however, were very broad and weak compared to the side chain resonances. The ternary carbon signal was not seen at all. Shorter contact times and even single pulse excitation failed to improve the intensity of the aryl signals and the ternary carbon in particular. In general, the absence of the ternary carbon peak is usually explained by the long contact time (3 ms), which may have led to effective $T_{1\rho}$ relaxation, whereas the quaternary carbon signals in the spectrum remained visible. The low signal intensity could be attributed to a molecular tumbling with a correlation time similar to the MAS rotor period, leading to a destructive interference and tremendous signal loss. This effect had been reported earlier for other octa-substituted phthalocyanines in the context of dipolar recoupling procedures[186]. Due to the poor intensity of the present compound, such methods have not been applied a priori.

The centres of the three visible lines were shifted to high field, indicating a columnar arrangement. Compared to the solution NMR results position **a** was found to be shifted by -3.1 ppm and sites **b** and **d** by about -2.0 ppm. This gradient from the centre to the periphery of the molecule could be interpreted as a less effective shielding of outer parts by the surrounding molecules. This was suggestive for disorder within the column, diminishing the shielding effect primarily at the periphery of the phthalocyanine ring. The molecules might rotate freely about the stacking axis, thus sense only an average impact of adjacent molecules. The outer positions thereby have a higher possibility to be located beside the benzo-subunits and possess a less pronounced high-field shift.

The low temperature spectrum shown in figure 4.8 c) was obtained at -43 °C. The signal intensity was better compared to the high temperature phase and an improved S/N ratio was achieved recording less scans. The side chain signals appeared broad, indicating decreased side chain dynamics. Signals of the aromatic region exhibit well resolved discrete lines. The ring current induced shifts of the $^{13}$C signals were unlikely to exceed those determined for the inner core protons (~6 ppm), therefore the most likely assignment was in accordance with the progression in the solution NMR data. The line at 145.9 ppm corresponded to position **a**, which was a little less shifted (only by -2.1 ppm with regard to $CDCl_3$ solution) as compared to the respective signal in the mesophase. The same tendency held for position **d**, which appeared at 138.6 ppm, shifted by -1.3 ppm.

The two other sites, i.e. positions **b** and **c** were split into a doublet of doublets (pos. **b**) and a triplet (pos. **c**), which may also consisted of four partially overlapping lines. With respect to the solution NMR results position **b** was shifted by +0.6, -0.3, -2.6 and -3.7 ppm, whereas position **c** was shifted by -2.1, -4.6 and -7.8 ppm. These distinct chemical shifts could hardly be explained by a common type of columnar packing, in particular because it was most pronounced for the in-between carbon sites. Moreover, the single lines of position **a** and **d** confirm that neither a disturbed tautomerism, nor frozen side chain conformations generated the non-equivalence of the positions **b** and **c**. However, a pure packing effect affecting predominantly the middle carbon positions is unprobable. Therefore it is very likely that the split resonances were the result of a ring distortion that has already been suggested for other phthalocyanines[184]. It should be noted, that a ring distortion is a clear indication for the herringbone arrangement, since even a slight twist of the planar geometry cannot be explained by a flat cofacial arrangement.

## 4.6. 2D WAXS Pattern

To obtain insight into the long-range order and the intercolumnar organisation 2D WAXS measurements have been done. The aim of this X-ray study was to elucidate the type of columnar arrangement present in both phases. Common aggregation types of liquid crystalline phthalocyanines are given in figure 4.9, i.e. basically the eclipsed (a)) and the staggered (b)) arrangement.

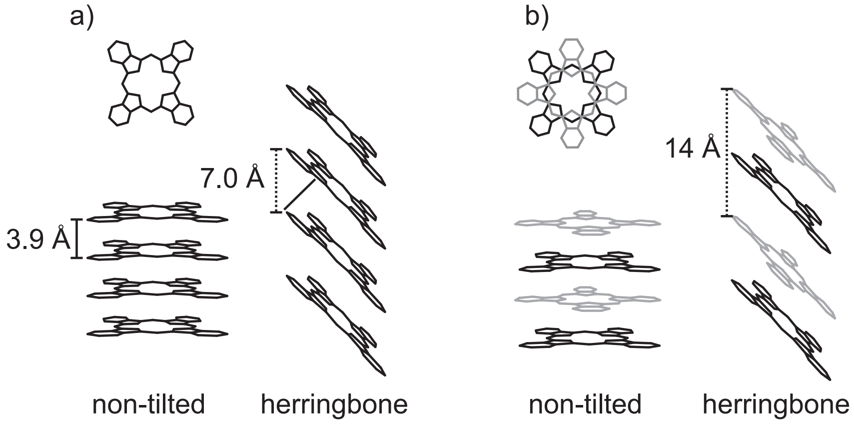

**Figure 4.9.** Four possible ordered arrangements of $H_2$Pc-*op*-S-C12: a) eclipsed, b) staggered.

2D WAXS pattern were recorded at 40 °C and -40 °C, i.e. at temperatures above and below the transition temperature. Since the fiber axis orientation was not vertical during the experiment, the meridian is tilted in both graphs (see Fig. 4.10). The low temperature

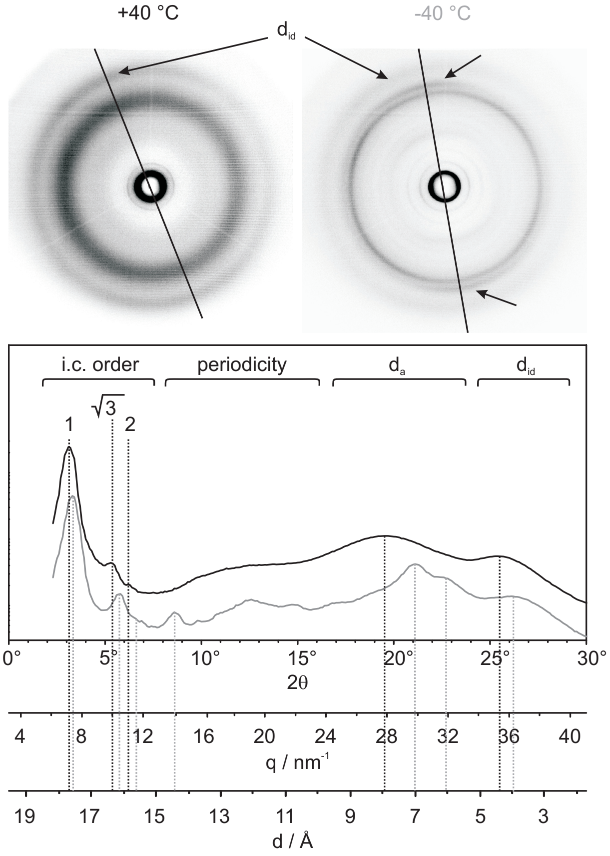

**Figure 4.10.** VT 2D WAXS measurements of $H_2$Pc-*op*-C-S-C12. Different sections in the pattern can be attributed to features of the compound emerging on different length scales: intercolumnar order (*i.c.*), the *periodicity* within the column, the length scale of translational symmetry ($d_a$) and the disc distance ($d_{id}$).

phase could be assigned to a columnar hexagonal packing due to the equatorial 100, 110 and 200 reflections with q-spacings in the ratio of $1 : \sqrt{3} : 2$. In case of the high temperature sample, however, the 200 reflection was very weak and therefore a different arrangement cannot be excluded.

Diffuse meridional reflections in the outer part could be related to the coplanar arrangement of molecules having a distance of 3.9 Å in the crystalline phase and of 4.4 Å in the mesophase, which is best seen in the integration plots of figure 4.10. Since the high-temperature phase was less organised, it seemed reasonable to focus on the crystalline phase.

The major goal of the X-ray investigation is the distinction between a non-tilted face-to-face stack or a tilted “herringbone” arrangement. It has to be pointed out that the data was not unambiguous, thus reflection could be found supporting both, a tilted and a non-tilted arrangement:

On the one hand the most intense and well separated wide-angle reflection at 21° $2\theta$ suggested a herringbone arrangement. This reflection could be attributed to the periodic distance of 7 Å between the phthalocyanine molecules, i.e. the distance of translational symmetry along the columnar axis. This almost isotropic ring matched the interdisc distance of 3.9 Å, provided the molecules are tilted by 55°. The data even left margin for a staggered arrangement as shown in figure 4.9 b). If one assumes the molecules to be rotated by 45°, the actual periodicity would be about 14 Å instead of 7 Å, because the distance between two equivalent discs would be twice as large. The observed reflection at 8.7 °$2\theta$ corresponded to a periodicity of 14.4 Å, hence it would be in agreement with this assumption. Noteworthy, in the high temperature pattern the 14.4 Å reflection observed for the low-temperature phase was missing. Rotation or fluctuations of the discs may have caused a loss of orientation relation of neighbouring molecules cancelling the long range translational symmetry.

On the other hand arguments supporting a non-tilted face-to-face arrangement could be found. First of all, the reflection specifying the interdisc distance of 3.9 Å was clearly meridional (short arrows), whereas in a tilted arrangement it is expected to be split into two off-meridional reflections. Moreover, the assumed tilt angle of 55° seemed quite large compared to the unsubstituted $\alpha$- or $\beta$-$H_2Pcs$[170] or to the $H_2Pc$ octaesters[181].

Eventually it has to be said, that neither a herringbone arrangement, nor a non-tilted arrangement could be confirmed on the basis of X-ray only. Moreover, an eclipsed arrangement could not be ruled out. However, a hexagonal disordered packing of molecules could be found with an interdisc distance of 3.9 Å in the crystalline phase, increasing to 4.4 Å in the mesophase.

### 4.6.1. A DFT Supported Review of $^1H$ Chemical Shift Data

A NICS map will be presented in this section in order to support one of the afore mentioned arrangements, i.e. a eclipsed or a staggered arrangement. The technical details of the calculation are given in appendix B. In general such NICS maps demonstrate the impact of a molecule on the chemical shift of its surroundings, *e.g.*, the neighbouring molecule in a columnar arrangement. Therefore, NICS maps provide valuable information about the supramolecular organisation. NICS maps have already been used for the assignment of $^1$H MAS NMR of benzene-tricarboxamides. For a more detailed introduction to the practical use of NICS maps, see therefore chapter 3 and section 3.2.3.2 in particular. For the sake of clarity, only the crystalline low-temperature phase will be considered here.

The interpretation benefits from the quite remarkable high-field shift of the inner core and the aryl protons. In section 4.4.1.1 the chemical shift of these protons was determined as -3.5 ppm in chloroform-*d* solution and -7.7 ppm in the bulk. The additional chemical shift of -4.2 ppm of the bulk peak compared to the solution could be ascribed to strong ring current effects of neighbouring phthalocyanines. The same held for the aryl proton resonances, shifted by -0.7 and -1.9 ppm from 8.4 ppm in solution to 7.7 and 6.5 ppm in the bulk, respectively.

The molecule used to generate the NICS map was the same simplified structure that was used in the calculation for the $^{13}$C chemical shift prediction in section 4.5.2. The slight asymmetry in the outer part of the bare NICS map in figure 4.11 a) was not surprising, since the dihedral angles of the attached methyl groups were different. Because the shape is apparently independent of the position of the inner core protons the centre of the map was remarkably homogeneous. The molecule causing an impact on the chemical shift of the surrounding atoms is given as *balls and sticks* representation, whereas the “probe molecule” is shown as a *wireframe* representation. On basis of the X-ray results the NICS map was generated using a distance of 3.9 Å coplanar with the phthalocyanine ring. The strength of the impact on the chemical shift is indicated by the colour code given on the right in figure 4.11. The green centre of the NICS map therefore indicated an additional high-field shift of -4.0 ppm with respect to a nucleus placed straight above the centre in a distance of 3.9 Å. The inner core protons were supposed to exchange quickly, hence were delocalised in the centre of the phthalocyanine. The two surrounding molecules on top and underneath affected the inner core protons to same amounts. Assuming, a columnar face-to-face arrangement without a tilt as seen in figure 4.11 b) and c), led to an additional high-field shift of -8.0 ppm in total, much more than the expected -4.2 ppm. It should be noted, that the effect of remote molecules in the column would lead to an even stronger high-field shift. Moreover, the non-tilted arrangement would imply eight equivalent aryl protons shifted by -1.5 ppm in both, the staggered and the eclipsed conformation. These cases are illustrated by only one uniform group of protons.

The shift values do not correspond to the experimental observation expecting a high-field shift of additional -4.2 ppm for the inner core protons and two separated aryl protons.

The non-tilted columnar arrangement could therefore be ruled out.

In order to meet the experimental chemical shift of the inner core protons, the centres of the molecules were displaced such that a shifting effect of only -2.1 ppm was achieved in contrast to the 4.0 ppm of the flat cofacial arrangement discussed before. It appeared, that a displacement of ~3 Å led to the desired additional shift of -2.1 ppm. The inner core protons of the molecule surrounded by two neighbours then sensed a total impact of -4.2 ppm, just as required.

The displacement could, however, be carried out in numerous directions. In order to investigate the details of the herringbone arrangement and to confirm either a staggered or an eclipsed arrangement, a couple of likely arrangements are given in figures 4.11 d) to f). In case of an eclipsed conformation the displacement might be in a direction between the benzo units as shown in figure 4.11 d) or parallel to them as given in figure 4.11 e). If a staggered conformation is assumed, there is only one possibility presented in figure 4.11 f).

In a second step the observed chemical shifts of the aryl protons in bulk and the chemical shifts suggested by the NICS map needed to be compared in order to support one or another situation. Each arrangement and their agreements with the experimentally derived additional aryl proton shifts of -0.7 and -1.9 ppm are examined. Since the aryl protons were not in the centre of the molecule, the protons were affected differently from the molecules above and below. For all three considered arrangements the aryl protons could be categorised into equivalent groups of protons having the same additional shift, illustrated by black and grey cicles in figure 4.11 d) to f). The quality of the agreements is given in table 4.2. As one can see the agreement of the herringbone arrangement with a displacement between the benzo units was slightly better (Fig. 4.11 d)), however, the re-

| | Peak 7.7 ppm | | Peak 6.5 ppm | |
|---|---|---|---|---|
| | additional shift: -0.7 ppm | | additional shift: -1.9 ppm | |
| | group 1 | *deviation* | group 2 | *deviation* |
| fig. 4.11 d) | -1.0 | -0.3 | -2.5 | -0.6 |
| fig. 4.11 e) | -1.2 | -0.5 | -2.8 | -0.9 |
| fig. 4.11 f) | -1.0 | -0.3 | -2.7 | -0.8 |

**Table 4.2.** Evaluation of different columnar arrangements by means of a comparison of experimental and calculated $^1$H chemical shifts. The different arrangements refer to the figures 4.11 d), e), and f).

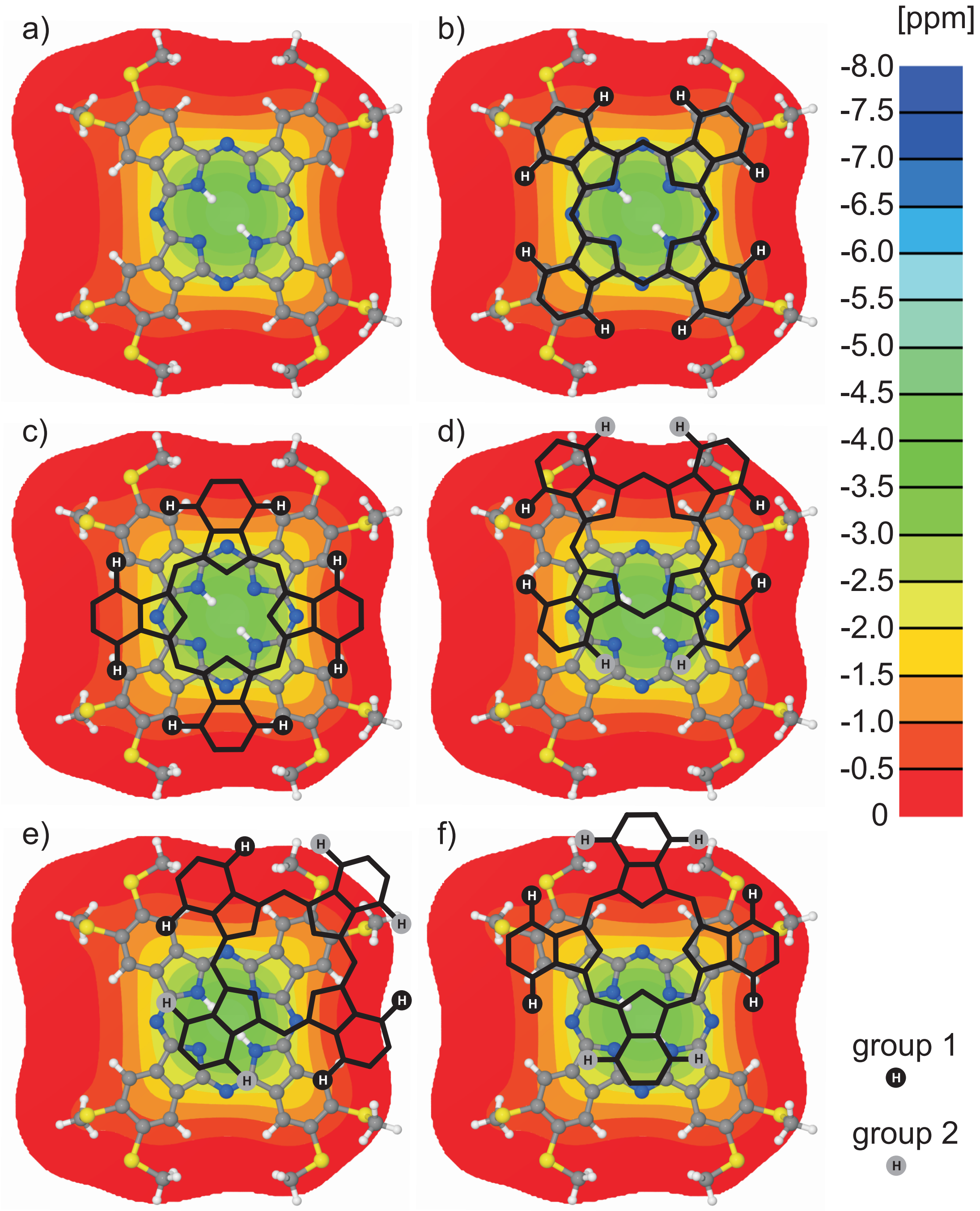

**Figure 4.11.** NICS maps of $H_2$Pc-*op*-S-C12 and different arrangements. a) only the NICS map, b) a non-tilted eclipsed arrangement, c) a non-tilted staggered arrangement, d) the tilted eclipsed arrangement 1, e) the tilted eclipsed arrangement 2, f) a tilted staggered arrangement. In case of the tilted arrangements, the protons become distinguishable and can be combined to two symmetry equivalent groups, coloured in black and grey.

maining arrangements could not be ruled out. It should be noted, that all models equally supported the high-field shift of the $SCH_2$-protons, derived from the cross-peaks in the SQ-DQ correlation pattern in figure 4.7.

In the high-temperature mesophase only a single resonance was observed. In general this could be related to a transition from a tilted to a non-tilted arrangement or a fast exchange of the proton sites in general. In the former case, the protons would be equivalent as in figure 4.11 b) or c). This would be accompanied with dramatic high-field shift of the inner core protons, though. Therefore, the transition could safely be assigned to the onset of an exchange of aryl protons, i.e. a rotation of phthalocyanine molecules about the $C_4$-axis. This finding was in line with other substituted phthalocyanines[181].

Remarkably, the resonance of the inner core protons was unaffected by the phase transition, possibly because the larger distance was compensated by a smaller tilt angle of the molecules. Possibly, although the inner core protons were further afar from the next molecule of the column, they were located in a more central part of the shielding cone which leaves the signal unchanged.

## 4.7. Conclusion

The investigated phthalocyanine $H_2Pc$-*op*-S-C12 provided a phase transition at 15 °C observed by DSC. It could be related to a mesophase transition as seen by $^1H$ MAS NMR in combination with $^1H$ DQF NMR. Due to the large line width of the $^1H$ peaks, a splitting of aryl and $SCH_2$-signals could only be determined by means of $^1H$-$^1H$ DQ-SQ correlation spectroscopy. These measurements revealed, more clearly than 1D single pulse spectra, a symmetry breaking of the $D_{4h}$-symmetric discs by a less symmetric packing. Like in the case of the benzene-1,3,5-tricarboxamides, a NICS map of the phthalocyanine ring provided insight into the effect of the tilting on the chemical shift within the columnar arrangement. Moreover, it was shown, that the high-field shifted sites are possibly located at that particular benzo unit with a higher in-plane character of side chains. This supports the herringbone packing, since the more shifted thiomethylene sites were apparently more covered, hence more likely in-plane than the peripheral positions which were capable of out-of-plane liberation motions.

The assignment of the $^{13}C$ NMR spectra in solution could be achieved by means of comparison with similar known compounds and by a supporting DFT study. The interpretation of the single pulse carbon spectrum of the low temperature phase of the compound remained unclear. The interpretation still lacks an explanation for the observed splitting, which was assumed to be due to ring deformations in combination with shielding effects of the adjacent molecules.

2D WAXS pattern of $H_2$Pc-*op*-S-C12 indicated a columnar disordered phase with adjacent molecules having distance of 3.9 Å in the crystalline phase and 4.4 Å in the mesophase. The high temperature phase provided a higher degree of dynamic, which could hardly be probed by solid-state NMR but rather caused tremendous signal losses, in particular in $^{13}$C NMR.

In order to summarise, $H_2$Pc-*op*-S-C12 stacks in a columnar hexagonal disordered arrangement ($Col_{hd}$). The molecules in the stack are probably tilted but not rotated, giving rise to the eclipsed herringbone arrangement, which is also in line with other substituted phthalocyanines. To the best of our knowledge no study has been performed yet, confirming a staggered arrangement of neighbouring *op*-substituted phthalocyanines in the crystalline phase. Even if the eclipsed face-to-face arrangement was prohibited by side chains attached flatways to the ring, the phthalocyanine molecule avoided the steric crowding by a small rotation angle rather than adopting a fully staggered conformation[187d)]. Due to the tilting, the symmetry in the stack reduces to $D_{2h}$, according to the carbon spectra the effective symmetry is even lower, though.

With respect to the aim of designing highly ordered LC phases for electronic applications it is to be said, that the organisation of $H_2$Pc-*op*-S-C12 is worse compared to other octa-substituted phthalocyanines. One reason might be the longer Van-der-Waals radius of the thio-linker or electronic effects of the attached sulphur atoms, that are actually supposed to provide a conversely stabilising effect.

---

d) However, in a recent theoretical study on alkoxycarbonyl substituted phthalocyanines, the carbonyl groups exhibit a pronounced tendency to tilt out of the ring plane, leading to a staggered conformation[188].

# 5. The Bulk Assembly of Oligo-(*p*-phenylenevinylene)s

The development of electric conductive organic materials began in the mid 1970s by the discovery of the electric conduction of the conjugated polymer polyacetylene (PA)[2]. Today, a well tested and commonly used material for fabricating such devices is poly-(*p*-phenylenevinylene) (PPV), consisting of vinyl and phenyl units in alternating order. Compared to the simpler PA it has superior electronic properties, *i.e.*, a zero band gap[a)]. In particular when the phenyl ring is substituted, the upper $\pi$-valence bands can be tuned according to the target operational mode[192]. Like most organic conducting materials PPV is a hole conductor, hence an p-type semiconductor like other potentially important polymers as poly-(3-hexylthiophene). Some liquid-crystalline phthalocyanines in contrast, as perfluorinated copper phthalocyanine, are examples for n-type semiconductors. This class of compounds has already been discussed in chapter 4.

## 5.1. OPVs: Conjugated Strands with three to five Repetition Units

Smaller PPV-like oligomers with three to five repetition units have been investigated as model compounds for PPV. Oligo-(*p*-phenylenevinylene)s (OPVs) enable a better understanding of physical properties, because of their well defined length and a better solubility, which eases the processing for scientific purposes or industrial applications[193]. In contrast to the PPV bulk, OPVs have no electronic band structure, but discrete energy levels. Their number increases with the conjugation length, implied by the rising number of redox states[194]. With the increasing number of states the colour of the material changes[195], since the energy difference between HOMO and LUMO levels decreases. The position of

---

[a)] The band gap of *trans*-PA is between 1.5-2.5 eV[189] (regardless of the impact of chain-chain interactions on the energy levels[190]), which impedes the use of the raw material. However, by doping this compound it is possible to tune the conductivity over 6 orders of magnitude[191].

the energy states can also be influenced by substituting single OPV rods with electron donating or withdrawing groups that enable fine-tuning of the colour and electric properties of the compound. Substitution by aliphatic or ether side chains rather increases the solubility of OPVs, which improves the processability[196].

OPVs have been used to functionalise poly(propylene imine) dendrimers in which they have been used as compatibiliser, enabling efficient energy transfer from an organic PPV substrate to a light emitting dye[197]. OPVs exhibit a pronounced tendency to construct $\pi$-stacked columnar arrangements leading to liquid-crystalline behaviour of the dendrimers[198]. Some work has been done on improving the relaxation behaviour by perturbing this intermolecular stacking of covalently interconnected OPVs either by implementing bulky terminal groups[199] or by adding ions to a solvent matrix[200] to counteract intramolecular stacking.

In fact, the accelerated relaxation of non-isolated OPVs is suggesting a remarkable interchromophoric coupling between adjacent rods being displayed in the $S_1$-$S_0$ absorption profile[201]. Their interaction strongly depends on the proximity of the rods, also shown by studies that have been carried out, investigating the formation at the air-water interface[202]. With regard to a possible use in photovoltaic applications the immediate relaxation causing fluorescence prevents an effective charge separation. A [60]fullerene acceptor molecule bound to the OPV donor can provide a fast quenching of the excited state energy by electron transfer either to a simple C60 acceptor[203,204] or via a C60 cage being part of a ruthenium metal ion complex[205]. In self-assembled helical stacks of functionalised OPVs, that can be found in alkane solutions different electronic effects can be observed[206,207]. Depending on the irradiation strength effects like exciton annihilation, exciton trapping and luminescence depolarisation can occur[208]. The energy transfer in these systems clearly depends on the intermolecular order[206,209,210], since defect positions would impose a high resistivity of the whole column. The importance of this order criterion even increases for columnar assemblies of alternating donor and acceptor molecules[211,212].

Introducing functional groups capable of forming hydrogen bonds facilitate a high degree of order and moreover control the final morphology of the sample[213]. Since the charge transfer efficiency would be relatively low, a precise face-to-face arrangement of adjacent molecules is not the desired arrangement in materials to be used for electronic applications[211]. In this case even a minor displacement towards a slipped-stacked arrangements is essential for the time constant of a photoinduced charge transfer reaction[b)]. A summary

---

[b)] The different assemblies refer to the concept of J- and H-aggregation. A more general introduction of recent research in the field of self-assembling OPV derivatives for application in organic electronics can be found in [216].

In this last experimental chapter the results on the self-assembly of chiral and achiral OPVs in the solid-state are presented. The current investigation involved different OPV molecules distinguished by the length of the conjugated phenylenevinylene backbone. This feature does not only control the colour and electronic properties of the compound, but also has its main impact on the capability of forming supramolecular arrangements, since the stability of the rod increases with the size of the $\pi$-$\pi$-overlap of adjacent molecules. The higher stacking energy also leads to an better crystallinity of the assembly, *i.e.*, larger systems having a higher order. A converse, disorder-introducing effect can be implemented by aliphatic side chains. The interplay between regularly aligned and disordered components in a molecule is a commonly used principle facilitating liquid crystallinity[217].

The study was established to probe the organisation of molecules in the bulk with respect to the competing effects of strong $\pi$-$\pi$-interactions and mobile side chains. The influence of the hydrogen bonds as a third structure controlling building block within the molecule was of special interest, since simultaneous $\pi$-stacking and hydrogen bonding impose high demands on the supramolecular assembly. Depending on the solvent and the investigated OPV, in solution these three determinating elements led to remarkable helical stacks of dimers[218]. The arrangement in the solid-state, however, remained basically unknown.

## 5.1.1. The OPVs of this Study

The macroscopic and microscopic organisation of a number of different OPVs have been probed by Differential Scanning Calorimetry (DSC), X-ray and Polarised Optical Microscopy (POM). The two smallest OPVs seemed suitable for a solid-state NMR investigation.

During the whole solid-state study OPVs with larger backbones have been investigated. On the microscopic scale, however, these compounds appeared less organised and exhibited phase transition temperatures above the experimental limits of current commercial probe heads capable of fast MAS. The aliphatic side chains, in most cases C12, but a C6 compound was investigated as well, were attached to the vinyl side of the OPV backbone

---

can be found in [214], or see [212, 215] for the context of charge transfer in OPV-perylene copolymers.

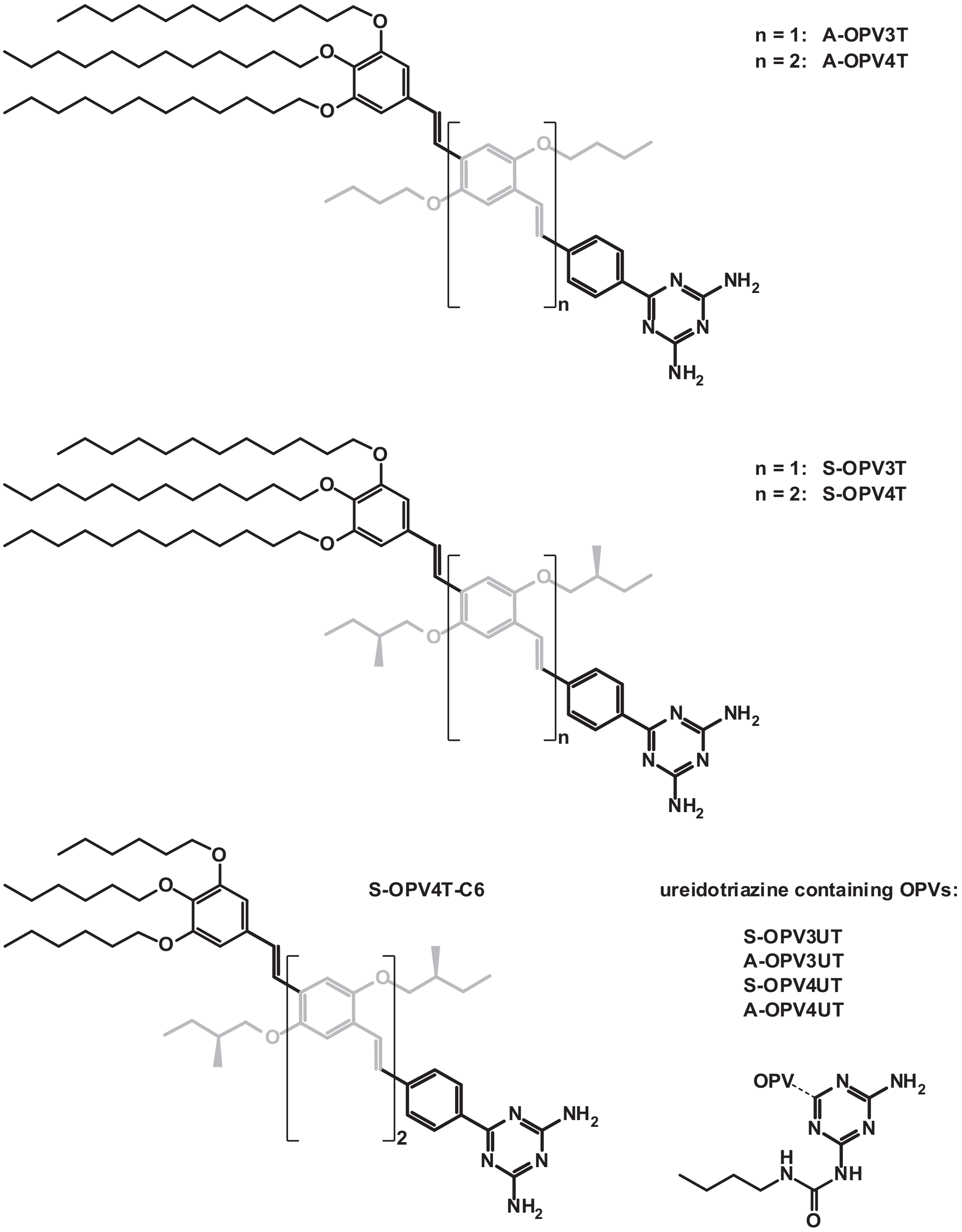

**Figure 5.1.** Collection of investigated OPVs.

via a 3,4,5-alkoxyphenyl group (see figure 5.1). Each phenylenevinylene unit was moreover equipped with smaller butoxy side chains located at the 2- and 5-positions of the backbone phenyl rings. Chirality was induced by exchanging the linear butoxy side chains of the achiral OPVs by chiral 2-*S*-methylbutoxy side chains. The phenyl terminus of the backbone was equipped with two kinds of polar head groups, capable of forming hydrogen bonds. The two head groups investigated were diaminotriazine and ureido-substituted diaminotriazine. The ureido-substituted diaminotriazine constituted a well established quadrupolar hydrogen bonding group commonly used as a self-complementary DADA motif[c)], known to form helical arrangements in the absence of a conjugated backbone[219]. It had been shown that the aggregation of the ureido-containing compounds follows a strictly hierarchal scheme. In dodecane solution the OPVs comprising this motif first combine to form dimers and further organise into stacks of up to 150 nm in length discovered by SANS measurements[220]. Related molecules even provide a helical superstructure, *i.e.*, single helices that combine to a coil-coiled rope, thus indicating the extraordinary ability of functionalised OPVs to form supramolecular arrangements[221]. The self-aggregation behavior of diaminotriazine and ureidodiaminotriazine containing OPVs have been investigated on the solid-liquid interface, revealing rosette-like arrangements of six OPV molecules in case of shorter diaminotriazine compounds[222] or a packing of dimers in case of longer diaminotriazines and ureido-diaminotriazine[222, 223]. Six-membered rosettes have also been found for diaminotriazine derivatives in solution[224], suggesting that a similar organisation might also be found in the solid-state.

### 5.1.2. Thermal Behaviour Invesigated by DSC and POM

Ureido-diaminotriazine containing OPVs (OPVUTs) were known to provide liquid-crystalline behaviour even at ambient conditions, however, decompose at relatively low temperatures (∼200 °C) due to cleavage of the urea group[225]. OPVs equipped with a diaminotriazine head group offered a much higher thermal stability and start to degrade at 320 °C. Introducing chiral side chains seems to have no effect on the thermal behaviour of the samples. ooo

In the DSC study, the shortest diaminotriazine compounds A-OPV3T and S-OPV3T were both liquid crystalline at ambient temperatures and had an isotropisation point at 136 °C (see figure 5.2) with almost similar enthalpies (A-OPV3T: 14.2 kJ mol$^{-1}$, S-OPV3T: 15.5 J mol$^{-1}$). Both curves overlapped perfectly indicating a similar thermal

---

c) D = hydrogen bond donor, A = hydrogen bond acceptor

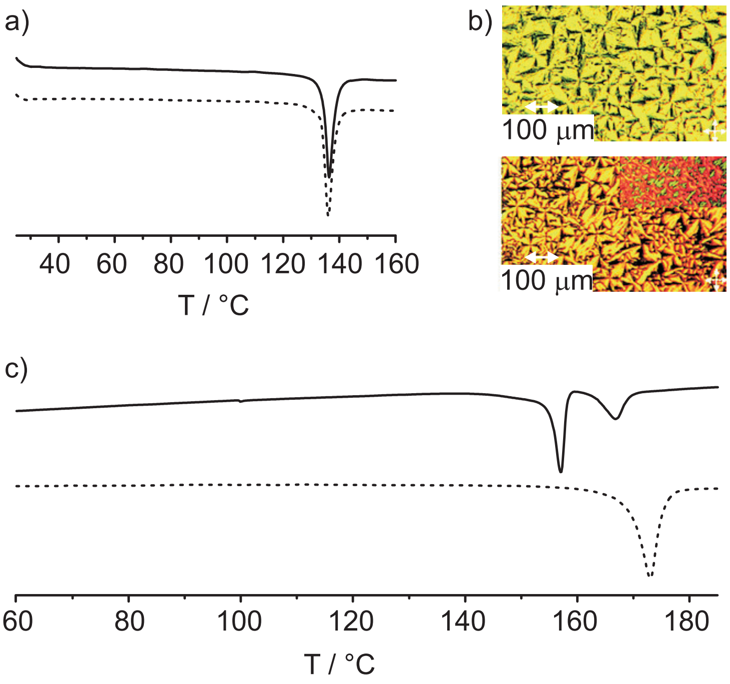

**Figure 5.2.** a) Second heating DSC scans of A-OPV3T (*solid line*) and S-OPV3T (*dashed line*). b)POM measurements of A-OPV3T and S-OPV3T revealed identical focal-conic textures. c) Second heating DSC scans of S-OPV4T (*solid line*) and S-OPV4T-C6 (*dashed line*).

behaviour of both compounds. The liquid-crystallinity of both compounds was indicated by the characteristic pseudo-focal conic textures[226] observed by POM measurements[227]. Elongation of the conjugated backbone, *i.e.*, by probing S-OPV4T, the liquid-crystallinity is restricted to a relatively narrow temperature range delimited by a solid-mesophase transition at 156 °C and a isotropisation point at 166 °C. The crystalline phase is less organised, having much smaller domain sizes compared to the liquid-crystalline phase.

The observation of a higher mesophase transition temperature was expected, since the weighting of the backbone increased, whereas the disorder introducing side chains did not change. In case of the analogue compound S-OPV4T-C6 the liquid-crystalline phase was coherently absent due to its shorter alkyl chains. It just melts at 172 °C.

### 5.1.3. Long-Range Organisation Probed by Wide Angle X-Ray Measurements

Wide-angle X-ray scattering experiments using 2D-detection (2D-WAXS) are a versatile tool to study the long-range organisation of supramolecular systems[228]. For this purpose the material was treated by fibre extrusion and measured partially aligned. The measurements revealed hexagonal columnar superstructures for all investigated OPVs, see figure 5.3. Its characteristic pattern was especially pronounced for S-OPV4T-C6 in figure 5.3 a. This compound combines a relatively large backbone with three phenylenevinylene units and much smaller hexyl side chains[227]. A higher crystallinity of this material was therefore expected.

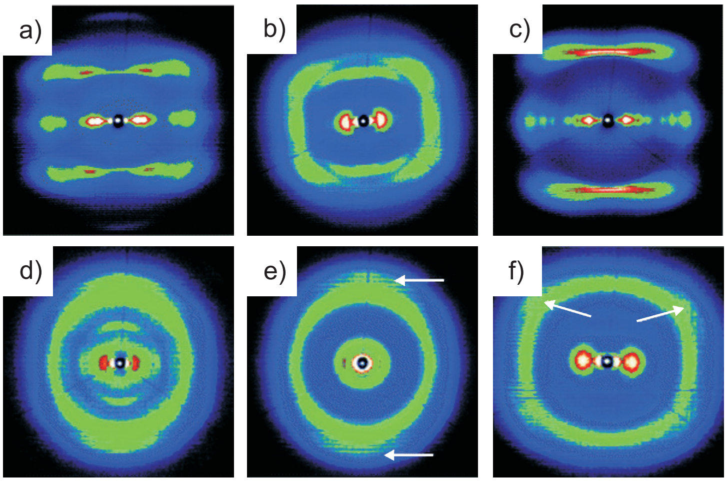

**Figure 5.3.** 2D-WAXS pattern of selected OPVs: a) S-OPV4T-C6, b) S-OPV4T, c) A-OPV4T, d) S-OPV3T, e) S-OPV3UT: Arrows indicate meridional reflections. f) A-OPV4UT: Arrows stress the off-meridional reflections, indicating a tilting of molecules (see text).

The compound showed a hexagonal packing with a unit cell parameter of 5.44 nm[d)] and a relatively large intracolumnar molecular distances of 0.55 nm was found. The distance between the molecules along the columnar axis, *i.e.*, the periodic distance, was determined as 0.65 nm which matched a tilt angle of ~30° implied by off-meridional reflections (see figure 5.3). In case of other *S*-chiral OPVs similar values have been obtained, which resembled those of flat arrangements at the solid-liquid interface[222], whereas for the achiral compound A-OPV4T an improved packing was found. Possibly, this was due to less steric hindrance of the butoxy side chain in contrast to 2-*S*-methylbutoxy.

Those OPVTs with a short backbone, S-OPV3T and A-OPV3T, demonstrated a non-tilted arrangement with similar stacking distances of 0.41 nm and 0.39 nm, respectively. Apparently the branched 2-*S*-methylbutoxy side chains were responsible for the slightly greater stacking distance and caused a destabilisation as observed for OPVUT derivatives in solution[229]. The lower degree of organisation in comparison with longer analogues A-OPV4T, S-OPV4T and S-OPV4T-C6 in particular was self-evident (see figure 5.3 a)

---

d) In case of a columnar hexagonal packing the unit cell parameter is equal to the distance of the columnar centres.

to d)). OPV3Ts were less organised within the columnar architecture, in particular the side chains were disordered, indicated by the broad halo. The lower organisation of the short diaminotriazine compounds at room temperature was in line with their liquid crystallinity at theses conditions. Heating the OPV4T compounds to their liquid-crystalline state at 160 °C, the 2D WAXS pattern resembled that of the OPV3Ts at ambient conditions, suggesting a similar arrangement (not shown).

A large *inter*columnar distance of more than 5 nm could be determined by equatorial reflections. This was sufficiently explained by the formation of dimers or larger hydrogen-bonded aggregates, which subsequently stacked and formed columns. The observation is also in agreement with a rosette-like arrangement of S-OPV4T-C6 molecules, which had also been proposed for dialkoxy-substituted biphenyl diaminotriazines[230]. The large *intra*columnar distance suggested either a low degree of order within the column or might be a result of a rotation of the OPV rods within the layer already proposed in [218].

OPVUTs showed a much lower degree of intramolecular order (see figure 5.3 e) and f)). Compounds having a linear butoxy side chain, however seemed to possess a tilting of 45°, indicated by off-meridional reflections. In case of 2-$S$-methylbutoxy side chains, these reflections were missing. The weak meridional reflections found instead were a sign of a non-tilted arrangement. Furthermore, an amorphous halo related to disordered side chains was indicative of liquid crystallinity of this compound.

## 5.2. Solid-State NMR on A-OPV3T and S-OPV3T

### 5.2.1. $^1$H MAS NMR Spectra of A-OPV3T and S-OPV3T

To investigate the impact of the chiral side chains in detail, the arrangement of the OPVs on the molecular scale was probed by solid-state NMR methods. Unfortunately, because of the length and $C_S$-symmetry of the molecules the carbon spectra were crowded and a reliable assignment could therefore not be achieved. However, limited information about the molecular assembly could be obtained by $^1$H MAS NMR. The study focussed on the two shortest OPVs, namely A-OPV3T and S-OPV3T, possessing a crystalline – liquid-crystalline phase transitions in the accessible temperature range.

The current OPVs offered poorly resolved $^1$H MAS NMR spectra at room temperature, even at MAS spinning frequencies of 30 kHz, indicated either a low degree of organisation or a non-uniform arrangement of molecules. At ambient conditions only four peaks were resolved. They could be assigned to protons of the conjugated backbone, aliphatic $OCH_2$

protons, and aliphatic protons of the middle side chains and of the methyl groups (see figure 5.4).

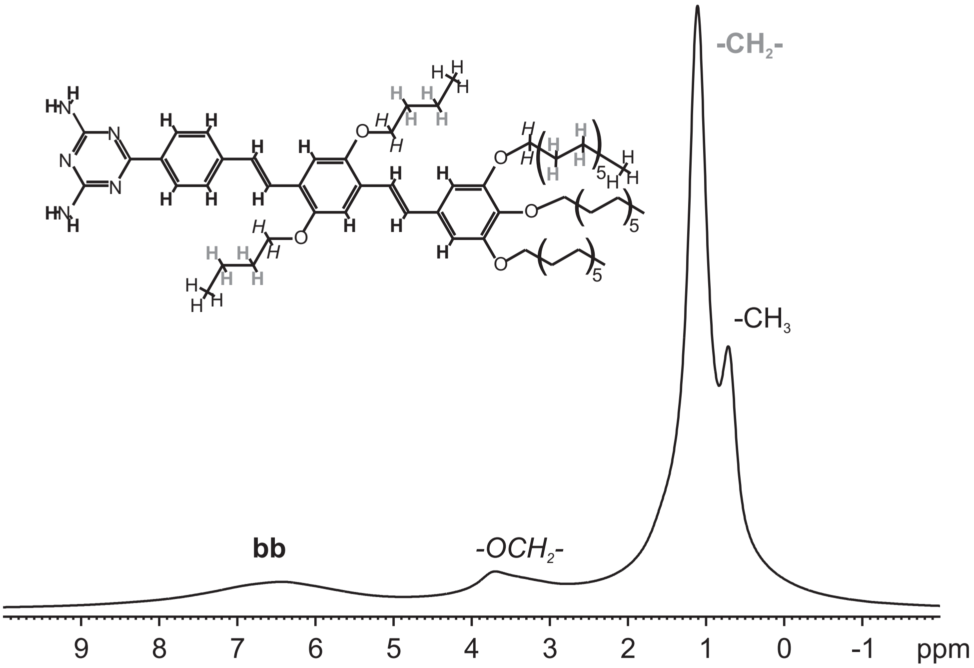

**Figure 5.4.** $^1$H MAS NMR spectrum of A-OPV3T recorded at 30 kHz MAS (T = 51 °C). One peak could be assigned to the backbone (**bb**) and three others to side chain which could be distinguished according to their position with respect to the to the oxy-linker. Three peaks could be attributed to aliphatic protons of the alkoxy (**-OCH$_2$-**), middle side chain (**-CH$_2$-**) and methyl (**-CH$_3$**) position.

The stack plots of the VT $^1$H MAS NMR spectra showed an almost identical temperature dependent behaviour of the chiral and non-chiral OPVs. However, subtle differences in the temperature dependence of the $^1$H chemical shifts could be identified, which pointed out differences between the two samples. The aromatic protons in close proximity to the triazine group should be noted explicitly, but also the aliphatic side chains showed a remarkable temperature dependence. The changing chemical shifts could be attributed to variations in the supramolecular organization in the solid state before the actual melting of the sample took place. The signal of the two aromatic protons near the triazine group had the highest chemical shift value and was well separated from other aromatic signals (see figure 5.5 a)). For the non-chiral A-OPV3T, this signal shifted continuously with increasing temperature from 7.52 ppm at 43 °C towards a higher ppm value of 7.79 ppm at 141 °C. An opposite trend could be observed for the signal of the aliphatic side chains (see figure 5.5b)), which shifted from 1.01 ppm to 0.92 ppm in a nearly linear manner in the same temperature range. In case of the chiral sample S-OPV3T a non-gradual be-

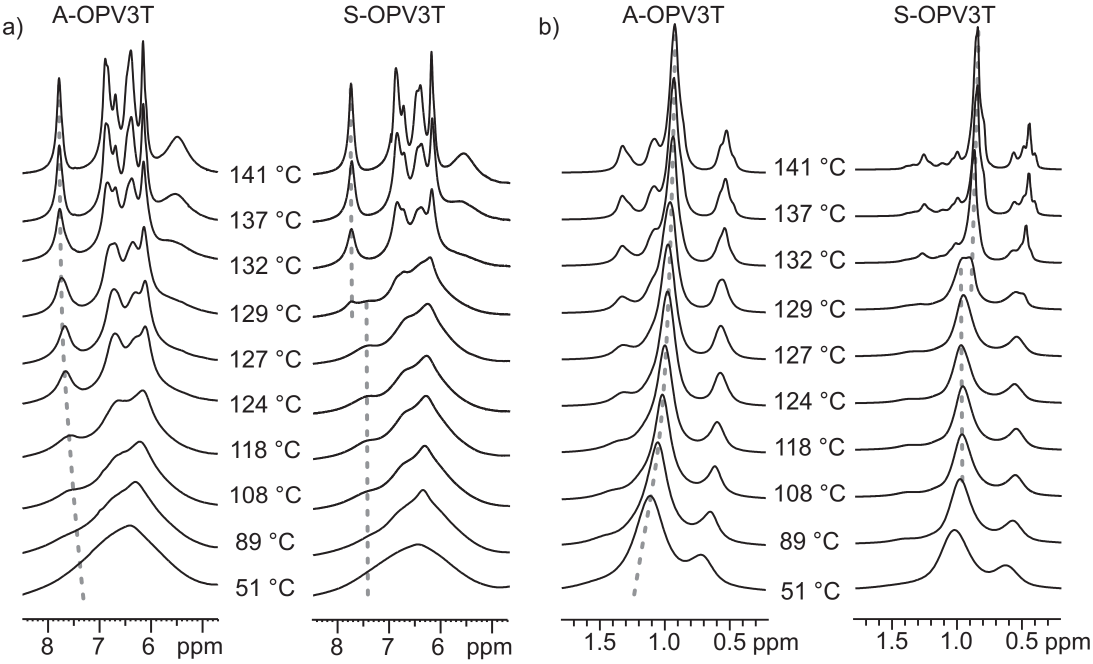

**Figure 5.5.** The stack plot shows a) the aromatic NMR signals and b) the aliphatic signals of A-OPV3T and S-OPV3T in direct comparison as a function of temperature.

haviour with increasing temperature was found in contrast. Both signals discussed above did not vary significantly between 100 °C and 125 °C, but provided an abrupt jump in the chemical shift at around 130 °C. At this point, the aromatic signal shifted from 7.38 ppm (at T = 127 °C) to 7.72 ppm (at T = 132 °C) and the signal of the aliphatic side chains from 0.96 ppm to 0.88 ppm. The spectrum recorded at T = 129 °C showed both, signals of the high and low-temperature phase simultaneously. This was most clearly seen for the triazine protons and those of the side chain.

Furthermore, VT $^1$H MAS revealed one more remarkable feature. With varying the sample temperature the formation of the broad peak at around 5.5 ppm was observed. This peak became visible at temperatures higher than 129° C in both samples and could be ascribed to the amino group protons. These could not be observed at lower temperatures, most likely due to a manifold of different hydrogen bonding arrangements resulting in the extreme broadening. The large line width as well as the hydrogen bond induced low-field shift led to severe overlapping of the amino signal with other aromatic and olefinic resonances. The appearance of this peak indicated a breaking or at least a substantial weakening of the hydrogen bonds around the melting temperature of both samples. It has to be pointed out that the intensity of the amino signal was less intense for the chiral compared to the achiral sample, however, the intensity difference could hardly be quantified due to the enormous line width of the peak and its overlapping with different aromatic signals. If the lower signal intensity was significant, it would imply a certain fraction of molecules still being captured in a hydrogen-bonded assembly, whereas the achiral OPV did not exhibit a similar retarded transition behaviour. This matched the observation of sudden jumps in the proton chemical shifts. The additional methyl groups of S-OPV3T apparently provided an additional hindrance to liberation motions leading to an abrupt activation and instantaneous melting.

### 5.2.2. Insights by $^2$H MAS NMR

Since certain aspects of the molecular behaviour at the phase transition remained unclear by interpreting $^1$H MAS NMR, $^2$H MAS NMR was applied in succession. For this purpose, the two compounds have been selectively deuterated at the amino position by dissolution in a 4:1 mixture of chloroform-$d$ and methanol-$d_4$. Thereby, labeled samples facilitated the observation of smaller differences at the onset of the transition in the chiral and achiral material. At ambient conditions the $^2$H MAS NMR spectra of both samples, A-OPV3T and S-OPV3T, resembled the MAS sideband pattern characteristic for rigid

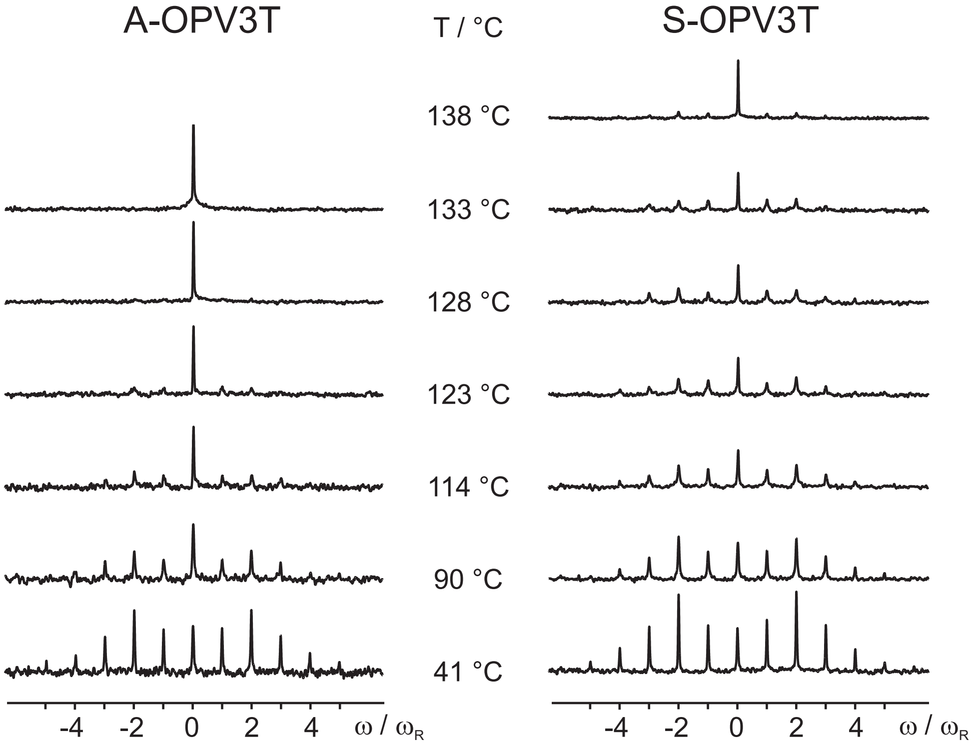

**Figure 5.6.** The stack plots show $^2$H MAS NMR pattern recorded at 25 kHz MAS frequency of the selectively deuterated compounds A-OPV3T (left) and S-OPV3T (right) at different temperatures.

deuteron sites (see figure 5.6). The slightly higher intensity of the central band observed for A-OPV3T was due to isotropic reorientation of deuterium sites, hence implied a higher molecular mobility of that sample. This trend was continued when heating the sample: The central band in case of the achiral sample A-OPV3T increased much faster than that of the chiral sample, indicating a significantly higher ratio of mobile to rigid deuterium sites, which were the building block of the hydrogen bonding network. Moreover, the MAS sideband pattern of the achiral sample narrowed with temperature. At 128 °C and above the pattern consisted only of a centre band with a non-lorentzian lineshape. This reflected a broad distribution of correlation times and dynamic processes in the melting. The temperature dependent spectra of the chiral sample S-OPV3T can be seen as a super-position of the spectrum of the rigid sample at ambient temperature with the centre band originating from mobile deuteron sites. Even at a temperature higher than the melting point of the sample, the $^2$H MAS spectrum showed a significant sideband pattern indicating a coexistence of hydrogen-bonded and free molecules in case of the chiral sample. The existence of two different kinds of amino sites in S-OPV3T explained the already mentioned lower intensity of the signal assigned to the free amino protons at around 5.5 ppm in the $^1$H MAS spectrum. The chirality of the S-OPV3T molecules apparently leads to more stable arrangements, despite of its slightly larger $\pi$-stacking distance[227].

### 5.2.3. Amino Protons observed by $^1$H-$^1$H DQ-SQ MAS NMR

Generally, DQF experiments did not contribute much to the understanding of the organisation of the investigated OPVs. A high relative DQF intensity of more than 12 % for backbone protons was found below 120 °C. On further heating the level decreased in an almost linear manner to below 1 % at the isotropisation point. Since similar results were obtained for both samples, the method did not allow to point out any difference between the two samples. In a 2D $^1$H-$^1$H DQ-SQ correlation experiment, however, some quite remarkable points could be made. The recorded $^1$H-$^1$H DQ SQ MAS NMR (see figure 5.7) displayed a relatively low intensity of the side chains with respect to the high proton abundance in this part of the molecule. The low intensity was due to a fast motion of the liquid-like side chains, which was in line with the liquid-crystallinity of the compound especially at the temperature of 132 °C close to the isotropisation point. However, the $OCH_2$ protons gave rise to a incisive auto peak at (3.3 ppm, 6.6 ppm). The strongest coupling could be identified between the different protons of the benzene linker (*magenta* and *blue*). This coupling was expected because of their proximity to the inner core of the hydrogen-bonded network; thus, they were relatively immobile. Moreover, both proton pairs belong to the same benzene ring and therefore underlie a given distance constraint of about 2.4 Å. The coupling was only diminished by orientational averaging of the whole segment which could definitely be excluded here.

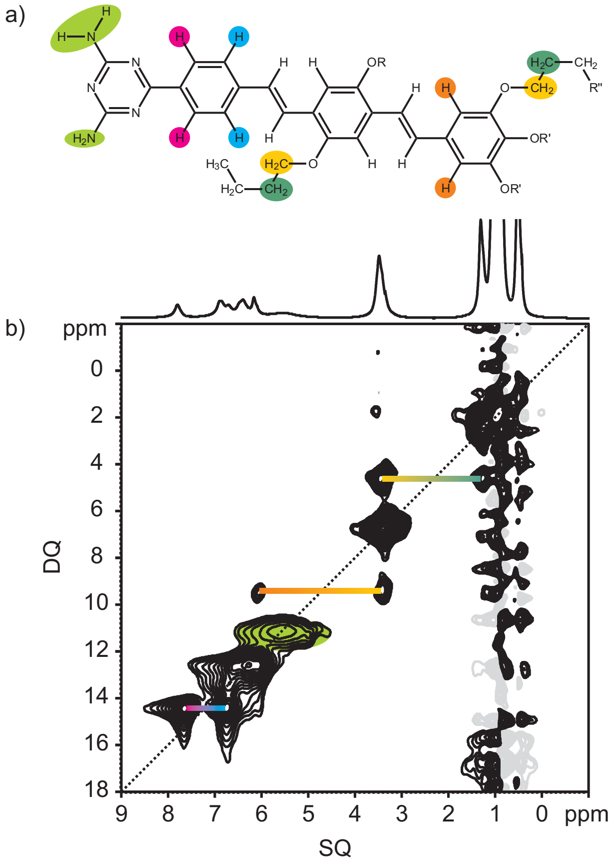

**Figure 5.7.** $^{1}$H-$^{1}$H DQ SQ correlation pattern of A-OPV3T recorded at a temperature close to the melting point (T = 137 °C) and a MAS frequency of 25 kHz. a) Molecular structure of A-OPV3T. b) Colour-coded correlation pattern of A-OPV3T with a vertical noise band on the right.

The most striking feature of the correlation pattern was the appearance of an amino auto peak at (5.6 ppm, 11.2 ppm), coloured in *green*. The width along the single quantum dimension and the significant intensity of the peak suggested that these protons were involved in hydrogen bonds. The $NH_2$ protons apparently still contributed to the integrity of the assembly, although the chemical shift of 5.6 ppm was close to the value of 5.1 ppm obtained in chloroform-*d* solution, indicating the presence of weak hydrogen bonds. It should be noted that a spectrum of S-OPV3T showing a comparable intensity of this auto peak could not be obtained. This might have been due the fact that in the chiral sample the amino protons were either involved in a rigid hydrogen bonding network or are mobile, as indicated by $^1$H and $^2$H MAS NMR. The latter situation suggested amino protons affected by hydrogen bonding on the one hand, which explained the broad line width in the proton spectrum. On the other hand they were able to move and achieved efficient averaging of dipolar interactions on the time scale of the experiment. A-OPV3T on the contrary, showed significant double quantum intensity of coupled amino protons. It also showed a weakening of the hydrogen bonds allowing observation of the amino protons in the first place, however, the hydrogen-bonded protons kept their relative orientations and did not move as quickly as in case of the isotropic solution.

The observation of dipolar coupled amino protons in A-OPV3T in combination with the rapid isotropisation observed in the $^2$H NMR spectra (see section 5.2.2) is a seeming dissent, however, it can be understood by taking into consideration the different nature of dipolar and quadrupolar couplings. Beginning with the quadrupolar coupling, it can be assumed that the principal value of the electric-field-gradient tensor is aligned with the N-$^2$H bond axis. In the amino group, the C-N axis and the N-$^2$H bond axis are oriented at an angle of about 70°, provided full $sp^3$-hybridisation. Assuming a quasi-$sp^2$-hybridisation of the nitrogen the rotation axis and the N-$^2$H bond axis spans an angle approximately 60° the, *i.e.*, very close to the magic angle. If dynamic processes involving a rotation of the amino groups occur more easily in A-OPV3T than in S-OPV3T, a faster isotropisation of the quadrupolar side band pattern in A-OPV3T is expected. From this point of view the appearance of the dipolar-coupled peak of amino protons for A-OPV3T is not surprising, but fully in line with the presumed rotation of the amino protons. The principal axis of the dipolar coupling tensor is defined by the connecting vector of both amino protons which is perpendicular to the rotation axis. The dipolar coupling is therefore not as averaged as the quadrupolar coupling, since even a fast rotation about the C-N axis leads to a decrease of a factor of 1/2 at most[e]. A detailed discussion of a similar behaviour of the quadrupolar coupling tensor can be found for example in [231].

---

[e]

$$\text{Quadrupolar coupling:}\quad P_2 = \frac{1}{2}\left(3\ cos^2(60^\circ) - 1\right) = -0.125$$

$$\text{Internal dipolar coupling:}\quad P_2 = \frac{1}{2}\left(3\ cos^2(90^\circ) - 1\right) = -0.5$$

## 5.3. Conclusions

In this study the supramolecular bulk assembly of oligo-(*p*-phenylenevinylene)s (OPVs) was investigated. All OPVs presented herein underlied a columnar structure formation. It is a non-covalent cooperative process promoted by phase separation between alkyl side chains and the aromatic rigid rods. In order to control the bulk supramolecular self-assembly and thermal behaviour of the OPVs either the polar head group might be changed, the side chain length altered or chiral substituents can be introduced. Crystallinity and long-range organisation was observed for OPV4T arrangements. In contrast, shorter OPV3Ts exhibit a low ordered liquid-crystalline state already at ambient temperatures . The structural analysis showed less order when hydrogen bonding ureidotriazine groups (see figure 5.1) were introduced instead of diaminotriazine functionalities. The lower supramolecular order may reflect the fact that diaminotriazine units were capable of forming hydrogen-bonded hexamers, while in case of ureidotriazine groups only dimers were formed.

The data was also suggesting a minor impact of the chirality itself. However, the intracolumnar order seemed to be sensitive to the steric influence of the alkyl substituents located at the backbone. This was demonstrated by the larger $\pi$-stacking distance in case of S- compared to A-OPVs. The smaller intracolumnar molecular distances of achiral OPVs might have led to a smaller penetration depth of neighbouring columns. This also explains a slightly increased intercolumnar distance of A-OPVs. The X-ray results are summarised in table 5.1.

On the microscopic scale, POM measurements pointed out that the molecular orientation upon the crystallisation process was parallel to the growth direction. Therefore it was assumed that the self-oragnisation was governed by the formation of the hydrogen bonds and $\pi$-$\pi$-interactions played only a secondary role[227]. Moreover, $^1$H MAS NMR measurements found certain differences at the isotropisation point. A-OPV3T provided a more gradual melting behaviour, whereas the transition in S-OPV3T was indicated by an abrupt change in line width. $^2$H MAS NMR pointed to a restricted liberation due to the steric demanding 2-$S$-methylbutoxy group, leading to either molten or rigid components. In case of the achiral OPV the onset of isotropisation was observed at much lower temperatures. This, in combination with the line width, was suggesting a multitude of different hydrogen bonding arrangements and correlation times related to those. Finally, $^1$H-$^1$H DQ-SQ MAS NMR further enlightened the elusive differences of amino protons in the chiral and achiral samples just below the isotropisation point. The amino protons of A-OPV3T seemed to be less mobile compared to their counterparts in S-OPV3T.

| OPV | T \ °C | $a_{hex}{}^{a}$ \ nm | $\pi$-$\pi^{b}$ \ nm | tilt[c] | i.c. order[d] |
|---|---|---|---|---|---|
| A-OPV3T | $Col_{hd}$ 136 I | 5.89 | 0.39 | – | low |
| S-OPV3T | $Col_{hd}$ 136 I | 5.18 | 0.41 | – | good |
| A-OPV4T | Cr 156 $Col_{hd}$ 166 I | 6.35 | 0.39 | 30° | distinct |
| S-OPV4T | 156 $Col_{hd}$ 166 I | 6.13 | 0.52 | 45° | good |
| S-OPV3T-C6 | Cr 172 I | 5.44 | 0.55 | 30° | distinct |
| A-OPV3UT | $Col_{hd}$ | 5.92 | 0.39 | 45° | poor |
| S-OPV3UT | $Col_{hd}$ | 5.68 | 0.42 | – | low |
| A-OPV4UT | $Col_{hd}$ | 6.35 | 0.39 | 45° | poor |
| S-OPV4UT | $Col_{hd}$ | 6.21 | 0.42 | – | low |

*a* intercolumnar distance

*b* intracolumnar molecular distance

*c* tilt angle with respect to the column purpendicular

*d* intracolumnar order

**Table 5.1.** X-ray results on the assembly of all investigated OPVs

In comparison to the well defined formation of helical stacks in alkane solution, pointing towards its possible use as nanowire[216], the solid-state arrangement exhibited a relatively low long range order. This study confirmed the importance of a careful molecular design of organic compounds for implementation in electronic devices. In order to evaluate the present OPVs it should be stated that OPVS show helical arrangements in solution, having electronic properties between molecular aggregates[232] and real conjugated polymers. Apart from the high degree of organisation in the liquid phase, however, they are lacking the desired self-assembling properties in the solid state, which is essential for efficient charge carrier transport.

# 6. Summary and Conclusion

Within this doctoral study three main types of molecules have been investigated, that is, benzene-1,3,5-tricarboxamides (BTAs), a substituted pthalocyanine, and oligo-(*p*-phenylenevinylene)s (OPVs). In order to probe their physical properties various solid-state NMR methods have been applied.

In Chapter 3 results of the investigation on benzene-1,3,5-tricarboxamides (BTAs) have been presented. Apart from their versatile applications, BTAs turned out to serve as excellent model compounds to study supramolecular interactions such as $\pi$-$\pi$-interactions, hydrogen bonding, and steric effects. Their thermal behaviour has been characterised as a function of their molecular design based on the benzene-1,3,5-tricarboxamide core and different side chains attached to it. Moreover, the materials have been investigated with respect to an inversion of the amide group. The second part of the study concerned with the N-centred BTAs, having the nitrogen atom directly attached to the benzene ring in comparison to the CO-centred BTAs.

For all five investigated CO-centred BTAs, a remarkable chemical shift of the backbone protons was found. The amide proton was low-field shifted by ~2.0 ppm at ambient conditions, whereas the aryl proton peak was high-field shifted by approximately -1.5 ppm. On the basis of CPMD simulations, the high-field shift could be ascribed to shielding effects of neighbouring molecules, which relates to the columnar assembly of the investigated BTAs.

The BTAs have also been investigated by $^1$H solid-state NMR methods with respect to the impact of different alkyl chains on the assembly. The study revealed tremendous differences between the series of BTAs, which manifests itself in the unique behaviour upon the phase transition. In case of the methoxyethyl containing BTA 1 an ordinary melting of the crystalline phase was found. For the two chirally branched BTAs, a side chain related transition in crystalline BTA 2 and a crystal-mesophase transition in BTA 3 have been observed. In general, the thermal behaviour of BTA 1 to 3 was in good agreement with reported phase transitions of these compounds, whereas the results on a linear chain compound BTA 4 revealed a more complex phase behaviour than reported.

For this linear chain BTA, a total number of five phases could be distinguished. It was discovered that only the mesophase above 102 °C forms a stable columnar structure, whereas at ambient conditions a non-columnar structure was preferred. This could be shown by 2D $^1$H-$^{13}$C correlation spectroscopy. The resemblance of proton and carbon NMR spectra of BTA 4 with the spectra of the methyl-capped reference compound BTA 5 with known crystal structure, suggested a similar sheet-like arrangement. Additionally, for BTA 4 kinetic measurements have been carried out to trace the phase transition from the supercooled columnar arrangement to the non-columnar crystalline phase. The experiments demonstrated that it is generally possible to use $^1$H MAS NMR in order to examine the inter-conversion of long-lived species.

The measurements performed on BTA 2 indicated that the chiral branching at the innermost side chain position leads to a high degree of organisation of the hydrogen-bonded scaffold. The crystal-crystal transition of this material could be ascribed to conformational changes within the side chain. The observed phase transition was related to a breaking of the $C_3$-symmetry as demonstrated by $^{13}$C-$^{13}$C through-bond correlation spectroscopy. This symmetry breaking is most likely caused by a specific intercolumnar packing of the side chains.

The N-centred BTAi revealed several striking differences compared to its CO-centred counterparts. Although the organisation was obviously columnar, as identified by 2D $^1$H-$^{13}$C correlation spectroscopy, the assembly lacked specific symmetry properties in contrast to BTA 1 to 4. The cancellation of the $C_3$-symmetry was indicated by the splitting of aryl proton resonances at room temperature. The assumption of the symmetry breaking was supported by the outcome of a molecular dynamics study, which showed an excellent agreement with experimental chemical shift values obtained from solid-state $^1$H NMR. The distinct chemical shifts of the aryl protons could be explained by a deviant hydrogen bonding scheme in case of the N-centred BTAi. Compared to the CO-centred BTAs one amide group is apparently rotated by 180°, thus giving rise to one antiparallel hydrogen bond per disk. The proposed assembly was supported by $^1$H-$^1$H DQ-SQ correlation spectroscopy, providing manifest evidence of a tilted ring plane in the columnar assembly of BTAi.

Furthermore, solid-state NMR enabled insight into the dynamics of BTAi. Variable temperature $^1$H MAS NMR revealed a merging of the three distinct aryl proton resonances at higher temperature. Exchange spectroscopy has been used to prove motional averaging of the protons, which could be ascribed to a fast permutation of the different hydrogen bonds. A line shape analysis of variable temperature $^{1}$H MAS NMR spectra allowed to deduce an activation energy of 82.9 ± 3.9 kJ mol$^{-1}$ for this particular process.

In Chapter 4, a peripherally octa-substituted phthalocyanine equipped with thiododecyl moieties has been investigated. A phase transition at 15 °C could be ascribed to a mesophase transition determined by 1D $^{1}$H solid-state NMR techniques. 2D WAXS pattern of the compound indicated a columnar disordered phase with adjacent molecules having an intermolecular distance of 3.9 Å in the crystalline phase and 4.4 Å in the mesophase. 2D $^{1}$H-$^{1}$H DQ-SQ correlation spectroscopy revealed a symmetry breaking of the $D_{4h}$ discs by a less symmetric arrangement, pointing to a herringbone packing of molecules. This assumption was supported by a NICS map of the phthalocyanine ring, indicating that the $^{1}$H chemical shifts could not be explained by molecules oriented perpendicular to the stacking axis. In the crystalline phase a splitting of signals of the ring carbon sites was observed by solid-state $^{13}$C MAS NMR. On the one hand, this was ascribed to shielding effects of the adjacent molecules. On the other hand, the complexity of the splitting strongly suggests ring deformations of the molecules within the columnar arrangement.

In Chapter 5 the results obtained for the supramolecular bulk assembly of oligo-(*p*-phenylenevinylene)s (OPVs) of varying length and with two different polar head groups (i.e., ureidotriazine or diaminotriazine) have been presented. In addition to the variation in length and the terminal group, the compounds were equipped with either chiral 2-*S*-methylbutoxy or achiral butoxy side chains located at the backbone.

All presented OPVs showed a columnar structure formation, which was promoted by phase separation between alkyl side chains and aromatic rigid rods. The structural analysis showed less order when ureidotriazine groups were introduced instead of diaminotriazine functionalities. For arrangements of longer OPVs, a high long-range organisation was observed, whereas shorter OPVs exhibited a low ordered liquid-crystalline state already at ambient temperatures.

The intracolumnar order was found to be sensitive to chiral alkyl substituents located at the backbone. Solid-state $^{1}$H MAS NMR measurements revealed differences upon the isotropisation, however, pointing rather to a steric influence of the additional methyl group of 2-*S*-methylbutoxy but not to the chirality itself. The melting of the short achiral A-OPV3T proceeded more gradually, whereas S-OPV3T provided an abrupt melting process. $^{2}$H MAS NMR indicated a restricted liberation due to the branched

2-*S*-methylbutoxy group, leading to either molten or rigid components. In case of the achiral A-OPV3T, the onset of isotropisation was observed at much lower temperatures, possibly due to the linear butoxy group. POM measurements suggested that the self-organisation is governed by the formation of the H-bonds and $\pi$-$\pi$-interactions play only a secondary role.

# Bibliography

[1] D. Filmore, Carbon Electronics, *Today's Chemist at Work*, **2002**.

[2] C. Chiang, C. Fincher, Y. Park, *et al.*, Electrical-Conductivity in Doped Polyacetylene, *Phys. Rev. Lett.*, 39, **1977**, 1098.

[3] J. H. Burroughes, D. D. C. Bradley, A. R. Brown, *et al.*, Light-Emitting-Diodes Based on Conjugated Polymers, *Nature*, 347, **1990**, 539.

[4] S. W. Lee, The LCD Revolution: The Third Wave, Technical report, Samsung, **2005**.

[5] X. Yang, J. Loos, Toward high-performance polymer solar cells: The importance of morphology control, *Macromolecules*, 40, **2007**, 1353.

[6] M. A. Rahman, P. Kumar, D.-S. Park, *et al.*, Electrochemical sensors based on organic conjugated polymers, *Sensors*, 8, **2008**, 118.

[7] H. Sirringhaus, Device physics of Solution-processed organic field-effect transistors, *Adv. Mater.*, 17, **2005**, 2411.

[8] J. Wu, W. Pisula, K. Muellen, Graphenes as potential material for electronics, *Chem. Rev.*, 107, **2007**, 718.

[9] J. Keeler, *Understanding NMR*, Wiley and Sons, $1^{st}$ edition, **2005**.

[10] M. H. Levitt, *Spin Dynamics: Basics of Nuclear Magnetic Resonance*, Wiley and Sons, $2^{nd}$ edition, **2008**.

[11] M. J. Duer, *Introduction to Solid-State NMR Spectroscopy*, Blackwell Publishing, $1^{st}$ edition, **2004**.

[12] A. Abragam, *The Priciples of Neclar Megnetism*, Oxford University Press, $1^{st}$ edition, **1983**.

[13] R. E. Ernst, G. Bodenhausen, A. Wokaun, *Principles of Nuclear Magnetic Resonance in One and in Two Dimensions*, Oxford University Press, $1^{st}$ edition, **1987**.

[14] M. Mehring, *Principles of High-Resolution NMR in Solids*, Springer, $2^{nd}$ edition, **1983**.

[15] K. Schmidt-Rohr, H. W. Spiess, *Multidimensional Solid-State NMR and Polymers*, Academic Press, $1^{st}$ edition, **1994**.

[16] W. Gordy, R. L. Cook, *Microwave Molecular Spectra*, Wiley and Sons, $1^{st}$ edition, **1984**.

[17] H. W. Kroto, *Molecular Rotation Spectra*, Dover Publications, $1^{st}$ edition, **1992**.

[18] J. J. Sakurai, *Modern Quantum Mechanics*, Addison Wesley Publishing Company, $1^{st}$, rev. edition, **1994**.

[19] R. N. Zare, *Angular Momentum: Understanding Spatial Aspects in Chemistry and Physics*, Wiley-VCH, $1^{st}$ edition, **1988**.

[20] M. M. Maricq, J. S. Waugh, NMR in Rotating Solids, *J. Chem. Phys.*, 70, **1979**, 3300.

[21] O. W. Sorensen, G. W. Eich, M. H. Levitt, *et al.*, Product Operator-Formalism for the Description of NMR Pulse Experiments, *Prog. Nucl. Magn. Reson. Spectrosc.*, 16, **1983**, 163.

[22] V. Macho, L. Brombacher, H. Spiess, The NMR-WEBLAB: an internet approach to NMR lineshape analysis, *Appl. Magn. Reson.*, 20, **2001**, 405.

[23] M. Wind, R. Graf, A. Heuer, *et al.*, Structural relaxation of polymers at the glass transition: Conformational memory in poly(n-alkylmethacrylates), *Phys. Rev. Lett.*, 91, **2003**, 155702.

[24] J. H. Ok, R. R. Vold, R. L. Vold, *et al.*, Deuterium Nuclear Magnetic-Resonance Measurements of Rotation snd Libration of Benzene in a Solid-State Cyclamer, *J. Phys. Chem.*, 93, **1989**, 7618.

[25] J. Lorieau, A. McDermott, Order parameters based on (CH)-C-13-H-1, (CH2)-C-13-H-1 and (CH3)-C-13-H-1 heteronuclear dipolar powder patterns: a comparison of MAS-based solid-state NMR sequences, *Magn. Reson. Chem.*, 44, **2006**, 334.

[26] E. Wigner, Einige Folgerungen aus der Schrödingerschen Theorie für die Termstrukturen, *Z. Phys.*, 45, **1927**, 624.

[27] C. Eckart, The application of group theory to the quantum dynamics of monatomic systems, *Rev. Mod. Phys.*, 2, **1930**, 0305.

[28] A. Jerschow, From nuclear structure to the quadrupolar NMR interaction and high-resolution spectroscopy, *Prog. Nucl. Magn. Reson. Spectrosc.*, 46, **2005**, 63.

[29] T. P. Das, E. L. Hahn, Nuclear Quadrupole Resonance Spectroscopy, in: *Solid State Physics, Supl. 1*, Academic Press, NY, **1958**, 83.

[30] G. E. Pake, Nuclear Resonance Absorption in Hydrated Crystals - Fine Structure of the Proton Line, *J. Chem. Phys.*, 16, **1948**, 327.

[31] M. Hesse, H. Meier, B. Zeeh, *Spektroskopische Methoden in der Organischen Chemie*, Thieme Verlag, $6^{th}$ edition, **2002**.

[32] H. Fribolin, *Ein- und zweidimensionale NMR-Spektroskopie*, Wiley-VCH, $3^{rd}$ edition, **1999**.

[33] E. Andrew, A. Bradbury, R. Eades, Nuclear Magnetic Resonance Spectra From A Crystal Rotated At High Speed, *Nature*, 182, **1958**, 1659.

[34] I. Lowe, Free Induction Decays of Rotating Solids, *Phys. Rev. Lett.*, 2, **1959**, 285.

[35] A. Samoson, T. Tuherm, J. Past, *et al.*, New horizons for magic-angle spinning NMR, *Top. Curr. Chem.*, 246, **2005**, 15.

[36] S. Brown, H. Spiess, Advanced solid-state NMR methods for the elucidation of structure and dynamics of molecular, macromolecular, and supramolecular systems, *Chem. Rev.*, 101, **2001**, 4125.

[37] K. Yamauchi, S. Kuroki, K. Fujii, *et al.*, The amide proton NMR chemical shift and hydrogen-bonded structure of peptides and polypeptides in the solid state as studied by high-frequency solid-state H-1 NMR, *Chem. Phys. Lett.*, 324, **2000**, 435.

[38] G. Goward, D. Sebastiani, I. Schnell, *et al.*, Benzoxazine oligomers: Evidence for a helical structure from solid-state NMR spectroscopy and DFT-based dynamics and chemical shift calculations, *J. Am. Chem. Soc.*, 125, **2003**, 5792.

[39] P. Schleyer, C. Maerker, A. Dransfeld, *et al.*, Nucleus-independent chemical shifts: A simple and efficient aromaticity probe, *J. Am. Chem. Soc.*, 118, **1996**, 6317.

[40] W. K. Rhim, A. Pines, J. S. Waugh, Time-Reversal Experiments in Dipolar-Coupled Spin Systems, *Phys. Rev. B: Condens. Matter*, 3, **1971**, 684.

[41] R. E. Taylor, R. G. Pembleton, L. M. Ryan, *et al.*, Combined Multiple Pulse NMR and Sample Spinning - Recovery of H-1 Chemical-Shift Tensors, *J. Chem. Phys.*, 71, **1979**, 4541.

[42] G. G. Brown, B. C. Dian, K. O. Douglass, *et al.*, A broadband Fourier transform microwave spectrometer based on chirped pulse excitation, *Rev. Sci. Instrum.*, 79, **2008**, 053103.

[43] D. Hoult, R. Richards, Critical Factors In Design Of Sensitive High-Resolution Nuclear Magnetic-Resonance Spectrometers, *Proc. R. Soc. London, Ser. A*, 344, **1975**, 311.

[44] G. Bodenhausen, R. Freeman, D. Turner, Suppression of Artifacts in 2-Dimensional J Spectroscopy, *J. Magn. Reson.*, 27, **1977**, 511.

[45] L. Muller, A. Kumar, R. R. Ernst, 2-Dimensional C-13 NMR-Spectroscopy, *J. Chem. Phys.*, 63, **1975**, 5490.

[46] J. Jeener, Oral presentation in Ampere International Summer School II, **1971**.

[47] D. J. States, R. A. Haberkorn, D. J. Ruben, A Two-Dimensional Nuclear Overhauser Experiment with Pure Absorption Phase in 4 Quadrants, *J. Magn. Reson.*, 48, **1982**, 286.

[48] D. Marion, K. Wüthrich, Application of Phase Sensitive Two-Dimensional Correlated Spectroscopy (COSY) for Measurements Of $H^1$-$H^1$ Spin-Spin Coupling-Constants In Proteins, *Biochem. Biophys. Res. Commun.*, 113, **1983**, 967.

[49] D. Marion, M. Ikura, R. Tschudin, *et al.*, Rapid Recording Of 2D Nmr-Spectra Without Phase Cycling - Application To The Study Of Hydrogen-Exchange In Proteins, *J. Magn. Reson.*, 85, **1989**, 393.

[50] G. A. Morris, R. Freeman, Enhancement of Nuclear Magnetic-Resonance Signals by Polarization Transfer, *J. Am. Chem. Soc.*, 101, **1979**, 760.

[51] A. Pines, M. G. Gibby, J. S. Waugh, Proton-Enhanced NMR of Dilute Spins in Solids, *J. Chem. Phys.*, 59, **1973**, 569.

[52] S. R. Hartmann, E. L. Hahn, Nuclear Double Resonance in Rotating Frame, *Phys. Rev.*, 128, **1962**, 2042.

[53] X. L. Wu, S. M. Zhang, X. W. Wu, 2-Stage Feature of Hartmann-Hahn Cross Relaxation in Magic-Angle Sample Spinning, *Phys. Rev. B: Condens. Matter*, 37, **1988**, 9827.

[54] G. Metz, X. L. Wu, S. O. Smith, Ramped-Amplitude Cross-Polarization in Magic-Angle-Spinning NMR, *J. Magn. Reson. Ser. A*, 110, **1994**, 219.

[55] O. B. Peersen, X. L. Wu, I. Kustanovich, *et al.*, Variable-Amplitude Cross-Polarization MAS NMR, *J. Magn. Reson. Ser. A*, 104, **1993**, 334.

[56] J. S. Waugh, Theory of Broad-Band Spin Decoupling, *J. Magn. Reson.*, 50, **1982**, 30.

[57] A. Bennett, C. Rienstra, M. Auger, *et al.*, Heteronuclear Decoupling in Rotating Solids, *J. Chem. Phys.*, 103, **1995**, 6951.

[58] B. Fung, A. Khitrin, K. Ermolaev, An improved broadband decoupling sequence for liquid crystals and solids, *J. Magn. Reson.*, 142, **2000**, 97.

[59] A. Detken, E. Hardy, M. Ernst, *et al.*, Simple and efficient decoupling in magic-angle spinning solid-state NMR: the XiX scheme, *Chem. Phys. Lett.*, 356, **2002**, 298.

[60] M. Weingarth, P. Tekely, G. Bodenhausen, Efficient heteronuclear decoupling by quenching rotary resonance in solid-state NMR, *Chem. Phys. Lett.*, 466, **2008**, 247.

[61] S. Dusold, A. Sebald, Dipolar recoupling under Magic-Angle Spinning conditions, in: *Annual reports on NMR spectroscopy*, Academic Press, **2000**, 185–264.

[62] M. Lee, W. I. Goldburg, Nuclear-Magnetic-Resonance Line Narrowing by a Rotating RF Field, *Phys. Rev.*, 140, **1965**, 1261.

[63] A. Bielecki, A. Kolbert, M. Levitt, Frequency-Switched Pulse Sequences – Homonuclear Decoupling and Dilute Spin NMR in Solids, *Chem. Phys. Lett.*, 155, **1989**, 341.

[64] A. Lesage, S. Steuernagel, L. Emsley, Carbon-13 spectral editing in solid-state NMR using heteronuclear scalar couplings, *J. Am. Chem. Soc.*, 120, **1998**, 7095.

[65] P. Charmont, A. Lesage, S. Steuernagel, *et al.*, Sample restriction using magnetic field gradients in high-resolution solid-state NMR, *J. Magn. Reson.*, 145, **2000**, 334.

[66] E. Vinogradov, P. Madhu, S. Vega, High-resolution proton solid-state NMR spectroscopy by phase-modulated Lee-Goldburg experiment, *Chem. Phys. Lett.*, 314, **1999**, 443.

[67] C. Coelho, J. Rocha, P. K. Madhu, *et al.*, Practical aspects of Lee-Goldburg based CRAMPS techniques for high-resolution H-1 NMR spectroscopy in solids: Implementation and applications, *J. Magn. Reson.*, 194, **2008**, 264.

[68] J. Jeener, B. H. Meier, P. Bachmann, *et al.*, Investigation of Exchange Processes by 2-Dimensional NMR-Spectroscopy, *J. Chem. Phys.*, 71, **1979**, 4546.

[69] I. Solomon, Relaxation Processes in a System of 2 Spins, *Phys. Rev.*, 99, **1955**, 559.

[70] T. Gullion, J. Schaefer, Rotational-Echo Double-Resonance NMR, *J. Magn. Reson.*, 81, **1989**, 196.

[71] L. Duma, W. Lai, M. Carravetta, *et al.*, Principles of spin-echo modulation by J-couplings in magic-angle-spinning solid-state NMR, *ChemPhysChem*, 5, **2004**, 815.

[72] J. Herzfeld, A. E. Berger, Sideband Intensities In NMR-Spectra Of Samples Spinning At The Magic Angle, *J. Chem. Phys.*, 73, **1980**, 6021.

[73] E. O. Stejskal, J. Schaefer, R. A. Mckay, High-Resolution, Slow-Spinning Magic-Angle C-13 Nmr, *J. Magn. Reson.*, 25, **1977**, 569.

[74] M. H. Levitt, Symmetry in the design of NMR multiple-pulse sequences, *J. Chem. Phys.*, 128, **2008**, 052205.

[75] M. H. Levitt, Symmetry-Based Pulse Sequences in Magic-Angle Spinning Solid-State NMR, in: *Encyclopedia of Nuclear Magnetic Resonance: Supplementary Volume*, **2002**, 165–196.

[76] D. P. Weitekamp, J. R. Garbow, A. Pines, Determination of Dipole Coupling-Constants Using Heteronuclear Multiple Quantum NMR, *J. Chem. Phys.*, 77, **1982**, 2870.

[77] E. deAzevedo, W. Hu, T. Bonagamba, *et al.*, Centerband-only detection of exchange: Efficient analysis of dynamics in solids by NMR, *J. Am. Chem. Soc.*, 121, **1999**, 8411.

[78] G. Bodenhausen, D. Ruben, Natural Abundance N-15 NMR by Enhanced Heteronuclear Spectroscopy, *Chem. Phys. Lett.*, 69, **1980**, 185.

[79] K. Saalwachter, R. Graf, H. Spiess, Recoupled polarization transfer heteronuclear H-1-C-13 multiple-quantum correlation in solids under ultra-fast MAS, *J. Magn. Reson.*, 140, **1999**, 471.

[80] K. Saalwachter, R. Graf, H. Spiess, Recoupled polarization-transfer methods for solid-state H-1-C-13 heteronuclear correlation in the limit of fast MAS, *J. Magn. Reson.*, 148, **2001**, 398.

[81] M. Feike, D. Demco, R. Graf, *et al.*, Broadband multiple-quantum NMR spectroscopy, *J. Magn. Reson. Ser. A*, 122, **1996**, 214.

[82] U. Friedrich, I. Schnell, D. Demco, *et al.*, Triple-quantum NMR spectroscopy in dipolar solids, *Chem. Phys. Lett.*, 285, **1998**, 49.

[83] I. Schnell, H. Spiess, High-resolution H-1 NMR spectroscopy in the solid state: Very fast sample rotation and multiple-quantum coherences, *J. Magn. Reson.*, 151, **2001**, 153.

[84] I. Schnell, Dipolar recoupling in fast-MAS solid-state NMR spectroscopy, *Prog. Nucl. Magn. Reson. Spectrosc.*, 45, **2004**, 145.

[85] S. P. Brown, Probing proton-proton proximities in the solid state, *Prog. Nucl. Magn. Reson. Spectrosc.*, 50, **2007**, 199.

[86] I. Schnell, A. Watts, H. Spiess, Double-quantum double-quantum MAS exchange NMR spectroscopy: Dipolar-coupled spin pairs as probes for slow molecular dynamics, *J. Magn. Reson.*, 149, **2001**, 90.

[87] H. Geen, J. J. Titman, J. Gottwald, *et al.*, Spinning Side-Band in ihe Fast-MAS Multiple-Quantum Spectra Of Protons In Solids, *J. Magn. Reson. Ser. A*, English, **1995**, 264.

[88] J. Gottwald, D. E. Demco, R. Graf, *et al.*, High-Resolution Double-Quantum NMR-Spectroscopy of Homonuclear Spin Pairs and Proton Connectivities in Solids, *Chem. Phys. Lett.*, 243, **1995**, 314.

[89] U. Friedrich, I. Schnell, S. Brown, *et al.*, Spinning-sideband patterns in multiple-quantum magic-angle spinning NMR spectroscopy, *Mol. Phys.*, 95, **1998**, 1209.

[90] R. Graf, D. Demco, J. Gottwald, *et al.*, Dipolar couplings and internuclear distances by double-quantum nuclear magnetic resonance spectroscopy of solids, *J. Chem. Phys.*, 106, **1997**, 885.

[91] B. Langer, Untersuchung supramolekularer Ordnungsphänomene mittels $^1$H MAS Mehrquanten NMR-Spektroskopie in festen und in Flüssigkristallinen Phasen, Ph.D. thesis, Universität Mainz, **2001**.

[92] R. Graf, D. Demco, S. Hafner, *et al.*, Selective residual dipolar couplings in cross-linked elastomers by H-1 double-quantum NMR spectroscopy, *Solid State Nucl. Magn. Reson.*, 12, **1998**, 139.

[93] A. Bax, R. Freeman, S. Kempsell, Natural Abundance C-13-C-13 Coupling Observed Via Double-Quantum Coherence, *J. Am. Chem. Soc.*, 102, **1980**, 4849.

[94] A. Bax, R. Freeman, T. A. Frenkiel, An NMR Technique For Tracing Out the Carbon Skeleton Of An Organic-Molecule, *J. Am. Chem. Soc.*, 103, **1981**, 2102.

[95] J. Buddrus, H. Bauer, Direct Identification Of The Carbon Skeleton Of Organic-Compounds Using Double Quantum Coherence C-13-Nmr Spectroscopy - The Inadequate Pulse Sequence, *Angew. Chem. Int. Ed.*, 26, **1987**, 625.

[96] R. Benn, Editing Of C-13-C-13 Satellite Spectra Via C-H Couplings, *J. Magn. Reson.*, 55, **1983**, 460.

[97] M. Baldus, B. Meier, Total correlation spectroscopy in the solid state. The use of scalar couplings to determine the through-bond connectivity, *J. Magn. Reson. Ser. A*, 121, **1996**, 65.

[98] M. Baldus, R. Iuliucci, B. Meier, Probing through-bond connectivities and through-space distances in solids by magic-angle-spinning nuclear magnetic resonance, *J. Am. Chem. Soc.*, 119, **1997**, 1121.

[99] R. Iuliucci, B. Meier, A characterization of the linear p-o-p bonds in M4+(P2O7) compounds: Bond-angle determination by solid-state NMR, *J. Am. Chem. Soc.*, 120, **1998**, 9059.

[100] A. Lesage, C. Auger, S. Caldarelli, *et al.*, Determination of through-bond carbon-carbon connectivities in solid-state NMR using the INADEQUATE experiment, *J. Am. Chem. Soc.*, 119, **1997**, 7867.

[101] C. A. Fyfe, H. Grondey, Y. Feng, *et al.*, Natural-Abundance 2-Dimensional Si-29 Mas Nmr Investigation Of The 3-Dimensional Bonding Connectivities In The Zeolite Catalyst Zsm-5, *J. Am. Chem. Soc.*, 112, **1990**, 8812.

[102] A. Lesage, M. Bardet, L. Emsley, Through-bond carbon-carbon connectivities in disordered solids by NMR, *J. Am. Chem. Soc.*, 121, **1999**, 10987.

[103] N. C. Nielsen, H. Thogersen, O. Sorensen, Doubling the Sensitivity of INADEQUATE for Tracing out the Carbon Skeleton of Molecules by NMR, *J. Am. Chem. Soc.*, 117, **1995**, 11365.

[104] N. C. Nielsen, H. Thogersen, O. W. Sorensen, A systematic strategy for design of optimum coherent experiments applied to efficient interconversion of double- and single-quantum coherences in nuclear magnetic resonance, *J. Chem. Phys.*, 105, **1996**, 3962.

[105] I. Podkorytov, Multipulse NMR - Part III. INADEQUATE pulse sequence, *Concepts Magn. Reson.*, 11, **1999**, 97.

[106] A. Meissner, O. Sorensen, Exercise in modern NMR pulse sequence design: INADEQUATE CR, *Concepts Magn. Reson.*, 14, **2002**, 141.

[107] S. Cadars, J. Sein, L. Duma, *et al.*, The refocused INADEQUATE MAS NMR experiment in multiple spin-systems: Interpreting observed correlation peaks and optimising lineshapes, *J. Magn. Reson.*, 188, **2007**, 24.

[108] I. Fischbach, T. Pakula, P. Minkin, *et al.*, Structure and Dynamics in Columnar Discotic Materials:  A Combined X-ray and Solid-State NMR Study of Hexabenzocoronene Derivatives, *J. Phys. Chem. B*, 106, **2002**, 6408.

[109] A. R. A. Palmans, E. W. Meijer, Amplification of chirality in dynamic supramolecular aggregates, *Angew. Chem. Int. Ed.*, 46, **2007**, 8948.

[110] A. R. A. Palmans, J. A. J. M. Vekemans, H. Kooijman, *et al.*, Hydrogen-bonded porous solid derived from trimesic amide, *Chem. Commun.*, **1997**, 2247.

[111] A. R. A. Palmans, J. A. J. M. Vekemans, H. Fischer, *et al.*, Extended-core discotic liquid crystals based on the intramolecular H-bonding in N-acylated 2,2'-bipyridine-3,3'-diamine moieties, *Chem. Eur. J.*, 3, **1997**, 300.

[112] A. Hoffmann, Characterisation of Supramolecular Structures by Novel Recoupling Methods in Solid-State NMR, Ph.D. thesis, Universität Mainz, **2005**.

[113] J. J. van Gorp, J. A. J. M. Vekemans, E. W. Meijer, C-3-symmetrical supramolecular architectures: Fibers and organic gels from discotic trisamides and trisureas, *J. Am. Chem. Soc.*, 124, **2002**, 14759.

[114] A. R. A. Palmans, J. A. J. M. Vekemans, E. E. Havinga, *et al.*, Sergeants-and-Soldiers Principle in Chiral Columnar Stacks of Disc-Shaped Molecules with $C_3$-Symmetry, *Angew. Chem. Int. Ed.*, 36, **1997**, 2648.

[115] M. M. Green, M. P. Reidy, R. D. Johnson, *et al.*, Macromolecular stereochemistry: the out-of-proportion influence of optically active comonomers on the conformational characteristics of polyisocyanates. The sergeants and soldiers experiment, *J. Am. Chem. Soc.*, 111, **1989**, 6452.

[116] M. M. Green, B. A. Garetz, B. Munoz, *et al.*, Majority Rules in the Copolymerization of Mirror Image Isomers, *J. Am. Chem. Soc.*, 117, **1995**, 4181.

[117] M. P. Lightfoot, F. S. Mair, R. G. Pritchard, *et al.*, New supramolecular packing motifs: pi-stacked rods encased in triply-helical hydrogen bonded amide strands, *Chem. Commun.*, 0, **1999**, 1945.

[118] A. F. Hollemann, E. Wiberg, N. Wiberg, *Lehrbuch der anorganischen Chemie*, de Gruyter, $101^{st}$ edition, **1995**.

[119] M. O. Sinnokrot, C. D. Sherrill, High-Accuracy Quantum Mechanical Studies of $\pi$-$\pi$ Interactions in Benzene Dimers, *J. Phys. Chem. A*, 110, **2006**, 10656.

[120] E. Fan, J. Yang, S. J. Geib, *et al.*, Hydrogen-bonding Control of Molecular Aggregation: Self-complementary Subunits lead to Rod-shaped Structures in the Solid State, *J. Chem. Soc., Chem. Commun.*, 12, **1995**, 1251.

[121] Y. Matsunaga, Y. Nakayasu, S. Sakai, *et al.*, Liquid Crystal Phases Exhibited by N,N',N"-Trialkyl-1,3,5-Benzenetricaboxamides, *Mol. Cryst. Liq. Cryst.*, 141, **1986**, 327.

[122] Y. Matsunaga, N. Miyajima, Y. Nakayasu, *et al.*, Design Of Novel Mesomorphic Compounds - N,N',N"-Trialkyl-1,3,5-Benzenetricarboxamides, *Bull. Chem. Soc. Jpn.*, 61, **1988**, 207.

[123] P. Stals, M. Smulders, R. MartÌn-RapÀôn, *et al.*, Asymmetrically Substituted Benzene-1,3,5-tricarboxamides: Self-Assembly and Odd-Even Effects in the Solid State and in Dilute Solution, *Chem. Eur. J.*, 15, **2009**, 2071.

[124] P. J. M. Stals, J. F. Haveman, R. Martin-Rapun, *et al.*, The influence of oligo(ethylene glycol) side chains on the self-assembly of benzene-1,3,5-tricarboxamides in the solid state and in solution, *J. Mater. Chem.*, 19, **2009**, 124.

[125] Y. Yasuda, E. Iishi, H. Inada, *et al.*, Novel low-molecular-weight organic gels: N,N',N"-tristearyltrimesamide/organic solvent system, *Chem. Lett.*, 7, **1996**, 575.

[126] T. Shikata, D. Ogata, K. Hanabusa, Viscoelastic behavior of supramolecular polymeric systems consisting of N,N',N"-tris(3,7-dimethyloctyl)benzene-1,3,5-tricarboxamide and n-alkanes, *J. Phys. Chem. B*, 108, **2004**, 508.

[127] K. Hanabusa, C. Koto, M. Kimura, *et al.*, Remarkable viscoelasticity of organic solvents containing trialkyl-1,3,5-benzenetricarboxamides and their intermolecular hydrogen bonding, *Chem. Lett.*, 5, **1997**, 429.

[128] H. Enomoto, Y. Einaga, A. Teramoto, Viscosity of aqueous solutions of a triple-helical polysaccharide schizophyllan, *Macromolecules*, 17, **1984**, 1573.

[129] F. Oosawa, M. Kasai, Theory of Linear and Helical Aggregates of Macromolecules, *J. Mol. Biol.*, 4, **1962**, 10.

[130] M. M. J. Smulders, A. P. H. J. Schenning, E. W. Meijer, Insight into the Mechanisms of Cooperative Self-Assembly: The SSergeants-and-SoldiersPPrinciple of Chiral and Achiral C3-Symmetrical Discotic Triamides, *J. Am. Chem. Soc.*, 130, **2008**, 606.

[131] J. van Gestel, Amplification of Chirality of the Majority-Rules Type in Helical Supramolecular Polymers: The Impact of the Presence of Achiral Monomers, *J. Phys. Chem. B*, 110, **2006**, 4365.

[132] A. J. Wilson, M. Masuda, R. P. Sijbesma, *et al.*, Chiral amplification in the transcription of supramolecular helicity into a polymer backbone, *Angew. Chem. Int. Ed.*, 44, **2005**, 2275.

[133] J. van Gestel, A. R. A. Palmans, B. Titulaer, *et al.*, “Majority-Rules” Operative in Chiral Columnar Stacks of C3-Symmetrical Molecules, *J. Am. Chem. Soc.*, 127, **2005**, 5490.

[134] T. Shikata, D. Ogata, K. Hanabusa, Viscoelastic behavior of a supramolecular polymeric system consisting of tri-3,7-dimethyloctyl cis-1,3,5-cyclohexanetricarboxamide and n-decane, *J. Soc. Rheol. Jpn.*, 31, **2003**, 229.

[135] P. P. Bose, M. G. B. Drew, A. K. Das, *et al.*, Formation of triple helical nanofibers using self-assembling chiral benzene-1,3,5-tricarboxamides and reversal of the nanostructure’s handedness using mirror image building blocks, *Chem. Commun.*, **2006**, 3196.

[136] M. Masuda, P. Jonkheijm, R. P. Sijbesma, *et al.*, Photoinitiated polymerization of columnar stacks of self-assembled trialkyl-1,3,5-benzenetricarboxamide derivatives, *J. Am. Chem. Soc.*, 125, **2003**, 15935.

[137] L. Brunsveld, A. P. H. J. Schenning, M. A. C. Broeren, *et al.*, Chiral amplification in columns of self-assembled N,N’,N”-tris((S)-3,7-dimethyloctyl)benzene-1,3,5-tricarboxamide in dilute solution, *Chem. Lett.*, 3, **2000**, 292.

[138] J. Roosma, T. Mes, P. Leclere, *et al.*, Supramolecular materials from benzene-1,3,5-tricarboxamide-based nanorods, *J. Am. Chem. Soc.*, 130, **2008**, 1120.

[139] M. Blomenhofer, S. Ganzleben, D. Hanft, *et al.*, Designer Nucleating Agents for Polypropylene, *Macromolecules*, 38, **2005**, 3688.

[140] C. Ochsenfeld, S. Brown, I. Schnell, *et al.*, Structure assignment in the solid state by the coupling of quantum chemical-calculations with NMR experiments: A columnar hexabenzocoronene derivative, *J. Am. Chem. Soc.*, 123, **2001**, 2597.

[141] T. F. A. de Greef, M. M. L. Nieuwenhuizen, P. J. M. Stals, *et al.*, The influence of ethylene glycol chains on the thermodynamics of hydrogen-bonded supramolecular assemblies in apolar solvents, *Chem. Commun.*, **2008**, 4306.

[142] T. F. A. de Greef, personal communication.

[143] D. Suwelack, W. P. Rothwell, J. S. Waugh, Slow Molecular-Motion Detected In The Nmr-Spectra Of Rotating Solids, *J. Chem. Phys.*, 73, **1980**, 2559.

[144] C. F. C. Fitié, Hydrogen Bonded Columnar Liquid Crystals for Nanostructured Materials, Ph.D. thesis, TU Eindhoven, **2010**.

[145] M. M. Elmahdy, M. Mondeshki, X. Dou, *et al.*, Slow kinetics of phase transformation in a dipole-functionalized discotic liquid crystal, *J. Chem. Phys.*, 131, **2009**, 114704.

[146] D. Ogata, T. Shikata, K. Hanabusa, Chiral amplification of the structure and viscoelasticity of a supramolecular polymeric system consisting of N,N',N"-tris(3,7-dimethyloctyl)benzene-1,3,5-tricarboxamide and n-decane, *J. Phys. Chem. B*, 108, **2004**, 15503.

[147] E. R. Andrew, A. Bradbury, R. G. Eades, *et al.*, Nuclear Cross-Relaxation Induced by Specimen Rotation, *Phys. Lett.*, 4, **1963**, 99.

[148] D. P. Raleigh, M. H. Levitt, R. G. Griffin, Rotational Resonance In Solid-State NMR, *Chem. Phys. Lett.*, 146, **1988**, 71.

[149] A. E. Tonelli, Calculated Gamma-Effects on C-13-NMR Spectra of 3,5,7,9,11,13,15-Heptamethylheptadecane Stereoisomers and Their Implications for Conformational Characteristics Of Polypropylene, *Macromolecules*, 11, **1978**, 565.

[150] M. Moller, W. Gronski, H. J. Cantow, *et al.*, Discrimination of Rotational Isomeric States in Cycloalkanes by Solid-State CP-MAS C-13 NMR-Spectroscopy, *J. Am. Chem. Soc.*, 106, **1984**, 5093.

[151] D. L. VanderHart, Influence of Molecular Packing on Solid-State C-13 Chemical-Shifts - The N-Alkanes, *J. Magn. Reson.*, 44, **1981**, 117.

[152] A. R. A. Palmans, personal communication.

[153] D. Massiot, F. Fayon, M. Capron, *et al.*, Modelling one- and two-dimensional solid-state NMR spectra, *Magn. Reson. Chem.*, 40, **2002**, 70.

[154] S. Brown, I. Schnell, J. Brand, *et al.*, The competing effects of pi-pi packing and hydrogen bonding in a hexabenzocoronene carboxylic acid derivative: A H-1 solid-state MAS NMR investigation, *Phys. Chem. Chem. Phys.*, 2, **2000**, 1735.

[155] A. Braun, J. Tcherniac, The products of the action of acet-anhydride on phthalamide., *Ber. Dtsch. Chem. Ges.*, 40, **1907**, 2709.

[156] C. E. Dent, R. P. Linstead, A. R. Lowe, Phthalocyanines part VI The structure of the phthalocyanines, *J. Chem. Soc.*, **1934**, 1033.

[157] J. M. Robertson, An X-ray study of the phthalocyanines - Part II Quantitative structure determination of the metal-free compound, *J. Chem. Soc.*, **1936**, 1195.

[158] B. F. Hoskins, S. A. Mason, J. C. B. White, Location of Inner Hydrogen Atoms of Phthalocyanine - A Neutron Diffraction Study, *J. Chem. Soc. D*, **1969**, 554.

[159] J. Mizuguchi, S. Matsumoto, Molecular distortion and exciton coupling effects in beta metal-free phthalocyanine, *J. Phys. Chem. A*, 103, **1999**, 614.

[160] A. B. P. Lever, The Phthalocyanines, in: *Adv. Inorg. Chem. Radiochem.*, volume 27, **1965**, 27–114.

[161] P. Gregory, Steamrollers, sports cars and security: Phthalocyanine progress through the ages, *J. Porphyrins Phthalocyanines*, 3, **1999**, 468.

[162] T. Nyokong, S. Vilakazi, Phthalocyanines and related complexes as electrocatalysts for the detection of nitric oxide, *Talanta*, 61, **2003**, 27.

[163] M. Bora, D. Schut, M. A. Baldo, Combinatorial detection of volatile organic compounds using metal-phthalocyanine field effect transistors, *Anal. Chem.*, 79, **2007**, 3298.

[164] R. Mason, G. A. Williams, P. E. Fielding, Structural Chemistry of Phthalocyaninato-cobalt(ii) and Manganese(ii), *J. Chem. Soc., Dalton Trans.*, **1979**, 676.

[165] K. Yase, N. Yasuoka, T. Kobayashi, *et al.*, Structure of Metal-free Phthalocyanine Stabilized By the Addition of Its 4-chloro Derivative, *Acta Crystallogr., Sect. C: Cryst. Struct. Commun.*, 44, **1988**, 514.

[166] K. Y. Law, Organic photoconductive materials: recent trends and developments, *Chem. Rev.*, 93, **1993**, 449.

[167] R. B. Hammond, K. J. Roberts, R. Docherty, *et al.*, X-form metal-free phthalocyanine: Crystal structure determination using a combination of high-resolution X-ray powder diffraction and molecular modelling techniques, *J. Chem. Soc., Perkin Trans. 2*, **1996**, 1527.

[168] J. H. Sharp, M. Lardon, Spectroscopic Characterization of A New Polymorph of Metal-free Phthalocyanine, *J. Phys. Chem.*, 72, **1968**, 3230.

[169] C. Piechocki, J. Simon, A. Skoulios, *et al.*, Discotic Mesophases Obtained From Substituted Metallophthalocyanines - Towards Liquid-crystalline One-dimensional Conductors, *J. Am. Chem. Soc.*, 104, **1982**, 5245.

[170] N. B. McKeown, *Phthalocyanine Materials*, Press Syndicate of the University of Manchester, 1$^{st}$ edition, **1998**.

[171] K. Ohta, L. Jacquemin, C. Sirlin, *et al.*, Influence of the Nature of the Side-chains On the Mesomorphic Properties of Octasubstituted Phthalocyanine Derivatives, *New J. Chem.*, 12, **1988**, 751.

[172] J. Simon, P. Bassoul, *Phthalocyanine based liquid crystals: Towards submicronic devices*, VCH, **1993**.

[173] D. Guillon, A. Skoulios, C. Piechocki, *et al.*, Discotic Mesophases of the Metal-free Derivative of Octa-(dodecyloxymethyl)-Phthalocyanine, *Mol. Cryst. Liq. Cryst.*, 100, **1983**, 275.

[174] M. K. Engel, P. Bassoul, L. Bosio, *et al.*, Mesomorphic Molecular Materials - Influence of Chain-length On the Structural-properties of Octa-alkyl Substituted Phthalocyanines, *Liq. Cryst.*, 15, **1993**, 709.

[175] G. J. Clarkson, N. B. Mckeown, K. E. Treacher, Synthesis and Characterization of Some Novel Phthalocyanines Containing Both Oligo(ethyleneoxy) and Alkyl Or Alkoxy Side-chains - Novel Unsymmetrical Discotic Mesogens, *J. Chem. Soc., Perkin Trans. 1*, **1995**, 1817.

[176] J. F. Vanderpol, E. Neeleman, J. W. Zwikker, *et al.*, Homologous Series of Liquid-crystalline Metal Free and Copper Octa-normal-alkoxyphthalocyanines, *Liq. Cryst.*, 6, **1989**, 577.

[177] P. G. Schouten, J. M. Warman, M. P. Dehaas, *et al.*, The Effect of Structural Modifications On Charge Migration In Mesomorphic Phthalocyanines, *J. Am. Chem. Soc.*, 116, **1994**, 6880.

[178] L. Dulog, A. Gittinger, Octaalkyl Esters of 2,3,9,10,16,17,23,24-(29h,31h)-phthalocyanineoctacarboxylic Acid - A New Homologous Series of Discotic Liquid-crystals, *Mol. Cryst. Liq. Cryst.*, 213, **1992**, 31.

[179] I. H. Cho, Y. S. Lim, Synthesis and Morphology of New Discogenic Phthalocyanine Derivatives, *Mol. Cryst. Liq. Cryst.*, 154, **1988**, 9.

[180] C. A. Hunter, J. K. M. Sanders, The Nature of Pi-pi Interactions, *J. Am. Chem. Soc.*, 112, **1990**, 5525.

[181] M. Mondeshki, Supramolecular Order and Dynamics of Functional Materials Studied by Solid State NMR, Ph.D. thesis, University of Mainz, **2007**.

[182] B. Wehrle, H. H. Limbach, NMR-Study of Enverironment Modulated Proton Tautomerism in Crystalline and Amorphous Phthalocyanine, *Chem. Phys.*, 136, **1989**, 223.

[183] S. Matsumoto, K. Matsuhama, J. Mizuguchi, beta metal-free phthalocyanine, *Acta Crystallogr., Sect. C: Cryst. Struct. Commun.*, 55, **1999**, 131.

[184] A. P. M. Kentgens, B. A. Markies, J. F. Vanderpol, *et al.*, A Structural Investigation of Octa-normal-undecoxyphthalocyanine In the Solid and Liquid-crystalline State and of Poly(octa-normal-undecoxyphthalocyaninato)siloxane by High-Resolution Solid-State NMR Spectroscopy, *J. Am. Chem. Soc.*, 112, **1990**, 8800.

[185] M. J. Cook, S. J. Cracknell, G. R. Moore, *et al.*, Solution Phase H-1 and C-13-nmr Studies of Some 1,4,8,11,15,18,22,25-octa-alkylphthalocyanines, *Magn. Reson. Chem.*, 29, **1991**, 1053.

[186] G. Zucchi, P. Viville, B. Donnio, *et al.*, Miscibility between Differently Shaped Mesogens: Structural and Morphological Study of a Phthalocyanine-Perylene Binary System, *J. Phys. Chem. B*, 113, **2009**, 5448.

[187] N. B. McKeown, M. Helliwell, B. M. Hassan, *et al.*, The self-ordering properties of novel phthalocyanines with out-of-plane alkyl substituents, *Chem. Eur. J.*, 13, **2007**, 228.

[188] S. Sergeyev, E. Pouzet, O. Debever, *et al.*, Liquid crystalline octaalkoxycarbonyl phthalocyanines: design, synthesis, electronic structure, self-aggregation and mesomorphism, *J. Mater. Chem.*, 17, **2007**, 1777.

[189] C. R. Fincher, M. Ozaki, A. J. Heeger, *et al.*, Donor and Acceptor States in Lightly Doped Polyacetylene, *Phys. Rev. B: Condens. Matter*, 19, **1979**, 4140.

[190] R. Pino, G. Scuseria, Importance of chain-chain interactions on the band gap of trans-polyacetylene as predicted by second-order perturbation theory, *J. Chem. Phys.*, 121, **2004**, 8113.

[191] M. Kertesz, C. Choi, S. Yang, Conjugated polymers and aromaticity, *Chem. Rev.*, 105, **2005**, 3448.

[192] M. Fahlman, M. Logdlund, S. Stafstrom, *et al.*, Experimental and Theoretical Studies of the Electronic Structur of Poy-(p-phenylenevinylene) and some Ring-Substituted Derivatives, *Macromolecules*, 28, **1995**, 1959.

[193] U. Stalmach, H. Detert, H. Meier, *et al.*, Relationship between structure and electroluminescence of oligo(y-phenylenevinylene)s, *Opt. Mater.*, 9, **1998**, 77.

[194] K. Meerholz, H. Gregorius, K. Müllen, *et al.*, Voltammetric Studies Of Solution and Solid-State Properties of Monodisperse Oligo(*P*-Phenylenevinylene)s, *Adv. Mater.*, 6, **1994**, 671.

[195] A. Ajayaghosh, V. K. Praveen, S. Srinivasan, *et al.*, Quadrupolar pi-gels: Sol-gel tunable red-green-blue emission in donor-acceptor-type oligo(p-phenylenevinylene)s, *Adv. Mater.*, 19, **2007**, 411.

[196] H. Detert, E. Sugiono, Soluble oligo(phenylenevinylene)s with electron withdrawing substituents for the use in light emitting diodes, *Synth. Met.*, 115, **2000**, 89.

[197] A. P. H. J. Schenning, E. Peeters, E. W. Meijer, Energy transfer in supramolecular assemblies of oligo(p-phenylene vinylene)s terminated poly(propylene imine) dendrimers, *J. Am. Chem. Soc.*, 122, **2000**, 4489.

[198] F. S. Precup-Blaga, A. P. H. J. Schenning, E. W. Meijer, Liquid crystalline oligo(p-phenylene vinylene)-terminated poly(propylene imine) dendrimers. Synthesis and characterization, *Macromolecules*, 36, **2003**, 565.

[199] F. S. Precup-Blaga, J. C. Garcia-Martinez, A. P. H. J. Schenning, *et al.*, Highly emissive supramolecular oligo(p-phenylene vinylene) dendrimers, *J. Am. Chem. Soc.*, 125, **2003**, 12953.

[200] R. Varghese, S. J. George, A. Ajayaghosh, Anion induced modulation of self-assembly and optical properties in urea end-capped oligo(p-phenylenevinylene)s, *Chem. Commun.*, **2005**, 593.

[201] S. C. J. Meskers, M. Bender, J. Hubner, *et al.*, Interchromophoric coupling in oligo(p-phenylenevinylene)-substituted poly(propyleneimine) dendrimers, *J. Phys. Chem. A*, 105, **2001**, 10220.

[202] P. Jonkheijm, M. Fransen, A. P. H. J. Schenning, *et al.*, Supramolecular organisation of oligo(p-phenylenevinylene) at the air-water interface and in water, *J. Chem. Soc., Perkin Trans. 2*, **2001**, 1280.

[203] P. A. van Hal, R. A. J. Janssen, G. Lanzani, *et al.*, Two-step mechanism for the photoinduced intramolecular electron transfer in oligo(p-phenylene vinylene)-fullerene dyads, *Phys. Rev. B: Condens. Matter*, 64, **2001**, art. no.

[204] E. H. A. Beckers, P. A. van Hal, A. P. H. J. Schenning, *et al.*, Singlet-energy transfer in quadruple hydrogen-bonded oligo(p-phenylenevinylene)-fullerene dyads, *J. Mater. Chem.*, 12, **2002**, 2054.

[205] A. El-ghayoury, A. P. H. J. Schenning, P. A. van Hal, *et al.*, Metallo-supramolecular oligo(p-phenylene vinylene)/[60] fullerene architectures: towards functional materials, *Thin Solid Films*, 403, **2002**, 97.

[206] C. Daniel, F. Makereel, L. M. Herz, *et al.*, The effects of supramolecular assembly on exciton decay rates in organic semiconductors, *J. Chem. Phys.*, 123, **2005**, 084902.

[207] A. P. H. J. Schenning, P. Jonkheijm, F. J. M. Hoeben, *et al.*, Towards supramolecular electronics, *Synth. Met.*, 147, **2004**, 43.

[208] L. M. Herz, C. Daniel, C. Silva, *et al.*, Exciton dynamics in supramolecular assemblies of p-phenylenevinylene oligomers, *Synth. Met.*, 139, **2003**, 839.

[209] F. J. M. Hoeben, A. P. H. J. Schenning, E. W. Meijer, Energy-transfer efficiency in stacked oligo(p-phenylene vinylene)s: Pronounced effects of order, *ChemPhysChem*, 6, **2005**, 2337.

[210] M. H. Chang, F. J. M. Hoeben, P. Jonkheijm, *et al.*, Influence of mesoscopic ordering on the photoexcitation transfer dynamics in supramolecular assemblies of oligo-p-phenylenevinylene, *Chem. Phys. Lett.*, 418, **2006**, 196.

[211] E. E. Neuteboom, S. C. J. Meskers, P. A. van Hal, *et al.*, Alternating oligo(p-phenylene vinylene)-perylene bisimide copolymers: Synthesis, photophysics, and photovoltaic properties of a new class of donor-acceptor materials, *J. Am. Chem. Soc.*, 125, **2003**, 8625.

[212] E. H. A. Beckers, Z. J. Chen, S. C. J. Meskers, *et al.*, The importance of nanoscopic ordering on the kinetics of photoinduced charge transfer in aggregated pi-conjugated hydrogen-bonded donor-acceptor systems, *J. Phys. Chem. B*, 110, **2006**, 16967.

[213] P. Jonkheijm, J. K. J. van Duren, M. Kemerink, *et al.*, Control of film morphology by folding hydrogen-bonded oligo(p-phenylenevinylene) polymers in solution, *Macromolecules*, 39, **2006**, 784.

[214] M. Shirakawa, S. Kawano, N. Fujita, *et al.*, Hydrogen-bond-assisted control of H versus J aggregation mode of porphyrins stacks in an organogel system, *J. Org. Chem.*, 68, **2003**, 5037.

[215] E. H. A. Beckers, S. C. J. Meskers, A. P. H. J. Schenning, *et al.*, Influence of intermolecular orientation on the photoinduced charge transfer kinetics in self-assembled aggregates of donor-acceptor arrays, *J. Am. Chem. Soc.*, 128, **2006**, 649.

[216] A. P. H. J. Schenning, E. W. Meijer, Supramolecular electronics; nanowires from self-assembled pi-conjugated systems, *Chem. Commun.*, **2005**, 3245.

[217] G. W. Gray, *The Molecular Physics of Liquid Crystals*, Academic Press, $1^{st}$ edition, **1977**.

[218] A. P. H. J. Schenning, P. Jonkheijm, E. Peeters, *et al.*, Hierarchical order in supramolecular assemblies of hydrogen-bonded oligo(p-phenylene vinylene)s, *J. Am. Chem. Soc.*, 123, **2001**, 409.

[219] J. H. K. K. Hirschberg, L. Brunsveld, A. Ramzi, *et al.*, Helical self-assembled polymers from cooperative stacking of hydrogen-bonded pairs, *Nature*, 407, **2000**, 167.

[220] P. Jonkheijm, F. J. M. Hoeben, R. Kleppinger, *et al.*, Transfer of pi-conjugated columnar stacks from solution to surfaces, *J. Am. Chem. Soc.*, 125, **2003**, 15941.

[221] S. J. George, A. Ajayaghosh, P. Jonkheijm, *et al.*, Coiled-coil gel nanostructures of oligo(p-phenylenevinylene)s: Gelation-induced helix transition in a higher-order supramolecular self assembly of a rigid pi-conjugated system, *Angew. Chem. Int. Ed.*, 43, **2004**, 3422.

[222] A. Miura, P. Jonkheijm, S. De Feyter, *et al.*, 2D self-assembly of oligo(p-phenylene vinylene) derivatives: From dimers to chiral rosettes, *SMALL*, 1, **2005**, 131.

[223] A. Gesquiere, P. Jonkheijm, F. J. M. Hoeben, *et al.*, 2D-Structures of quadruple hydrogen bonded oligo(p-phenylenevinylene)s on graphite: Self-assembly behavior and expression of chirality, *Nano Lett.*, 4, **2004**, 1175.

[224] P. Jonkheijm, A. Miura, M. Zdanowska, *et al.*, pi-conjugated oligo-(p-phenylenevinylene) rosettes and their tubular self-assembly, *Angew. Chem. Int. Ed.*, 43, **2004**, 74.

[225] L. Stradella, M. Argentero, A study of the thermal decomposition of urea, of related compounds and thiourea using DSC and TG-EGA, *Thermochim. Acta*, 219, **1993**, 315.

[226] I. Dierking, *Textures of Liquid Crystals*, Wiley-VCH, Weinheim, $1^{st}$ edition, **2003**.

[227] W. Pisula, Z. Tomovic, M. Wegner, *et al.*, Liquid crystalline hydrogen bonded oligo(p-phenylenevinylene)s, *J. Mater. Chem.*, 18, **2008**, 2968.

[228] W. Pisula, Z. Tomovic, C. Simpson, *et al.*, Relationship between core size, side chain length, and the supramolecular organization of polycyclic aromatic hydrocarbons, *Chem. Mater.*, 17, **2005**, 4296.

[229] S. J. George, Z. Tomovic, M. M. J. Smulders, *et al.*, Helicity induction and amplification in an oligo(p-phenylenevinylene) assembly through hydrogen-bonded chiral acids, *Angew. Chem. Int. Ed.*, 46, **2007**, 8206.

[230] K. E. Maly, C. Dauphin, J. D. Wuest, Self-assembly of columnar mesophases from diaminotriazines, *J. Mater. Chem.*, 16, **2006**, 4695.

[231] Y. J. Lee, T. Murakhtina, D. Sebastiani, *et al.*, H-2 solid-state NMR of mobile protons: It is not always the simple way, *J. Am. Chem. Soc.*, 129, **2007**, 12406.

[232] C. Daniel, L. M. Herz, C. Silva, *et al.*, Exciton bimolecular annihilation dynamics in supramolecular nanostructures of conjugated oligomers, *Phys. Rev. B: Condens. Matter*, 68, **2003**, 235212.

[233] J. Hutter, *et al.*, Computer code CPMD, version 3.12, **1990-2005**, Copyright IBM Corp. and MPI-FKF Stuttgart, `http://www.cpmd.org`.

[234] W. Kohn, L. J. Sham, Self-Consistent Equations Including Exchange and Correlation Effects, *Phys. Rev. Lett.*, 140, **1965**, A1133.

[235] R. Car, M. Parrinello, A combined approach to DFT and molecular dynamics, *Phys. Rev. Lett.*, 55, **1985**, 2471.

[236] A. D. Becke, Density-functional exchange-energy approximation with correct asymptotic behavior, *Phys. Rev. A: At. Mol. Opt. Phys.*, 38, **1988**, 3098.

[237] C. Lee, W. Yang, R. G. Parr, Development of the Colle-Salvetti correlation-energy formula into a functional of the electron density, *Phys. Rev. B: Condens. Matter*, 37, **1988**, 785.

[238] S. Goedecker, M. Teter, J. Hutter, Separable dual-space Gaussian pseudopotentials, *Phys. Rev. B: Condens. Matter*, 54, **1996**, 1703.

[239] C. Hartwigsen, S. Goedecker, J. Hutter, Relativistic separable dual-space Gaussian pseudopotentials from H to Rn, *Phys. Rev. B: Condens. Matter*, 58, **1998**, 3641.

[240] D. Sebastiani, M. Parrinello, A new method to compute NMR chemical shifts in periodic systems, *J. Phys. Chem. A*, 105, **2001**, 1951.

# List of Figures

# List of Tables

# A. Pulse Progams and Automatations

## A.1. Standard Experiments

### A.1.1. Single Pulse Excitation

```
1 ze
2 d1
  (p1 pl1 ph1):f1
  go=2 ph31
  wr #0
exit

ph1= 0 2 1 3
ph31=0 2 1 3
```

### A.1.2. HARTMANN-HAHN CP

```
1 ze
2 d1 do:f2
  (p1 pl12 ph1):f2
  (p15 pl1 ph2):f1 (p15 pl2 ph10):f2
  (p3 pl3 ph3):f1 (1u cpds2):f2
  go=2 ph31
  1m do:f2
  wr #0
exit

ph0= 0
ph1= 1 3
ph2= 0 0 2 2 1 1 3 3
ph3= 1 1 3 3 2 2 0 0
ph10= 0
ph31= 0 2 2 0 1 3 3 1
```

### A.1.3. *ramp*-CP

```
1 ze
2 d1 do:f2
  (p3 pl12 ph1):f2
  (p15 pl1 ph2):f1 (p15:sp0 ph10):f2
  go=2 ph31
  1m do:f2
  wr #0
exit

ph0= 0
ph1= 1 3
ph2= 0 0 2 2 1 1 3 3
ph3= 1 1 3 3 2 2 0 0
ph10= 0
ph31= 0 2 2 0 1 3 3 1
```

# A.2. Recoupling Experiments

## A.2.1. Heteronuclear Dipolar Recoupling: *REPT-HSQC*

```
"l31=td1/l30"
"p2=p1*2"
"d4=(0.5s/cnst31)-p1*2" ; l31 = nu_R / 10
"d11=(0.5s/cnst31)-p1"
"d12=(0.5s/cnst31)-p1*1.5"
"d13=0.5*p1"
"l1=(l5-1)/2"
"l2=l1"
"l0=l5-1-l1*2"

1 ze
2 d1 do:f2
  ;1u fq=cnst22:f2
  10u pl1:f1 pl2:f2

3 (p1 ph20^):f1
  13m
  (p1 ph21^):f1
  7m
  (p1 ph22^):f1
  1m
  (p1 ph23^):f1
  3m
  lo to 3 times 4

  d5

  (p1 ph1):f2
  d11
4 (p2 ph6):f1
  d4
  (p2 ph7):f1
  d4
  lo to 4 times l1
5 (p2 ph6):f1
  d4
  lo to 5 times l0
  (p2 ph8):f2
6 d4
  (p2 ph6):f1
  d4
  (p2 ph7):f1
  lo to 6 times l1
7 d4
  (p2 ph6):f1
  lo to 7 times l0
  d12

  d0

  (p1 ph2):f1   (p1 ph3):f2
  d12
8 (p2 ph6):f2
  d4
  (p2 ph7):f2
  d4
  lo to 8 times l2
9 (p2 ph6):f2
  d4
  lo to 9 times l0
  (p2 ph9):f1
  d4
10 (p2 ph6):f2
  d4
  (p2 ph7):f2
  d4
  lo to 10 times l2
11 (p2 ph6):f2
  d4
  lo to 11 times l0
  d13
  (p1 ph4):f1
  d6 pl12:f2
  (p1 ph5):f1
  go=2 ph31 cpd2:f2
  2m do:f2
  30m wr #0 if #0 zd
  1m ip3
  lo to 2 times l30
  1m id0
  lo to 2 times l31
  exit

ph1= 0 2 1 3 2 0 3 1  2 0 3 1 0 2 1 3
ph2= 1 3 2 0 3 1 0 2
ph3= 1 1 2 2 3 3 0 0
ph4= 2 2 3 3 0 0 1 1

ph5 = 0 0 1 1 2 2 3 3  2 2 3 3 0 0 1 1

ph6= 0
ph7= 1
ph8= 1 3 2 0 3 1 0 2
ph9= 2 0 3 1 0 2 1 3
ph31= 1 1 2 2 3 3 0 0

; sat comb
ph20= 0 1 2 3
ph21= 1 2 3 0
ph22= 2 3 0 1
ph23= 3 0 1 2
```

## A.2.2. Homonuclear Dipolar Recoupling: *2D Back-to-Back* aka $^1$H-$^1$H *DQ-SQ Correlation*

```
"d3=1s/(cnst31*2)-p1*2"
"d5=1s*l5/(cnst31)"
"l31=td1/l30"

1 ze
  1m pl1:f1

2 (p1 ph20^):f1
  13m
  (p1 ph21^):f1
  7m
  (p1 ph22^):f1
  1m
  (p1 ph23^):f1
  3m
  lo to 2 times 8

  d1

3 p1 ph0
  d3
  p1 ph0
  p1 ph1
  d3
  p1 ph3
  p1 ph0
  d3
  p1 ph0
  p1 ph3
  d3
  p1 ph1
  p1 ph2
  d3
  p1 ph2
  p1 ph3
  d3
  p1 ph1
  p1 ph2
  d3
  p1 ph2
  p1 ph1
  d3
  p1 ph3
  lo to 3 times l1

  d0

4 p1 ph10
  d3
  p1 ph10
  p1 ph11
  d3
  p1 ph13
  p1 ph10
  d3
  p1 ph10
  p1 ph13
  d3
  p1 ph11
  p1 ph12
  d3
  p1 ph12
  p1 ph13
  d3
  p1 ph11
  p1 ph12
  d3
  p1 ph12
  p1 ph11
  d3
  p1 ph13
  lo to 4 times l1

  d5
  p1 ph30
  go=2 ph31
  100m wr #0 if #0 zd
  1m ip0
  1m ip1
  1m ip2
  1m ip3
  lo to 2 times l30
  1m id0
  lo to 2 times l31
exit

ph0 = (8) 0 2 4 6
ph1 = (8) 2 4 6 0
ph2 = (8) 4 6 0 2
ph3 = (8) 6 0 2 4
ph10= 0
ph11= 1
ph12= 2
ph13= 3
ph30= 0 0 0 0 2 2 2 2 1 1 1 1 3 3 3 3
ph31= 0 2 0 2 2 0 2 0 1 3 1 3 3 1 3 1

ph20= 0 1 2 3
ph21= 1 2 3 0
ph22= 2 3 0 1
ph23= 3 0 1 2
```

The given sequence corresponds to a $^1$H-$^1$H DQ-SQ correlation experiment with four rotor period excitation / reconversion time. It should be noted that the phases are arranged in a supercycled manner, however, for shorter excitation / reconversion times (1 $\tau_R$, 2 $\tau_R$) the scheme has to be truncated (see 1D implementation of back-to-back in A.2.3).

### A.2.3. Homonuclear Dipolar Recoupling: *1D Back-to-Back* aka $^1$H *DQF NMR*

```
"d3=1s/(cnst31*2)-p1*2"
"d5=1s*l5/(cnst31)"
1 ze
  2m pl1:f1
2 (p1 ph20^):f1
  13m
  (p1 ph21^):f1
  7m
  (p1 ph22^):f1
  1m
  (p1 ph23^):f1
  3m
  lo to 2 times 8
  d1
3 p1 ph0
  d3
  p1 ph2
  p1 ph1
  d3
  p1 ph3
  lo to 3 times l1
  d0
4 p1 ph10
  d3
  p1 ph12
  p1 ph11
  d3
  p1 ph13
  lo to 4 times l1
  d5
  p1 ph30
  go=2 ph31
  wr #0
exit
ph0 = (8) 0 2 4 6
ph1 = (8) 2 4 6 0
ph2 = (8) 4 6 0 2
ph3 = (8) 6 0 2 4
ph10= 0
ph11= 1
ph12= 2
ph13= 3
ph30= 0 0 0 0 2 2 2 2 1 1 1 1 3 3 3 3
ph31= 0 2 0 2 2 0 2 0 1 3 1 3 3 1 3 1
ph20= 0 1 2 3
ph21= 1 2 3 0
ph22= 2 3 0 1
ph23= 3 0 1 2
```

The given sequence corresponds to a typically used $^1$H DQF NMR experiment with one rotor period excitation / reconversion time. It should be noted that the phase cycling scheme is commonly more complex for longer recoupling times (2 $\tau_R$, 4 $\tau_R$) in order to suppress offset effects and impacts of pulse imperfections (see 2D implementation of back-to-back in A.2.2).

## A.3. Saturation Recovery

```
1 ze
  2m pl1:f1
2 d1
3 5m
  (p1 ph20^):f1
  13m
  (p1 ph21^):f1
  7m
  (p1 ph22^):f1
  1m
  (p1 ph23^):f1
  lo to 3 times 8
  1u
  vd
  p1 ph30
  go=2 ph31
```

```
  30m wr #0 if #0
  ivd
  zd
  lo to 2 times td1
exit

ph20= 0 1 2 3
ph21= 1 2 3 0
ph22= 2 3 0 1
ph23= 3 0 1 2

ph1 = 0
ph2 = 1
ph3 = 2

ph30= 0 1 2 3
ph31= 0 1 2 3
```

## A.4. *t*-dependent recording of $^1$H MAS and DQF NMR spectra

```
;zg
;avance-version
;1D sequence
;d7: z-filter
;l1: number of rotor periods z-filter
;l1: number of full DQF phase cycles
;l31: number of spectra of each kind
;d5: sampling rate, note: Determines D1
"d4=d5-72s"
"l31=td1/2"
"d3=1s/(2*cnst31)-2*p1"
"d7=l1*1s/(cnst31)-p1"
"d1=((d5-220m)/(16*l2)-73*p1-4*d3-d7-384m-2*aq)/2"

#include <Avance.incl>
#include <trigg.incl>

1 ze

2 (p1 ph20^):f1                ;saturation comb
  13m
  (p1 ph21^):f1
  7m
  (p1 ph22^):f1
  1m
  (p1 ph23^):f1
  3m
  lo to 2 times 8

  d1

3 (p1 ph25):f1
  go=2 ph26
  10m wr #0 if #0 zd

  200m

4 (p1 ph20^):f1                ;saturation comb
  13m
  (p1 ph21^):f1
  7m
  (p1 ph22^):f1
  1m
  (p1 ph23^):f1
  3m
  lo to 4 times 8

  d1

5 p1 ph0                       ;exc.
  d3
  p1 ph2
  p1 ph1
  d3
  p1 ph3                       ;d0 entfernt

6 p1 ph10                     ;rec.
  d3
  p1 ph12
  p1 ph11
  d3
  p1 ph13

  d7                         ;z-filter
  p1 ph31
  go=4 ph30
  10m wr #0 if #0 zd
lo to 2 times l31
exit

ph0 = (8) 0 2 4 6
ph1 = (8) 2 4 6 0
ph2 = (8) 4 6 0 2
ph3 = (8) 6 0 2 4

ph10= 0
ph11= 1
ph12= 2
ph13= 3

ph30= 0 2 0 2 2 0 2 0 1 3 1 3 3 1 3 1
ph31= 0 0 0 0 2 2 2 2 1 1 1 1 3 3 3 3

ph20= 0 1 2 3
ph21= 1 2 3 0
ph22= 2 3 0 1
ph23= 3 0 1 2
```

```
ph25=0 2 1 3   ; SPE
ph26=0 2 1 3
```

# A.5. Through-Bond Correlation

## A.5.1. mwinadequate_ref_va_tausetup.2d

```
;SETUP FOR: Refocused inadequate 2D experiment for powdered solids
;
;A. Lesage, M. Bardet, L. Emsley,
;J. Am. Chem. Soc. volume 121, page 10987 (1999)
;This pulse program was obtained from the ENS-Lyon Pulse Program Library
;http://www.ens-lyon.fr/STIM/NMR/pp.html
;The program is intended as a guideline only.
;The authors do not provide any guarantee as to the usability of the program.
;Use of this program may lead to serious damage to your spectrometer.
;The authors are not responsible for any damage resulting from the use of this program.
;Note that all the parameters need to be properly adjusted for the program to work.
;This program may be freely copied and modified as long as the whole of this header
;is included in any copied or modified version.

;$COMMENT=refocuused INADEQUATE for solids
;$CLASS=Solids
;$DIM=1D
;$TYPE=
;$SUBTYPE=simple 1D
;$OWNER=wegnerm
#include <Avance.incl>

;modifications:
;08_08_28 WEGNER        enabled ramp-CP (ramp on protons)
;08_08_28 WEGNER        enabled decoupling albeit cw
;08_08_28 WEGNER        d10 defined as (15) times one rotor perriod
;08_10_10 WEGNER        overall duration of RF power, d31/d1*100=duty cycle in %
;09_08_19 WEGNER        optimisation for eco delay
;09_08_27 WEGNER        enabled variable incrementtion of tau
;                       A. Lesage, C. Auger, S. Caldarelli, L. Emsley,
;                       J. Am. Chem. Soc. volume 119, page 7867 (1997)


;HINTS
;p1 = 90 degree pulse
;p15 = contact pulse
;pl1 = 13C contact power
;pl2 = 1H 90deg. power leven
;pl3 = 1H contact power
;pl11 = 13C 90deg. power level
;pl12 = 1H power for decoupling
;d9 = synchronised tau delay 1
;d10 synchronised tau delay 2,3,4
;cpd decoupling is used. The decoupling sequence (e.g. tppm) needs to be defined.
;l10 number of rotor periods for incrementation

define delay taumax
"taumax=(1s*l10/cnst31)*td1"

"in10=taumax/td1"
"in9=in10"

;starting values of tau:
"d10=(1s/cnst31)-3.75u"
"d9=d10-2.75u"

define delay duty
"duty=3*p1+2*p2+p15+aq+2u+((1s/cnst31)*td1*l10*4)-17.75u"

define delay Jmin
"Jmin=0.001/(4*taumax)"
  Jmin
  duty
1 ze
2 d1 do:f2                          ;for safety
  (p1 pl2 ph1):f2                         ;proton 90 pulse
  (p15 pl1 ph2):f1 (p15:sp0 ph3):f2 ;cross-polarization

  2u pl12:f2
  2u cpd2:f2                        ;set & start decoupling (TPPM or SPINAL, ...)
  d9                                ;first tau evolution period
  (p2 ph4 pl11):f1                  ;pi pulse on carbon
  d10                               ;second tau evolution period
  (p1 ph5):f1                       ;first pi/2 pulse on carbon and creation of double quantum coherence
  d0                                ;d0 is zero here
  (p1 ph6):f1                       ;second pi/2 pulse on carbon and reconversion into antiphase coherence
  d10                               ;third tau evolution period
  (p2 ph7):f1                       ;second pi pulse
  d10                               ;fourth tau evolution period

  go=2 ph31
  1m do:f2

  30m wr #0 if #0 zd

  1m id9
  1m id10
  lo to 2 times td1
exit

ph0=0
ph1=1 3
ph2=(8) 2 2 4 4 6 6 0 0             ;phase definition as multiple of 45 degrees
ph4=(8) 0 0 2 2 4 4 6 6 2 2 4 4 6 6 0 0
        4 4 6 6 0 0 2 2 6 6 0 0 2 2 4 4
ph5=(8) 0 0 2 2 4 4 6 6
ph3=0
```

```
ph6=0
ph7=1
;ph10= (360) 15
;ph11= (360) 345
ph31=0 2 2 0 0 2 2 0 2 0 0 2 2 0 0 2
```

## A.5.2. mwinadequate_ref_va.2d

```
;SETUP FOR: Refocused inadequate 2D experiment for powdered solids
;
;A. Lesage, M. Bardet, L. Emsley,
;J. Am. Chem. Soc. volume 121, page 10987 (1999)
;This pulse program was obtained from the ENS-Lyon Pulse Program Library
;http://www.ens-lyon.fr/STIM/NMR/pp.html
;The program is intended as a guideline only.
;The authors do not provide any guarantee as to the usability of the program.
;Use of this program may lead to serious damage to your spectrometer.
;The authors are not responsible for any damage resulting from the use of this program.
;Note that all the parameters need to be properly adjusted for the program to work.
;This program may be freely copied and modified as long as the whole of this header
;is included in any copied or modified version.

;$COMMENT=refocuused INADEQUATE for solids
;$CLASS=Solids
;$DIM=1D
;$TYPE=
;$SUBTYPE=simple 1D
;$OWNER=wegnerm
#include <Avance.incl>


;modifications:
;08_08_28 WEGNER        enabled ramp-CP (ramp on protons)
;08_08_28 WEGNER        enabled decoupling albeit cw
;08_08_28 WEGNER        d10 defined as (15) times one rotor perriod
;08_10_10 WEGNER        overall duration of RF power, d31/d1*100=duty cycle in %
;09_08_19 WEGNER        optimisation for eco delay
;09_08_27 WEGNER        enabled variable incrementtion of tau
;09_08_28 WEGNER        enabled ramp CP
;09_09_02 WEGNER        added delay for non-rotorsynchronised echos
;                       A. Lesage, C. Auger, S. Caldarelli, L. Emsley,
;                       J. Am. Chem. Soc. volume 119, page 7867 (1997)


;HINTS
;p1 = 90 degree pulse
;p15 = contact pulse
;pl1 = 13C contact power
;pl2 = 1H 90deg. power leven
;sp0 = 1H ramp power
;pl11 = 13C 90deg. power level
;pl12 = 1H power for decoupling
;d9 = synchronised tau delay 1
;d10 synchronised tau delay 2,3,4
;d15 desynch.of MAS & echos (0.0 means sychronised)
;cpd decoupling is used. The decoupling sequence (e.g. tppm) needs to be defined.
;l9 number of rotor periods used for tau
;ino given by tR*l10/l11
;l10 number of rotor periods used as T1 (d0) increment
;l11 fraction of a rotor period used as T1 (d0) increment

;NOTE:
;States-TPPI    ND1 = 1, l30 = 2
;TPPI           ND1 = 2, l30 = 1

"l31=td1/l30"
;synchronise values of tau:
"d10=(1s/cnst31)*l9-3.75u"
"d9=d10-2.75u"
#ifdef synT1
"in0=(1s/cnst31)*(l10/l11)"
#endif
define delay duty
"duty=((3*p1+2*p2+p15+aq+2u+3*d10+d9+d0+l31*in0+4*d15)/d1)*100.0"
define delay Jeff
"Jeff=1s/(4*l9/cnst31)"
define pulse dummy
"dummy=duty*Jeff"
1 ze
2 d1 do:f2                          ;for safety
  (p1 pl2 ph1):f2                   ;proton 90 pulse
  (p15 pl1 ph2):f1 (p15:sp0 ph3):f2 ;cross-polarization
  2u pl12:f2
  2u cpd2:f2                        ;set & start decoupling (TPPM or SPINAL, ...)
  d9                                ;first tau evolution period
  d15
  (p2 ph4 pl11):f1                  ;pi pulse on carbon
  d10                               ;second tau evolution period
  d15
  (p1 ph5):f1                       ;first pi/2 pulse on carbon and creation of double quantum coherence
  d0                                ;d0 is zero here
  (p1 ph6):f1                       ;second pi/2 pulse on carbon and reconversion into antiphase coherence
  d10                               ;third tau evolution period
  d15
  (p2 ph7):f1                       ;second pi pulse
  d10                               ;fourth tau evolution period
  d15
  go=2 ph31
  1m do:f2
```

```
  30m wr #0 if #0 zd
  1m ip2
  1m ip4
  1m ip5
  lo to 2 times l30
  id0
  lo to 2 times l31
exit
ph0=0
ph1=1 3
ph2=(8) 2 2 4 4 6 6 0 0             ;phase definition as multiple of 45 degrees
ph4=(8) 0 0 2 2 4 4 6 6 2 2 4 4 6 6 0 0
        4 4 6 6 0 0 2 2 6 6 0 0 2 2 4 4
ph5=(8) 0 0 2 2 4 4 6 6
ph3=0
ph6=0
ph7=1
;ph10= (360) 15
;ph11= (360) 345
ph31=0 2 2 0 0 2 2 0 2 0 0 2 2 0 0 2
```

## A.6. NOESY

The used NOESY sequence with PMLG aided suppression of homonuclear dipolar couplings.

### A.6.1. mwnoesy8.2d

```
;mwnoesy8
;noesy pulse sequence
;for H high power amp
;p1: 1H 90 deg. pulse length
;pl1: 1H 90 deg. power level
;d7: mixing time
;l7: complete rotor cycles
;zgoptns : -Dnormal -Dpmlg
#ifdef normal
;d6: adjusted delay of mixing time
#endif
#ifdef pmlg
;l5: number of PMLG cycles
;p6: magic angle flip / flip back
;cnst20: LG freq. offset (lower than 120000 Hz)
;cnst19: cancel offset (always 0)
;p5: pulse length of PMLG dec.
;pl5: pulse power of PMLG dec.(use 100kHz)
#endif
"l31=td1/l30"
"cnst19=0"

define delay PMLG
"PMLG=10*p5"
"l7=(d7-p1-2*p6-2u)/(1s/cnst31)"
"l5=(((1s/cnst31)*l7))/PMLG"
"d6=(1s/cnst31)*l7-p1"

define delay synchronise
"synchronise=l7*(1s/cnst31)-l5*PMLG"

1 ze
#ifdef pmlg
  PMLG
#endif
  5u pl1:f1
2 5m
  (p1 ph20^):f1                 ;saturation comb
  13m
  (p1 ph21^):f1
  7m
  (p1 ph22^):f1
  1m
  (p1 ph23^):f1
  lo to 2 times 8
  d1
  (p1 ph1):f1
  d0
  (p1 ph2):f1
#ifdef pmlg
;----PMLG start----------------------------------
  (p6 pl1 ph6):f1
  1u fq=cnst20:f1 ;(apply frequ shift)
3 (p5 pl5 ph5^):f1
  (p5 pl5 ph5^):f1
  (p5 pl5 ph5^):f1
  (p5 pl5 ph5^):f1
  (p5 pl5 ph5^):f1
  (p5 pl5 ph5^):f1
  (p5 pl5 ph5^):f1
```

```
  (p5 pl5 ph5^):f1
  (p5 pl5 ph5^):f1
  (p5 pl5 ph5^):f1
  lo to 3 times l5
  1u fq=cnst19:f1  ;(cancel frequ shift)

  (p6 pl1 ph6):f1
  synchronise

;----PMLG end-----------------------------------
#endif

#ifdef normal
  d6
#endif

  (p1 pl1 ph3):f1
  go=2 ph31
  100m wr #0 if #0 zd
  ip1
  lo to 2 times l30
  3u id0
  lo to 2 times l31
exit

ph1 = 0 0 0 0 2 2 2 2
ph2 = 0
ph3 = 0 1 2 3
ph6 = 1 3 1 3 1 3 1 3
ph31= 0 1 2 3 2 3 0 1
ph5=(36000) 33920 29766 25610 21454 17298 35298 3454 7610 11766 15922

ph20= 0 1 2 3
ph21= 1 2 3 0
ph22= 2 3 0 1
ph23= 3 0 1 2
```

# A.7. Heteronuclear Decoupling

## A.7.1. Example: PISSARRO5

```
;$OWNER=Wegner
;Bodenhausen et.al.,CPL,466,2008,247-251.
;PISSARRO CPD sequence with N = 5
  0.5u pl=pl12
1 pcpd:0
  pcpd:180
lo to 1 times 5
2 pcpd:180
  pcpd:0
lo to 2 times 5
3 pcpd:90
  pcpd:270
lo to 3 times 5
4 pcpd:270
  pcpd:90
lo to 4 times 5
jump to 1
```

# A.8. Topspin Automations

## A.8.1. mwzipper

```
int td;
int i4;
int i5;
int startEXPNO;
char proc[200]; char proccopy[200]; char nm1[40];
char DELETERAWDATA[100];
GETCURDATA
SETCURDATA
FETCHPAR1S("TD",&td)
strcpy(nm1,name);

i2=1;i4=1;
GETINT("Enter number of components in your 2D dataset",i2)
GETINT("Enter EXPNO from which number these data sets are to be stored",i4)
startEXPNO=expno;
td=td/i2;
i1=0;
i3=0;

DATASET(nm1,i4,1,disk,user)
TIMES(i2)
    SETCURDATA
    STOREPAR1S("TD",td)
    STOREPAR1("TD",td)
    IEXPNO
END

TIMES(i2)
  i3=i3+1;
  i1=i3;
  i5=0;
  TIMES2(td)
```

```
    i5=i5+1;
    DATASET(nm1,startEXPNO,1,disk,user)
    SETCURDATA
    RSER(i1,-1,1)
    DATASET("~TEMP",1,1,disk,user)
    SETCURDATA
    WSER(i5,nm1,i4+i3-1,1,disk,user)
    i1=i1+i2;
  END
END

QUITMSG("---done!---")
```

# B. Technical Details of the DFT Simulations

All simulations have been performed with the quantum chemical program package CPMD[233], which is based on the KOHN-SHAM formulation of Density Functional Theory[234], using plane waves as basis set and the CAR-PARRINELLO method for molecular dynamics simulations[235]. In all simulations the exchange and correlation energy was modeled with the BLYP functional[236, 237] and pseudopotentials of the GOEDECKER-type were employed[238, 239]. The plane wave cutoff was set to 80 Ry. Before the calculation of the NMR parameters, the structures were optimized using a force threshold of $5 \cdot 10^{-4}$ atomic units. The NMR chemical shifts were calculated fully from first principles [240]. The computed nuclear shieldings were referenced directly to computed shieldings of tetramethylsilane. For a better comparison with experimental spectra, we convoluted the computed shift values with Gaussians.